A-posteriori Correction Methods for Antenna Measurements by Wavelets

Alice Quennelle

▶ **To cite this version:**

Alice Quennelle. A-posteriori Correction Methods for Antenna Measurements by Wavelets. Electronics. Université de Toulouse, 2024. English. NNT : 2024TLSES075 . tel-04925295

HAL Id: tel-04925295

https://theses.hal.science/tel-04925295v1

Submitted on 2 Feb 2025

HAL is a multi-disciplinary open access archive for the deposit and dissemination of scientific research documents, whether they are published or not. The documents may come from teaching and research institutions in France or abroad, or from public or private research centers.

L'archive ouverte pluridisciplinaire **HAL**, est destinée au dépôt et à la diffusion de documents scientifiques de niveau recherche, publiés ou non, émanant des établissements d'enseignement et de recherche français ou étrangers, des laboratoires publics ou privés.

RÉPUBLIQUE FRANÇAISE
Liberté Égalité Fraternité

Université de Toulouse

Doctorat de l'Université de Toulouse

préparé à l'Université Toulouse III - Paul Sabatier

Méthode de correction a-posteriori de mesures d'antennes par ondelettes

Thèse présentée et soutenue, le 11 avril 2024 par

Alice QUENNELLE

École doctorale
GEETS - Génie Electrique Electronique,Télécommunications et Santé : du système au nanosystème

Spécialité
Electromagnétisme et Systèmes Haute Fréquence

Unité de recherche
ENAC-LAB - Laboratoire de Recherche ENAC

Thèse dirigée par
Alexandre CHABORY

Composition du jury
M. Olivier PASCAL, Président, Université Toulouse III - Paul Sabatier
Mme Geneviève MAZÉ-MERCEUR, Rapporteure, CEA CESTA
M. Christophe ROBLIN, Rapporteur, Institut Polytechnique de Paris
M. Nicolas MÉZIÈRE, Examinateur, Centre National d'Etudes Spatiales
M. Laurent LE COQ, Examinateur, Université de Rennes
M. Alexandre CHABORY, Directeur de thèse, Ecole Nationale d'Aviation Civile

Membres invités
M. Gildas KUBICKÉ, DGA

Acknowledgement

Je voudrais remercier, dans un premier temps, la Direction Générale de l'Armement (DGA) ainsi que le Centre National d'Études Spatiales (CNES) pour m'avoir proposé ce sujet de thèse et pour le financement de ces travaux. Je tiens également à remercier l'École Nationale de l'Aviation Civile (ENAC) pour l'accueil dans son laboratoire TELECOM-EMA (Électromagnétisme et Antenne). Je remercie aussi l'école doctorale Génie Électrique, Électronique, Télécommunications et Santé (GEETS) pour l'encadrement de la thèse.

Je tiens à remercier les membres du jury, en particulier les rapporteurs Mme Geneviève Mazé-Merceur et M. Christophe Roblin, qui ont pris le temps de relire et commenter mon manuscrit. Merci à M. Olivier Pascal (président), M. Laurent Le Coq (examinateur), Nicolas Mézière (examinateur CNES), Gildas Kubické (invité/examinateur DGA) et Alexandre Chabory (directeur de thèse), pour avoir accepté de faire partie de mon jury. Je les remercie grandement pour leur enthousiasme et toutes leurs questions.

Je remercie grandement mes encadrants pour leur expertise et leur engagement. Je remercie donc Alexandre Chabory (professeur à l'ENAC et responsable du laboratoire EMA) pour avoir cru en moi, pour sa patience, pour toutes ses connaissances et son expertise, pour sa disponibilité et son perfectionnisme qui m'ont permis de terminer cette thèse en beauté (quoiqu'un peu en retard). Merci à Romain Contreres, mon ancien directeur de stage au CNES, qui m'a proposé de mener cette thèse, pour son enthousiasme et sa bonne humeur. Je remercie Gwenn Lefur du CNES, qui a pu apporter son expertise en mesure d'antenne au début du doctorat. Et finalement, je remercie Nicolas Mézières pour son expertise également et toutes les relectures qu'il a faites de mon manuscrit. Je remercie mes encadrants de la DGA, Philippe Pouliguen et Janic Chauveau, pour le suivi de mes travaux et la visite des infrastructures de mesure à Bruz.

Ensuite, je voudrais remercier le laboratoire TELECOM, et donc Christophe Macabiau, de m'avoir bien accueillie dans une ambiance chaleureuse. Merci à Lucille Kuhler, Rémi Douvenot, Jérémy Vézinet, Hélène Galiègue, Julien Lesouple, Paul Thévenon, Zeina El Ahdab, Mathieu Élineau, Christophe Morlaas, Antoine Blais, Anaïs Martineau, Anne-Christine Escher, Axel Garcia Pena et Carl Milner. Merci pour les pauses café qui pouvaient durer une heure, les discussions intéressantes, les potins sur les élèves et les telecom drinking! Merci aussi à Hélène Weiss d'être tellement sympa.

Bien sûr, je remercie toutes les personnes avec qui j'ai partagé le bureau et les doctorant.e.s que j'ai croisés en chemin : Uighar avec qui j'ai bu mon premier café en tant que doctorante, Alexandre Chardin et ses gâteaux (qui est maintenant un collègue de THALES), Maxandre Coulomb et Thomas Verheyde pour avoir été des exemples d'assiduité au travail (...). Merci à Guillaume Novella, David Morales et Bruno de Araújo pour leur calme et leur gentillesse. Merci à Arielle Gantelet de m'avoir fait rêver de Nouméa. Je remercie Nicolas

Gault, qui m'a le premier rejoint dans la F011 après le déménagement dans les nouveaux locaux. Merci à Émile Guizot -la Guiz- pour son calme et ses réponses à mes questions en traitement du signal et en Python. Merci à Victor Darchy pour le rugby. Ensuite, c'est Hakim Cherfi qui nous a rejoints, merci le H. Il y avait une sacré bonne ambiance dans la F011, mais je ne rentrerai pas dans les détails, ça va cringer Nico. Merci à Anthony Guillard pour la bonne humeur qu'il apportait quand il passait au labo. Et merci aux cracks de la recherche ENAC : Mathieu Hussong, Mehdi Djelloul et Loïc Chigari. Je ne vous remercie pas pour les math meetings, initiés par Nico, je n'en ai pas fait un seul.

Je souhaite bon courage aux nouveaux/nouvelles : Anne-Laure Vergnes, Clémence Alietta et Audric Boiteau.

Merci à mes amis du bâtiment Z, qui étaient déjà des amis de l'ENAC pour la plupart. Merci pour les cafés 'en terrasse' : Denis Berezia, Corentin Conan (partis trop tôt), Mathieu Verdoucq, Geoffrey Scozzaro, Ridwane Aissaoui, Timothée Gavin. Merci à Clarisse Benali pour être venue nous tenir compagnie régulièrement dans le bureau.

Merci aux autres représentants des doctorants.

Merci à la grande famille du rugby à l'ENAC : merci Patoche, Yannick, Nico et Pascal et à Agnès et Yoyo. Et un immense merci au VII ENAC : Alexia, Cassandra, Elise, Lucy, Lucille, Pauline, Emma, Louison, Estelle, etc. Ma vie en thèse aurait été moins drôle sans vous.

Merci à mes amis de Toulouse et de l'ENAC pour leur indéfectible talent pour kiffer la life : ceux que je voyais très souvent Aristée, Charline, Marie, Emma Dina, Leo-Paul. Ceux que je vois un peu plus maintenant à Paris : Maureen, Matthieu, Guilhem, Morgan, Jérôme, Théo et Thibault.

Merci à mes amis d'enfance qui sont toujours là : Lauren, Ariane, Léa, Axel, Juliette et Milena. Et seront toujours là, j'espère.

Merci à ma coloc Annelise Caplot. Regarder SNK et la CDM de rugby avec toi était mon moment de détente pendant les longs mois de rédaction.

Un grand merci à mon chéri Preston Monguélé pour m'avoir supportée en télétravail pendant le confinement au début de la thèse et pour être ensuite descendu de la grande cité de Reims régulièrement. Heureusement que je ne t'ai pas écouté et que je n'ai pas tenté de rentrer dans la DGAC avant de finir ma thèse.

Merci à ma famille : Papa, Maman, Mamie, Sophie, Florence et Mathieu, pour leur soutien indéfectible bien que je ne sois pas la première docteure de la famille, Sophie a même deux thèses. Merci à mon beau frère le docteur Clément Hénin de m'avoir encouragé. Merci à Émile Henin, mon neveu, d'être né pendant cette thèse.

Merci à mes collègues de THALES et à mon manager de m'avoir accueillie dans le monde des radios HF avec enthousiasme et bienveillance. Merci de m'avoir laissé terminer ma thèse en parallèle de mon arrivée.

Merci à Jason Mcewen et Yves Wiaux pour leurs travaux sur lesquels je me suis amplement appuyée.

J'espère n'avoir oublié personne. Trois ans, c'est long et court à la fois et j'ai eu la chance d'y rencontrer plein de gens formidables.

Docteure Alice Quennelle.

Contents

This document may not be reproduced, modified, adapted, published, translated in any way, in whole or in part, nor disclosed to a third party without the prior written consent of ENAC. © 2023, ENAC

Introduction

Context

Nowadays, the designing of new antennas always begins with weeks or months of simulations. However, at some point, the system is manufactured and has to go into a necessary measurement phase [1]. This phase aims at assessing the performances of the Antenna Under Test (AUT), in accordance with specified criteria, and verifying its functionality in various applications, such as wireless communication, radar systems, and satellite communication [2, 3].

The measurement process entails evaluating the radiation pattern in both co and cross-polarisation across all directions, either when the antenna is alone or installed on its designated platform, the whole forming the Device Under Test (DUT). Ideally, the measurement signal is collected with a probe, generally another antenna placed far enough from the AUT, to respect the far-field conditions [4, 5]. This condition is fulfilled when the distance is larger than

$$d > \frac{2D^2}{\lambda}, \tag{1}$$

with D the size of the AUT and λ the wavelength.

However, this condition can yield unrealistic distances between the probe and the antenna. Consequently, measurements are usually performed in specific facilities, adapted to emulate far-field conditions like compact range systems or to post-process the signal like in near-field range systems [2].

These facilities are also designed in order to avoid perturbations, so that the radiation of the AUT or DUT can be considered to be in free space. Generally, these facilities are anechoic chamber, which are rooms with walls covered by absorbing materials.

However spurious reflections, noise and multipath remain, even for the most precise devices. These perturbations come from numerous sources like reflections on metallic measurement devices, electronic noise, thermal noise, cosmic rays or coupling. Moreover, the raw measurement data needs to be processed in order to extract the usefull information. Consequently, in addition to research on improving the materials, post-processing methods are developed in order to improve measurement accuracy and times. Several methods of post-processing exist in the literature. Firstly, Near-field to Far-Field Transformation (NFFT) methods allow to determine the far-field radiation pattern of an antenna based on near-field measurements [6, 7, 8]. Methods are also developed to shorten antenna measurement times, for example by increasing the sparsity of the measurement sampling points [9, 10]. Finally, many methods intend to attenuate the effect of the environment, such as time-gating methods that take advantage of the delays existing between multipath to isolate the signal of interest [11]. Current reconstruction methods and spatial filtering

This document may not be reproduced, modified, adapted, published, translated in any way, in whole or in part, nor disclosed to a third party without the prior written consent of ENAC. © 2023, ENAC

rely on the equivalent current representation of the AUT [12, 13]. In particular, in many methods, the correction relies on the expansion of the field in harmonics like in probe correction [6, 14], spectral filtering [15] or test zone field compensation methods [16, 17, 18]. These methods take advantage of different properties of the spectrum and aims to split as precisely as possible the radiation pattern of the antenna from the electromagnetic environment.

In the case of antenna measurement, data are mostly organised spherically, as antenna far-field patterns are defined on a sphere, and many antenna measurement facilities are designed for spherical measurements. This is the reason why spherical tools have been developed. In particular the spherical harmonics are the most well-known expansion basis for antenna measurement analysis [6]. Additionally, antenna radiations are fields of vectors, that is the reason why the spin concept is attractive. This has been developed and applied to spherical harmonics by Penrose [19, 20]. This concept allows to express fields of vectors tangent to a sphere in terms of spin components, which have promising rotation properties. Moreover, McEwen & Wiaux have developed fast and stable spin spherical harmonic transform algorithms, along with sampling theorem on the sphere [21].

Additionally, these researchers have also led recent works on wavelets on the sphere. Wavelets are commonly used to compress images (JPEG), to perform deconvolution or denoising in many domains of physics and engineering [22, 23]. Specific spherical wavelets have recently been developed to analyse data on the sphere [24] and the multiresolution analysis in wavelet has been used to describe the cosmic microwave background [25]. McEwen & Wiaux have also developed fast spin spherical wavelet algorithms in [26]. Consequently, this type of expansion could bring another dimension to analyse antenna measurements on the sphere and develop correction methods. In particular, the wavelet transform allows to determine the regions where contributors to the field are observed in both space and spectral domains, which would add up to the spherical harmonics analysis to better discriminate unwanted perturbations to the measurement.

Objectives

The main objectives of this PhD thesis are to develop analysis and correction methods for spherical antenna measurements based on spin spherical harmonics and wavelets. These methods have to meet computation-time and accuracy requirements. The detailed objectives of the thesis are:

- To analyse the benefits of spin spherical harmonics, in the domain of antennas and to formulate their link with the spherical harmonics as defined by Hansen [6].
- To develop the use of spin spherical wavelets as radiation analysis tools.
- To rigorously formulate the antenna measurement problem, from basic electromagnetism theorems.
- To test correction methods, on a simulated simplified case, based on deconvolution and denoising, with Fourier and wavelet transform.

Outline

The thesis is composed of six chapters:

In the **first chapter**, a state of the art on antenna measurement is proposed. To begin with, the antenna measurement facilities are introduced. Measurements can be performed in various environments and configurations, depending on their specifications. Various equipments are presented. They play an important role, ensuring the measurement is as fast and precise as possible. The elements such as the absorbing materials, the probe and the positioners are discussed.

In the **second chapter**, the spherical analysis and post-processing tools for antenna measurements are presented. Firstly, spherical coordinate systems and operators are reminded: the spherical coordinates, the Euler angles and the rotation operators are given. Then the spherical harmonics, as defined by Hansen, are introduced. They are the standard harmonics, used for antenna measurements. Examples of spherical harmonic transforms of antenna radiation pattern are given. Finally, a review of antenna measurement post-processing methods is proposed.

In the **third chapter**, a spherical harmonic formulation developed by Penrose in the 60's [19], the spin spherical harmonics is presented. Firstly, a state of the art on spin spherical harmonics is proposed. In particular, the spin formulation is accurate to describe fields on the sphere and possesses remarkable local and global rotation properties. These functions have been developed to describe data over the sphere, in parallel with a sampling theorem and a fast spin spherical harmonics transform. A relation between this formulation and the Hansen formulation exists, and is derived in this chapter, enabling the use of spin for the analysis of antenna measurement. Consequently, examples of analyses of radiation patterns and RCS by means of spin spherical harmonics are given, both from simulated and measured data.

In the **fourth chapter**, spin spherical wavelets are introduced. For pedagogical purposes, multiresolution wavelets for 1D signals are presented first, as this is commonly used in 1D data analysis. The wavelet transform of both continuous and discrete signals is derived. Then spherical wavelets are introduced, as developed by J. McEwen and Y. Wiaux. They allow the wavelet transform of spin spherical data, in continuity with the spin spherical harmonics. Finally, examples of spin spherical wavelet transforms are presented.

In the **fifth chapter**, the objective is to demonstrate that the measurement can be formulated as a convolution between the AUT and the probe radiation in the measurement environment, to which a noise term is added. This is done using traditional electromagnetism theorems such as the equivalence principle and the reciprocity theorem. Then, the antenna rotation during the measurement yields the convolution. Consequently, the antenna measurement formula is obtained in this section and developed in terms of spin. Simulations are performed in order to validate the main hypothesis of this formulation.

In the **sixth chapter**, antenna measurement corrections are performed in a 2D configuration. Firstly, the measurement formula is adapted to the studied situation. Then a deconvolution method combining spectral and wavelet transform is presented. Finally, this deconvolution method is tested on a simulated measurement case in 2D.

This document may not be reproduced, modified, adapted, published, translated in any way, in whole or in part, nor disclosed to a third party without the prior written consent of ENAC. © 2023, ENAC

Chapter 1

Antenna measurement

1.1 Introduction

The performances of an AUT are characterised by far-field parameters such as radiation pattern, gain, directivity and polarisation [5]. They are typically obtained from the measurement of a transmission, through the S_{21} parameter, via a Vector Network Analyzer (VNA) that is then processed. Measurements are usually performed in specific facilities with proper devices that collect the field radiated by antennas. They are frequently characterised embedded on the structure that will carry it (satellite, aircraft), the whole being rather named DUT. Indeed, the structure often plays a role in the radiation of the AUT.

The objective of this chapter is to draw up a state of the art in antenna measurements.

Section 1.2 presents usual environments and configurations of antenna measurement ranges [2]. Then Section 1.3 describes common equipments found in such facilities. The methods developed in this thesis will be tested on measurements performed in the ENAC antenna test range that is described briefly in Section 1.4.

1.2 Antenna measurement ranges

1.2.1 Introduction

An antenna test range usually consists of a measurement chamber or an open space with specialised equipment and instrumentation: one or several probes, network analysers, spectrum analysers, signal generator, etc. The range also contains one or several turntables or positioners to rotate or move the antenna and the probe for different measurement configurations. The AUT can be in reception and the probe in transmission or the opposite, which is equivalent as they both are reciprocal [27]. In this chapter, if not explicitly written, the AUT is in reception and the probe in transmission.

The choice of the test range depends on the antenna type, the frequency range, and the specific measurement requirements. The range and the instrumentation constitute the physical environment of the measurement. The electromagnetic environment on the other hand, is defined as every radiation in the measurement volume that is not part of the

This document may not be reproduced, modified, adapted, published, translated in any way, in whole or in part, nor disclosed to a third party without the prior written consent of ENAC. © 2023, ENAC

antenna radiation pattern. Both of them have a considerable influence on the accuracy of the measurement.

In this section, measurement facilities are presented. In Section 1.2.2 they are classified by the physical environment the measurement is run into. Given that the objective of the antenna measurement is to obtain the far-field radiation pattern of an antenna, Section 1.2.3 presents the different configurations allowing this measurement. Firstly, it focuses on measurements where the AUT and the probe are in the far-field zone of each other. However, this method inducing strong constraints on the measurement configuration, alternative solutions are also described.

1.2.2 Measurement environments

1.2.2.1 Unconfined measurement range

Unconfined test ranges concern antenna measurements in open area, without any chamber or layout that would isolate the AUT from exterior perturbations. This can be done in a lab or outside, as shown in Figure 1.1.

When performed in a lab, this type of measurement is cheap but very limited in terms of accuracy. This solution is notably sometimes used for short-range high-frequencies systems (beyond X band).

Outdoor measurement ranges are convenient to perform large antenna measurements in far-field conditions. They can be either fixed or portable, depending on the application [28].

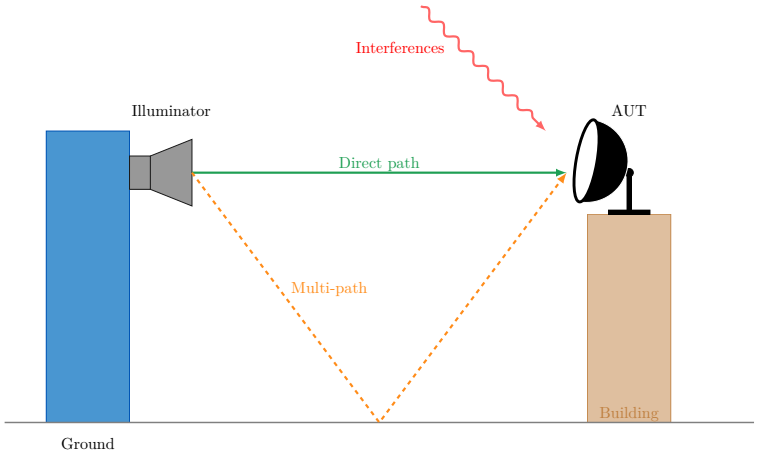

Figure 1.1: Scheme of an outdoor range

However, this type of measurements suffers from a lot of disturbances, e.g. multipath or interferences. For the latter, usual causes are mobile communications, radar, or telemetry systems [2]. Consequently most antenna measurements are performed in specific chambers, within which the environment is controlled.

1.2.2.2 Shielded enclosures

A shielded enclosure is a Faraday-cage-type room, according to [2]. This is typically a box made of conductive materials, such as metal, that stops electromagnetic waves.

This design ensures that any external electromagnetic waves are effectively blocked or attenuated, preventing them from interfering with the antenna measurement process.

Most of the antenna measurement ranges are in shielded rooms as it provides a controlled environment for accurate antenna testing by reducing the influence of interferences and ambient electromagnetic fields as well as reducing the constraints for measurements in protected frequency bands.

To prevent diffraction on edges or the entrance of electromagnetic signals, a shielded enclosure needs to be equipped with specific doors and RF-tight seals. Additionally, connectors and waveguides are specifically installed to enable the transmission of signals both in and out of the room, without jeopardising the sealing of the room.

1.2.2.3 Reverberation chamber

According to [29], a reverberation chamber is a shielded room with an arbitrarily-shaped metallic rotating paddle (stirrer or tuner). The paddle is designed to be non-symmetric and to create a continuously changing boundary condition of the electromagnetic fields in the chamber. Rotating the paddle yields a statistical environment that is of interest in the domain of electromagnetic compatibility, i.e. the ability of a system to work acceptably in its electromagnetic environment. They are less commonly used for antenna measurement. Nevertheless, the waves generated by the AUT propagate within the chamber, they bounce off the highly reflective walls and scattering elements. This results in multiple reflections and a complex interference pattern. The waves mix and interact with each other, creating a statistically steady-state field distribution, which can be distinguished from the statistical environment of the chamber with correlation calculations [30], [31]. For example measurement of the performance of a mobile terminal antenna in a reverberating chamber is described in [32].

1.2.2.4 Anechoic chamber

An anechoic range is a room designed to control the environment of the AUT [2]. Its walls are totally covered with absorbing materials to diminish reflections. Generally, they are also shielded to eliminate external electromagnetic interferences. Its size and instrumentation vary depending on the application (type of antennas, size, frequency band, ...). The chamber contains positioning equipment allowing the measurement of the field radiated by the AUT on different surfaces depending on the configuration. This thesis focuses particularly on measurements made in anechoic chambers.

The CNES anechoic chamber is shown in Figure 1.2 and the ENAC anechoic range in Figure 1.3.

This document may not be reproduced, modified, adapted, published, translated in any way, in whole or in part, nor disclosed to a third party without the prior written consent of ENAC. © 2023, ENAC

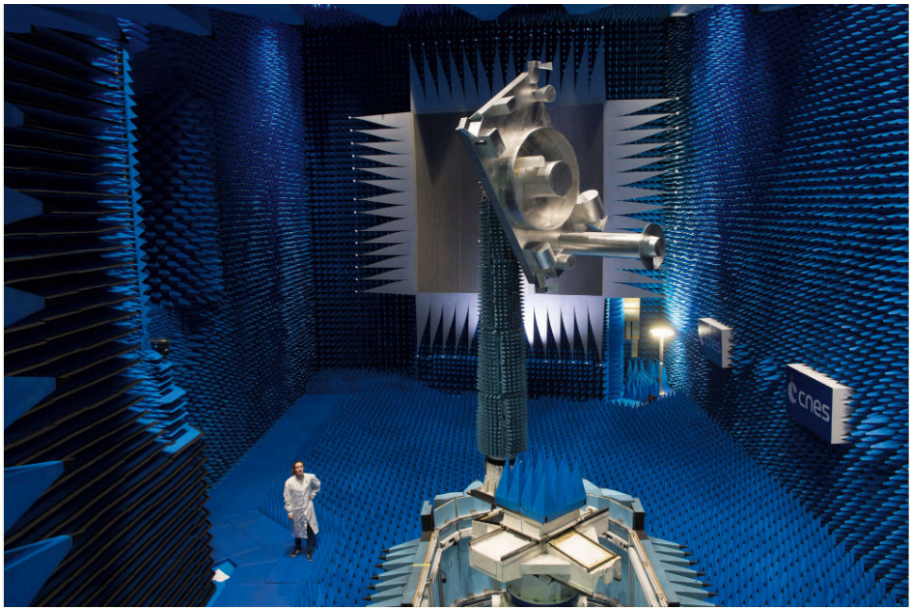

Figure 1.2: CNES compact range [33]

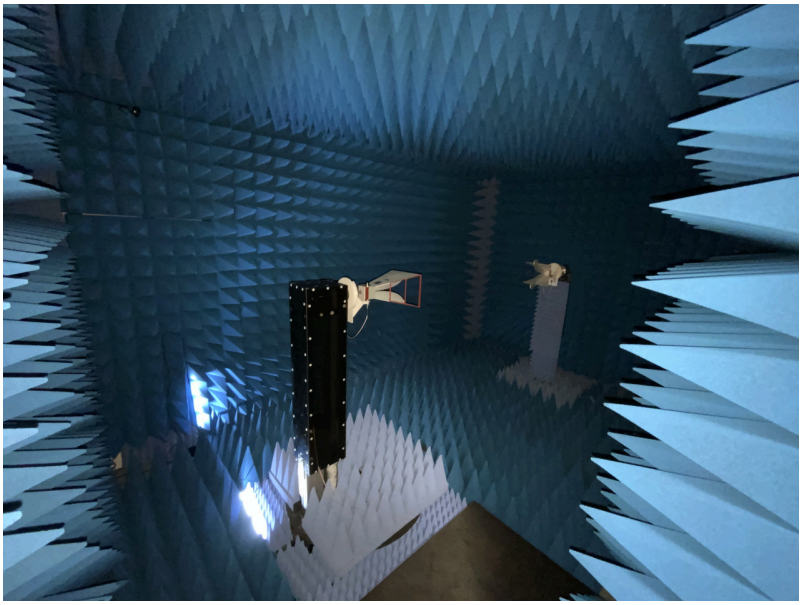

Figure 1.3: ENAC antenna measurement near-field range

Sometimes, for cost and practicability reasons, walls are only partially covered with absorbing materials placed on strategic places of the room. They are then named semi-anechoic. Solange, the Direction Générale de l'Armement (DGA) range is a semi-anechoic range, as shown in Figure 1.4. This range is designed to measure Radar Cross Sections (RCS).

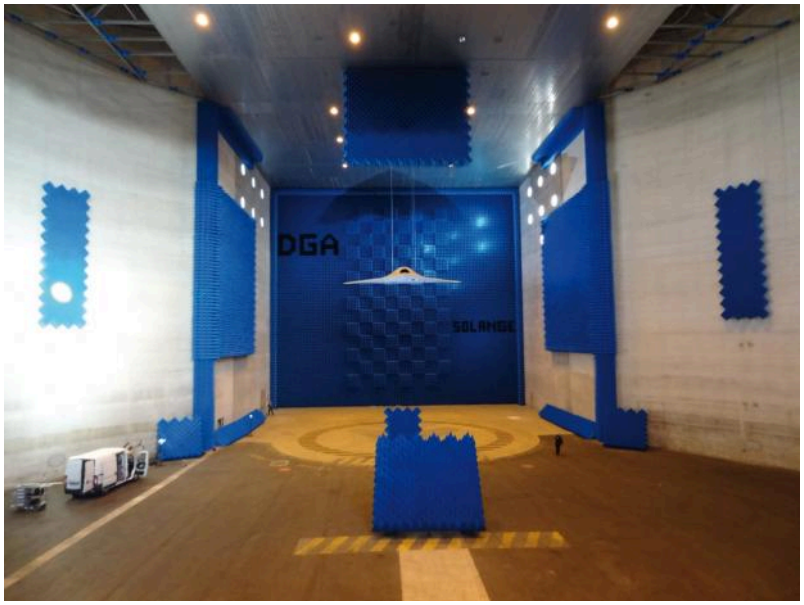

Figure 1.4: Solange Anechoic Facility, Bruz, DGA-MI, the french Department of Defense [34]

1.2.3 Measurement configurations

1.2.3.1 Far-field measurements

In most cases, the objective of an antenna measurement is to obtain the far-field radiation pattern of the AUT. This pattern is directly measured if the probe is far enough from the AUT, [2, 5]. The far-field distance is defined by

$$d > \frac{2D^2}{\lambda}, \tag{1.1}$$

with D the size of the AUT and λ the wavelength. An illustration of the far-field limit is plotted in Figure 1.5.

This document may not be reproduced, modified, adapted, published, translated in any way, in whole or in part, nor disclosed to a third party without the prior written consent of ENAC. © 2023, ENAC

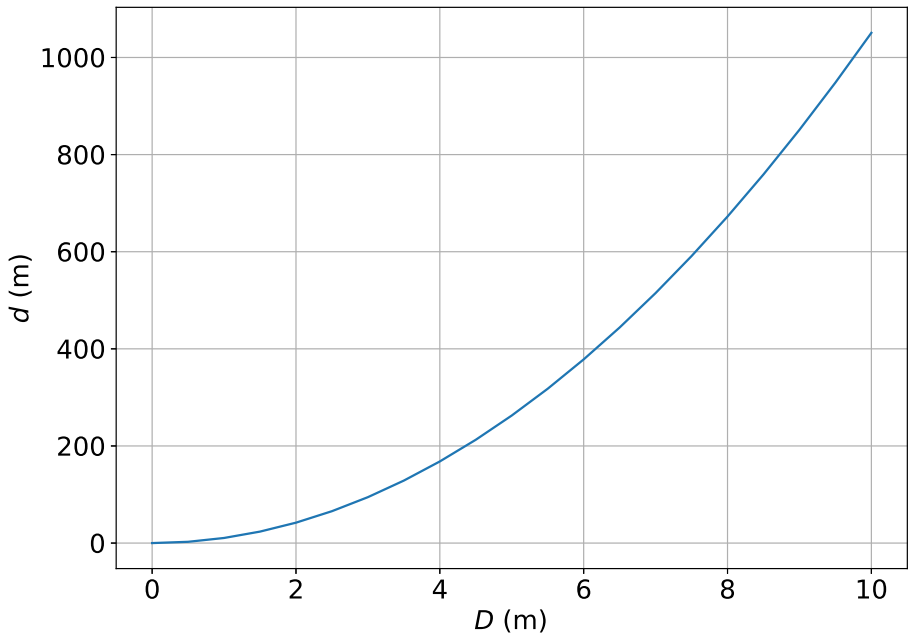

Figure 1.5: Far-field distance d, with regards to the size of the antenna D, for the GPS L1 frequency $f = 1.575$ GHz

Then, to obtain the radiation pattern, the rotation of the AUT with a fixed probe is only required. This is usually made about two axes with a dual-polarised probe.

However, this condition means that for electrically large antennas (high D/λ), the size of the measurement range would be unreachable. For example, an antenna operating at 30 GHz, mounted on a satellite having a size of 2 m has a far-field region at 80 m. To avoid this, specific antenna facilities and post-processing methods have been developed [1, 3].

1.2.3.2 Compact Antenna Test Range (CATR)

In compact range systems, the far-field conditions are reached by illuminating the AUT by an emulated plane wave. This field is generally obtained by positioning the AUT in the quiet zone of a large-size reflector, illuminated by a horn antenna, as shown in Figure 1.6.

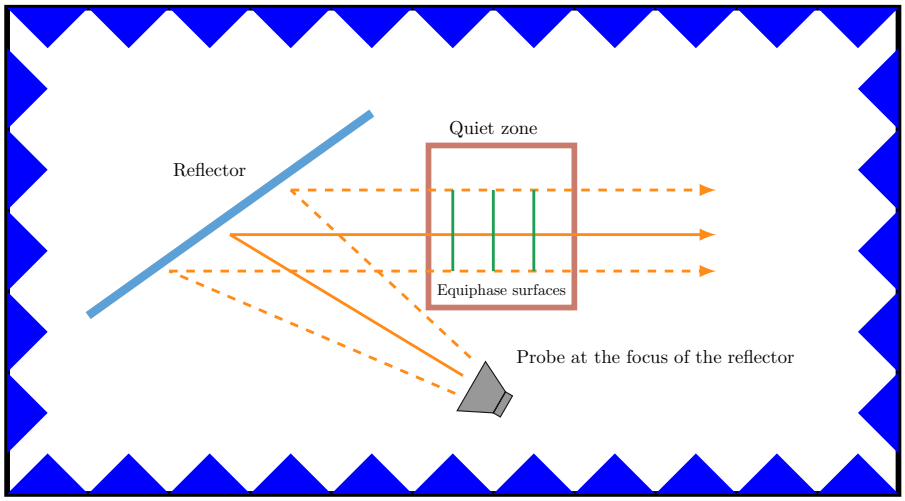

Figure 1.6: Compact range schema

One of the challenges of the CATR is the reduction of the influence of the reflector on the quiet zone field [35, 36]. Besides, the direct radiation of the source often pollutes the quiet zone. For this reason absorbing materials are often placed between the AUT and the source. Figure 1.2 is a picture of the Centre National d'Etudes Spatiales (CNES) compact range which main characteristics are listed below:

- The size of the chamber is 22 m x 12.5 m for the horizontal section and 12 m high.
- The reflector is a serrated reflector i.e. a reflector with sharp indentations all along its rim, to attenuate the edge diffraction.
- The frequency range goes from 400 MHz to 400 GHz.
- The positioner has 7 axes of rotation, with a maximum load of 350 kg.

The specifications are:

- In terms of uncertainty:
  - ±0.25 dB for the gain,
  - ±0.5 dB to -20 dB under the maximum point, of the main polarisation,
  - ±1.5 dB to -30 dB for secondary lobes,
  - ±1 dB to -20 dB in cross polarisation under the maximum of the main polarisation.
- The size of the quiet zone goes from 1 m × 1 m × 1 m up to 4 m × 4 m × 4 m depending on the frequency.

Airbus Defense and Space also owns a CATR as shown in Figure 1.7.

This document may not be reproduced, modified, adapted, published, translated in any way, in whole or in part, nor disclosed to a third party without the prior written consent of ENAC. © 2023, ENAC

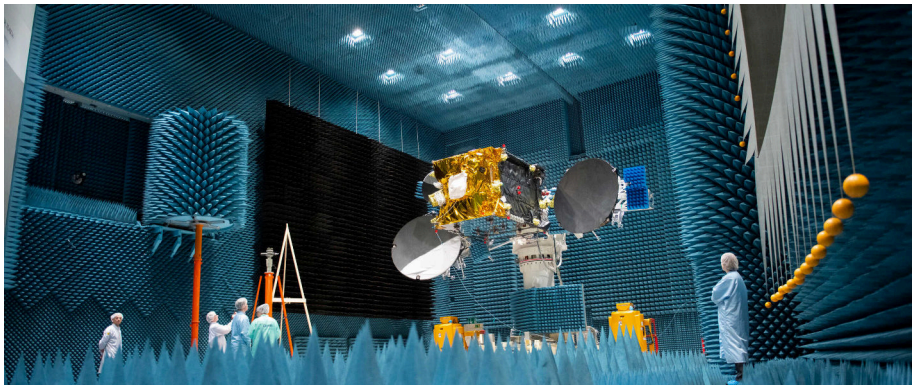

Figure 1.7: Satellite EDRS-C in Airbus's Compact Antenna Test Range facility [37]

To remove the reflector and reduce the distance between the antenna and the probe, it has also been proposed to emulate the plane wave by means of dielectric or metallic lenses or different types of arrays [2]. Besides, MVG has recently developed a plane wave generator, an array generating an approximate plane wave over a finite volume [38].

1.2.3.3 Near-field measurements

To overcome the constraint of the measurement distance induced by far-field measurements, near-field techniques have also been developed [6, 39]. This is also an alternative to CATR which remain large and expensive rooms, whereas near-field ranges are more affordable, with moderate dimensions. They can be of size few meters, depending on the frequency range.

Near-field measurements are usually performed either in planar or spherical configurations. Planar configuration is advantageous for highly directive antennas, when only the forward radiation is considered [40], as shown in Figure 1.8. In this case, the probe samples a plane in front of the AUT, most commonly on a square grid of size $\leq \frac{\lambda}{2}$, to satisfy the Niquist criterion. However, due to the geometry of an antenna, spherical configuration is necessary to obtain the complete radiation pattern of an antenna. An illustration of a spherical measurement configuration is shown in Figure 1.9.

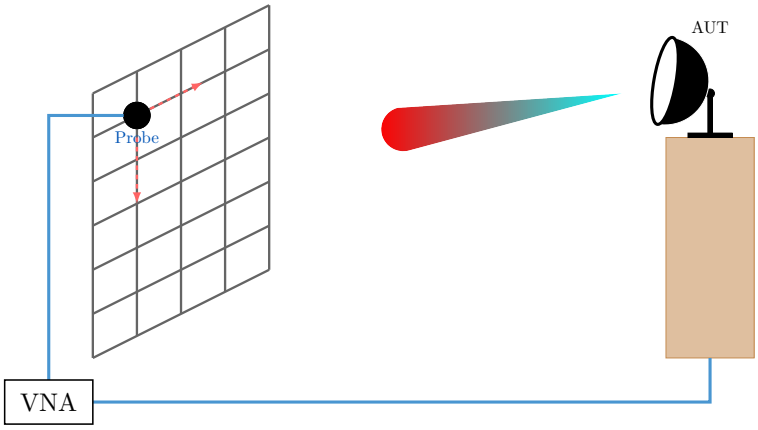

Figure 1.8: Illustration of a planar near-field range

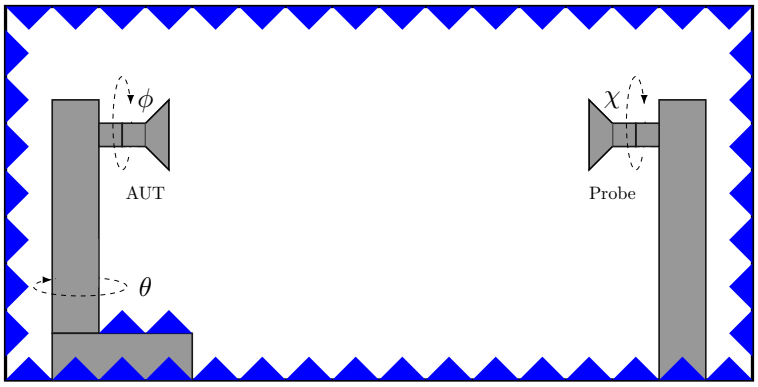

Figure 1.9: Illustration of a spherical near-field range

The probe being in the near field of the antenna, the far-field radiation pattern cannot be obtained directly. Thus a post-processing method performing the near-field to far-field transform, generally including a probe compensation, has to be applied [8, 14]. Further explanations are given in Section 2.5.2.

Figure 1.10 presents the Starlab, a near-field antenna measurement range developed by MVG [41]. The ENAC measurement range is also a near-field range, as shown in Figure 1.3.

Figure 1.10: Starlab near-field range (Max. weight of DUT of 15 kg and dimension of 45 cm in diameter) [42]

1.2.4 Conclusion

In this section, different antenna ranges have been introduced. Firstly, several measurement environments have been presented : antenna measurement can be performed in open

This document may not be reproduced, modified, adapted, published, translated in any way, in whole or in part, nor disclosed to a third party without the prior written consent of ENAC. © 2023, ENAC

spaces, shielded rooms, reverberation chambers or anechoic chambers. Secondly, different measurement configurations have been considered : far-field measurements, compact range and finally near-field measurements. Throughout the rest of the document it is assumed that measurements are performed in anechoic chambers, in spherical near-field or far-field configurations.

1.3 Antenna measurements equipments

1.3.1 Introduction

Antenna test ranges are equipped with many devices in order to achieve the measurement. The choice of those equipments is of high importance to achieve the characterisation at the requested accuracy and expected bandwidth. This section introduces the main equipments present in most antenna test ranges.

Firstly, in Section 1.3.2, the layout of an usual measurement chamber is presented in order to introduce the different elements of the measurement chain. Secondly, Section 1.3.3 presents absorbing materials covering anechoic chambers walls to prevent reflections and thus emulate free space conditions. Then Section 1.3.4 gives an overview on several probe solutions to collect measurement data. Section 1.3.5 describes positioning systems that execute the movements of the antenna in the chamber so that the probe can measure the radiation on the measurement surface.

1.3.2 Layout of the measurement chamber

The measurement of the AUT is made possible by the use of several electric devices, as shown in Figure 1.11. The rotation of the antenna is assured by a positioner, that includes one or several motors, rotary joints and a controller. The positioner is controlled via cables with a dedicated software. The VNA simultaneously feeds the probe in transmission and collects the measurements from the AUT in reception. The information is transported to the VNA by RF coaxial cables [2]. The probe can either be dual-polarised, then a switch controls its polarisation, or it can be rotated by a positioner. Then the data is processed by a computer.

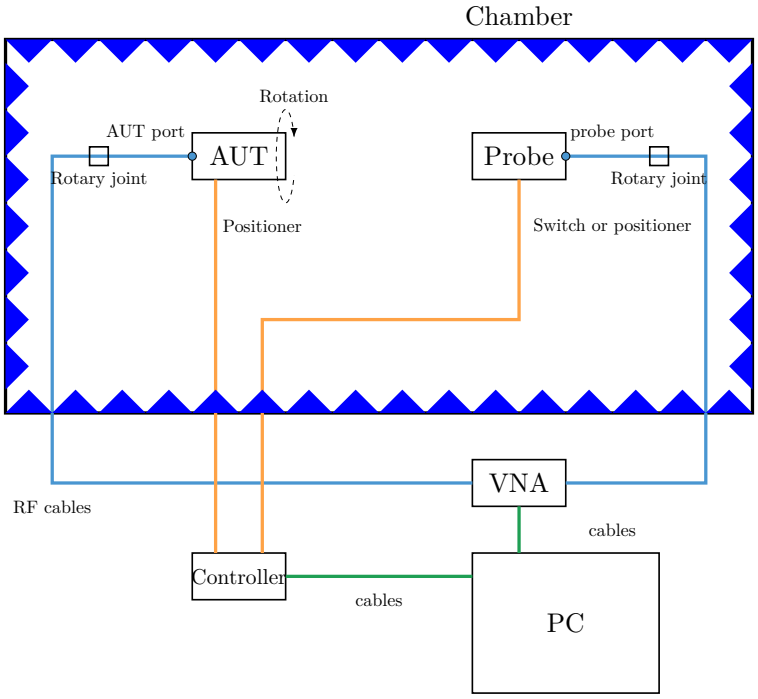

Figure 1.11: RF measurement range

Some of the antenna characteristics can only be obtained with an absolute measurement. This is notably the case for determining the gain and the efficiency, which requires to remove all sources of perturbations that are not associated with the AUT itself. To do so, a first solution consists in performing a calibration so that the VNA measures the S21 parameter between the antenna and the probe ports. This allows to get rid of the cables, connectors and rotary joints. Several types of calibrations can be performed:

- The Short Open Load Through (SOLT) calibration method is based on four calibration measurement : one with a short circuit connected to the VNA measurement port, one with an open circuit, one with a matched load standard and finally with a transmission line, with known electrical length and characteristic impedance, between the VNA two ports.
- Another method called the *Unknown Through* method is the same method as the SOLT calibration but the properties of the transmission line are unknown.

Another solution consists in performing a preliminary measurement with a reference antenna, which characteristics are known, as briefly described in Section 1.4.3.

However calibration is not always necessary, for example for gain measurement, the three antennas gain comparison method does not require calibration [1].

To prevent scattering and interferences, most the equipements shown in Figure 1.11 are placed outside the anechoic chamber. Finally, the quality of the measurement is greatly influenced by the choice of the absorbing materials.

This document may not be reproduced, modified, adapted, published, translated in any way, in whole or in part, nor disclosed to a third party without the prior written consent of ENAC. © 2023, ENAC

1.3.3 Absorbing Materials

Absorbing materials, commonly known as absorbers, are designed to attenuate electromagnetic waves across a broad frequency range, regardless of the polarisation and angle of incidence. They are typically pyramidal structures composed of carbon-loaded foam or specialised ferrite tiles that possess high-loss properties. By absorbing the incident waves, these materials effectively reduce the reflections and prevent them from interfering with the measurements [2, 43, 44, 45].

Pyramidal absorbers attenuates signals by two effects: scattering and absorption. The waves are scattered at the tip of the pyramids shapes, that are cut at angles that maximise the number of bounces a wave makes within the structure. With each bounce, the wave loses energy to the foam material and thus exits with lower signal strength. The scattering also occurs within the foam structure, with the suspended carbon particles promoting destructive interference [46].

To reach the best performances, all internal surfaces of anechoic measurement ranges walls must be covered with this type of materials, with the tips of the pyramids pointing inward the chamber.

Flat absorbers also exist but they are less efficient, they are often used for the floor where people have to walk to manipulate devices or in tight enclosures to facilitate manual operations.

The performances of absorbers are limited and are given in data-sheets from the constructors like Holland Shielding Systems BV [47] or Siepel [48], as shown in Figure 1.12.

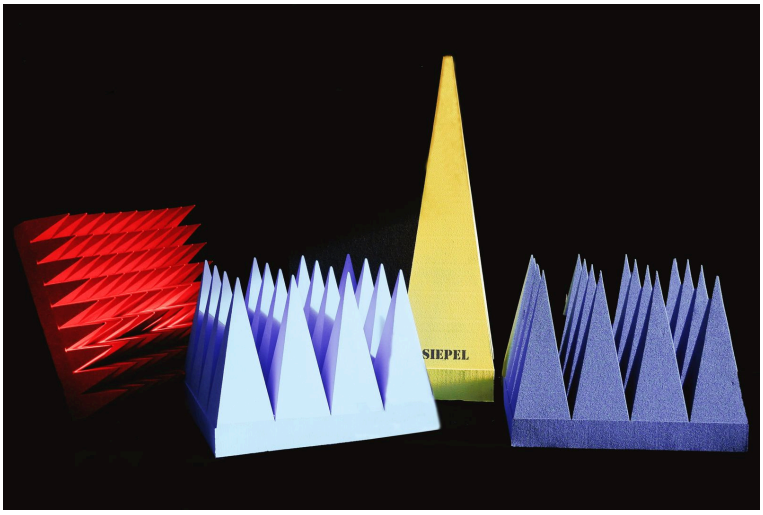

(a) Pyramidal absorbing material picture from Siepel website [48]

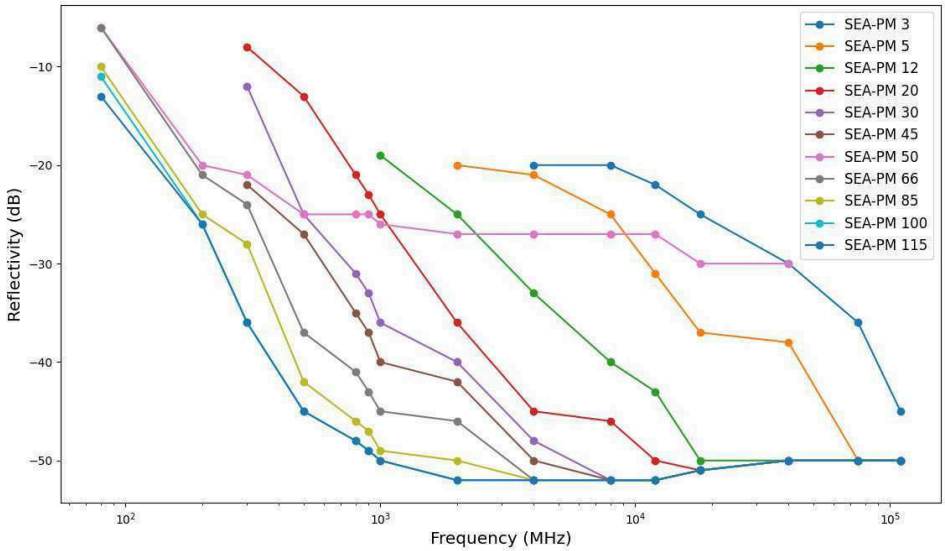

(b) Siepel absorbers reflectivity performances, (Values in dB at normal incidence)

Figure 1.12: Absorbers and their reflectivity performance from data sheets

The frequency limitations are due to three main phenomena:

- to decrease the minimal frequency limit, the pyramid has to be thicker,
- to increase the maximal frequency, the tip of the pyramid has to be sharper,
- the density of the elements inside the pyramids is distributed in a way that optimises the mitigation of a certain frequency range.

The absorbers emulate free space conditions around the AUT. The antenna radiation pattern is then measured by the probe.

This document may not be reproduced, modified, adapted, published, translated in any way, in whole or in part, nor disclosed to a third party without the prior written consent of ENAC. © 2023, ENAC

1.3.4 Probe

1.3.4.1 Simple probe

The probe is the sensor that collects the characteristics of the AUT during measurements. They are commonly chosen wide-band, with a stable pattern with respect to the frequency. The probe should be mechanically stable and durable to withstand repeated use over extended measurement sessions. They can have many different characteristics, depending on the measurement configuration:

- In far field, the probe needs a good polarisation purity and a good stability in frequency. This can be judicious to choose a directive probe to avoid radiation coming from the side of the probe but this increases the far-field distance between the antenna and the probe.
- In near field, the radiation pattern of the probe is often chosen according to the probe correction that will be performed in post-processing (see section 2.5.3.1). In planar geometry, the probe has to be chosen in order to avoid distortion due to the "slant illumination" [49]. In spherical geometry the radiation pattern needs to present symmetries, so that only spherical harmonics of order $m = \pm 1$ are non-negligible (see Section 2.3). This often limits the frequency band over which this type of probe can be used.
- In compact test range, the probe is often a horn antenna with a good stability of the phase center. Some of those probes are shown in Figure 1.13. Major issues encountered in CATR are tapering, that yields diffraction over the edges of the reflector, and spill over, that disturbs the quiet zone. A compromise has to be done between the size of the quiet zone, the frequency range of the chamber and the disturbing effects.

Figure 1.13: Compact range feed horn developed by MVG, it can be used for direct range illumination or reflector illumination [41]

Probes are often dual-polarised with a good polarisation discrimination. This allows the AUT to be rotated about 2 axes only during the measurement, and still obtain the complete radiation pattern. In Figure 1.14 an example of dual-polarised probes developed by NSI-MI is shown.
Another solution is to split the measurement in two with a monopolarised probe, with a weak cross-polarisation : the first part of the measurement is performed with the probe straight and then to rotate it of 90° in the second part of the measurement. The ENAC

measurement range, see Section 1.4, includes a monopolarised probe developed by RF SPIN [50], as shown in Figure 1.18a.

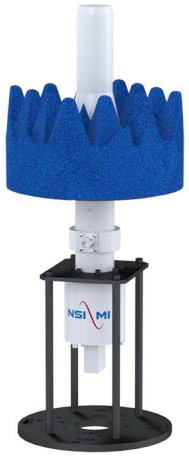

Figure 1.14: Dual polarised probe [51].

However having only one probe requires to be able to make a lot of rotations, which is demanding for the positioner capacities and time-consuming.

1.3.4.2 Multiprobe range

The time required for the determination of the 3-D radiation pattern of an AUT is greatly influenced by the number of required measurement positions when using a single probe [52] [53]. Multiprobe systems present several probes, disposed around the AUT, that are activated one after the other, replacing the rotations. This is faster and more stable than rotating the antenna. The Starlab range, as shown in Figure 1.10 is a multiprobe range developed by MVG [42]. Probes are disposed all along the arch overlooking the AUT and a positioner performs its rotation about the vertical axis. Most of the time the rotation about one axis of the AUT is still required as in [54], [55].

However, RF probes impact the measurement of the antenna radiation pattern, especially in near-field measurement, but it also have an impact on the electromagnetic environment in the case of far-field or CATR configurations.

1.3.4.3 Non invasive probe

To avoid the disturbance on the measured signal, several equipments have been developed with specific materials that do not disturb the radiation of the antenna. Indeed, in near-field measurement, the proximity of the probe and the presence of the cables impacts the radiation pattern of the AUT. Alternative kind of probes have thus been developed. The dielectric probe developed by Kapteos [56] turns the electromagnetic signal into an optical signal with a RF to optical transducer. The information is then conveyed through an optical fiber, that does not disturb the radiation [57]. The EMIR Method, invented at ONERA and developed by Anyfields [58], uses infrared thermography to make fast

This document may not be reproduced, modified, adapted, published, translated in any way, in whole or in part, nor disclosed to a third party without the prior written consent of ENAC. © 2023, ENAC

antenna measurements. However, the thermofilm only reacts to the amplitude of the field so the phase and the polarisation are not measured. This type of measurement has been presented during the COMET seminar at CNES in 2018, dedicated to novel antenna measurement techniques [59].

The work of this thesis focuses on correction methods for antenna measurement that get rid of perturbations, including the probes. Those methods are supposed to be applicable to all kind of probes listed above, except the EMIR method, as in this thesis the measurement is assumed to provide S-parameters via a VNA.

1.3.5 Mechanical systems

The positioners perform the movements of the antenna in the chamber in order for the probe to measure the radiation pattern over the whole measurement surface. The positioning system includes some or all of the following elements [2]: positioner for probe, positioner for AUT, position controller, position measurement devices, local control unit, control cables.

The choice of the mechanical components are critical points for the measurement. They have to be precise, non-resonating, made of dielectric or recovered by absorbing material to avoid reflection and should have a good thermal stability. Some examples of positioners are given in Figure 1.15. The movements are parameterised in specific coordinate systems, that will be detailed in Section 2.2.

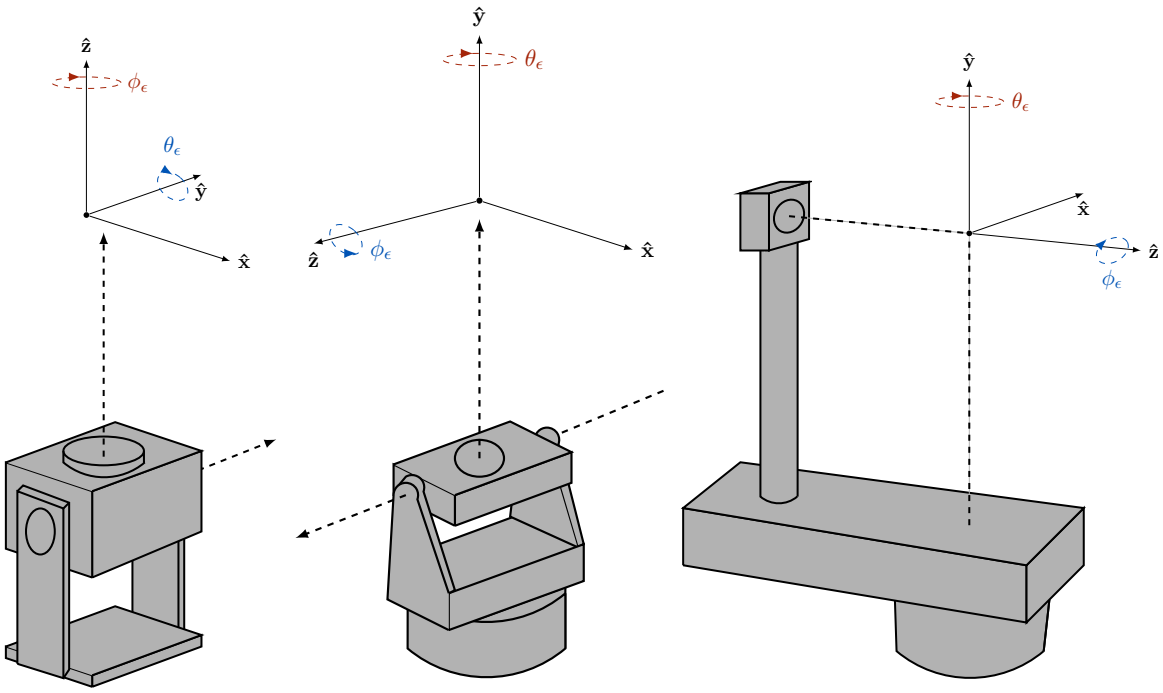

(a) Azimuth-over-elevation. (b) Elevation-over-azimuth. (c) Roll-over-azimuth.

Figure 1.15: Different examples of positioners [2]

The PAMS (Portable near-field Antenna Measurement System) [57] is another example of positionning system, where the probe is moving around the DUT like in Figure 1.16.

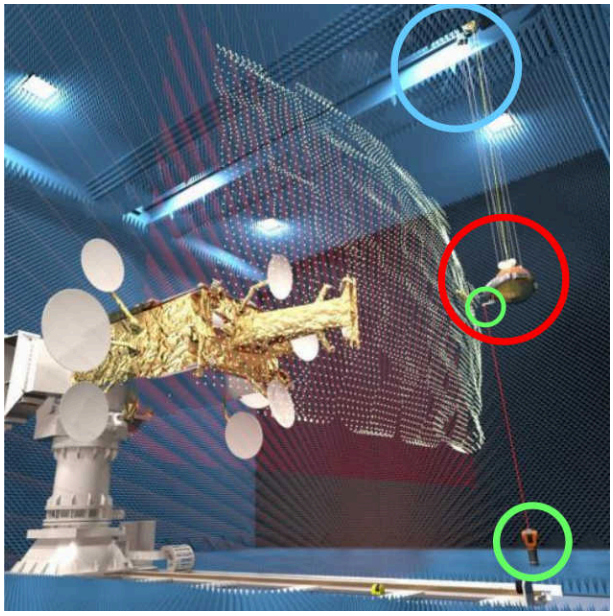

Figure 1.16: Picture of PAMS [57]

Robotic positioning arms have also been introduced to antenna ranges [60]. They are programmable and allows scanning on an arbitrary point cloud without being restricted to grids [60]. They often have more degrees of freedom than traditional positioners. This is also becoming common to use Unmanned Aerial Vehicles (UAVs) as probe supports [28].

1.3.6 Conclusion

In this section, an overview of typical antenna measurement ranges has bee given. Then different materials and devices specific to antenna measurement have been introduced: the properties of absorbing materials and the choice of the probe are essential matters for precise acquisitions. Positioners, that operates the movements with respect to the coordinate systems have also been presented.

1.4 Antenna measurement range for the thesis experiments

1.4.1 Introduction

The work of this thesis is focused on correction of antenna measurements. The ENAC antenna measurement range has constituted a real asset to manipulate and perform such measurements. This section is a presentation of the ENAC measurement range currently used for research and teaching.
Section 1.4.2 is about the characteristics of the range and Section 1.4.3 presents an example of antenna measurement in the chamber.

This document may not be reproduced, modified, adapted, published, translated in any way, in whole or in part, nor disclosed to a third party without the prior written consent of ENAC. © 2023, ENAC

1.4.2 Characteristics of the ENAC measurement range

The ENAC measurement range is a non-shielded anechoic chamber of size 3.60×2.40×2.20m as shown in Figure 1.3. This is intended for near-field and far-field measurements. The total bandwidth goes from 1 to 14 GHz (L, S, C, X and the beginning of the Ku bands). The measurements are defined in the frame $(\hat{\mathbf{x}}, \hat{\mathbf{y}}, \hat{\mathbf{z}})$, as displayed in Figure 1.17.

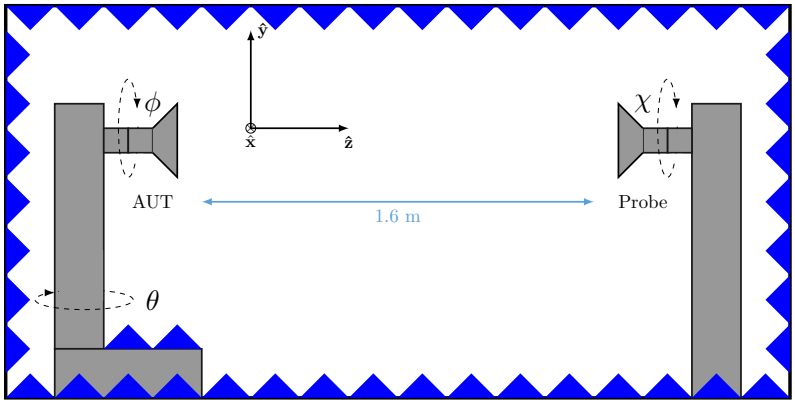

Figure 1.17: Sketch of the ENAC measurement range

Inside the anechoic room, two rotation positioners CTS118-2 and CTS261, developed by CT systems [61], support the antenna and the probe, respectively. Both positioners are controlled by the software ANT32. The support of the AUT is a roll-over-azimuth as shown in Figure 1.15c, with a maximum load of 1.5 kg. This can successively rotate about two axes. As shown in Figure 1.17, the first rotation is parameterised by the angle $\theta \in [0°,360°[$, with a 0.05° precision, and the second one by the angle $\phi \in [0°,180°[$ with a 0.01° precision. For $\theta = 0°$ the axis $\hat{\mathbf{z}}$ is pointing from the AUT to the probe.
The probe can turn about the axis $\hat{\mathbf{z}}$ with an angle $\chi \in \{0°,90°\}$ to measure both polarisation components of the field.
This parameterisation of the rotations is the usual one to obtain the complete pattern of the AUT, even though the positioners are capable of angular redundancy. For example, the θ and χ rotations can be performed on $[0°,360°]$ intervals.

The ENAC test range includes two reference antennas, both being able to be the probe or the calibration antenna: The RF SPIN DRH18EX antenna has a frequency range of 800 MHz to 18 GHz, and the RF SPIN DRH10E has a frequency range of 700 MHz to 10.5 GHz. They both are linearly polarised. Their radiation patterns are illustrated in Figure 1.18.

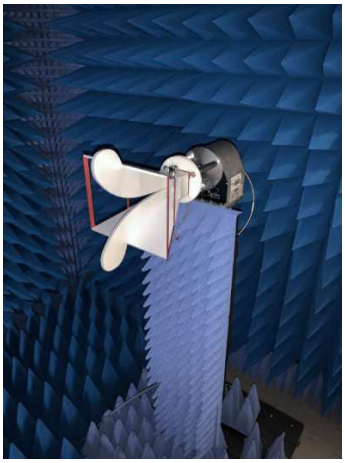

(a) RF SPIN DRH18EX antenna

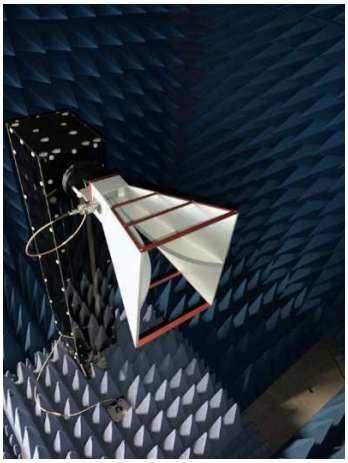

(b) RF SPIN DRH10E antenna

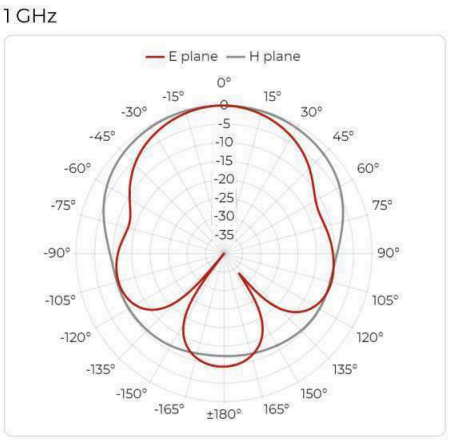

(c) RF SPIN DRH18EX radiation pattern

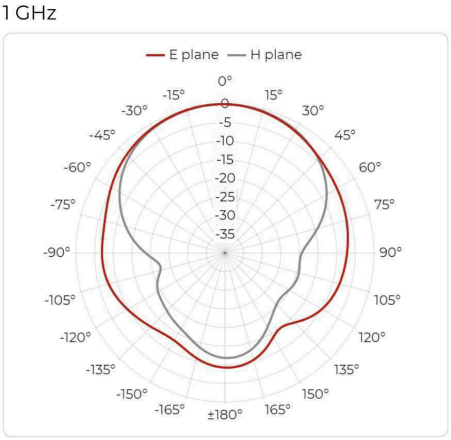

(d) RF SPIN DRH10E radiation pattern

Figure 1.18: Reference antennas with their radiation pattern at 1 GHz, [50] [62].

Both antennas are connected to a vectorial network analyser (VNA) ZNL14 Rhodes & Schwarz. This VNA has a power going from -40 dBm to 0 dBm. The ANT32 software commands the VNA, and the controller commands the positionners via ethernet ports. For each position, the S parameters of the antenna are obtained and stored into ASCII and/ or SQLITE files. They are then post-processed by Processing of ANtenna TEsts REsults (PANTERE), a Python library developed at ENAC. A calibration *Unknown Through* can be done before the measurement. The absorbers are Siepel absorbers SEA-PM30, their performances in terms of reflectivity are depicted in Figure 1.12b.

1.4.3 Example of measurement

As an example, a linearly polarised rectangular patch has been measured in the chamber. A picture of the antenna is given in the Figure 1.19a. Its dimensions are 3 cm × 3 cm with a ground plane of 18.5 cm × 18.5 cm. The substrate is FR4 of 1.5 mm width, with relative permittivity $\epsilon_r = 4.5$. The central frequency is 2.454 GHz.

This document may not be reproduced, modified, adapted, published, translated in any way, in whole or in part, nor disclosed to a third party without the prior written consent of ENAC. © 2023, ENAC

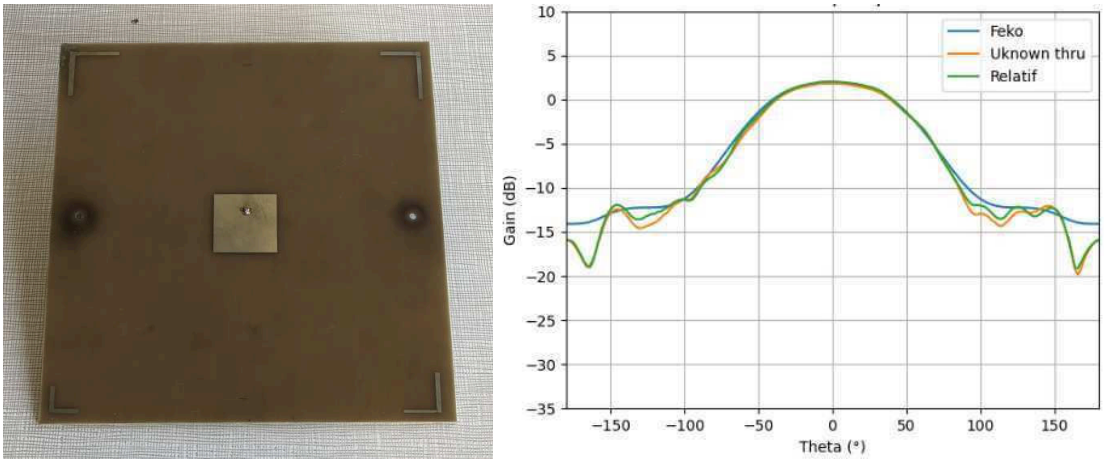

(a) Patch antenna

(b) Gain in the plane $\phi = 0°$

Figure 1.19: Measurement of a rectangular patch antenna

The gain of the antenna, obtained with three different methods is plotted in Figure 1.19b:

- The first one is obtained by a Altair Feko simulation. At boresight, the gain is 1.86dBi.
- The second one is the gain computed by a mesurement in the ENAC test range, after undergoing a calibration process referred to as "Unknown Through," as detailed in Section 1.3.2. This computation is specifically conducted under far-field conditions and takes into account the known probe gain. In the axis, the gain is 1.86dBi.
- The third one is the gain measured with a relative calibration, performed with the RF SPIN DRH10 as the calibration antenna [2].

The measured gain patterns agree with simulation, serving as an illustration of the performances of the ENAC anechoic room, which is not an industrial room.

1.4.4 Conclusion

This section has introduced the ENAC measurement facility. The measurement range has been presented, along with an example of measurement. Through this section, it has been clear that mathematical tools are needed to describe and parameterise the motion of the antenna in the measurement process. This work, in particular, focuses on antenna measurements made in spherical geometries.

1.5 Conclusion

This chapter has established the context of the thesis and the main experimental aspects of antenna measurements.

Firstly, a presentation of antenna measurement ranges has been conducted: various antenna measurement environments and configurations has been described and comparisons have been made in order to understand which environment and configuration is the most

accurate, depending on the type of AUT, the required accuracy, the available time to perform the measurement, etc.

Secondly, typical antenna measurement equipments have been listed: the RF measurement chain has been given to depict the global function of each piece of equipment. Then the absorbing materials and their properties, different kind of probes, and mechanical systems performing motions in the measurement range have been introduced.

Finally, the antenna range that has been used to perform antenna measurement during this thesis has been presented. Its characteristics have been given along with a measurement example.

This document may not be reproduced, modified, adapted, published, translated in any way, in whole or in part, nor disclosed to a third party without the prior written consent of ENAC. © 2023, ENAC

Chapter 2

Theoretical tools for spherical antenna measurements

2.1 Introduction

This chapter assesses two main aspects of antenna measurement. Firstly, due to the geometry of the radiation of an AUT, spherical geometry is the best to provide a realistic representation of antenna radiation pattern [14]. Moreover, antenna measurements are often post-processed, either to attenuate disturbances coming from the environment [63], noise from the cables and electronical devices or to emulate far-field conditions [64]. Consequently adequate mathematical parameterizing and analysing tools have to be developed, along with adapted correction methods.

The objective of this chapter is to draw up a state of the art in antenna measurements post-processing, in spherical geometry.

Firstly, Section 2.2 reminds the geometrical aspects to consider in a measurement problem defined over a sphere. Those considerations lead to Section 2.3 that introduces spherical harmonics as defined by Hansen [6], a widespread and powerful tool to analyse antenna radiation pattern and post-process antenna measurements. Illustrations of spherical harmonics expansions are then presented in Section 2.4. Finally, Section 2.5 addresses common methods of measurement post-processing [14, 18].

2.2 Coordinate systems and operators

2.2.1 Introduction

The measurement of antenna radiation patterns involves the determination in one way or another of signal levels with respect to position or direction in space. The objective of this section is to introduce the geometrical tools and operators to parameterize measurements over the sphere. Section 2.2.2 is a reminder of the spherical coordinates, Section 2.2.3 introduces the Euler angles and the rotation group and finally Section 2.2.4 presents the rotation operators over the sphere.

This document may not be reproduced, modified, adapted, published, translated in any way, in whole or in part, nor disclosed to a third party without the prior written consent of ENAC. © 2023, ENAC

2.2.2 Spherical coordinates

Due to the nature of the far-field radiation, the spherical coordinate system is widely used in antenna problems. For measurement, it is necessary to precisely position the AUT in the spherical coordinates, and then to rotate it in order to expose the entire pattern to the probe.

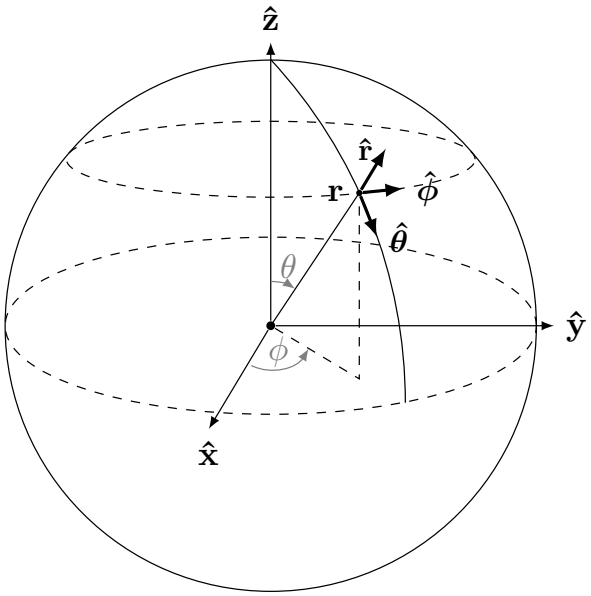

Figure 2.1: Spherical coordinate system

Spherical coordinates are reminded in Figure 2.1. They are related to the cartesian coordinates by

$$\begin{aligned} x &= r\sin\theta\cos\phi, \\ y &= r\sin\theta\sin\phi, \\ z &= r\cos\theta \end{aligned} \tag{2.1}$$

with $r \in [0, +\infty[$, $\theta \in [0, \pi]$ et $\phi \in [0, 2\pi[$. The associated local direct frame $(\hat{\boldsymbol{r}}, \hat{\boldsymbol{\theta}}, \hat{\boldsymbol{\phi}})$ is given by

$$\begin{aligned} \hat{\boldsymbol{r}} &= \sin\theta\cos\phi\hat{\boldsymbol{x}} + \sin\theta\sin\phi\hat{\boldsymbol{y}} + \cos\theta\hat{\boldsymbol{z}}, \\ \hat{\boldsymbol{\theta}} &= \cos\theta\cos\phi\hat{\boldsymbol{x}} + \cos\theta\sin\phi\hat{\boldsymbol{y}} - \sin\theta\hat{\boldsymbol{z}}, \\ \hat{\boldsymbol{\phi}} &= -\sin\phi\hat{\boldsymbol{x}} + \cos\phi\hat{\boldsymbol{y}}. \end{aligned} \tag{2.2}$$

This local basis is constituted by a radial vector and two tangent vectors on the sphere $\mathcal{S}^2$. In this PhD thesis, calculations are either performed on a unitary sphere, i.e. of radius 1 or on a sphere of radius r. They are denoted $\mathcal{S}^2$, and $\mathcal{S}_r^2$, respectively.

The output of the measurement is a scalar or tangent vector signal defined on $L^2(\mathcal{S}^2)$, the group of square integrable, i.e. of finite power, functions over the sphere.

2.2.3 The Euler angles and the rotation group

As described in Sections 1.3 and 1.4, rotations are performed during measurement acquisition. They have to be parameterized, that is why the Euler angles have to be introduced.

The Euler angles are three angles $\epsilon = (\phi_\epsilon, \theta_\epsilon, \chi_\epsilon)$, introduced by Leonhard Euler to describe the orientation of a rigid body with respect to a fixed coordinate system. They can also be used to orient one coordinate system with respect to another one.

In the Euler or *zyz* convention, any rotation can be described by three successive rotations about three specific axes. At each rotation, the frame is modified, it will be noted $(\hat{\mathbf{x}}, \hat{\mathbf{y}}, \hat{\mathbf{z}})$, $(\hat{\mathbf{x}}_\mathbf{1}, \hat{\mathbf{y}}_\mathbf{1}, \hat{\mathbf{z}}_\mathbf{1})$ and $(\hat{\mathbf{x}}_\mathbf{2}, \hat{\mathbf{y}}_\mathbf{2}, \hat{\mathbf{z}}_\mathbf{2})$, as shown in Figure 2.2. The rotations are as follows:

- First rotation is made about the axis $\hat{\mathbf{z}}$ of an angle ϕ_ϵ, as shown in Figure 2.2a,
- Second rotation about the axis $\hat{\mathbf{y}}_\mathbf{1}$ of an angle θ_ϵ, as shown in Figure 2.2b,
- Last rotation is made about the axis $\hat{\mathbf{z}}_\mathbf{2}$ of an angle χ_ϵ, as shown in Figure 2.2c.

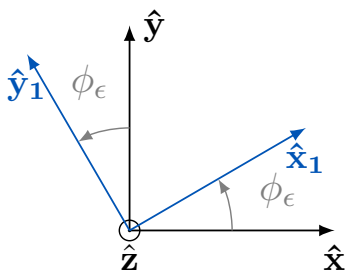

(a) First Euler rotation

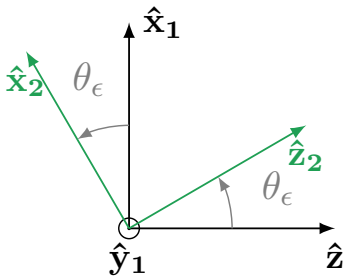

(b) Second Euler rotation

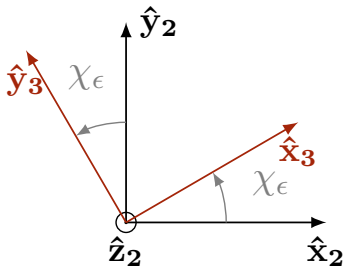

(c) Third Euler rotation

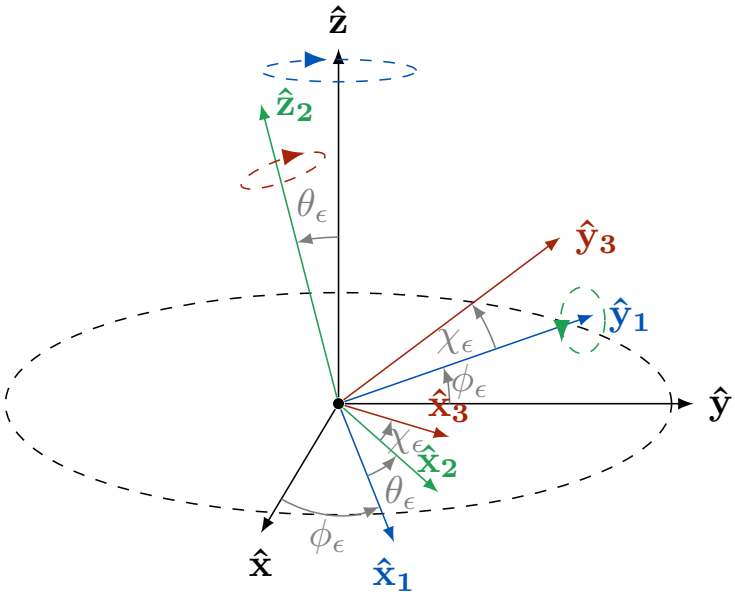

(d) 3D representation of the Euler angles

Figure 2.2: Euler rotation angles following the '*zyz*' convention

This document may not be reproduced, modified, adapted, published, translated in any way, in whole or in part, nor disclosed to a third party without the prior written consent of ENAC. © 2023, ENAC

Although many other conventions exist to describe rotations, the 'zyz' Euler convention is standard in antenna measurements. The Euler angles are a manner to describe a rotation and are parameters of the 3D rotation group, often denoted SO(3), the group of all rotations about the origin of three-dimensional Euclidean space $\mathbb{R}^3$ [65]. As spherical antenna measurements depend on rotations, they belong to $L^2(\mathrm{SO}(3))$, the group of finite power square integrable functions over the rotation group.

2.2.4 Rotation over the sphere

Rotations on the sphere can be characterized by the rotation matrix $\mathbf{R}_\epsilon$ which can be parametized by the Euler angles $(\phi_\epsilon, \theta_\epsilon, \chi_\epsilon)$. This corresponds to the rotations described in Figure 2.2. In this case, $\mathbf{R}_\epsilon$ can be written as

$$\mathbf{R}_\epsilon = \mathbf{R}_{z_2}(\chi_\epsilon)\mathbf{R}_{y_1}(\theta_\epsilon)\mathbf{R}_{z_1}(\phi_\epsilon), \tag{2.3}$$

with $\mathbf{R}_{z_1}(\phi_\epsilon)$, $\mathbf{R}_{y_1}(\theta_\epsilon)$ defined as

$$\mathbf{R}_{z_1}(\phi_\epsilon) = \begin{pmatrix} \cos\phi_\epsilon & -\sin\phi_\epsilon & 0 \\ \sin\phi_\epsilon & \cos\phi_\epsilon & 0 \\ 0 & 0 & 1 \end{pmatrix}, \tag{2.4}$$

$$\mathbf{R}_{y_1}(\theta_\epsilon) = \begin{pmatrix} \cos\theta_\epsilon & 0 & \sin\theta_\epsilon \\ 0 & 1 & 0 \\ -\sin\theta_\epsilon & 0 & \cos\theta_\epsilon \end{pmatrix}, \tag{2.5}$$

and $\mathbf{R}_{z_2}(\chi_\epsilon)$ is built as $\mathbf{R}_{z_1}(\phi_\epsilon)$.

For a function $u \in L^2(\mathcal{S}^2)$, the rotation consists in reproducing the same function, elsewhere over the sphere. Rotations are specified by elements of the rotation group SO(3), parameterized by the Euler angles $\epsilon = (\phi_\epsilon, \theta_\epsilon, \chi_\epsilon)$. The position over the sphere is parameterized by the unitary radial vector $\hat{\boldsymbol{r}}$. For further convenience in the incoming formulations, an operator is defined to relate the coordinates over the sphere (θ, ϕ) and the corresponding position vector $\hat{\boldsymbol{r}}$ such as

$$\begin{aligned} \kappa : [0, \pi[\times [0, 2\pi[&\mapsto \mathcal{S}^2 \\ (\theta, \phi) &\mapsto \hat{\boldsymbol{r}}. \end{aligned} \tag{2.6}$$

This operator provides the positions as defined in (2.1), for r=1. The rotation of u is represented by the rotation operator $\mathcal{R}_\epsilon$, and it is defined as

$$(\mathcal{R}_\epsilon u)(\hat{\boldsymbol{r}}_1) \equiv u(\hat{\boldsymbol{r}}_0), \tag{2.7}$$

with $\hat{\boldsymbol{r}}_0$ the previous position and $\hat{\boldsymbol{r}}_1$ the new position vector of the function over the sphere. This new position, see Figure 2.3 is calculated with the three-dimensional rotation matrix $\mathbf{R}_\epsilon$ using

$$\hat{\boldsymbol{r}}_1 = \mathbf{R}_\epsilon^{-1}\hat{\boldsymbol{r}}_0 \tag{2.8}$$

over the sphere. The convention chosen is that the rotation is a transition from a reference frame to a new one, linked to the rotated object, here the antenna.

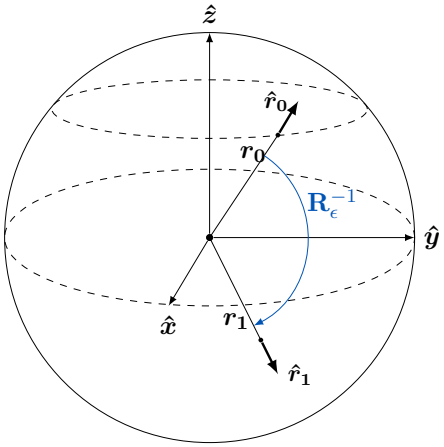

Figure 2.3: Vector rotation

2.2.5 Conclusion

In this section antenna measurement coordinate systems and operators have been presented. They are used to mathematically describe the movement of the antenna required to obtain the full radiation pattern. The data acquired is then post-processed by means of algorithms based on mathematical models. Some of the most frequently used are based on the spherical harmonics.

2.3 Standard vector spherical harmonics for antennas

2.3.1 Introduction

Spherical harmonics are a very helpful tool in the antenna measurement domain. They are particular solutions to the Maxwell's equations and form an orthonormal basis of $L^2(\mathcal{S}^2)$. Thus any field defined on a sphere can be written as a sum of these functions. A parallel can be drawn with Fourier series that permits the expression of periodic functions as a sum of sines and cosines. In electromagnetic and antenna measurements, these functions are used to analyse radiated fields on the measurement sphere. Vector spherical harmonics are standard tools in electromagnetics, as detailed in classical books written by Stratton [27], Felsen and Marcuvitz [66], and Van Bladel [67]. They are used to generate solutions to the Maxwell's equations or vector wave equation in spherical coordinates.

The objective of this section is to describe the standard vector spherical harmonics, as defined by Hansen, which is a common convention in antenna measurements [6].

In Section 2.3.2 the scalar spherical harmonics are defined. Then in Section 2.3.3 vector spherical harmonics are presented. In Section 2.3.4, the expansion of an electromagnetic field is given. Then the number of modes in spherical wave expansions is discussed in Section 2.3.5.

This document may not be reproduced, modified, adapted, published, translated in any way, in whole or in part, nor disclosed to a third party without the prior written consent of ENAC. © 2023, ENAC

2.3.2 Scalar spherical harmonics

In an homogeneous medium, in the spherical coordinates system (r, θ, ϕ), scalar spherical harmonics are associated with the source-free Helmholtz equation with separate spherical variables

$$(\nabla^2 + k^2)u(r, \theta, \phi) = 0, \tag{2.9}$$

where k is the wavenumber. According to [21], the scalar spherical harmonics can be written as

$$Y_{m,n}(\theta, \phi) = \frac{1}{\sqrt{2\pi}} \bar{P}_n^{|m|}(\cos\theta) \mathrm{e}^{im\phi}, \tag{2.10}$$

with $n \in \mathbb{N}$, $m \in \{-n, \cdots, n\}$ and $\bar{P}_n^m$ the normalized associated Legendre functions. They form the canonical orthogonal basis for $L^2(\mathcal{S}^2)$ scalar functions on the sphere.

Any square integrable scalar function on the sphere $u \in L^2(\mathcal{S}^2)$ can be expanded on spherical harmonics. This can be written as

$$u(\theta, \phi) = \sum_{n=0}^{\infty} \sum_{m=-n}^{n} C_{m,n} Y_{m,n}(\theta, \phi), \tag{2.11}$$

with $C_{m,n}$ corresponding to spherical harmonics coefficients given by the usual projection

$$C_{m,n} = \langle u, Y_{m,n} \rangle = \int_0^{\pi} \int_0^{2\pi} u(\theta, \phi) Y_{m,n}^*(\theta, \phi) \sin\theta d\theta d\phi = \iint_{\mathcal{S}^2} u(\theta, \phi) Y_{m,n}^*(\theta, \phi) dS, \tag{2.12}$$

where $\langle , \rangle$ denotes the scalar product and * the conjugate of $Y_{m,n}$.
The definition of the scalar product is such as

$$< u, v >= \iint_{\mathcal{S}^2} u(\theta, \phi) v^*(\theta, \phi) dS. \tag{2.13}$$

In order to describe the propagation of waves along r, a propagation term $z_n^{(c)}$ is added to the scalar spherical harmonics [6]. This yields the following solutions to the Helmholtz equation

$$F_{m,n}^{(c)}(r, \theta, \phi) = A_{m,n} z_n^{(c)}(kr) \bar{P}_n^{|m|}(\cos\theta) \mathrm{e}^{im\phi}. \tag{2.14}$$

The normalisation coefficients $A_{m,n}$ are given by

$$A_{m,n} = \frac{s_m}{\sqrt{2\pi}} \frac{1}{\sqrt{n(n+1)}}, \tag{2.15}$$

with

$$s_m = \begin{cases} 1 & \text{for } m = 0, \\ (-\text{sign } m)^m & \text{for } m \neq 0. \end{cases} \tag{2.16}$$

The radial function can be of four types. Two of them are associated with spherical Bessel and Neumann functions that yield stationary fields. They are not used in this manuscript. The two others are given by

$$\begin{aligned} c = - \quad & \text{First-kind spherical Hankel} \quad z_n^{(-)} = h_n^{(1)}(kr) \quad \text{ingoing}, \\ c = + \quad & \text{Second-kind spherical Hankel} \quad z_n^{(+)} = h_n^{(2)}(kr) \quad \text{outgoing}. \end{aligned} \tag{2.17}$$

Here are few details about these 2 types of harmonics:

- Second-kind spherical Hankel functions yield outgoing waves traveling away from the coordinate system center, *i.e*, towards $r \to \infty$. They are singular at O. The radiation of an antenna, *e.g.* the far-field pattern, can be represented with these waves.
- First-kind spherical Hankel functions yield ingoing waves traveling towards O the coordinate system center, *i.e*, towards $r \to 0$. They are singular at O.

Although scalar spherical harmonics are convenient to manipulate, they are inconsistent to describe vector quantities. Indeed at the poles of the sphere, the θ and ϕ components of the field are subject to artificial fast variations, due to the orientation of the spherical coordinates local unit vectors that changes in an uncontinuous way, as shown in Figure 2.4. Since the electromagnetic fields are represented by vectors fields, vector spherical harmonics are chosen for this work.

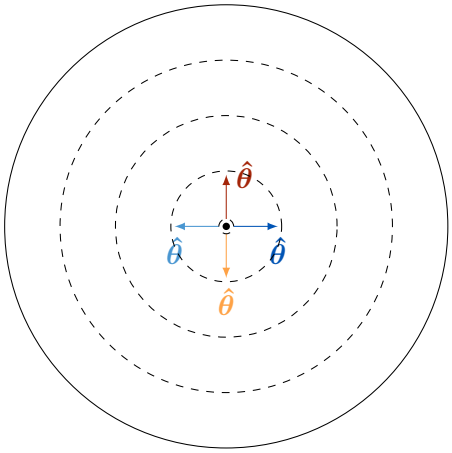

Figure 2.4: Fast variation of the orientation of the $\hat{\boldsymbol{\theta}}$ vector close to the pole of the sphere

2.3.3 Vector spherical harmonics

To describe vectors over a sphere from scalar quantities, e.g. an electric field, the potential theory [68] is generally used. This yields spherical harmonics that are either Transverse Electric (TE) or Transverse Magnetic (TM), with respect to r. In this manuscript, vector spherical harmonics are denoted by means of lowercase bold letters, which is the usual convention for modes inside a waveguide [66].

The TE vector spherical harmonics for the electric field are given by

$$\boldsymbol{e}_{m,n}^{\mathrm{TE},(c)} = k\sqrt{\zeta}\nabla F_{m,n}^{(c)} \times \boldsymbol{r}. \tag{2.18}$$

For the TM field, we have

$$\boldsymbol{e}_{m,n}^{\mathrm{TM},(c)} = k^{-1}\boldsymbol{\nabla} \times \boldsymbol{e}_{\mathrm{t}\,m,n}^{\mathrm{TE},(c)}. \tag{2.19}$$

After the calculation of the derivatives, this yields for the transverse fields

$$\begin{aligned}
\boldsymbol{e}_{\mathrm{t}\,m,n}^{\mathrm{TE},(c)} &= k\sqrt{\zeta}A_{mn}z_n^{(c)}(kr)e^{im\phi}\left[\frac{im\bar{P}_n^{|m|}(\cos\theta)}{\sin\theta}\hat{\boldsymbol{\theta}} - \frac{\mathrm{d}\bar{P}_n^{|m|}(\cos\theta)}{\mathrm{d}\theta}\hat{\boldsymbol{\phi}}\right], \\
\boldsymbol{e}_{\mathrm{t}\,m,n}^{\mathrm{TM},(c)} &= k\sqrt{\zeta}A_{mn}\frac{1}{kr}\frac{\mathrm{d}}{\mathrm{d}kr}\left(krz_n^{(c)}(kr)\right)e^{im\phi}\left[\frac{\mathrm{d}\bar{P}_n^{|m|}(\cos\theta)}{\mathrm{d}\theta}\hat{\boldsymbol{\theta}} + \frac{im\bar{P}_n^{|m|}(\cos\theta)}{\sin\theta}\hat{\boldsymbol{\phi}}\right].
\end{aligned} \tag{2.20}$$

This document may not be reproduced, modified, adapted, published, translated in any way, in whole or in part, nor disclosed to a third party without the prior written consent of ENAC. © 2023, ENAC

For the radial component that will less often be used, we have

$$\begin{aligned} e_{r\ m,n}^{\mathrm{TE},(c)} &= 0, \\ e_{r\ m,n}^{\mathrm{TM},(c)} &= k\sqrt{\zeta} A_{mn} \frac{n(n+1)}{kr} z_n^{(c)}(kr) \bar{P}_n^{|m|}(\cos\theta) e^{im\phi}. \end{aligned} \tag{2.21}$$

The expressions for the magnetic field can be obtained by applying the Maxwell-Faraday equation $\boldsymbol{\nabla} \times \boldsymbol{E} = -i\omega\mu\boldsymbol{H}$. For the transverse field, this yields

$$\begin{aligned} \boldsymbol{h}_{\mathrm{t}\ m,n}^{\mathrm{TE},(c)} &= \frac{ik}{\sqrt{\zeta}} A_{mn} \frac{1}{kr} \frac{\mathrm{d}}{\mathrm{d}kr} \left(kr z_n^{(c)}(kr) \right) e^{im\phi} \left[\frac{\mathrm{d}\bar{P}_n^{|m|}(\cos\theta)}{\mathrm{d}\theta} \hat{\boldsymbol{\theta}} + \frac{im\bar{P}_n^{|m|}(\cos\theta)}{\sin\theta} \hat{\boldsymbol{\phi}} \right], \\ \boldsymbol{h}_{\mathrm{t}\ m,n}^{\mathrm{TM},(c)} &= \frac{ik}{\sqrt{\zeta}} A_{mn} z_n^{(c)}(kr) e^{im\phi} \left[\frac{im\bar{P}_n^{|m|}(\cos\theta)}{\sin\theta} \hat{\boldsymbol{\theta}} - \frac{\mathrm{d}\bar{P}_n^{|m|}(\cos\theta)}{\mathrm{d}\theta} \hat{\boldsymbol{\phi}} \right]. \end{aligned} \tag{2.22}$$

For the radial components, we have

$$\begin{aligned} h_{r\ m,n}^{\mathrm{TE},(c)} &= \frac{ik}{\sqrt{\zeta}} A_{mn} \frac{n(n+1)}{kr} z_n^{(c)}(kr) \bar{P}_n^{|m|}(\cos\theta) e^{im\phi}, \\ h_{r\ m,n}^{\mathrm{TM},(c)} &= 0. \end{aligned} \tag{2.23}$$

2.3.4 Expansion of a field on spherical harmonics

According to [6], the electric field in a source-free region of space may be written as a weighted sum of spherical harmonics. For the transverse components of the fields, this can be expressed as

$$\begin{aligned} \boldsymbol{E}_{\mathrm{t}} &= \sum_{n=1}^{\infty} \sum_{m=-n}^{n} Q_{m,n}^{\mathrm{TE},(+)} \boldsymbol{e}_{\mathrm{t}\ m,n}^{\mathrm{TE},(+)} + Q_{m,n}^{\mathrm{TE},(-)} \boldsymbol{e}_{\mathrm{t}\ m,n}^{\mathrm{TE},(-)} + Q_{m,n}^{\mathrm{TM},(+)} \boldsymbol{e}_{\mathrm{t}\ m,n}^{\mathrm{TM},(+)} + Q_{m,n}^{\mathrm{TM},(-)} \boldsymbol{e}_{\mathrm{t}\ m,n}^{\mathrm{TM},(-)}, \\ \boldsymbol{H}_{\mathrm{t}} &= \sum_{n=1}^{\infty} \sum_{m=-n}^{n} Q_{m,n}^{\mathrm{TE},(+)} \boldsymbol{h}_{\mathrm{t}\ m,n}^{\mathrm{TE},(+)} + Q_{m,n}^{\mathrm{TE},(-)} \boldsymbol{h}_{\mathrm{t}\ m,n}^{\mathrm{TE},(-)} + Q_{m,n}^{\mathrm{TM},(+)} \boldsymbol{h}_{\mathrm{t}\ m,n}^{\mathrm{TM},(+)} + Q_{m,n}^{\mathrm{TM},(-)} \boldsymbol{h}_{\mathrm{t}\ m,n}^{\mathrm{TM},(-)}. \end{aligned} \tag{2.24}$$

In a more condensed way, this can also be expressed as

$$\begin{aligned} \boldsymbol{E}_{\mathrm{t}} &= \sum_{p=\mathrm{TE,TM}} \sum_{c=\pm} \sum_{n=1}^{\infty} \sum_{m=-n}^{n} Q_{m,n}^{p,(c)} \boldsymbol{e}_{\mathrm{t}\ m,n}^{p,(c)}(r,\theta,\phi), \\ \boldsymbol{H}_{\mathrm{t}} &= \sum_{p=\mathrm{TE,TM}} \sum_{c=\pm} \sum_{n=1}^{\infty} \sum_{m=-n}^{n} Q_{m,n}^{p,(c)} \boldsymbol{h}_{\mathrm{t}\ m,n}^{p,(c)}(r,\theta,\phi), \end{aligned} \tag{2.25}$$

where

- $\zeta = \sqrt{\frac{\mu}{\varepsilon}}$ is the wave impedance of the medium, in free-space, $\zeta_0 \approx 120\pi\ \Omega$.
- $Q_{m,n}^{p,(c)}$ are the spherical harmonics coefficients, with $p = \mathrm{TE}$ or $p = \mathrm{TM}$, they are computed from the orthogonality relation [6], which is given by

$$\begin{aligned} Q_{m,n}^{p,(-)} &= \frac{(-1)^m}{2} \iint_{S_r^2} \left[\boldsymbol{E}_{\mathrm{t}} \cdot \left(\boldsymbol{h}_{\mathrm{t},m,n}^{p,(+)} \times \hat{\boldsymbol{r}} \right) - \boldsymbol{H}_{\mathrm{t}} \cdot \left(\hat{\boldsymbol{r}} \times \boldsymbol{e}_{\mathrm{t},m,n}^{p,(+)} \right) \right] dS_r, \\ Q_{m,n}^{p,(+)} &= \frac{(-1)^{-m}}{2} \iint_{S_r^2} \left[\boldsymbol{H}_{\mathrm{t}} \cdot \left(\hat{\boldsymbol{r}} \times \boldsymbol{e}_{\mathrm{t},-m,n}^{p,(-)} \right) - \boldsymbol{E}_{\mathrm{t}} \cdot \left(\boldsymbol{h}_{\mathrm{t},-m,n}^{p,(-)} \times \hat{\boldsymbol{r}} \right) \right] dS_r, \end{aligned} \tag{2.26}$$

with $dS_r = r^2 \sin\theta d\theta d\phi$.

From now on, the summation in (2.25) will be noted

$$\sum_{p=\mathrm{TE,TM}} \sum_{c=\pm} \sum_{n=1}^{\infty} \sum_{m=-n}^{n} = \sum_{pcmn} . \tag{2.27}$$

This summation over c, p, m and n may be depicted in an (n, m) coordinate system (the nm plane) where all values of n and m present in the summation can be indicated. To each of these points correspond four terms of the summation, i.e. the terms with p=TE or p=TM and $c = +$ or $c = -$. The index transformation and the nm plane is illustrated in Figure 2.5.

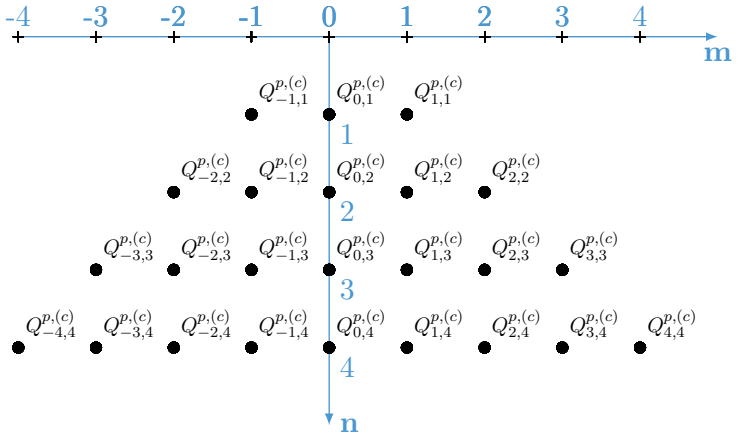

Figure 2.5: Table of the spherical waves coefficients

The spherical wave functions are power normalized such that the radiated power is given by

$$P_{\mathrm{rad}} = \frac{1}{2} \sum_{pmn} |Q^{p,(c)}_{m,n}|^2. \tag{2.28}$$

Finally, Figure 2.1 gives an illustration of the first spherical harmonics. As expected, the first harmonics with $n = 1$ have slow variations, either in elevation or azimuth. When n increases, the field associated with the spherical harmonics shows more variations, in different directions.

This document may not be reproduced, modified, adapted, published, translated in any way, in whole or in part, nor disclosed to a third party without the prior written consent of ENAC. © 2023, ENAC

n/|m|	0	1	2	3
1	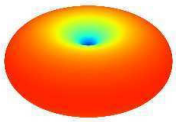	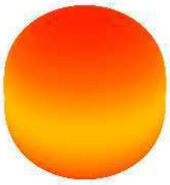		
2	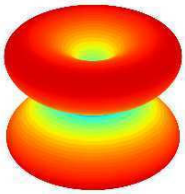	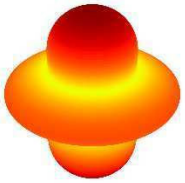	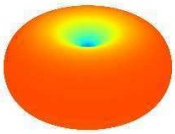	
3	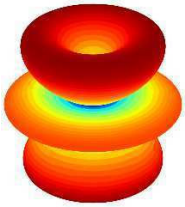	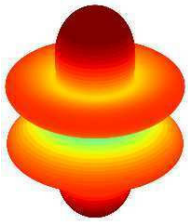	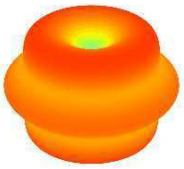	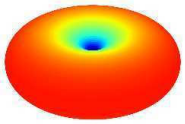

Table 2.1: Amplitude of the spherical harmonics electric field for $n \in [1, 3]$ and $m \in [-3, 3]$

The norm of the electric field has the same shape for p =TE,TM but the components of $\boldsymbol{E}$ are not the same. The spherical harmonics also present variations in ϕ that are not visible in $||\boldsymbol{E}||$, as it only impacts the phase. These variations are visible in 2.6 where the real part of E_ϕ is displayed for $n = 1$, $m = 1$ and p =TE,TM.

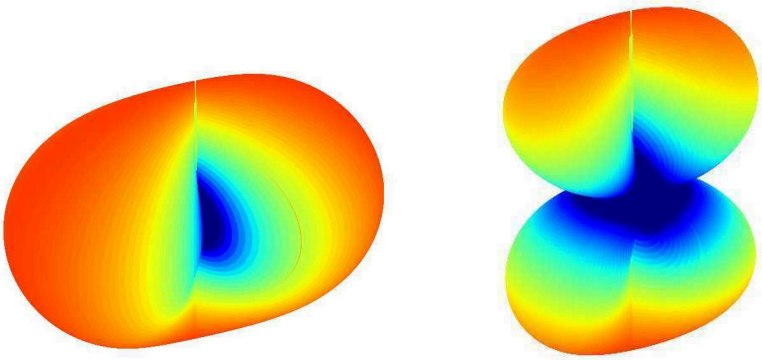

(a) TE component of $Re(E_\phi)$ for $n = 1$, $m = 1$ (b) TM component of $Re(E_\phi)$ for $n = 1$, $m = 1$

Figure 2.6: Behavior of the real part of the E_ϕ component of the spherical harmonics, for $n = 1$ $m = 1$ and p =TE,TM.

2.3.5 Number of modes in spherical wave expansions

In theory, an electromagnetic field may contain an infinity of modes. However, for a given antenna, the modes can be considered to be of limited bandwidth in n, that depends on its size relatively to the wavelength. The active and reactive power of the spherical harmonics are associated with the real and imaginary part of the Poynting vector $\boldsymbol{S} = \frac{1}{2}\boldsymbol{E} \times \boldsymbol{H}^*$, respectively. The active power corresponds to the radiation power which is the propagating part of the radiation.

To study the behavior of the radiation, the wave impedance is interesting as its real part is associated to the active power and the imaginary part to the reactive power. For a spherical harmonic, for $c = +$, in the case TE and TM, this impedances are is given by

$$\begin{aligned}
\zeta_{m,n}^{\mathrm{TM},(+)} &= \frac{E_\theta^{\mathrm{TE},(+)}}{H_\phi^{\mathrm{TE},(+)}} = -\frac{E_\phi^{\mathrm{TE},(+)}}{H_\theta^{\mathrm{TE},(+)}} = i\zeta \frac{\frac{1}{kr}\frac{d}{dkr}\left(krz_n^{(c)}(kr)\right)}{z_n^{(c)}(kr)}, \\
\zeta_{m,n}^{\mathrm{TE},(+)} &= \frac{E_\theta^{\mathrm{TE},(+)}}{H_\phi^{\mathrm{TE},(+)}} = -\frac{E_\phi^{\mathrm{TE},(+)}}{H_\theta^{\mathrm{TE},(+)}} = -i\zeta \frac{z_n^{(c)}(kr)}{\frac{1}{kr}\frac{d}{kr}\left(krz_n^{(c)}(kr)\right)}.
\end{aligned} \tag{2.29}$$

From (2.29), it is noticeable that the wave impedance depends on r. The phase of $\zeta_{m,n}^{\mathrm{TM},(+)}$ is plotted in Figure 2.7. The TE harmonics yield a similar result.

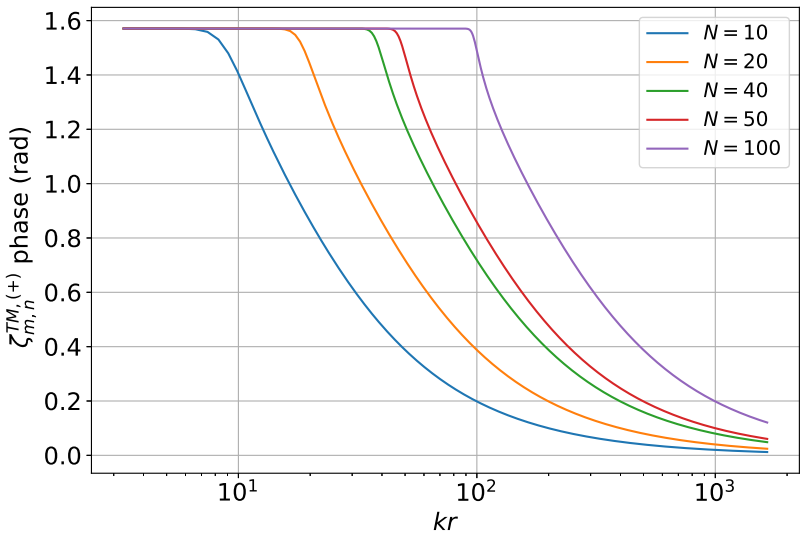

Figure 2.7: Phase of the TM mode impedance $\zeta_{m,n}^{\mathrm{TM},(+)}$

For $kr < n$, the value of the phase yields $\mathfrak{Im}(\zeta_{m,n}) > \mathfrak{Re}(\zeta_{m,n})$. This means that the reactive power is stronger than the active power. Thus, the associated harmonic stores more reactive energy than it propagates. Consequently, inside a sphere of radius r, only harmonics such that $n < kr$, i.e. with a strong enough radiative power, can be efficiently excited. Thus the maximum harmonic level radiated by the antenna, noted N_{AUT}, is given by

This document may not be reproduced, modified, adapted, published, translated in any way, in whole or in part, nor disclosed to a third party without the prior written consent of ENAC. © 2023, ENAC

$$N_{\mathrm{AUT}} = [kr_0] + n_1, \tag{2.30}$$

where r_0 is the radius of the smallest sphere surounding the antenna, the square brackets indicate the largest integer smaller than or equal to kr_0 and the integer n_1 depends on the required accuracy [6]. The value N_{AUT} is named the bandlimit. Its evolution with r_0 is shown in Figure 2.8. As the number of modes influences the variations of the radiation pattern of the antenna, the larger an antenna is the more its pattern can present fast fluctuations.

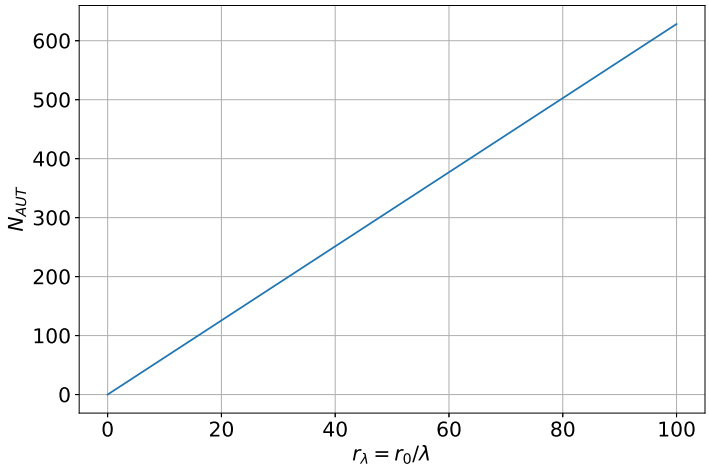

Figure 2.8: Band-limit N_{AUT} with regards to the size of the antenna

2.3.6 Conclusion

This section has presented the vector spherical harmonics, a key tool in post-processing of antenna measurements. First, scalar spherical harmonics have been presented then the construction of vector spherical harmonics and the expansion of a field on spherical harmonics have been detailed. Finally the truncation of the number of harmonics has been discussed. This basis is exploited in the next section to analyse the field of representative examples of antennas.

2.4 Examples of antenna radiation pattern analysis with spherical harmonics

2.4.1 Introduction

The main purpose of this section is to illustrate the use of spherical harmonics on different types of radiation patterns. Different AUT cases used in the sequel are also presented. Note that in this seciton spherical harmonics coefficients are normalized so as to have a radiated power of 1 W. The first subsection 2.4.2 is the demonstration of the analytical calculation of the spherical harmonic coefficients of an elementary dipole. Then subsections 2.4.3 and 2.4.4 are the spherical-harmonics analysis of an half-wave dipole and of an horn antenna,

respectively. Finally subection 2.4.5 presents the analysis of a measurement performed in the ENAC range.

2.4.2 Canonical test : electric and magnetic elementary dipoles

The objective of this section is to analytically derive the spherical harmonic spectrum of a theoretical field. The fields of electric and magnetic elementary dipoles are established as example, as their spectrum can be obtained analytically. The radiation of such dipoles is studied thus only the outgoing part of the field is considered by setting $c = +$ in the equations.

The far-field radiation pattern of an electric elementary dipole located at the origin is given by [69]

$$\begin{aligned} \boldsymbol{E}_e^z(r,\theta,\phi) &= -k^2 c\zeta \frac{\mathrm{e}^{-ikr}}{4\pi r} \hat{\boldsymbol{r}} \times (\hat{\boldsymbol{r}} \times \boldsymbol{p_e}), \\ &= -k\omega\zeta \frac{\mathrm{e}^{-ikr}}{4\pi r} \hat{\boldsymbol{r}} \times (\hat{\boldsymbol{r}} \times \boldsymbol{p_e}), \end{aligned} \tag{2.31}$$

with ω the pulsation and $\boldsymbol{p_e} = p_e \hat{\boldsymbol{z}}$ the elementary dipole moment. If the dipole is oriented along z, expanding the cross product yields

$$\boldsymbol{E}_e^z(r,\theta,\phi) = -k\omega\zeta \frac{\mathrm{e}^{-ikr}}{4\pi r} p_e \sin\theta \hat{\boldsymbol{\theta}}. \tag{2.32}$$

It is possible to recognize the far-field expression of the spherical harmonic

$$\boldsymbol{e}_{\mathrm{t}\,0,1}^{\mathrm{TM},(+)} = -\sqrt{\zeta} \frac{i\sqrt{6}}{4\sqrt{\pi}} \frac{\mathrm{e}^{-ikr}}{r} \sin\theta \hat{\boldsymbol{\theta}}, \tag{2.33}$$

from the expression of the spherical harmonics detailed in [6].

Finally, the far-field radiation of the elementary dipole in terms of spherical harmonics is given by

$$\boldsymbol{E}_e^z(r,\theta,\phi) = Q_{0,1}^{\mathrm{TM},(+)} \boldsymbol{e}_{\mathrm{t}\,0,1}^{\mathrm{TM},(+)}(r,\theta,\phi), \tag{2.34}$$

$$\boldsymbol{H}_e^z(r,\theta,\phi) = Q_{0,1}^{\mathrm{TM},(+)} \boldsymbol{h}_{\mathrm{t}\,0,1}^{\mathrm{TM},(+)}(r,\theta,\phi), \tag{2.35}$$

with

$$Q_{0,1}^{\mathrm{TM},(+)} = -\frac{i\omega k\sqrt{\zeta}}{\sqrt{6\pi}} p_e. \tag{2.36}$$

There is only one non-zero coefficient in the expansion.

A typical representation of the field and of the TE and TM spherical harmonics decomposition is presented in Figure 2.9, for a z-oriented elementary dipole at 96.7 MHz. The far-field radiation of the elementary dipole has been computed from a Feko simulation and is represented on the unitary sphere in Figure 2.9a. The expansion of the field in terms of spherical harmonics, in the Hansen convention is shown in Figure 2.9b.

This document may not be reproduced, modified, adapted, published, translated in any way, in whole or in part, nor disclosed to a third party without the prior written consent of ENAC. © 2023, ENAC

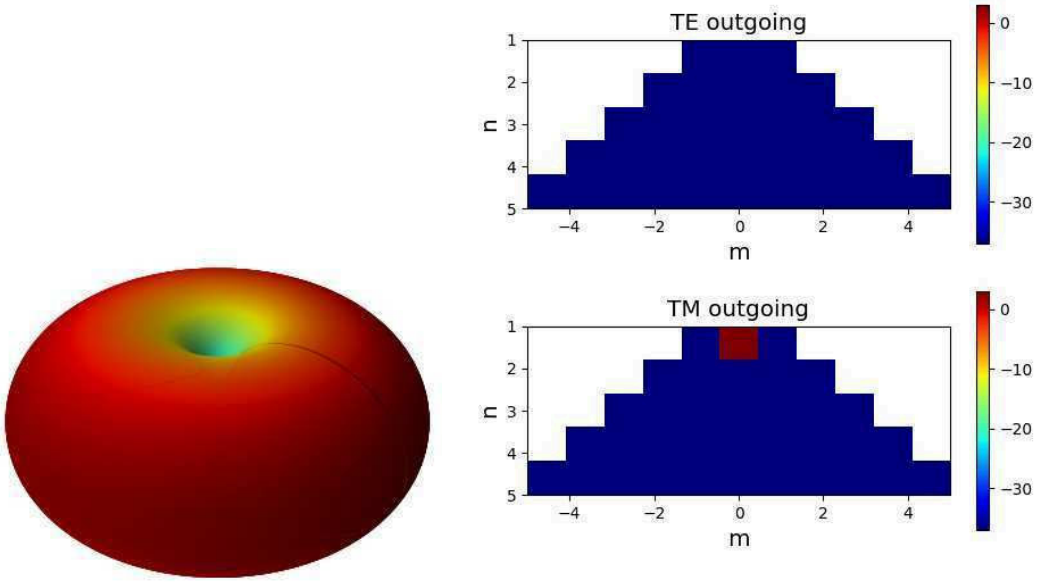

(a) Radiation pattern (dB)

(b) Normalised TE and TM spherical harmonics coefficients (dB)

Figure 2.9: Electric elementary dipole oriented along z

The fields produced by a elementary x-directed dipole and a elementary y-directed dipole located at the origin are respectively given by

$$\boldsymbol{E}_e^x(r,\theta,\phi) = Q_{-1,1}^{\mathrm{TM},(+)} \boldsymbol{e}_{\mathrm{t}\,-1,1}^{\mathrm{TM},(+)}(r,\theta,\phi) + Q_{1,1}^{\mathrm{TM},(+)} \boldsymbol{e}_{\mathrm{t}\,1,1}^{\mathrm{TM},(+)}(r,\theta,\phi), \tag{2.37}$$

with $Q_{1,1}^{\mathrm{TM},(+)} = -Q_{-1,1}^{\mathrm{TM},(+)} = i\omega k\sqrt{\zeta}/\sqrt{12\pi} p_e$ according to [6] and

$$\boldsymbol{E}_e^y(r,\theta,\phi) = Q_{-1,1}^{\mathrm{TM},(+)} \boldsymbol{e}_{\mathrm{t}\,-1,1}^{\mathrm{TM},(+)}(r,\theta,\phi) + Q_{1,1}^{\mathrm{TM},(+)} \boldsymbol{e}_{\mathrm{t}\,1,1}^{\mathrm{TM},(+)}(r,\theta,\phi), \tag{2.38}$$

with $Q_{1,1}^{\mathrm{TM},(+)} = -Q_{-1,1}^{\mathrm{TM},(+)} = -i\omega k\sqrt{\zeta}/\sqrt{12\pi} p_e$.

Similar expressions exist for magnetic dipoles oriented along either x, y or z [6].

2.4.3 Half-wave dipole

The analysis in terms of spherical harmonics of an electric half-wave dipole located at the origin and oriented along the z-axis is performed in this section. The far-field pattern of the dipole is simulated with Altair FEKO at 96.7 MHz and the analysis is performed by means of a numerical evaluation of (2.26). Results are presented in Figure 2.10, in which it is noticeable that the dipole only radiates TM modes.

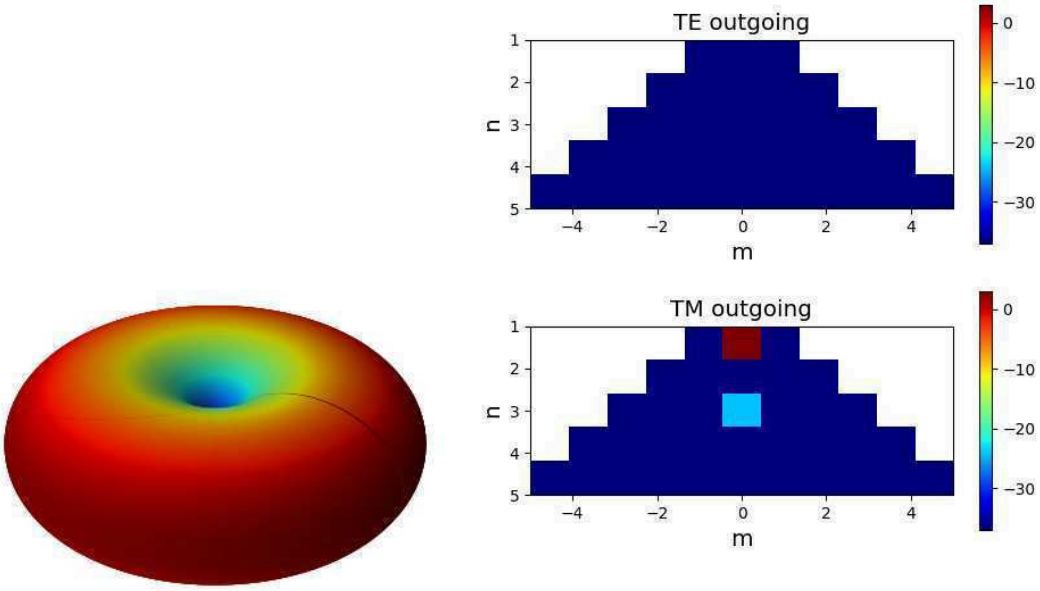

(a) Radiation pattern (dB) (b) Normalised TE and TM spherical harmonic coefficients (dB)

Figure 2.10: Electric half wave dipole oriented along z

The radiation pattern does not present any variation along ϕ, because of the rotational symmetry about the vertical axis and the feeding of the antenna, so the only non-zero coefficients satisfy $m = 0$. Moreover, the symmetry with respect to the plane $z = 0$ implies that only coefficients for which n is odd are non-zero. Finally, as the antenna is larger than the elementary dipole, the radiated field involves more harmonic coefficients.

2.4.4 Horn antenna

The third case is a horn at 5 GHz, fed by a waveguide with one mode TE10. This radiation is computed with the method of moments. The corresponding far-field radiation given by Altair Feko is shown in Figure 2.11 and the analysis in terms of Hansen spherical harmonics computed with a numerical evaluation of (2.26) is represented in Figure 2.12.

This document may not be reproduced, modified, adapted, published, translated in any way, in whole or in part, nor disclosed to a third party without the prior written consent of ENAC. © 2023, ENAC

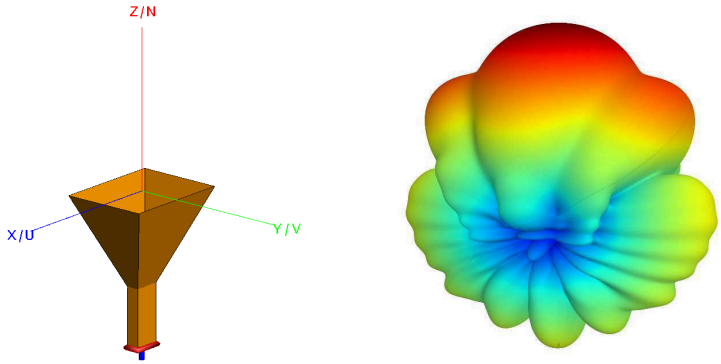

(a) Horn antenna

(b) E-field radiated by the Horn (dB)

Figure 2.11: Horn antenna characteristics

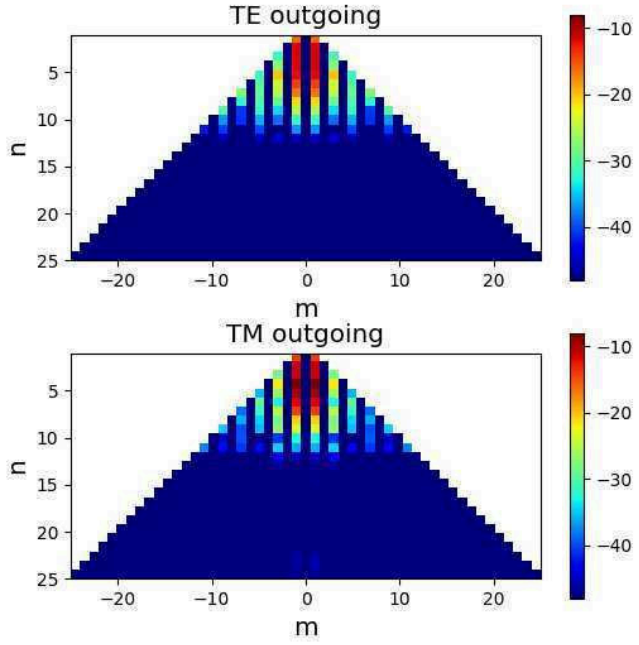

Figure 2.12: Normalised TE and TM spherical harmonic coefficients of the horn antenna (dB)

As the antenna is larger, the radiation pattern presents more variations and the number of non-zero coefficients increases. The antenna presents symmetries about two planes, $y = 0$ and $x = 0$. As a consequence every coefficients with m even are equal to zero. Due to its size ($r_0 = 0.27$m), the antenna cannot radiate coefficients of order greater than $N_{\text{AUT}} = 28$, as explained in Section 2.3.5.

2.4.5 Measurement example

After testing the expansions on simulations, spherical harmonics analyses are performed on measurement data acquired in the ENAC anechoic chamber. The gain of the antenna under test is here obtained from the S21 parameter using an 'unknown through' calibration, assuming that the far-field condition is fullfilled and that the propagation is as in free space, i.e. without disturbances. The antenna chosen for this study, developed by the ENAC lab, is intended to be mounted on a drone to perform secondary radar measurement *in situ*, for the D2R2 ('Mesure par Drone de Diagrammes de Rayonnement Radar') project. This antenna is a monopole antenna mounted on a patch antenna, as shown in Figure 2.13a. Thus this antenna works on two frequencies : 1030 MHz with a vertical polarization and at 1575.42 MHz with a circular polarization. Those frequencies correspond to the secondary radar frequency and to the GPS-L1 frequency, respectively.

A measurement of the antenna and the expansion in spherical harmonics of the field are performed at the GPS frequency.

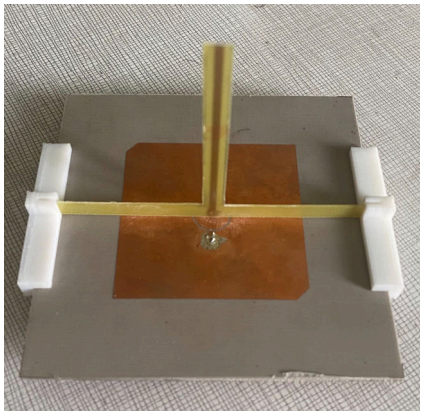

(a) D2R2 antenna

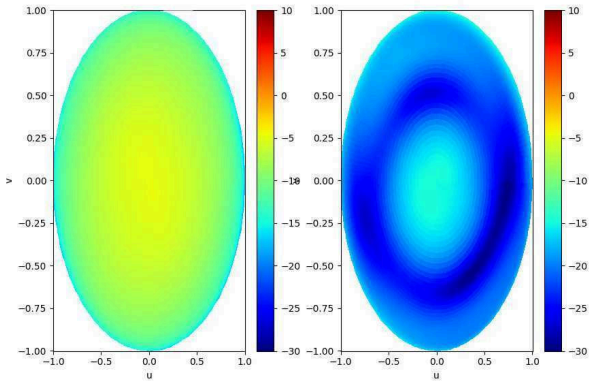

(b) Radiation pattern of the patch antenna (dB)

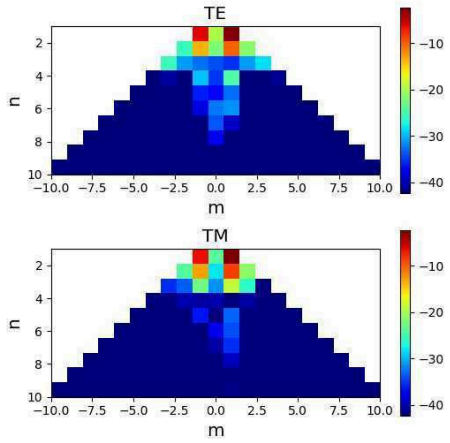

(c) Normalised expansion in spherical harmonics (dB)

Figure 2.13: Analysis of the D2R2 antenna

This document may not be reproduced, modified, adapted, published, translated in any way, in whole or in part, nor disclosed to a third party without the prior written consent of ENAC. © 2023, ENAC

This antenna is very small relatively to the wavelength (20 cm), with $r_0 = 8$ cm. Consequently, the bandlimit N_{AUT} of this antenna is $N_{\text{AUT}} \simeq 3$, according to (2.30) which corresponds to the result in Figure 2.13c. However, higher order coefficients appear. This is due to the defaults of the anechoic chamber. This antenna is asymmetrical, because of the shape of the patch with two truncated corners and the single feeding. This is why its spherical analysis is not perfectly symmetrical. However, the expected strong coefficients are presents, for $n = \{1, \cdots, 4\}$ and $m = \pm 1$.

2.4.6 Conclusion

This section has shown examples of antenna analysis in terms of Hansen spherical harmonics. First of all, the mathematical expression of the elementary dipole far-field has been analysed in terms of spherical harmonics. Then spherical harmonic spectrums of different simulated antennas have been numerically computed: a half-wave dipole and a horn. Finally, the measured field of an antenna in the ENAC anechoic room has been analysed. This type of analysis is part of a typical post-processing of the radiation pattern measurement.

2.5 Antenna measurement post-processing

2.5.1 Introduction

The measured data, in the form of S-parameters, provides valuable information about the performance of the antenna and can be used to validate simulations. However, the raw measurement data always needs to be processed and analysed to extract useful information about the antenna's radiation pattern, gain, directivity, and other properties. This is where antenna measurement post-processing comes into play.

This section is an introduction to antenna measurement post-processing. In Section 2.5.2, the near-field to far-field transformation is presented, then procedure to mitigate effects of the environment are presented in Section 2.5.3. Finally in Section 2.5.4, methods used to shorten measurement time are mentioned.

2.5.2 Near-Field to Far-field transformation

NFFT is a technique used in antenna measurement to determine the far-field radiation pattern of an antenna based on measurements taken in its near-field region [6]. This technique is used to avoid the need for large open spaces required for far-field measurements. Firstly, the near-field pattern is expanded in spherical harmonics, then the contribution of the probe in the expansion is compensated. This computation, generally done by means of spherical harmonics, becomes simpler if the probe only radiates spherical harmonics such that $m = \pm 1$. Finally, the field of the antenna is reconstructed at any distance from the antenna from its harmonic expansion [14].

2.5.3 Correction of perturbations coming from the environment

Antenna measurements can be spoiled by perturbations coming from the measurement environment. These perturbations can stem from a multitude of sources, ranging from nearby structures to electromagnetic interferences and signal multipath effects. This section presents post-processing correction methods acting on various aspects of the measured signal.

2.5.3.1 Probe correction

In near-field measurements, the radiation of the probe has an influence on the measurement signal. During the NFFT, it is essential to isolate the radiation of the AUT in the measurement signal. In spherical geometry, this signal is modeled by an equation in which the spherical harmonic expansion of the probe plays a role. Considering that harmonic coefficients of the probe are known, it is then possible to identify the coefficients corresponding to the radiation of the AUT and obtain its far-field radiation pattern [6, 14]. Consequently, the choice of the probe is very important. Most of the time, they are chosen relatively to the complexity of their spherical harmonic expansion, in order to obtain efficient and robust correction. As a consequence, probes are commonly designed to radiate only spherical harmonics with $m = \pm 1$. For example dual polarized near-field probes with only first-azimuthal modes are developed by MVG [41], as shown in Figures 2.14, and NSI-MI [51].

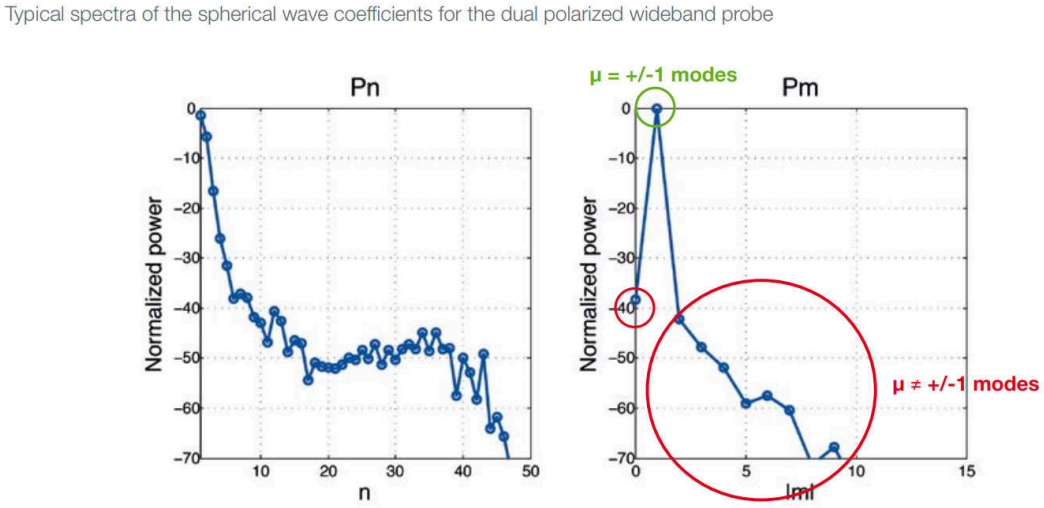

Figure 2.14: Spherical harmonics spectrum of the dual polarized near-field probes developed by MVG [41]

However, the probe is not the only source of perturbation as other phenomena such as multipath coming from the measurement chamber and its equipments.

2.5.3.2 Time gating

In antenna measurements, time gating is a technique that isolates the response of an antenna in the presence of unwanted reflections or interferences. This method is based on

This document may not be reproduced, modified, adapted, published, translated in any way, in whole or in part, nor disclosed to a third party without the prior written consent of ENAC. © 2023, ENAC

the hypothesis that the undesired signals are delayed compared to the signal of interest, as shown in Figure 2.15. If the measurement is made on a wide frequency range, an Inverse Fast Fourier Transform (IFFT) of the measurement can be done in order to obtain the impulse response of the channel [70]. Then, a time gating is performed by setting to zero the signals delayed compared to the signal of interest, before performing a Fast Fourier Transform (FFT) to come back to the harmonic domain. Thus this method is particularly efficient for measurements in large chambers, where consequent delays exist between the signal of interest and the reflections. This method is limited by the bandwidth of the different elements: the probe, the AUT etc. Indeed, the delay between the multipath must satisfy the condition [71]

$$|B\tau| \gg 1 \tag{2.39}$$

with B the bandwidth of the RF channel, defined by the bandwidth of the measurement chain, τ the delay between the multipath and the signal of interest. Thus this method cannot be efficient in small test range or with antennas having a small bandwidth B.

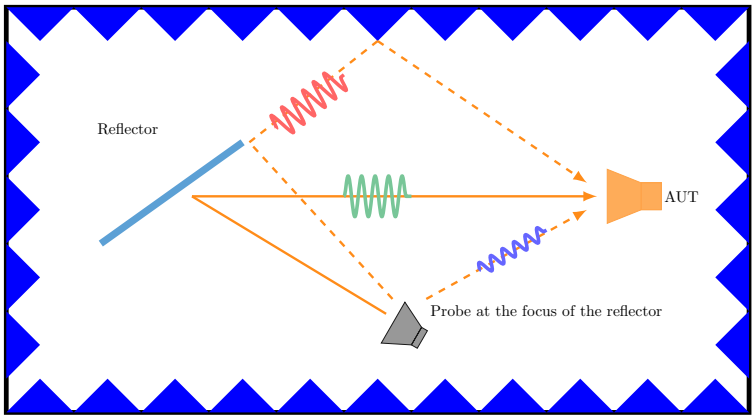

(a) Multipath in measurement chamber

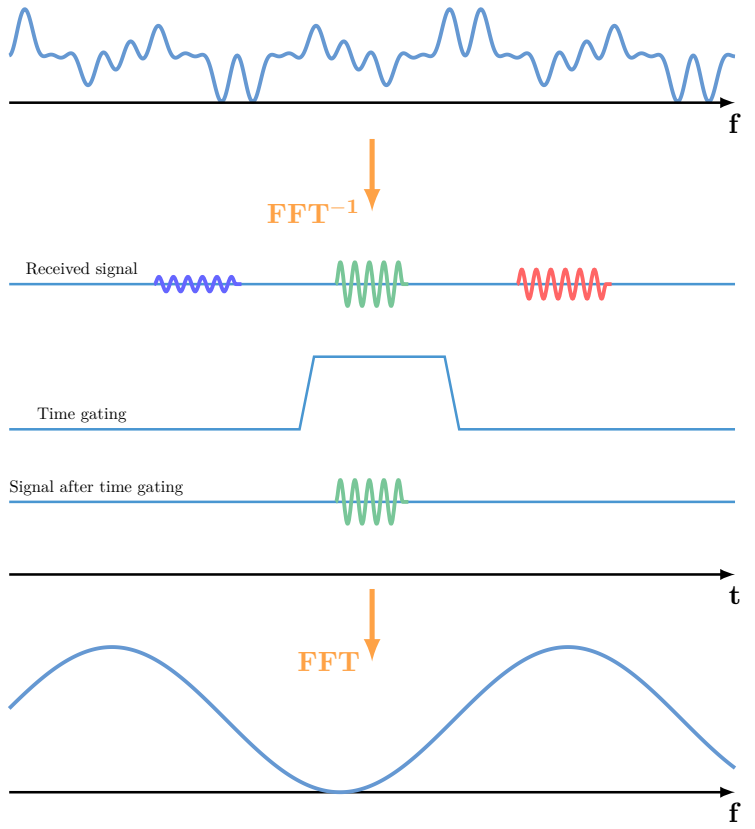

(b) Signal post-processing

Figure 2.15: Principle of time gating in antenna measurements

2.5.3.3 Current reconstruction and spatial filtering

A recent post-processing method relying on the equivalent current representation of the antenna has been developed [12, 13, 72]. This method consists in measuring the near-field antenna radiation pattern and to convert it to equivalent current on a volume, often called a Huygens box. This equivalent current representation has many utilizations, it can characterize an antenna, be embedded to a Electromagnetic Compatibility (EMC) simulation, or used to localize unexpected sources of radiation in the near field of the

This document may not be reproduced, modified, adapted, published, translated in any way, in whole or in part, nor disclosed to a third party without the prior written consent of ENAC. © 2023, ENAC

AUT [13]. Based on this equivalent current representation, it is possible to eliminate undesired radiations, this method is called spatial filtering [73].

The Insight software developed by MVG [12], is based on this approach. This software allows to yield an equivalent model in the form of a near-field Huygens box, starting from the antenna measurement. Simulations and measurements can be used simultaneously in the software. A typical case of utilization is presented in Figure 2.16.

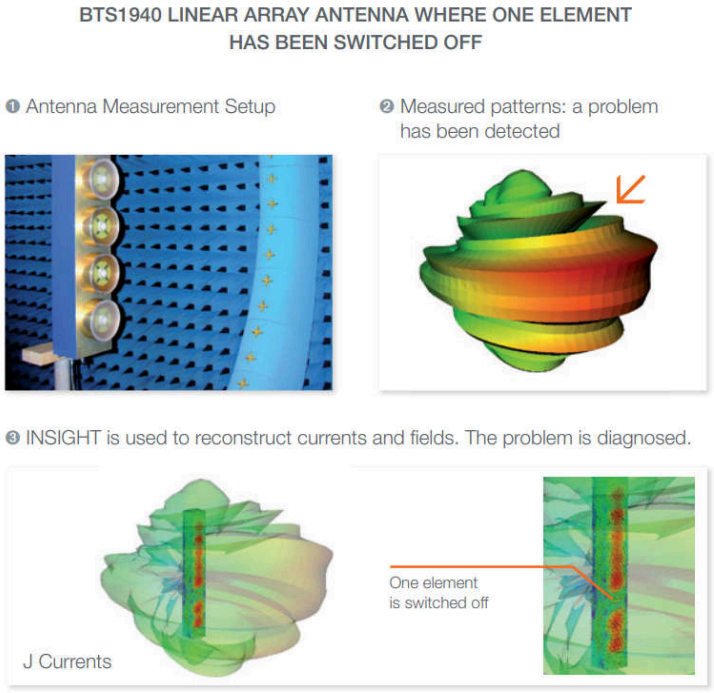

Figure 2.16: Insight use for antenna radiation pattern diagnostics [12]

It is also possible to correct signals in the spectral domain, on spherical harmonics [74].

2.5.3.4 Spectral filtering

Spectral or mode filtering consists in post-processing the spherical harmonics spectrum of the radiation pattern of a measured antenna. The method relies on three steps: firstly the spherical harmonic maximum level N_{AUT} the AUT can radiate has to be calculated, according to (2.30). Secondly the analysis in terms of spherical harmonics of the measurement is performed, to a harmonic level n superior to the N_{AUT} calculated above, which implies a measurement sphere sampling larger than the antenna. Thirdly, every coefficients above N_{AUT} are put to zero, indeed they cannot correspond to the AUT radiation, its size does not allow it. Finally the inverse spherical harmonic transform is performed to retrieve the partially corrected radiation pattern of the AUT.

This method has been tested at ENAC, as part of a student project, on measurements of an array patch antenna, as shown in Figures 2.17, 2.18 and 2.19. The measurement has been performed outside of the anechoic range, to maximize perturbations, which is why the figure 2.19b is very noisy. This spherical analysis is performed and truncated, as

shown in Figure 2.18. Finally the field is reconstructed and compared with simulation in Figure 2.19.

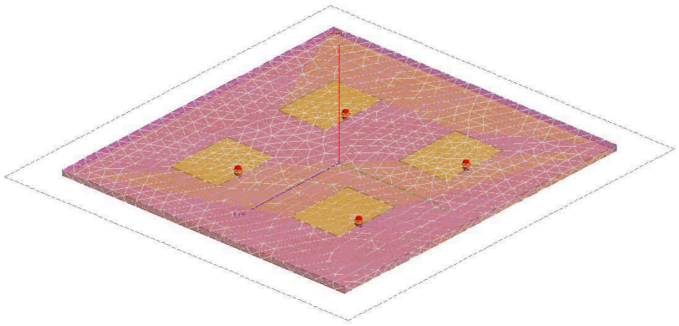

Figure 2.17: AUT simulated with Feko, with a central frequency of 5.8 GHz,

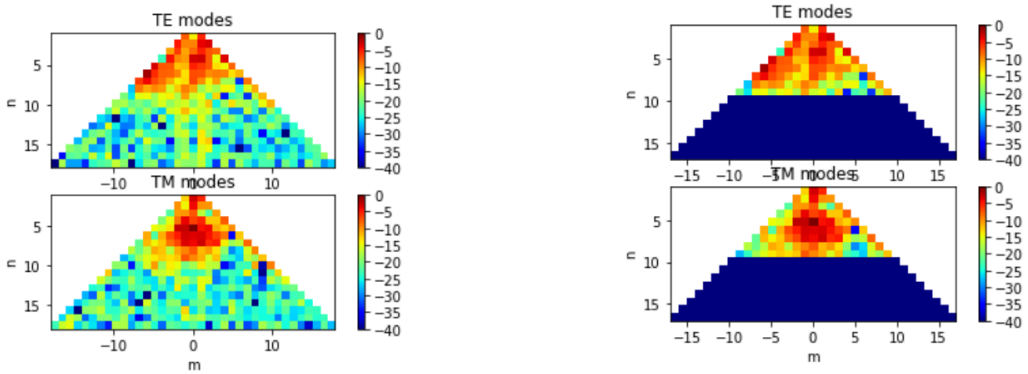

Figure 2.18: Unfiltered and filtered spherical harmonic spectrums of the measured patch array

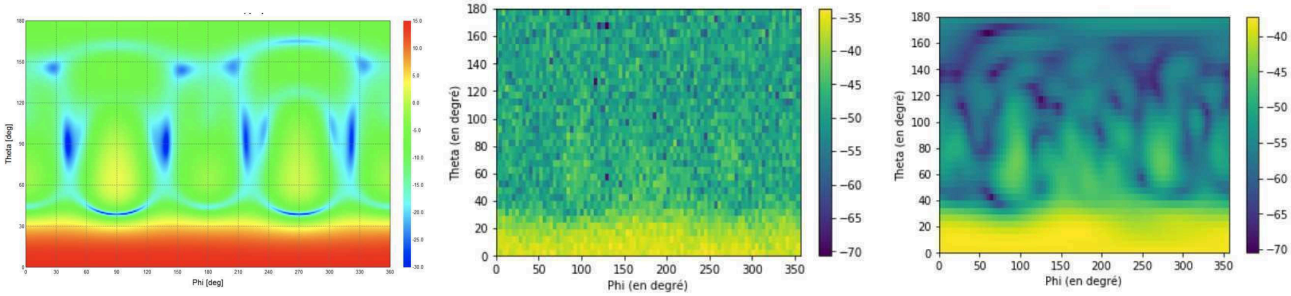

(a) Simulated radiation pattern with Feko (b) Measured radiation pattern (c) Filtered radiation pattern

Figure 2.19: Effect of the spectral filtering technique on the radiation pattern

Despite the poor quality of the measurement, significant improvements in the correspondence of the simulated pattern and the filtered pattern is obtained in the process.

In [15] an evolution of this spatial filtering is done in order to suppress scattering. The main principle of the technique is to position the AUT with an offset from the measurement

This document may not be reproduced, modified, adapted, published, translated in any way, in whole or in part, nor disclosed to a third party without the prior written consent of ENAC. © 2023, ENAC

rotation center, while antennas are usually positioned in the center. In this way, r_0, the radius surrounding the rotating system is larger, and the spherical wave analysis goes up to a higher N'_{AUT}. However, the antenna does not radiate higher order waves relatively to its own coordinate system. Then a computation is performed to modify the spectrum as if the antenna were at the center of the frame. Now every coefficients that are non-zero between the level N_{AUT} and N'_{AUT} correspond to scattering.

However this method has no action on the coefficients of order $n \leq N_{\mathrm{AUT}}$ so the information is only partially corrected. Other methods have been developed to separate the contribution of the AUT from radiation of the environment, by means of spherical harmonics.

2.5.3.5 Test zone field compensation

The Test Zone Field (TZF) compensation method is a technique developed in [17] [18]. The TZF is the field illuminating the zone inside which the measured antenna is placed. This method works by compensating for the effects of the test environment on the measurement of the AUT.

This breaks down in two steps. In the first step, the TZF is determined by placing a reference antenna (with known radiation characteristics) in the test zone. In the second step, the knowledge of the TZF is utilized in solving the radiation characteristics of the AUT. The method is schematized in Figure 2.20.

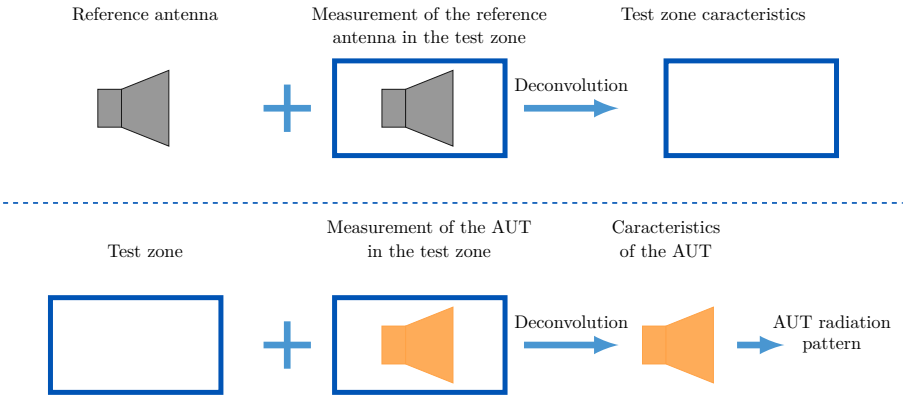

Figure 2.20: Test zone field compensation

The method is based on the spherical-harmonics theory, as presented in Section 2.3 and is applicable to both single-polarized and multi-polarized probes and multi-probe measurement systems. The simulations and measurement results presented in [18] demonstrate that the method works reliably in various kinds of surroundings.

2.5.4 Speeding up antenna measurement

A major issue in characterization of antenna radiation patterns over the sphere is the long field acquisition time. This is partially due to the sampling of the measurement sphere: for example in near field, at least $2 \times L_\theta \times L_\phi$ measurement points are needed in order to retrieve the entire spherical harmonics spectrum, for both polarizations, where L_θ and L_ϕ are the number of sampling points along θ and ϕ, respectively. They depend on the

size of the antenna [6]. For an equiangular grid, the number of points is then of order 4 L_θ^2. For a grid of step 1°, this means that 131044 measurements are required. Besides, an equiangular grid over the sphere does not provide an uniform sampling of the sphere because poles are oversampled.
Consequently, methods have been developed to downsample the antenna measurement to speed up the acquisition of the field. One of them consists in leveraging the sparsity of the radiated field spectrum into spherical harmonic basis. This is made possible by regularities and symmetries exhibited in the radiation pattern of the AUT. Indeed these properties allow the spherical harmonic spectrum to be sparse. This has been noticed in [75] and exploited for antenna characterization in [9] and [10]. The sampling of the sphere has also been reconsidered. New sampling theorem and techniques have been developed in [76, 77, 78] and [79]. Sparse sampling method for antenna characterization are put forward in [80]. Other bases than spherical harmonics can also be used as in [81] where a reduced-order model approach is proposed.

2.5.5 Conclusion

This section has introduced common post-processing and correction methods, often applied to data acquired from antenna measurement. The near-field to far-field transformation has been introduced, four types of corrections of the environment have been presented: probe correction, time gating, spatial and spectral filtering and test zone field compensation. Finally, methods to decrease measurement time have been described.

2.6 Conclusion

This chapter has presented the tools and methods to post-process antenna measurement in spherical geometries.

Firstly, the coordinate system and operators have been established, they are essential to describe motions in the range. The spherical coordinates have been reminded, followed by the mathematical tools and operators that relate to rotations over the sphere.

Standard vector spherical harmonics for antennas have been derived in the consecutive section, firstly the scalar, then the vector spherical harmonics. Then the expansion of electromagnetic fields has been detailed. This type of expansion is truncated because of the properties of the spherical harmonics.

The following section has illustrated the previous ones by showing examples of expansions in terms of spherical harmonics. They have been performed for several radiation patterns.

Finally, antenna measurement post-processing methods have been briefly introduced in the last section of the chapter. The concept of near-field to far-field transformation, correction of perturbations coming from the environment and methods to speed-up antenna measurements have been presented.

This document may not be reproduced, modified, adapted, published, translated in any way, in whole or in part, nor disclosed to a third party without the prior written consent of ENAC. © 2023, ENAC

Chapter 3

Spin spherical harmonics

3.1 Introduction

Spherical harmonics analyses are commonly encountered in the post-processing of antenna measurement, and are prominent in many other science and engineering fields. Indeed, data are often represented on spheres: in computer graphics [82], chemistry [83, 84], geophysics [85, 86, 87], planetary science [88, 89, 90, 91], solar physics and astrophysics [92, 93], among many others. For example, the anisotropy of the cosmic microwave background has recently been studied over a sphere and analysed in terms of spherical harmonics [93], [20]. As a consequence, exact and fast algorithms for spherical harmonic analysis, based on sampling theorems have been developed, notably in [21]. Many formulations of the spherical harmonics exist, in particular, the notations and formalism as described in Hansen's book are often used in antennas measurement, as defined in Chapter 1.

The present chapter focuses on an alternative formulation for describing electromagnetic fields with spherical harmonics, inspired by theoretical physics. This formulation is peculiar to signals defined over a sphere and has advantageous properties for formulating rotations. This leads to spin-weighted spherical harmonics, for which sampling theorems and transform algorithms exist that are both stable and fast.

The plan of this chapter is as follows. In Section 3.2, the theory of the spin spherical harmonics is presented. In Section 3.3 the sampling theorem and the fast algorithms that allow the computation of the spin spherical harmonics transform are described. The contribution of this PhD thesis begins in Section 3.4, where the relation between the Hansen and the spin spherical harmonics is derived. Finally, Section 3.5 shows that the spin can benefit to antenna radiation pattern analysis through selected examples.

3.2 Theory of spin spherical harmonics

3.2.1 Introduction

Spin functions have been introduced by Penrose and Newman in quantum physics in [94] to describe gravitational radiation. These functions are convenient to represent band-limited signals, i.e. for which a limit exists in the fastness of the variations on the sphere. They provide a unifying framework over the sphere, where spin $s = 0$ is suitable to describe

This document may not be reproduced, modified, adapted, published, translated in any way, in whole or in part, nor disclosed to a third party without the prior written consent of ENAC. © 2023, ENAC

scalar signals and $s = \pm 1$ functions allow the representation of the tangent vector fields to the sphere. Higher spin orders can be used to parameterize tensors [95], but this topic is beyond the scope of this PhD thesis. Moreover, the spin has advantageous rotation properties. In this section, the objective is to make a general presentation of the spin spherical harmonics and its properties.
This section reviews the theory of spin spherical harmonics. To begin with, Section 3.2.2 gives the definition of spin functions. Then Section 3.2.3 presents the spin spherical harmonics and Section 3.2.4 derives the expansion of a spin function on these harmonics. Next, Section 3.2.5 relates tangent vectors over a sphere to signals of spin ± 1. Finally, global rotation properties of spin functions and associated tangent vectors are detailed in Section 3.2.6.

3.2.2 Spin functions

Spin functions are square integrable functions on the sphere, parameterised by the integer spin $s \in \mathbb{Z}$, noted $u_s \in L^2(\mathcal{S}^2)$. As explained in [95], a spin function is defined by its behavior under a local rotation, i.e. a rotation by $\chi_l \in [0, 2\pi[$ in the tangent plane centered on any spherical coordinates (θ, ϕ), with $\theta \in [0, \pi]$ and $\phi \in [0, 2\pi[$, as shown in Figure 3.1. Local rotations yield a spin dependent phase shift given by

$$u'_s(\theta, \phi) = \mathrm{e}^{-is\chi_l} u_s(\theta, \phi), \tag{3.1}$$

where the prime designates the local rotation of u_s by $\chi_l \in [0, 2\pi[$. This is a local rotation as every point on the sphere is associated with a different rotation, whereas a global rotation consists in shifting the entire signal on the sphere and could be represented by an element of SO(3).

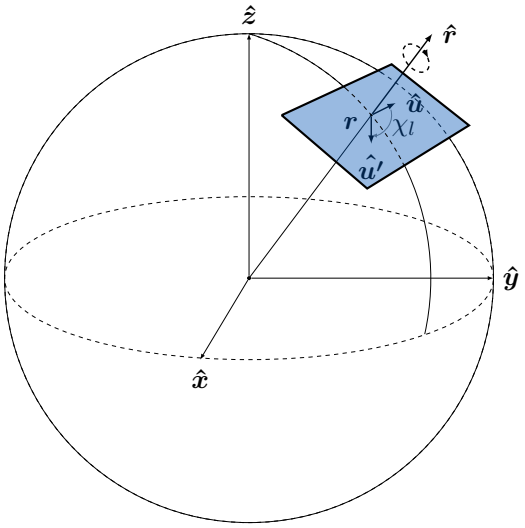

Figure 3.1: Local rotation in the tangent plane to the sphere at a given point

Spin functions belongs to $L^2(\mathcal{S}^2)$, which means that they could be expanded in terms of standard spherical harmonics. However the spin feature of these functions yields the introduction of spin spherical harmonics.

3.2.3 Spin spherical harmonics

The spin spherical harmonics are based on the scalar spherical harmonics defined in Section 2.3.2. They are noted $Y_{smn} \in L^2(\mathcal{S}^2)$ with $s \in \mathbb{Z}$, $n \geq |s|$, and $|m| \leq n$. They form an orthogonal basis for $L^2(\mathcal{S}^2)$ spin-s functions over the sphere. These harmonics can be expressed using the spin raising and lowering operators, $\eth$ (pronounced "eth") and $\bar{\eth}$, defined by

$$\begin{aligned} \eth &\equiv -\sin^s\theta \left(\frac{\partial}{\partial\theta} + \frac{i}{\sin\theta}\frac{\partial}{\partial\phi}\right)\sin^{-s}\theta, \\ \bar{\eth} &\equiv -\sin^{-s}\theta \left(\frac{\partial}{\partial\theta} - \frac{i}{\sin\theta}\frac{\partial}{\partial\phi}\right)\sin^{s}\theta, \end{aligned} \tag{3.2}$$

with s the spin order of the signal to which $\eth$ or $\bar{\eth}$ is applied. Spin spherical harmonics are related to scalar (spin-zero) harmonics by

$$\begin{aligned} Y_{smn}(\theta,\phi) &= \left[\tfrac{(n-s)!}{(n+s)!}\right]^{1/2} \eth^s Y_{mn}(\theta,\phi), && \text{for } 0 \leq s \leq n, \\ Y_{smn}(\theta,\phi) &= (-1)^s \left[\tfrac{(n+s)!}{(n-s)!}\right]^{1/2} \bar{\eth}^{-s} Y_{mn}(\theta,\phi), && \text{for } -n \leq s \leq 0, \end{aligned} \tag{3.3}$$

where $\eth^s$ and $\bar{\eth}^{-s}$ mean the operators are applied $|s|$ times and Y_{mn} denotes the scalar spherical harmonics as defined in (2.10). A signal of spin s can be expanded on spin-s spherical harmonics over the sphere. In this PhD thesis, we will consider exclusively functions with spin $s = \{-1, 0, 1\}$.

From (3.3) and (2.10), the spin+1 harmonic is can be expressed as

$$\begin{aligned} Y_{1,m,n} &= -\left(\frac{(n-1)!}{(n+1)!}\right)^{1/2} \left(\frac{\partial}{\partial\theta} + \frac{i}{\sin\theta}\,\frac{\partial}{\partial\phi}\right) Y_{m,n} \\ &= -\left(\frac{(n-1)!}{(n+1)!}\right)^{1/2} \left(\frac{\partial}{\partial\theta} + \frac{i}{\sin\theta}\,\frac{\partial}{\partial\phi}\right) \left(\frac{1}{\sqrt{2\pi}}\bar{P}_n^{|m|}(\cos\theta)e^{im\phi}\right) \\ &= -\frac{1}{\sqrt{2\pi}\sqrt{n(n+1)}} \left(\frac{\mathrm{d}\bar{P}_n^{|m|}(\cos\theta)}{\mathrm{d}\theta} - \frac{m\bar{P}_n^{|m|}(\cos\theta)}{\sin\theta}\right) e^{im\phi}. \end{aligned} \tag{3.4}$$

Similarly, the spin−1 harmonic are given by

$$\begin{aligned} Y_{-1,m,n} &= \left(\frac{(n-1)!}{(n+1)!}\right)^{1/2} \left(\frac{\partial}{\partial\theta} - \frac{i}{\sin\theta}\,\frac{\partial}{\partial\phi}\right) Y_{m,n} \\ &= \left(\frac{(n-1)!}{(n+1)!}\right)^{1/2} \left(\frac{\partial}{\partial\theta} - \frac{i}{\sin\theta}\,\frac{\partial}{\partial\phi}\right) \left(\frac{1}{\sqrt{2\pi}}\bar{P}_n^{|m|}(\cos\theta)e^{im\phi}\right) \\ &= \frac{1}{\sqrt{2\pi}\sqrt{n(n+1)}} \left(\frac{\mathrm{d}\bar{P}_n^{|m|}(\cos\theta)}{\mathrm{d}\theta} + \frac{m\bar{P}_n^{|m|}(\cos\theta)}{\sin\theta}\right) e^{im\phi}. \end{aligned} \tag{3.5}$$

3.2.4 Expansion of a spin function on spin spherical harmonics

According to [21] the orthogonality and completeness of the spin spherical harmonics allows any square integrable spin s function, $u_s(\theta,\phi)$ to be expressed over the sphere as

This document may not be reproduced, modified, adapted, published, translated in any way, in whole or in part, nor disclosed to a third party without the prior written consent of ENAC. © 2023, ENAC

$$u_s(\theta,\phi) = \sum_{n=|s|}^{\infty} \sum_{m=-n}^{n} C^s_{m,n} Y_{s,m,n}(\theta,\phi), \tag{3.6}$$

with $C^s_{m,n}$ corresponding to spin spherical harmonics coefficients given by the usual projection

$$C^s_{m,n} = \langle u_s, Y_{s,m,n} \rangle = \iint_{\mathcal{S}^2} u_s(\theta,\phi) Y^*_{s,m,n}(\theta,\phi) dS. \tag{3.7}$$

3.2.5 Spin components of tangent vectors over the sphere

Let us consider an arbitrary field $\boldsymbol{V}$ that can be expanded on its radial and tangent component as

$$\boldsymbol{V} = \boldsymbol{V}_{\mathrm{t}} \ + \boldsymbol{V}_r. \tag{3.8}$$

The tangent vector $\boldsymbol{V_t}$ on $\mathcal{S}^2$, can be expanded in two components such that

$$\boldsymbol{V_t}(\theta,\phi) = V_{+1}(\theta,\phi)\hat{\boldsymbol{u}}_{+1} + V_{-1}(\theta,\phi)\hat{\boldsymbol{u}}_{-1}, \tag{3.9}$$

with $\hat{\boldsymbol{u}}_{+1}, \hat{\boldsymbol{u}}_{-1}$, unit vectors defined by

$$\begin{aligned} \hat{\boldsymbol{u}}_{+1} &= \frac{\hat{\boldsymbol{\theta}} - i\hat{\boldsymbol{\phi}}}{\sqrt{2}}, \\ \hat{\boldsymbol{u}}_{-1} &= \frac{\hat{\boldsymbol{\theta}} + i\hat{\boldsymbol{\phi}}}{\sqrt{2}}, \end{aligned} \tag{3.10}$$

as in [96]. The unit vectors $(\hat{\boldsymbol{\theta}}, \hat{\boldsymbol{\phi}})$ are defined in Figure 2.1.

These vectors are rotation invariant, up to a phase term. Indeed, after a local rotation χ_l, the unit vectors $\hat{\boldsymbol{\theta}}$ and $\hat{\boldsymbol{\phi}}$ become

$$\begin{aligned} \hat{\boldsymbol{\theta}}' &= \cos\chi_l \hat{\boldsymbol{\theta}} + \sin\chi_l \hat{\boldsymbol{\phi}}, \\ \hat{\boldsymbol{\phi}}' &= -\sin\chi_l \hat{\boldsymbol{\theta}} + \cos\chi_l \hat{\boldsymbol{\phi}}. \end{aligned} \tag{3.11}$$

Then the definition of the spin unit vectors gives

$$\begin{aligned} \hat{\boldsymbol{u}}'_{+1} &= \frac{\hat{\boldsymbol{\theta}}' - i\hat{\boldsymbol{\phi}}'}{\sqrt{2}} \\ &= \frac{\cos\chi_l \hat{\boldsymbol{\theta}} + \sin\chi_l \hat{\boldsymbol{\phi}} + i\sin\chi_l \hat{\boldsymbol{\theta}} - i\cos\chi_l \hat{\boldsymbol{\phi}}}{\sqrt{2}}, \\ &= \mathrm{e}^{i\chi_l} \hat{\boldsymbol{u}}_{+1}. \end{aligned} \tag{3.12}$$

Similar results are obtained with

$$\hat{\boldsymbol{u}}'_{-1} = \mathrm{e}^{-i\chi_l} \hat{\boldsymbol{u}}_{-1}. \tag{3.13}$$

Consequently, under a local rotation, the components of the tangent vector become

$$\begin{aligned} V'_{+1}(\theta,\phi) &= \boldsymbol{V}_\mathrm{t}\cdot\hat{\boldsymbol{u}}^*_{+1}{}' = \boldsymbol{V}_\mathrm{t}\cdot\hat{\boldsymbol{u}}^*_{+1}\mathrm{e}^{-i\chi_l}, \\ V'_{-1}(\theta,\phi) &= \boldsymbol{V}_\mathrm{t}\cdot\hat{\boldsymbol{u}}^*_{-1}{}' = \boldsymbol{V}_\mathrm{t}\cdot\hat{\boldsymbol{u}}^*_{-1}\mathrm{e}^{i\chi_l}. \end{aligned} \tag{3.14}$$

This means that $V_{+1}(\theta,\phi)$ and $V_{-1}(\theta,\phi)$ are of spin $+1$ and spin -1, respectively. Thus, they can be expanded on spin spherical harmonics of their respective spin, and (3.9) becomes

$$\boldsymbol{V_t}(\theta,\phi) = \sum_{n=0}^{\infty}\sum_{m=-n}^{n} V_{+1,m,n}Y_{1,m,n}\hat{\boldsymbol{u}}_{+1} + V_{-1,m,n}Y_{-1,m,n}\hat{\boldsymbol{u}}_{-1}. \tag{3.15}$$

As for the radial component of $\boldsymbol{V}$, it is unchanged under local rotation. Thus, the radial component of a vector field is decomposed with spin $s=0$ and can be expressed as

$$\boldsymbol{V}_r = V_r\hat{\boldsymbol{r}} = \sum_{n=0}^{\infty}\sum_{m=-n}^{n} V_{0,m,n}Y_{m,n}\hat{\boldsymbol{r}}. \tag{3.16}$$

Nevertheless, in this PhD thesis, the radial component is not often considered, as the entire field can be characterized from the tangent components, according to the unicity theorem [5].

Remarkably, the unit vectors of (3.10) show a strong resemblance with the definition of left and right polarisations of a field, meaning that in the far-field zone, a spin expansion on $s=\pm1$ unit vectors is only about expanding the field on the right-hand and left-hand circular components.

Spin signals also present a global rotation property, or rotation over the sphere, which induces a particular phase shift.

3.2.6 Global rotation of a spin function over the sphere

Let us consider a rotation over the sphere, parameterized by the Euler angles, $\epsilon = (\phi_\epsilon,\theta_\epsilon,\chi_\epsilon)$. The positions before and after the rotation are defined, according to the operator κ defined in (2.6), either by their spherical coordinates (θ_0,ϕ_0) and (θ_1,ϕ_1) or by their unit vectors $\hat{\boldsymbol{r}}_0$ and $\hat{\boldsymbol{r}}_1$, respectively.

The rotation $\mathcal{R}_{s\epsilon}$ of the spin function $u_s \in L^2(\mathcal{S}^2)$ over the sphere is defined as

$$(\mathcal{R}_{s\epsilon}u_s)(\hat{\boldsymbol{r}}_1) = e^{-is\chi_g}u_s(\mathbf{R}_\epsilon^{-1}\hat{\boldsymbol{r}}_0), \tag{3.17}$$

with $\mathbf{R}_\epsilon$ the 3D rotation matrix. Furthermore, $\chi_g \in [0,2\pi]$ is defined as the third Euler angle of the rotation $\mathbf{R}_{\epsilon'} = \mathbf{R}_\epsilon^{-1}\mathbf{R}_{(\theta,\phi,0)}$ i.e. $\epsilon' = (.,.,\chi_g)$.

The exponential factor appearing in (3.17) is required to ensure that the rotation of a spin s function results in a function with the same spin order. The magnitude of a spin function is rotated in the usual manner (i.e. through a coordinate rotation), however the additional phase factor means that the real and imaginary components of the signal are not rotated solely by a coordinate rotation. For analysing scalar signals for which $s=0$, (3.17) reduces to the typical rotation operator defined solely through a rotation of the coordinate system. For the case $s=\pm1$, the occurrence of this phase shift is demonstrated in Appendix A.

This document may not be reproduced, modified, adapted, published, translated in any way, in whole or in part, nor disclosed to a third party without the prior written consent of ENAC. © 2023, ENAC

3.2.7 Conclusion

Firstly this section has presented the notion of spin function, characterized by their local rotation properties. Secondly, spin spherical harmonics have been introduced in order to analyse spin functions over the sphere. Next, the spin spherical harmonic transform of a spin function has been derived. Then the expression of tangent vectors over the sphere has been given in terms of signals of spin ± 1. Finally, the specificity of the global rotation of a spin function over the sphere has been reported. The next section will detail the spin spherical harmonic computation over the sphere.

3.3 Sampling for spin spherical harmonic transform

3.3.1 Introduction

To perform numerical spin spherical transform, a sampling of the problem has to be done. According to the sampling theory established by Shannon in [97], the entire information content of a band-limited signal can be captured by a finite number of samples. This means that there must exist a grid over the sphere that is suitable to expand band-limited spin functions in terms of spin spherical harmonics. This Section is based on the work of J. McEwen and Y. Wiaux [21] and introduces their sampling theorem, along with their algorithm for fast spin transform..

Firstly, Section 3.3.2 presents the sampling theorem, Section 3.3.3 presents the fast algorithm and Section 3.3.4 presents its performances.

3.3.2 Sampling theorem

A band-limited signal has the property to be fully recoverable from its samples, and to be expandable on a finite number of harmonics N_{AUT}, as defined in 2.3.5 for the case of antenna radiation, at the condition that the sampling rate respects the Nyquist-Shannon condition. A common issue in sphere sampling is to find a judicious θ-ϕ grid that minimizes the number of samples L. Indeed this configuration inevitably induces oversampling on the poles of the sphere. As it is shown in Figure 3.2, sampling points are more concentrated around the poles. The objective is to define a sampling grid as sparse as possible, without losing information of the data defined on the sphere.

Many sampling grids exist to describe band-limited signals on the sphere. In particular, the Gauss-Legendre quadrature may be used to construct exact spherical harmonic transforms, that requires $L_{\mathrm{GL}} \sim 2N_{\mathrm{AUT}}^2$ sampling points [21]. The canonical equiangular in θ and ϕ sampling theorem on the sphere of Discroll & Healy [98] is also commonly used, which requires roughly $L_{\mathrm{DH}} \sim 4N_{\mathrm{AUT}}^2$ samples on the sphere.

In this thesis, the McEwen and Wiaux [21] sampling theorem is used which uses a number of samples of $2N_{\mathrm{AUT}}^2$. The proposed sampling, equiangular in θ and ϕ, is given by

$$\begin{aligned} \theta_{p_\theta}^{N_{\mathrm{AUT}}} &= \frac{\pi(2p_\theta + 1)}{2N_{\mathrm{AUT}} - 1}, && \text{for } p_\theta \in \{0, 1, ..., N_{\mathrm{AUT}} - 1\}, \\ \phi_{p_\phi}^{N_{\mathrm{AUT}}} &= \frac{2\pi p_\phi}{2N_{\mathrm{AUT}} - 1}, && \text{for } p_\phi \in \{0, 1, ..., 2N_{\mathrm{AUT}} - 2\}, \end{aligned} \tag{3.18}$$

where N_{AUT} is the maximal spherical harmonic order, *i.e.*, the band-limit of the signal.

This grid is represented and compared with the Driscoll & Healy and Gauss-Legendre grids in Figure 3.2. Notice that the Driscoll and Healy sampling theorem requires approximately twice as many samples on the sphere. The McEwen & Wiaux algorithm requires less samples than the Gauss-Legendre sampling: $L_{\mathrm{GL}} - L_{\mathrm{MW}} = 3(N_{\mathrm{AUT}} - 1)$, which for small band-limit can be significant. Finally, this is the only grid from which a sampling theorem has been derived for spin signals. Every spin spherical harmonic transform performed in this thesis is based on this sampling, represented in Figure 3.2c.

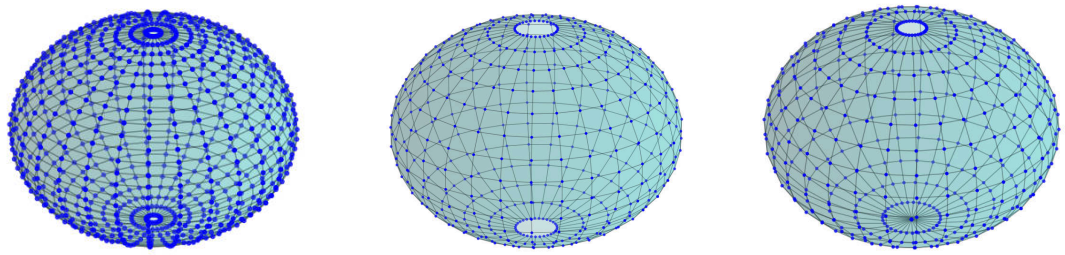

(a) Driscoll & Healy grid (b) Gauss-Legendre grid (c) McEwen & Wiaux grid

Figure 3.2: Sampling schemes for the exact representation of a band-limited signal for $N_{\mathrm{AUT}} = 16$.

Note that N_{AUT}, the band-limit of a given antenna under test is defined by Hansen in (2.30). However, the objective of the PhD thesis is to correct defaults in the measurement signal that can radiates higher harmonics than the antenna itself. Indeed, spurious scatterings often yield fast variations in the measured signal. Thus, to be able to detect those fast variations, computing more harmonics than the one theoretically radiated by the AUT is of interest. Consequently an oversampling of the sphere has to be done. In this case, the McEwen & Wiaux sampling step will be defined by the truncation level $N \in \mathbb{N}$ with $N \geq N_{\mathrm{AUT}}$.

3.3.3 Fast Spin Spherical Harmonics Transform

This section provides the key elements of the fast spherical harmonic transform algorithm developed by McEwen & Wiaux in [99] and [21]. They allow to perform exact spherical harmonic transforms based on fast Fourier transforms. The objective is to compute the spin spherical harmonic coefficients u_{smn} from the spin signal u_s, as defined in Section 3.2.2.

3.3.3.1 Formulation with Wigner functions

The Wigner functions $D^n_{m,m'}(\alpha, \beta, \gamma)$ for $n \in \mathbb{N}$ and $m, m' \in \mathbb{Z}^2$ form an orthogonal basis for $\mathrm{L}^2(\mathrm{SO}(3))$ the space of square integrable functions on the rotation group. These functions can be parameterized by the Euler angles (α, β, γ), see Section 2.2.3. Spin spherical harmonics correspond to particular values of the Wigner functions [100]. Indeed, we have

$$Y_{s,m,n} = (-1)^s \sqrt{\frac{2n+1}{4\pi}} D^{n*}_{m,-s}(\phi, \theta, 0). \tag{3.19}$$

This document may not be reproduced, modified, adapted, published, translated in any way, in whole or in part, nor disclosed to a third party without the prior written consent of ENAC. © 2023, ENAC

Besides, the Wigner functions can be written as

$$D^n_{m,m'}(\alpha,\beta,\gamma) = \mathrm{e}^{-im\alpha} d^n_{m,m'}(\beta) \mathrm{e}^{-in\gamma}, \tag{3.20}$$

where the d-functions $d^n_{m,m'}$ are defined by

$$d^n_{m,m'}(\beta) = \sqrt{\frac{(n+m')!(n-m')!}{(n+m)!(n-m)!}} \left(\sin\frac{\beta}{2}\right)^{m'-m} \times \left(\cos\frac{\beta}{2}\right)^{m'+m} P^{(m'-m,m'+m)}_{n-m'}(\cos\beta), \tag{3.21}$$

where $P^{(a,b)}_n(.)$ are the Jacobi polynomials. These functions can also be defined by

$$d^n_{m,m'}(\beta) = i^{m-m'} \sum_{p=-n}^{n} \Delta^n_{pm} \Delta^n_{pm'} \mathrm{e}^{ip\beta}, \tag{3.22}$$

where $\Delta^n_{m'm} \equiv d^n_{m'm}(\frac{\pi}{2})$. The exponential factors in (3.20) and (3.22) allow one to make use of Fourier series to express the spin signal u_s defined in Section 3.2.2.

3.3.3.2 Forward and Inverse Fourier transform protocol

For a band-limited signal, inserting (3.20) and (3.22) in (3.7), the spin spherical transform can be written as

$$C^s_{m,n} = (-1)^s i^{m+s} \sqrt{\frac{2n+1}{4\pi}} \sum_{p=-(N-1)}^{N-1} \Delta^n_{pm} \Delta^n_{p,-s} G_{smp}, \tag{3.23}$$

where

$$G_{smp} = \int_0^{\pi} \sin\theta G_{sm}(\theta) \mathrm{e}^{-ip\theta} d\theta \tag{3.24}$$

and

$$G_{sm}(\theta) = \int_0^{2\pi} u_s(\theta,\phi) \mathrm{e}^{-im\phi} d\phi. \tag{3.25}$$

This formulation shows similarities with Fourier series, thus FFT could be used to compute the forward spherical harmonic transforms rapidly, after the sampling of the sphere. However, this type of transform is only defined for periodic functions. Consequently, a periodic extension in θ has to be done, by extending (3.24) to 2π in θ [21]. The sphere becomes a torus, as shown in Figure 3.3. This extension has to ensure the symmetry of the representation in the new domain. Thus the extension of G_{sm} is defined as

$$\tilde{G}_{sm}(\theta) = \begin{cases} G_{sm}(\theta), & \text{for } \theta \in [0,\pi] \\ (-1)^{m+s} G_{sm}(2\pi-\theta), & \text{for } \theta \in [\pi,2\pi]. \end{cases} \tag{3.26}$$

Then spin spherical harmonic coefficients u_{smn} are computed from (3.23).

Finally, to perform the inverse transform and obtain $u_s(\theta,\phi)$, similar steps are followed, in reverse, as detailed in [21]. The additional samples computed for the extension in the θ domain (π, 2π) are discarded.

(a) $f_s \in \mathrm{L}^2(\mathrm{S}^2, \mathrm{d}\Omega(w))$ (b) $\tilde{f}_s \in \mathrm{L}^2(\mathrm{S}^2, \mathrm{d}^2\boldsymbol{x})$

Figure 3.3: Representation of the periodic extension of earth topography on the sphere from [99], from the sphere to the torus

Note that the choice of N as a power of 2 optimises the computation of the fast Fourier transform.

3.3.4 Performances of the fast algorithm

This section discusses the advantageous performances of the McEwen & Wiaux algorithm. The objective is to show the advantage of this algorithm, compared with the Driscoll & Healy algorithm and the Gauss-Legendre algorithm. Firstly the complexity of the algorithm will be discussed in subsection 3.3.4.1. Afterwards, its numerical accuracy and computation time will be analysed in subsection 3.3.4.2.

3.3.4.1 Complexity of the algorithm

The forward algorithm consists in two FFTs to compute (3.25) and (3.24), with computational complexity $O(N^2 \log_2 N)$ and a sum for (3.23) that is $O(N^3)$ [21]. Consequently, the overall complexity is $O(N^3)$, same for the inverse transform.

It is possible to reduce the cost of the computation by precomputing and storing the values of the Wigner functions. This precomputation requires $O(N^3)$ storage, this is what is done in the Driscoll and Healy algorithm. However, for high band-limit signals, the storage is very demanding, for example for $N = 4069$, the required storage would be of 77 GB. Consequently, McEwen & Wiaux have proposed not to perform precomputation and to prefer recursion to compute the Wigner d-functions, using the method of Risbo [101].

3.3.4.2 Numerical accuracy and computation time

The following experiment has been proposed in [21] and tested within the framework of this thesis. In this paragraph and in the following sections and chapters of this thesis, experiments are performed on a 1.9 GHz Intel CPU computer, with 8 cores and 16 GB or RAM. A band-limited test signal defined by uniformly random spherical harmonic coefficients is generated on the sphere, by the use of an inverse transform. Then a forward transform is performed, with the SSHT library [102], to compute back harmonic coefficients.

- Numerical accuracy is measured by the maximum absolute error between the ini-

This document may not be reproduced, modified, adapted, published, translated in any way, in whole or in part, nor disclosed to a third party without the prior written consent of ENAC. © 2023, ENAC

tial spherical harmonic coefficients u^o_{smn} and the recomputed values u^r_{smn}, i.e., $e_r = \max_{m,n} |u^r_{smn} - u^o_{smn}|$, as shown in Figure 3.4a.

- Computation time corresponds to the time taken by the algorithm to perform the inverse and forward transforms, as shown in Figure 3.4b.

The results of the tests on numerical accuracy and computation time are shown in Figure 3.4, with respect to the band-limit N. The performances are compared with the following algorithms: the Driscoll & Healy algorithm and the Gauss-Legendre algorithm.

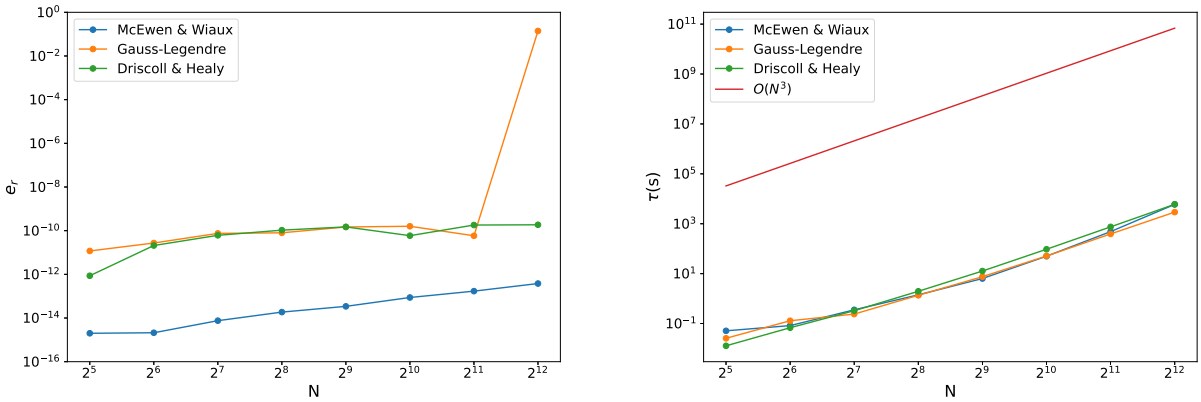

(a) Numerical accuracy

(b) Computation time

Figure 3.4: Performances of the sampling theorems.

For each algorithm, the accuracy is very high, and goes approximately to the machine precision, even if the error increases with the band-limit. The Gauss-Legendre algorithm goes unstable between $N = 1024$ and $N = 2048$, while the McEwen & Wiaux algorithm and the Driscoll & Healy algorithms do not suffer such a limitation. The McEwen & Wiaux algorithm is slightly more accurate [101].

3.3.5 Conclusion

This section has introduced the sampling theorem developed by McEwen & Wiaux, on which is based the fast spin spherical harmonic transform algorithm presented afterward. Finally the performance of this method have been discussed. This algorithm has presented great advantages in terms of calculation time, precision and stability, and is thus of high interest regarding the analysis of spherical antenna measurements.

3.4 Relation between Hansen and spin spherical harmonics

3.4.1 Introduction

This thesis introduces two approaches for formulating spherical harmonics, each with its own set of advantages and limitations. The Hansen approach represents the commonly

employed method in antenna radiation pattern analysis, accounting for wave propagation effects. The specificity of the spin is its capacity to expand data into various forms (scalar, vector, tensor), its stability under global and local rotations, and its suitability for high bandwidth applications. Additionally, the spin harmonics have been developed along with efficient and stable algorithms. However, the spin harmonics does not inherently capture wave propagation characteristics. Consequently, it is of interest to establish a relationship between these harmonics.

Hansen spherical harmonics and spin spherical harmonics are very close. The objective of this section is to show and formulate this correspondence. To begin with, the quantities and expansions considered are reminded in Section 3.4.2 and the relations between the coefficients are given in Section 3.4.3.

3.4.2 Field components expanded in spherical harmonics

In this section, we will work on the spherical harmonic transform of the following tangent vectors

$$\frac{r}{\sqrt{\zeta}}\boldsymbol{E}_{\mathrm{t}}(r,\theta,\phi), \qquad \text{and} \qquad -ir\sqrt{\zeta}\boldsymbol{H}_{\mathrm{t}}(r,\theta,\phi). \tag{3.27}$$

The constants are chosen so that the precision of the transform is not dependent on r and so that $\boldsymbol{E}_{\mathrm{t}}$ and $\boldsymbol{H}_{\mathrm{t}}$ are of the same order of magnitude. The expansion can be written as

$$\begin{aligned}
\boldsymbol{E}_{\mathrm{t}}(r,\theta,\phi) &= \frac{\sqrt{\zeta}}{r}\sum_{s,m,n} C_{m,n}^{(\mathrm{E}),s}(r)\; Y_{s,m,n}(\theta,\phi)\; \hat{\boldsymbol{u}}_s(\theta,\phi),\\
\boldsymbol{H}_{\mathrm{t}}(r,\theta,\phi) &= \frac{i}{r\sqrt{\zeta}}\sum_{s,m,n} C_{m,n}^{(\mathrm{H}),s}(r)\; Y_{s,m,n}(\theta,\phi)\; \hat{\boldsymbol{u}}_s(\theta,\phi),
\end{aligned} \tag{3.28}$$

with $C_{m,n}^{(\mathrm{E}),s}$ and $C_{m,n}^{(\mathrm{H}),s}$, the spin coefficients associated with the transverse fields $\boldsymbol{E}_{\mathrm{t}}$ and $\boldsymbol{H}_{\mathrm{t}}$. They are given by

$$\begin{aligned}
C_{m,n}^{(\mathrm{E}),s}(r) &= \frac{r}{\sqrt{\zeta}}\iint_{\mathcal{S}^2}\boldsymbol{E}_{\mathrm{t}}(r,\theta,\phi)Y_{s,m,n}^{*}(\theta,\phi)\hat{\boldsymbol{u}}_s^{*}(\theta,\phi)dS,\\
C_{m,n}^{(\mathrm{H}),s}(r) &= -ir\sqrt{\zeta}\iint_{\mathcal{S}^2}\boldsymbol{H}_{\mathrm{t}}(r,\theta,\phi)Y_{s,m,n}^{*}(\theta,\phi)\hat{\boldsymbol{u}}_s^{*}(\theta,\phi)dS.
\end{aligned} \tag{3.29}$$

3.4.3 Relation between harmonic coefficients

The relations between the spin and the Hansen spherical harmonics coefficients are derived here. The objective of this section is to express the spin coefficients $C_{m,n}^{(\mathrm{E}),s}$ and $C_{m,n}^{(\mathrm{H}),s}$ in function of the Hansen coefficients $Q_{m,n}^{p,(c)}$. From (3.28) and (2.25) the transverse electric field can be written as

$$\boldsymbol{E}_{\mathrm{t}} = \frac{\sqrt{\zeta}}{r}\sum_{s,m,n} C_{m,n}^{(\mathrm{E}),s}(r)\; Y_{s,m,n}\;\hat{\boldsymbol{u}}_s = \sum_{p,c,m,n} Q_{m,n}^{p,(c)}\boldsymbol{e}_{\mathrm{t}\;m,n}^{\;p,(c)}. \tag{3.30}$$

The computation of the transform, according to (3.7), gives for any values of s', m', n'

This document may not be reproduced, modified, adapted, published, translated in any way, in whole or in part, nor disclosed to a third party without the prior written consent of ENAC. © 2023, ENAC

$$\begin{aligned}\langle \boldsymbol{E}_{\mathrm{t}}, Y_{s',m',n'}\hat{\boldsymbol{u}}_{s'}\rangle &= \frac{\sqrt{\zeta}}{r}C^{(\mathrm{E}),s'}_{m',n'}(r)\\ &= \sum_{p,c,m,n} Q^{p,(c)}_{m,n}\left\langle \boldsymbol{e}^{\,p,(c)}_{\mathrm{t}\,m,n}, Y_{s',m',n'}\,\hat{\boldsymbol{u}}_{s'}\right\rangle\\ &= \sum_{c,m,n} Q^{(\mathrm{TE}),(c)}_{m,n}\left\langle \boldsymbol{e}^{\,(\mathrm{TE}),(c)}_{\mathrm{t}\,m,n}, Y_{s',m',n'}\,\hat{\boldsymbol{u}}_{s'}\right\rangle\\ &\qquad + Q^{(\mathrm{TM}),(c)}_{m,n}\left\langle \boldsymbol{e}^{\,(\mathrm{TM}),(c)}_{\mathrm{t}\,m,n}, Y_{s',m',n'}\,\hat{\boldsymbol{u}}_{s'}\right\rangle.\end{aligned} \tag{3.31}$$

For the sake of conciseness, we introduce the notation

$$\frac{1}{kr}\frac{\mathrm{d}}{\mathrm{d}kr}\left(krz^{(c)}_n(kr)\right) = \mathrm{d}z^{(c)}_n(kr). \tag{3.32}$$

We are going to develop here each term of the sum, for $p = \{\mathrm{TE}, \mathrm{TM}\}$ and $c = \pm$.

For $s' = +1$, the TE term of the sum becomes

$$\begin{aligned}\left\langle \boldsymbol{e}^{\,\mathrm{TE},(c)}_{\mathrm{t}\,m,n}, Y_{1,m',n'}\,\hat{\boldsymbol{u}}_1\right\rangle = \iint_{\mathcal{S}^2} k\sqrt{\zeta}A_{mn}z^{(c)}_n(kr)e^{im\phi}\\ \left[\frac{im\bar{P}^{|m|}_n(\cos\theta)}{\sin\theta}\hat{\boldsymbol{\theta}} - \frac{\mathrm{d}\bar{P}^{|m|}_n(\cos\theta)}{\mathrm{d}\theta}\hat{\boldsymbol{\phi}}\right]\cdot Y^*_{1,m',n'}\,\hat{\boldsymbol{u}}^*_1 dS.\end{aligned} \tag{3.33}$$

By computing the inner product between the unit vectors, we end up with

$$\begin{aligned}\left[\frac{im\bar{P}^{|m|}_n(\cos\theta)}{\sin\theta}\hat{\boldsymbol{\theta}} - \frac{\mathrm{d}\bar{P}^{|m|}_n(\cos\theta)}{\mathrm{d}\theta}\hat{\boldsymbol{\phi}}\right]\cdot\hat{\boldsymbol{u}}^*_1 &= \left[\frac{im\bar{P}^{|m|}_n(\cos\theta)}{\sin\theta}\hat{\boldsymbol{\theta}} - \frac{\mathrm{d}\bar{P}^{|m|}_n(\cos\theta)}{\mathrm{d}\theta}\hat{\boldsymbol{\phi}}\right]\cdot\left(\frac{\hat{\boldsymbol{\theta}}+i\hat{\boldsymbol{\phi}}}{\sqrt{2}}\right)\\ &= \frac{i}{\sqrt{2}}\left(\frac{m\bar{P}^{|m|}_n(\cos\theta)}{\sin\theta} - \frac{\mathrm{d}\bar{P}^{|m|}_n(\cos\theta)}{\mathrm{d}\theta}\right),\end{aligned} \tag{3.34}$$

which corresponds to $Y_{1,m,n}$, the spin harmonic of (3.4), up to a multiplicative constant. We finally have

$$\left[\frac{im\bar{P}^{|m|}_n(\cos\theta)}{\sin\theta}\hat{\boldsymbol{\theta}} - \frac{\mathrm{d}\bar{P}^{|m|}_n(\cos\theta)}{\mathrm{d}\theta}\hat{\boldsymbol{\phi}}\right]\cdot\hat{\boldsymbol{u}}^*_1 = \frac{i}{\sqrt{2}s_mA_{mn}e^{im\phi}}Y_{1,m,n}, \tag{3.35}$$

from (2.15), (2.16) and (3.4).

Thus, due to the orthogonality of the spin spherical harmonics [95], (3.33) becomes

$$\begin{aligned}\left\langle \boldsymbol{e}^{\,\mathrm{TE},(c)}_{\mathrm{t}\,m,n}, Y_{1,m',n'}\,\hat{\boldsymbol{u}}_1\right\rangle &= \frac{is_m}{\sqrt{2}}k\sqrt{\zeta}z^{(c)}_n(kr)\iint_{\mathcal{S}^2} Y^*_{1,m',n'}Y_{1,m,n}dS\\ &= \frac{is_m}{\sqrt{2}}k\sqrt{\zeta}z^{(c)}_n(kr)\delta_{m,m'}\delta_{n,n'},\end{aligned} \tag{3.36}$$

with δ the Kronecker symbol.

The calculation is similar for $p = \mathrm{TM}$ and $s' = +1$ and is developed in Annex C. This yields

$$\left\langle \boldsymbol{e}_{\mathrm{t}\,m,n}^{\mathrm{TM},(c)}, Y_{1,m',n'}\ \hat{\boldsymbol{u}}_1 \right\rangle = -\frac{s_m}{\sqrt{2}} k\sqrt{\zeta} \mathrm{d}z_n^{(c)}(kr)\delta_{m,m'}\delta_{n,n'}. \tag{3.37}$$

Finally, the electric field spin +1 coefficients are related to the Hansen coefficients by

$$C_{m',n'}^{(\mathrm{E}),+1}(r) = \frac{s_m}{\sqrt{2}} kr \sum_c \left[iQ_{m',n'}^{\mathrm{TE},(c)} z_{n'}^{(c)}(kr) - Q_{m',n'}^{\mathrm{TM},(c)} \mathrm{d}z_{n'}^{(c)}(kr) \right]. \tag{3.38}$$

Now, for $s' = -1$, the inner products of (3.31) become

$$\begin{aligned} \left\langle \boldsymbol{e}_{\mathrm{t}\,m,n}^{\mathrm{TE},(c)}, Y_{-1,m',n'}\ \hat{\boldsymbol{u}}_{-1} \right\rangle &= \frac{is_m}{\sqrt{2}} k\sqrt{\zeta} z_n^{(c)}(kr)\delta_{m,m'}\delta_{n,n'}, \\ \left\langle \boldsymbol{e}_{\mathrm{t}\,m,n}^{\mathrm{TM},(c)}, Y_{-1,m',n'}\ \hat{\boldsymbol{u}}_{-1} \right\rangle &= \frac{s_m}{\sqrt{2}} k\sqrt{\zeta} \mathrm{d}z_n^{(c)}(kr)\delta_{m,m'}\delta_{n,n'}. \end{aligned} \tag{3.39}$$

The computation are detailed in Annex C. Finally, for $s' = -1$, the relation between the spin and the Hansen spherical harmonic coefficients is

$$C_{m',n'}^{(\mathrm{E}),-1}(r) = \frac{s_m}{\sqrt{2}} kr \sum_c \left[iQ_{m',n'}^{\mathrm{TE},(c)} z_{n'}^{(c)}(kr) + Q_{m',n'}^{\mathrm{TM},(c)} \mathrm{d}z_{n'}^{(c)}(kr) \right]. \tag{3.40}$$

Similar computations are derived to obtain $C_{m,n}^{(\mathrm{H}),s}(r)$. The final relations can be gathered in a matrix form given by

$$\begin{bmatrix} C_{m,n}^{(\mathrm{E}),+1}(r) \\ C_{m,n}^{(\mathrm{E}),-1}(r) \\ C_{m,n}^{(\mathrm{H}),+1}(r) \\ C_{m,n}^{(\mathrm{H}),-1}(r) \end{bmatrix} = kr\frac{s_m}{\sqrt{2}} \begin{bmatrix} iz_n^{(+)}(kr) & iz_n^{(-)}(kr) & -dz_n^{(+)}(kr) & -dz_n^{(-)}(kr) \\ iz_n^{(+)}(kr) & iz_n^{(-)}(kr) & dz_n^{(+)}(kr) & dz_n^{(-)}(kr) \\ -dz_n^{(+)}(kr) & -dz_n^{(-)}(kr) & iz_n^{(+)}(kr) & iz_n^{(-)}(kr) \\ dz_n^{(+)}(kr) & dz_n^{(-)}(kr) & iz_n^{(+)}(kr) & iz_n^{(-)}(kr) \end{bmatrix} \begin{bmatrix} Q_{m,n}^{\mathrm{TE},(+)} \\ Q_{m,n}^{\mathrm{TE},(-)} \\ Q_{m,n}^{\mathrm{TM},(+)} \\ Q_{m,n}^{\mathrm{TM},(-)} \end{bmatrix}. \tag{3.41}$$

The inverse matrix is calculated by means of a Gaussian elimination and the properties of the Wronksian associated with spherical Hankel functions

$$dz_n^{(+)}(kr)z_n^{(-)}(kr) - dz_n^{(-)}(kr)z_n^{(+)}(kr) = \frac{-2i}{(kr)^2}. \tag{3.42}$$

These operations are detailed in the section B.2 of Annex C. The matrix obtained is

$$\begin{bmatrix} Q_{m,n}^{\mathrm{TE},(+)} \\ Q_{m,n}^{\mathrm{TE},(-)} \\ Q_{m,n}^{\mathrm{TM},(+)} \\ Q_{m,n}^{\mathrm{TM},(-)} \end{bmatrix} = \frac{s_m kr}{2\sqrt{2}} \begin{bmatrix} -dz_n^{(-)}(kr) & -dz_n^{(-)}(kr) & -iz_n^{(-)}(kr) & iz_n^{(-)}(kr) \\ dz_n^{(+)}(kr) & dz_n^{(+)}(kr) & iz_n^{(+)}(kr) & -iz_n^{(+)}(kr) \\ -iz_n^{(-)}(kr) & iz_n^{(-)}(kr) & -dz_n^{(-)}(kr) & -dz_n^{(-)}(kr) \\ iz_n^{(+)}(kr) & -iz_n^{(+)}(kr) & dz_n^{(+)}(kr) & dz_n^{(+)}(kr) \end{bmatrix} \begin{bmatrix} C_{m,n}^{(\mathrm{E}),+1}(r) \\ C_{m,n}^{(\mathrm{E}),-1}(r) \\ C_{m,n}^{(\mathrm{H}),+1}(r) \\ C_{m,n}^{(\mathrm{H}),-1}(r) \end{bmatrix}. \tag{3.43}$$

Finally, we have obtained a rigorous formulation, under the form of an invertible matrix, to pass from a convention to another.

This document may not be reproduced, modified, adapted, published, translated in any way, in whole or in part, nor disclosed to a third party without the prior written consent of ENAC. © 2023, ENAC

3.4.4 Conclusion

The connection between the Hansen and the spin spherical harmonics has been established. This connection finds its primary utility in transforming a given field using the spin spherical transform and subsequently converting it into Hansen coefficients. The primary benefit lies in the efficiency of the McEwen & Wiaux algorithm, along with the added convenience of the spin convention when exploring the polarisation characteristics of the field.

3.5 Analyses of antenna radiation patterns by means of spin spherical harmonics

3.5.1 Introduction

This section presents spherical harmonics analyses for different types of antennas for which radiated fields come from theory, simulations or measurements. The main objectives are to illustrate the theoretical formulations provided in this chapter and to test the performance of the SSHT algorithm. We want to evaluate the benefit of the spin for antenna radiation analysis. The simulations are all performed with a total radiated power of 1 W.

Firstly, in Section 3.5.2 the study of the spherical harmonic transform of elementary dipoles illustrates the specificities of the spin harmonics and the relation with the Hansen harmonics.

Secondly, in Section 3.5.3, the spin spherical harmonic transform of a simulated horn antenna radiation illustrates the performances of the spin transform.

Next, spin spherical harmonic transforms are applied on measurements performed in the ENAC anechoic chamber 3.5.4.

Then, in Section 3.5.5 this transform is applied to the radiation pattern of an antenna mounted on an aircraft, to observe the ability of the spin expansion to analyse such radiating large object.

Finally the bistatic RCS of an aircraft is simulated in Section 3.5.6 and analysed up to a very high band-limit, highlighting the accuracy and performance of the algorithms used in this thesis for very large systems.

3.5.2 Elementary dipoles

In this section, we focus on the case of the elementary dipole, as described in Chapter 1. Here, the objective is to formulate and illustrate its transform in terms of spin spherical harmonics. Note that in this section and the following, the amplitude of the coefficients should not depend on r since the computation is performed in the far-field zone of the antenna. Indeed, in the far-field zone the functions $z_n^{(+)}$ and $\frac{d}{dkr}\left(krz_n^{(+)}(kr)\right)$ in the matrix (3.41) behaves in amplitude in $\frac{1}{kr}$. The far-field radiation of the z-oriented elementary dipole in terms of spherical harmonics is given by (2.34) and (2.35). The only non-zero coefficient is $Q_{0,1}^{\mathrm{TM},(+)}$, so according to (3.41), the only non-zero coefficients of the spin spherical harmonic transform are such that $n = 1$, $m = 0$. In terms of spin spherical harmonics, (2.34) can be written as

$$\begin{aligned}\boldsymbol{E}_e^z(r,\theta,\phi) &= \frac{\sqrt{\zeta}}{r}\Big(C_{0,1}^{(\mathrm{E}),+1}(r)\; Y_{+1,0,1}\; \hat{\boldsymbol{u}}_{+1} + C_{0,1}^{(\mathrm{E}),-1}(r)\; Y_{-1,0,1}\; \hat{\boldsymbol{u}}_{-1}\Big),\\ \boldsymbol{H}_e^z(r,\theta,\phi) &= \frac{i}{r\sqrt{\zeta}}\Big(C_{0,1}^{(\mathrm{H}),+1}(r)\; Y_{+1,0,1}\; \hat{\boldsymbol{u}}_{+1} + C_{0,1}^{(\mathrm{H}),-1}(r)\; Y_{-1,0,1}\; \hat{\boldsymbol{u}}_{-1}\Big),\end{aligned} \tag{3.44}$$

with

$$\begin{aligned}C_{0,1}^{(\mathrm{E}),+1}(r) &= -C_{0,1}^{(\mathrm{E}),-1}(r) = -kr\frac{s_m}{\sqrt{2}}Q_{0,1}^{\mathrm{TM},(+)}dz_n^+(kr),\\ C_{0,1}^{(\mathrm{H}),+1}(r) &= C_{0,1}^{(\mathrm{H}),-1}(r) = kr\frac{s_m}{\sqrt{2}}Q_{0,1}^{\mathrm{TM},(+)}iz_n^+(kr),\end{aligned} \tag{3.45}$$

according to (3.30) and (3.41).

To serve as an illustration, the far-field radiation of the elementary dipole has been computed from a Feko simulation and the spin spherical harmonic coefficients have been computed with SSHT. The amplitude of the spin coefficients is represented in Figure 3.5. The spin coefficients of the electric field is represented in Figure 3.5a and the ones of the H-fields in Figure 3.5b. We observe that this computation corresponds to the theoretical analysis of (3.45) as the only non-zero coefficients are the ones with $n = 1$, $m = 0$.

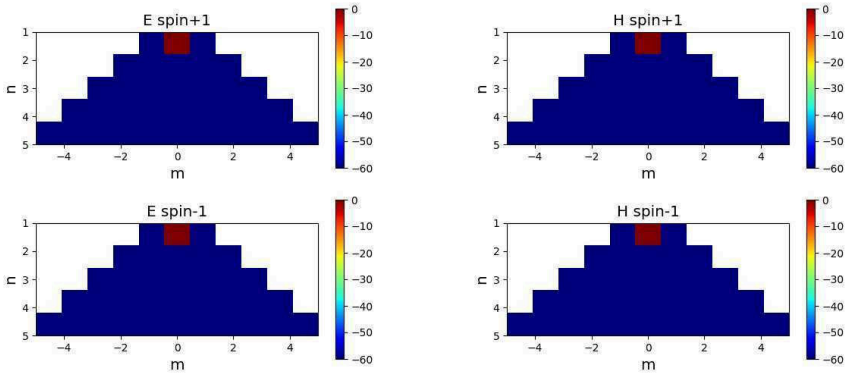

(a) Normalised amplitude of the spin spherical harmonic coefficients of the E field (dB)

(b) Normalised amplitude of the spin spherical harmonic coefficients of the H field (dB)

Figure 3.5: Spin spherical harmonic transform (dB) of the elementary dipole radiation

In order to illustrate the relation between the polarisation of the field and the sign of the spin, a simulation of a purely circularly right polarised field has been performed in Feko, for a frequency $f = 96.7$ MHz. This antenna is built from the addition of an electric elementary dipole and a magnetic elementary dipole in phase quadrature, both oriented along z. The spin spherical harmonics transform of the simulated far field is given in Figure 3.6.

This document may not be reproduced, modified, adapted, published, translated in any way, in whole or in part, nor disclosed to a third party without the prior written consent of ENAC. © 2023, ENAC

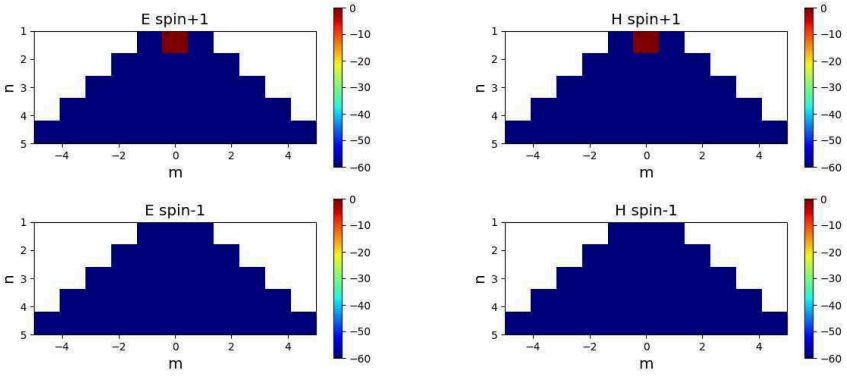

Figure 3.6: Spin spherical harmonics transform (dB) of a single polarisation elementary dipole

As expected, this transform shows that a field in right-hand circular polarisation only yields +1 spin spherical harmonics.

3.5.3 Horn antenna

The antenna considered here is the same horn antenna as in Section 2.4.4. The objective is to compare the performance of the spherical harmonic transform algorithm proposed in this thesis (spin transform with SSHT and conversion into Hansen coefficients), with the algorithm implemented in a commercial over the shell software. To do so, spherical harmonics are computed either with our Python algorithm or directly in Feko.

The horn and its radiation pattern are represented in Figure 3.7. The radiation patterns in co and cross polarisations for $\phi = 0°$ and $\phi = 90°$ are represented in Figure 3.7b. The co and cross polarisations of the field, as defined by the Ludwig-3 definition, are illustrated on the unit sphere, in Figure 3.7c and 3.7d, respectively. The spherical harmonic transform is illustrated in Figure 3.8.

The McEwen & Wiaux grid is used, with the sampling grid parameterized by $N = 256$. This means that the spherical transform of the field is computed up to $N = 256$. The sphere is oversampled because the antenna being quite small ($r_0 = 0.27$m), according to (2.30), it only radiates spherical coefficients up to $N_{\text{AUT}} = 28$. Consequently, the coefficients until $N = 256$ have not been represented in Figure 3.8.

Once computed, we can observe that the highest coefficient order is $n = 13$. Indeed if we consider that the aperture radiates, rather than the entire antenna, r_0 is reduced to 0.12 m, which makes $N_{\text{AUT}} = 13$.

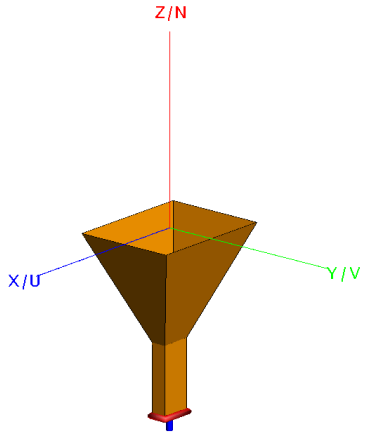

(a) Horn antenna

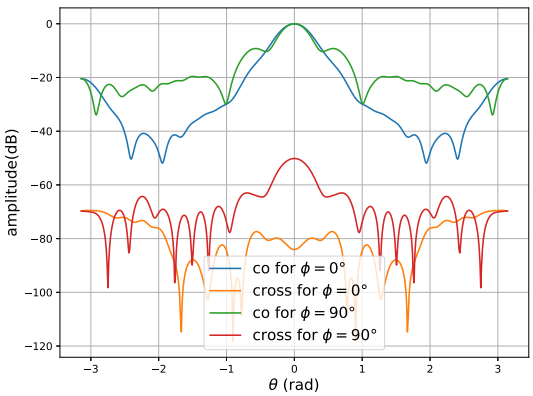

(b) Normalised co and cross-polarisation patterns, for $\phi = 0°$ and $\phi = 90°$ (dB)

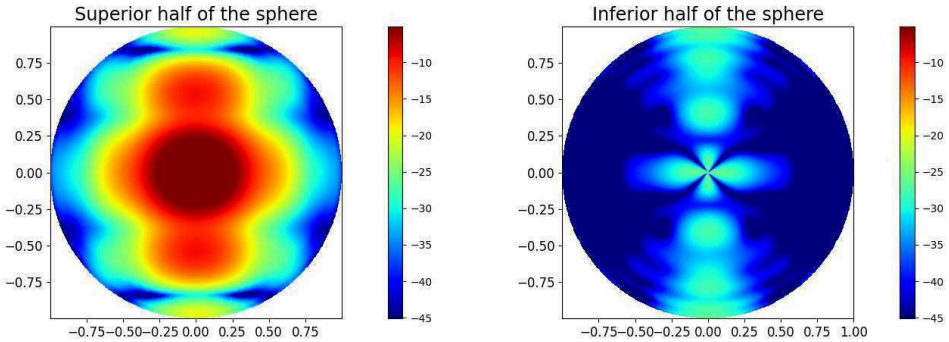

(c) Normalised co-polarisation pattern (dB)

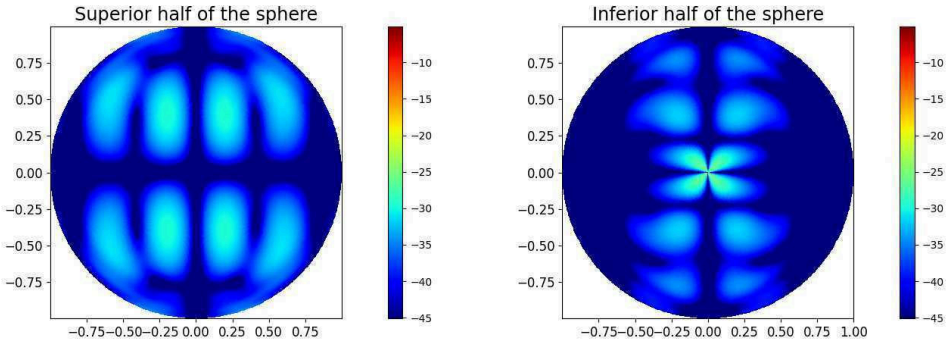

(d) Normalised cross-polarisation pattern (dB)

Figure 3.7: Horn antenna characteristics

The co-polarisation of the horn is linear. A linear polarisation can be written as the sum of a RHCP and a LHCP components. Thus, the spin spherical harmonic coefficients are of the same order between the spin +1 and spin -1. The conversion to Hansen spherical harmonics has been performed and the results for TE/TM and for ingoing and outgoing components are shown in Figure 3.9.

This document may not be reproduced, modified, adapted, published, translated in any way, in whole or in part, nor disclosed to a third party without the prior written consent of ENAC. © 2023, ENAC

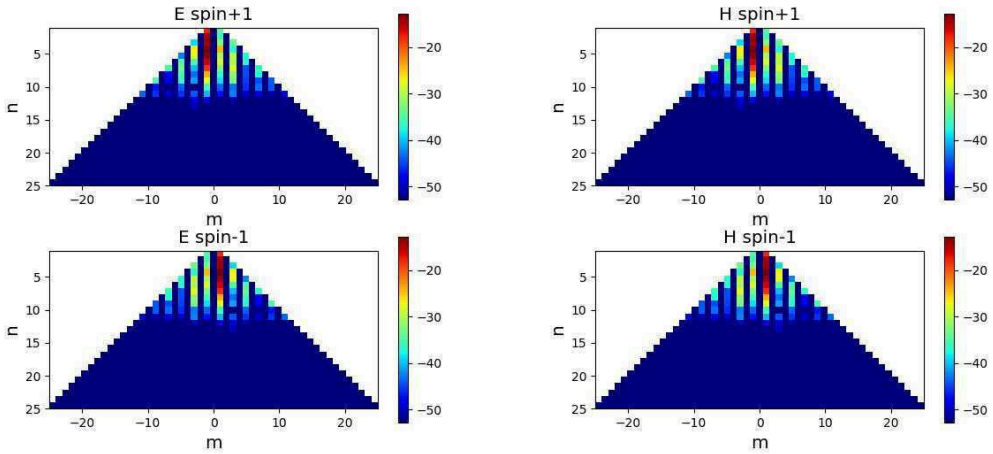

Figure 3.8: Spin +1 and -1 expansion of the simulated field of a linearly polarised horn antenna (dB)

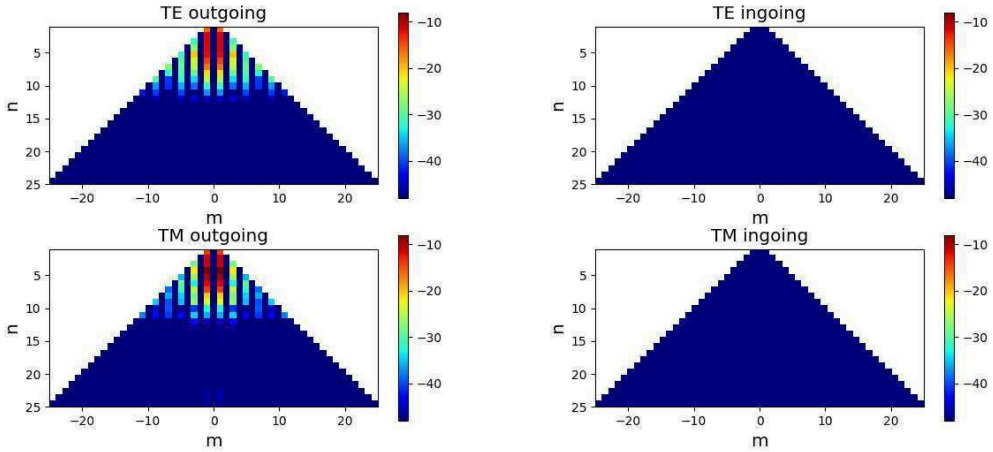

Figure 3.9: Hansen expansion of the radiated field of the horn computed from the spin expansion (dB)

As expected, the ingoing coefficients are negligible, because the entire field comes from the antenna. This is noticeable that for both types of harmonics, every even coefficient is equal to zero, due to the symmetries of the antenna.

To test the performance of the algorithms in terms of computation time, the expansion of the radiated field until $N = 256$ is performed with Altair Feko. Firstly, the McEwen & Wiaux fast transform takes 0.95 s. Then, the conversion to Hansen coefficients with algorithms developed during this thesis, that has not been optimized, takes 6.24 s, which means the entire process takes 7.2 s. Altair Feko takes 38 min 34 s, on the same computer, to obtain the same coefficients. This test is performed for different N and the computation times using SSHT and Feko are plotted in Figure 3.10. The theoretical complexity of the algorithm in $O(N^3)$, is plotted to compare the slopes of the plots.

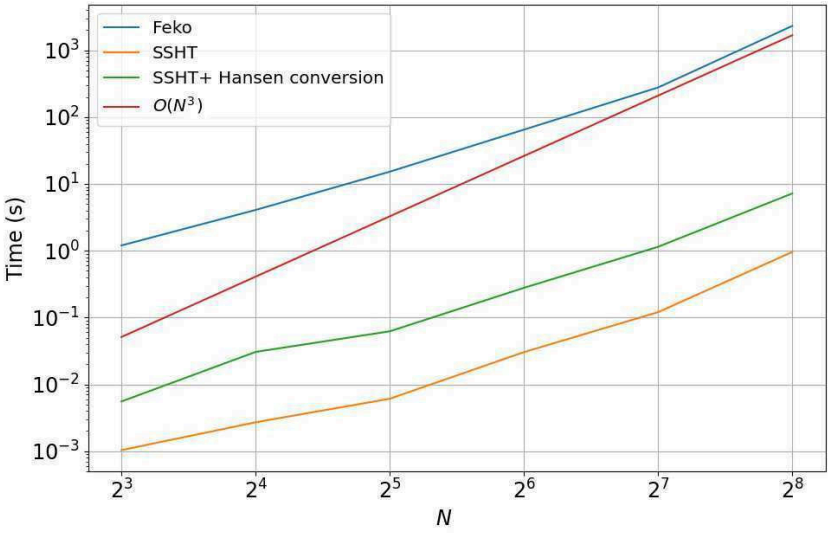

Figure 3.10: Computation time for the spherical harmonic tranform.

This is noticeable that Feko also seems to have a complexity in $O(N^3)$. However SSHT is much faster, for any N. Thus this fast algorithm seems to be efficient for computing transforms with large N such as electrically large antennas.

In terms of accuracy, Feko and SSHT show similar results. The Root Mean Square Error (RMSE) between the values of the coefficients computed with Feko and the one computed with SSHT is -98 dB.

To conclude, the main advantage of the method used in this thesis is its fast computation time for large N. In the next section, this transform is tested on antenna measurements performed in the ENAC lab.

3.5.4 Spin spherical harmonics transform on measurements

The measurement transformed into spin spherical harmonics in this section is the patch antenna named D2R2 presented in Section 2.4.5. The spin spherical harmonic transform is presented in Figure 3.11.

This document may not be reproduced, modified, adapted, published, translated in any way, in whole or in part, nor disclosed to a third party without the prior written consent of ENAC. © 2023, ENAC

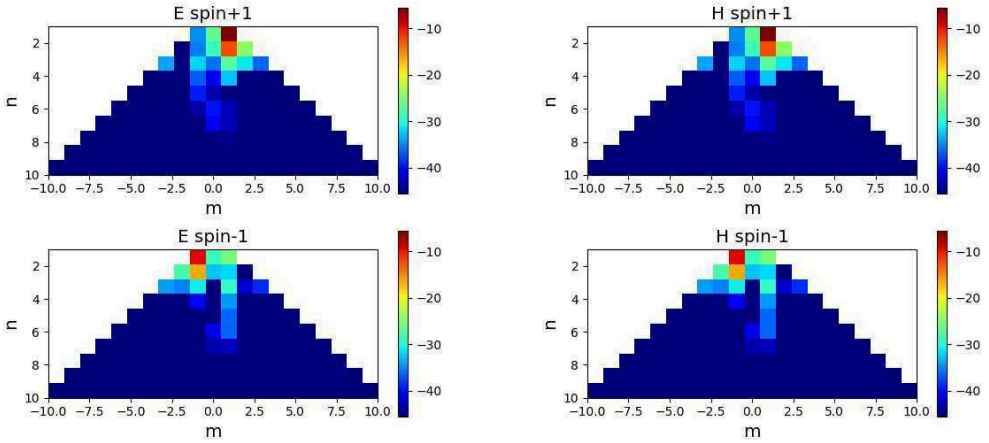

Figure 3.11: Spin spherical harmonic coefficents (dB) of the measurement of the D2R2 antenna for $f = 1.57542$ GHz

Remarkably, the +1-spin coefficients are higher, which correspond to the co-polarisation of the antenna, that is circularly right-polarised. In the next sections, we study larger simulated objects that radiate a greater number of coefficients.

3.5.5 GPS antenna on an aircraft

This section presents the simulation of a Global Positioning System (GPS) antenna mounted on top of an aircraft. The objective is to demonstrate that it is possible to analyse the radiation up to very high coefficient orders. Consequently, we choose to study a large object: a simplified model of an aircraft with a mounted antenna. We expect the creation of scattering yielding fast variations in the total radiation pattern. Note that this simulation is slightly out of the scope of the thesis, since it is not possible to measure such a big DUT in the majority of anechoic chambers but is here to assess the performance of the algorithm even on very large structures.

Firstly, the characteristics of the antenna alone are presented. Afterwards it is studied once mounted on the aircraft. The antenna studied is a GPS antenna developed at ENAC, [103]. This is a dual-band (L1-L5) stack-patch antenna, fed by 4 ports, situated between the ground plane and the cylinder, as observed in the Feko design in Figure 3.12a. The dimension of the ground plane are 0.23 m $\times$ 0.17 m, with and $\epsilon_r = 4$. This is simulated for $f = 1.57542$ GHz and its radiation pattern is shown in Figure 3.12b. The co- and cross-polarisation components of the field are also plotted, in Figures 3.12c and 3.12d.

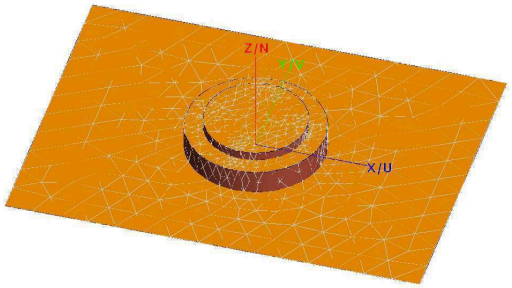

(a) Design of the GPS antenna

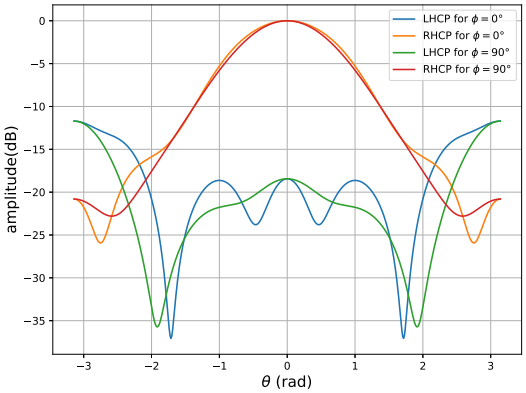

(b) E-field normalised amplitude radiated by the antenna, for $\phi = 0°$ and $\phi = 90°$ (dB)

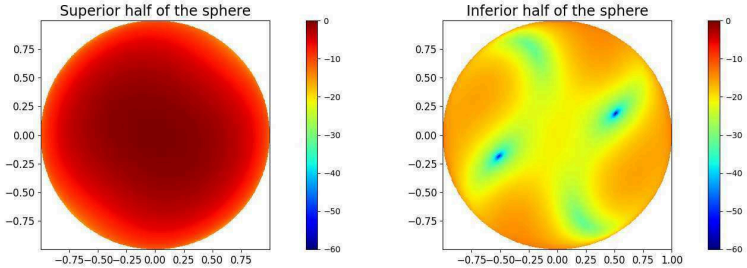

(c) Normalised co-polarisation pattern (RHCP) (dB)

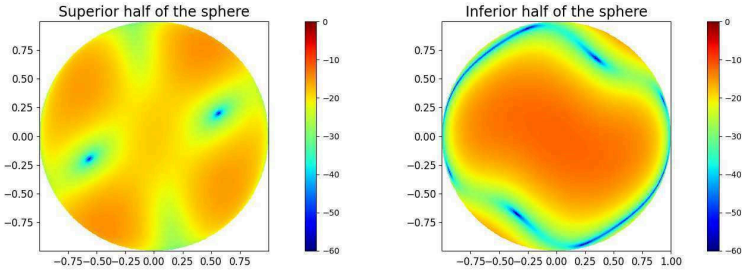

(d) Normalised cross-polarisation pattern (LHCP) (dB)

Figure 3.12: GPS antenna and its radiation pattern simulated with Feko

Accounting for the ground plane size, the radius of the minimal sphere containing the antenna is of 14.3 cm. According to (2.30), the band-limit of this antenna is about $N_{\mathrm{AUT}} = 5$. In Figures 3.13a, 3.13b and 3.13c, we can see slightly higher order coefficients, up to $N = 8$ due to the large dynamic chosen. They show the spin and Hansen coefficients of the antenna, with only the outgoing Hansen coefficients being plotted since the ingoing coefficients are all zero.

The aim is to compare it with the radiation in presence of the aircraft, yielding the choice of parameters fitting both cases. Thus, the amplitude variation is set at 80 dB, because for the study of the antenna on the aircraft, we aim to detect a large number of coefficients, including the weakest ones.

This document may not be reproduced, modified, adapted, published, translated in any way, in whole or in part, nor disclosed to a third party without the prior written consent of ENAC. © 2023, ENAC

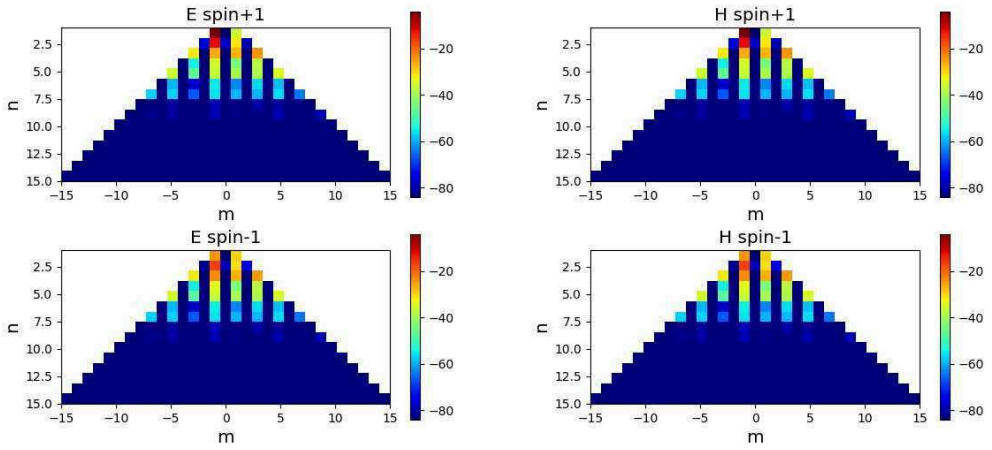

(a) Electric field spin coefficients (dB)

(b) Magnetic field spin coefficients (dB)

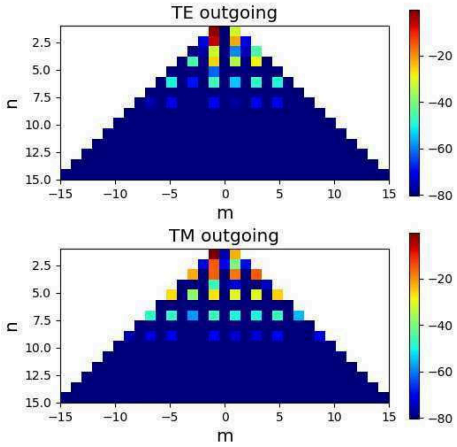

(c) Hansen outgoing coefficients(dB)

Figure 3.13: Spin and Hansen spherical harmonics coefficients.

An illustration of the simulation of the antenna surrounded by elements corresponding to the main parts of an aircraft is shown in Figure 3.14a. This simulation comes from the Capucine Amielh's PhD thesis, [103]. The antenna is mounted on a metallic cylinder corresponding to the fuselage, and metallic elements representing the wings and the empennage of the aircraft are disposed around. Only the main interacting elements are conserved to save computation time. The size of the aircraft corresponds to the dimension of an Airbus A320. Together they form a DUT with a radius $r_0 = 36$m, radiating at 1.57542 GHz. According to (2.30), the band-limit of this radiating object is $N_{\text{DUT}} = 1116$.

In Figure 3.14b, the radiation pattern of the DUT is shown. In Figure 3.14c and 3.14d, the co- and cross-polarisation of the antenna are represented. We can notice that the GPS antenna is affected by the elements of the plane and we observe faster variations on the radiation pattern, as shown in Figure 3.14b and on the co- and cross-polarisation in Figure 3.14c and 3.14d.

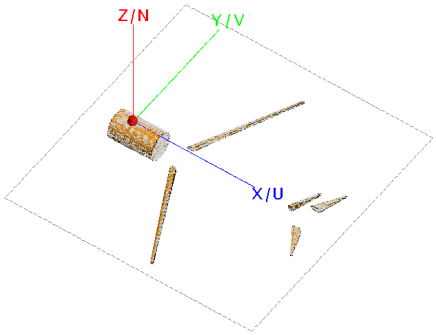

(a) Simulation of the antenna on top of the aircraft

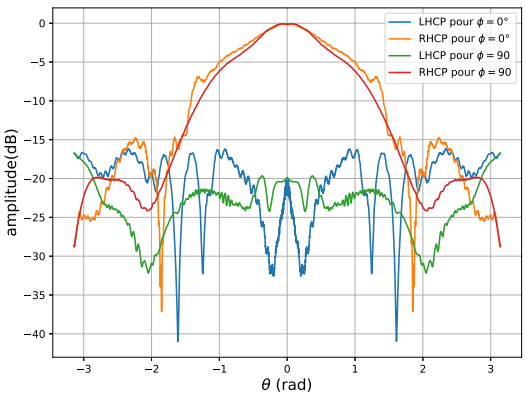

(b) E-field normalised amplitude radiated by the antenna on the aircraft, for $\phi = 0°$ and $\phi = 90°$ (dB)

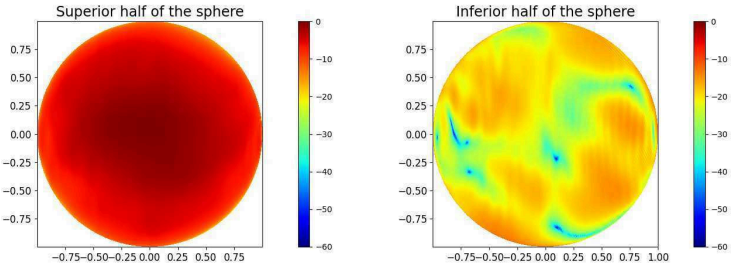

(c) Co-polarisation patten (RHCP) (dB)

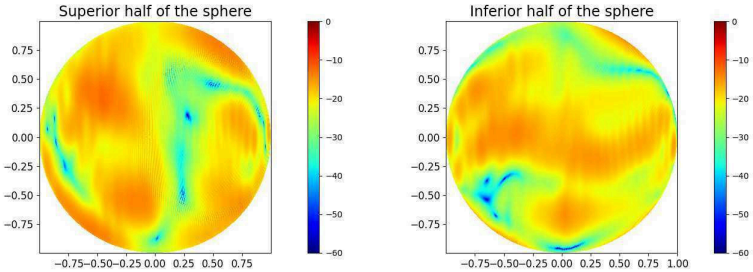

(d) Cross-polarisation pattern (LHCP) (dB)

Figure 3.14: GPS antenna on top of the aircraft

The spin coefficients are plotted in Figures 3.15 and the Hansen coefficients are plotted in Figure 3.16. Only the coefficients for a truncation order of N=80 are shown, as higher coefficients are very weak. A wide dynamic range (80 dB) is used to reveal the weak coefficients resulting from the scattering of the antenna's radiation on the different parts of the aircraft.

Both steps of the transform (spin transform + Hansen conversion) are accomplished in 128 seconds.

Even though the strongest coefficients correspond to the antenna radiation, we observe significantly more coefficients than in Figure 3.13. This means that scattering on the elements of the aircraft do introduce variations to the whole radiation, as expected. Besides,

This document may not be reproduced, modified, adapted, published, translated in any way, in whole or in part, nor disclosed to a third party without the prior written consent of ENAC. © 2023, ENAC

even if we can't see them directly on the diagram, it is possible that some very weak coefficients exist at high n levels. When n increases, the power is distributed on a larger number of coefficients in m. Consequently, even if their amplitudes are weak, their sum can be significant and have an impact on the radiation of the antenna. Thus, the power radiated, for each value of n (summing in m) is plotted in Figure 3.17 for the antenna alone and for the complete DUT.

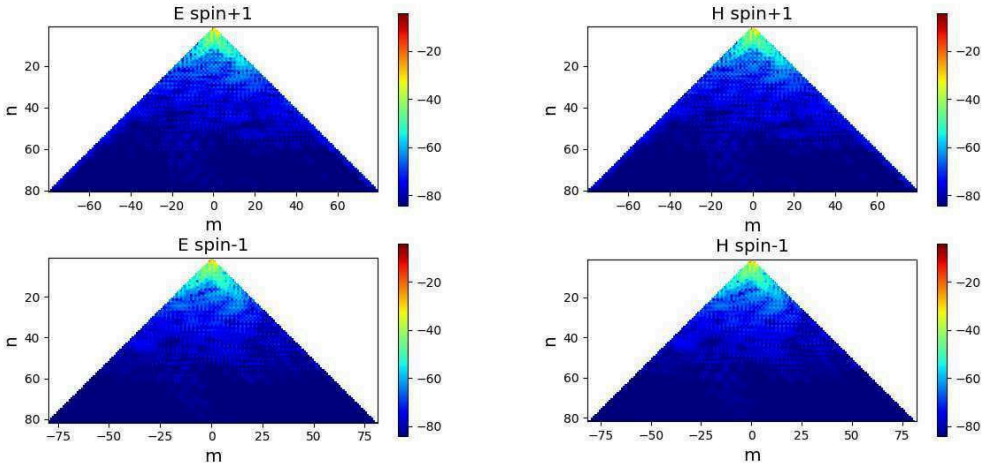

Figure 3.15: Zoom on the 80 first lines of the spin analysis coefficients (dB)

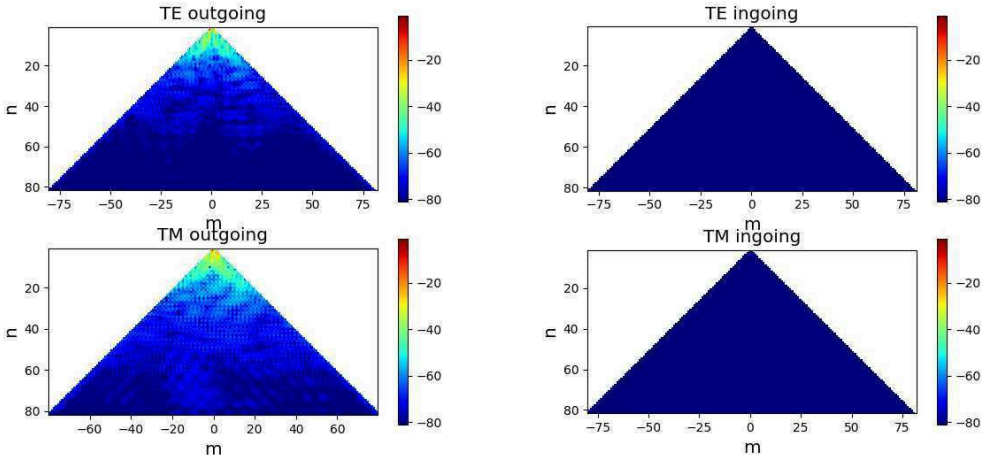

Figure 3.16: Zoom on the 80 first lines of the Hansen analysis coefficients (dB)

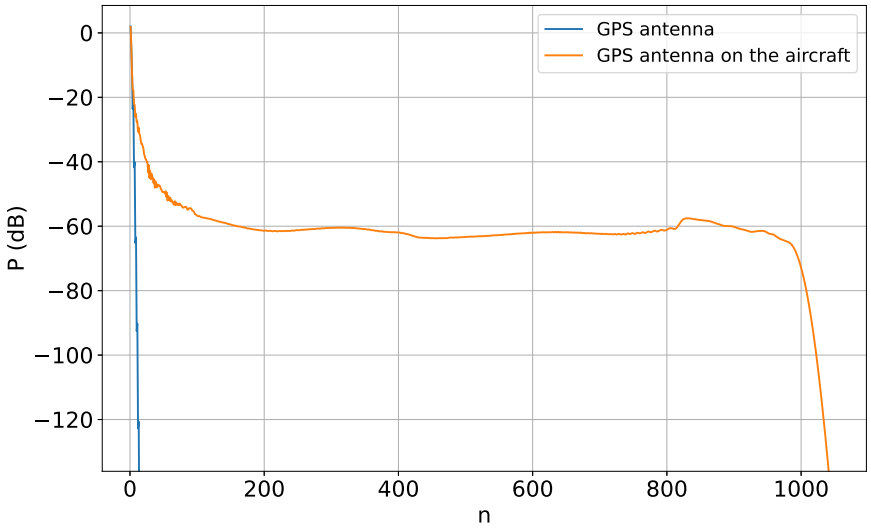

(a) Normalised power for each n level of the expansion

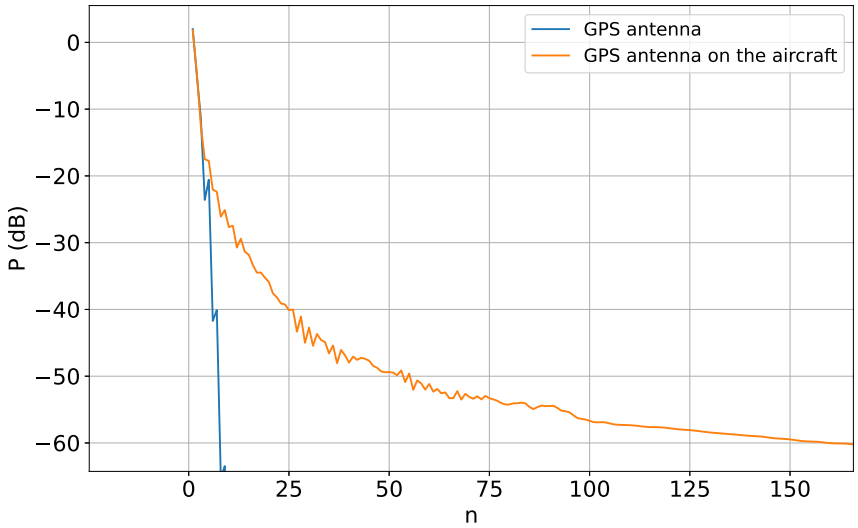

(b) Zoom on the first coefficients

Figure 3.17: Power of the coefficients, depending on the n level.

In the case of the antenna, we can see that the power is concentrated on the lower n-orders, up to $n \approx 10$, with no significant power in the higher orders. For the antenna on the aircraft, however, the power is also the strongest for the first orders, but decreases more slowly, until $n \approx 150$. Then the amplitude of the coefficients remains around -70 dB until $n \approx 1000$ and then decreases very fastly. The last steep drop is due to (2.30), linked with the size of the DUT. The plateau means that even if they have a very small amplitudes, there is always non-zero coefficients on every n-level of the transform diagram, until $N \approx 1000$. That explains why we notice fast variations on the radiation pattern of the antenna, likely due to scattering from the aircraft's components.

This document may not be reproduced, modified, adapted, published, translated in any way, in whole or in part, nor disclosed to a third party without the prior written consent of ENAC. © 2023, ENAC

This test has shown the ability of the spin transform algorithm to analyse the radiation pattern of an antenna on a large size carrier.

3.5.6 Bistatic RCS of an aircraft

In this section, we explore another domain of eletromagnetic measurement, the Radar Cross Section RCS of a large target. The objective is to simulate and expand into spherical harmonics the bistatic RCS of an aircraft. This transform is conducted to assess the performance of the transform algorithm.

We consider the simulation of an aircraft with characteristics similar to an Airbus A320 in a bistatic configuration. The aircraft is illuminated by a plane wave coming from the front, in vertical polarisation, as shown in Figure 3.18, for a frequency $f = 2$ GHz. The far-field scattering caused by the aircraft is calculated using Feko's large element physical optics method. While this method may not be the most precise, it offers a valuable compromise between computation precision and speed.

The theoretical band-limit, as defined by Hansen in (2.30), is $N_{\mathrm{DUT}} = 1676$ for a distance of $r_0 = 40$ m, which corresponds to the wingspan of the aircraft. Since the SSHT algorithm is optimized for N being a power of two, we oversample so that $N = 2048$. Consequently, the computation is performed on a McEwen Wiaux grid with dimensions of 2048×4096. This implies that the RCS is computed using a grid consisting of 8,388,608 points.

An illustration of the Feko simulation is presented in Figure 3.18. The horizontal cut of the scattered radiation pattern is shown in Figure 3.19. The RCS presents a dominant peak oriented along the y-axis, corresponding to a direction along the aircraft fuselage. The RCS also exhibits peaks in various directions around the origin, signifying diffractions and reflections of the plane wave on different parts of the aircraft, as shown in Figure 3.18. Finally, a second major peak can be observed in Figure 3.19, for $\phi = 0°$, this corresponds to the scattering of the plane wave on the nose of the aircraft. Obviously, this RCS presents much more fast variations than the previous tests performed on antenna radiation patterns, we can thus expect very high order coefficients in the spherical harmonics transform.

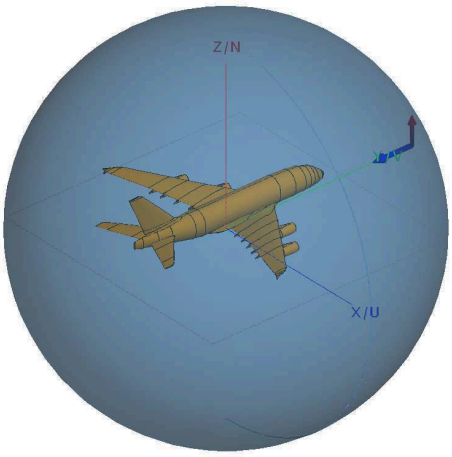

Figure 3.18: Simulation of the aircraft RCS

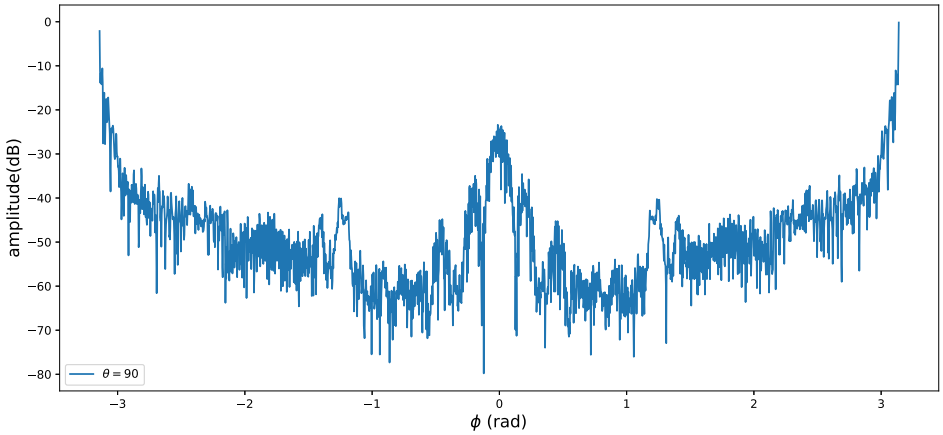

Figure 3.19: Normalised scattered radiation pattern cut, $\theta = 90°$, of the simulated aircraft, in dB

The co and cross polarisations of the RCS are depicted in Figure 3.20. In these Figures, the front and back peaks may not be as distinctly visible but they exhibit distinctive arc-shaped signatures in the diagrams which are less pronounced in the other diagrams. These arcs likely result from reflections on the wings and empennage of the aircraft.

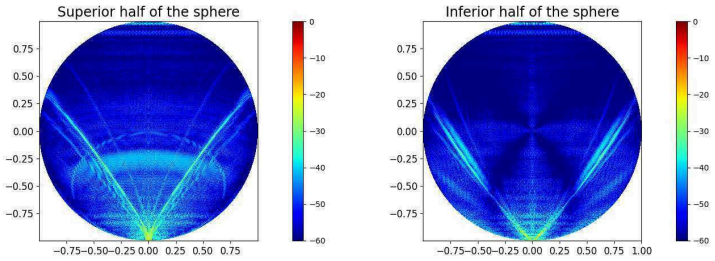

(a) Co-polarisation (dB) of the scattered radiation pattern

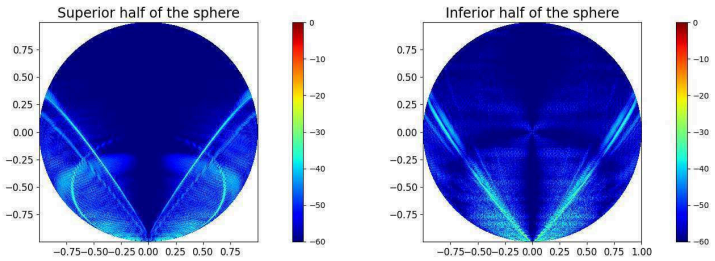

(b) Cross-polarisation (dB) of the scattered radiation pattern

Figure 3.20: Normalised co and cross polarisations pattern on the unit sphere of the RCS

Firstly, the spin spherical harmonic transform is performed, and the coefficients for the E and H fields are presented in Figure 3.21. In total, $4N(N+2)$ coefficients are computed, resulting in a total of 16,793,600 coefficients. This initial step consumes 4 minutes.

This document may not be reproduced, modified, adapted, published, translated in any way, in whole or in part, nor disclosed to a third party without the prior written consent of ENAC. © 2023, ENAC

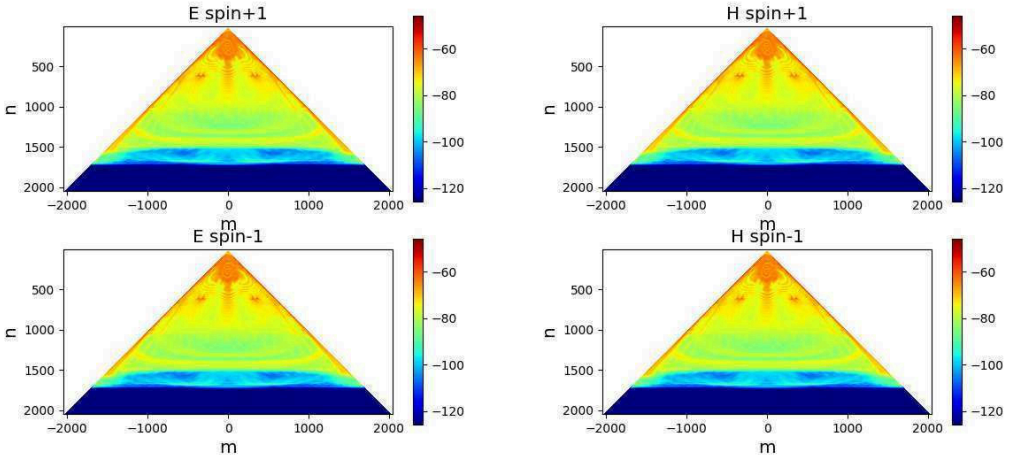

Figure 3.21: Spin spherical harmonic transform for $N = 2048$

A significant number of non-zero coefficients can be observed, with pronounced amplitudes occurring at the extreme values of m up to $n = 1500$. Notably, the strongest amplitudes of coefficients are not concentrated within the initial ranks but become prominent from $n = 100$ onwards. We can also observe the effect of the oversampling as every coefficient above $n = 1676$ are very weak. Then the conversion into ingoing and outgoing spherical harmonics as defined by Hansen is performed and is shown in Figure 3.22. This second step took 5 min 24s.

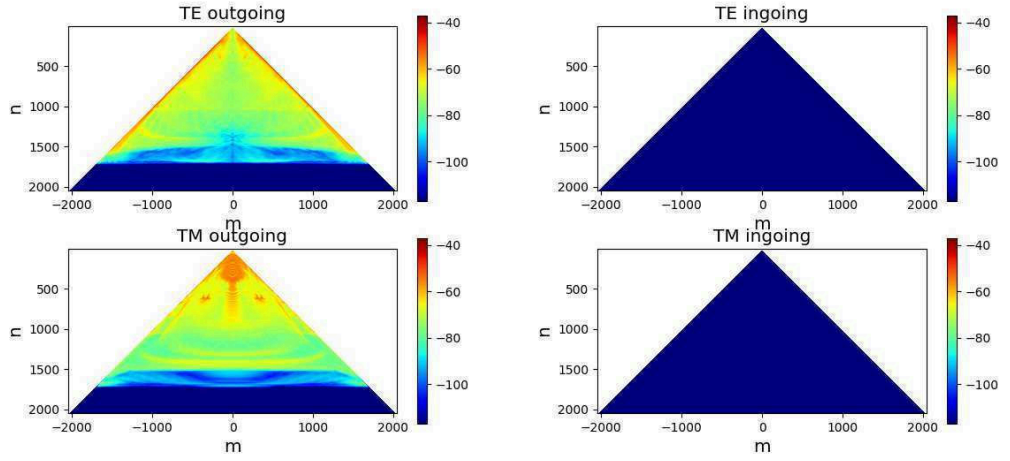

(a) Coefficients of outgoing waves (dB)

(b) Coefficients of ingoing waves (dB)

Figure 3.22: Spherical harmonic transform (dB)

The conversion into spherical harmonic coefficients has highlighted two distinct groups of strong coefficients, the TE component possesses fast variations with high values of $|m|$ and the TM component has more significant coefficients centered around $m = 0$.

The power for each rank n of incoming and outgoing coefficients is plotted in Figure 3.23.

We can observe that the power increases in a first part, remain of the same order between $n \approx 250$ and $n \approx 1500$ and then decreases abruptly. This pattern aligns with the information provided by the Hansen expansion. In fact, in Figure 3.22a, we can observe a reduction in the amplitude of each coefficient as n increases. This reduction is compensated by the increasing number of coefficients, resulting in the total power remaining approximately constant.

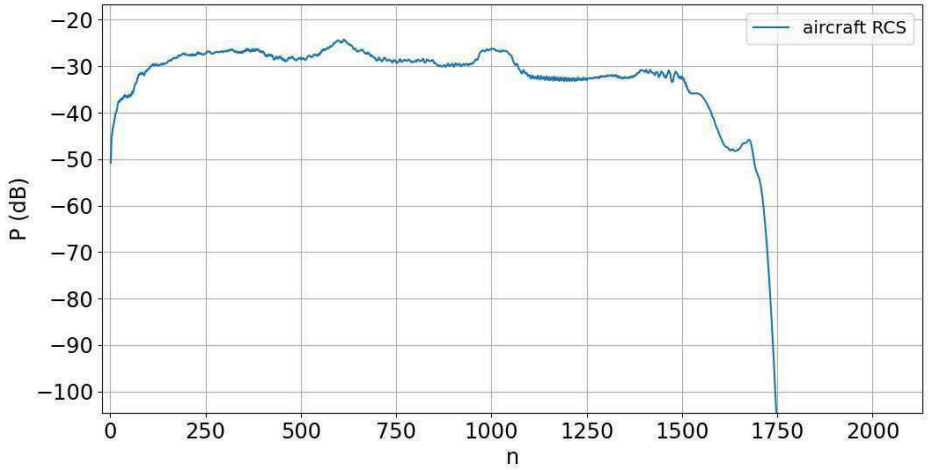

Figure 3.23: Normalised power of the coefficients (dB), depending on the n level.

To conclude, the spin spherical harmonic transform of the RCS of an airplane is performed on spherical harmonics up to the order $N = 2048$ in 9 minutes and 24 seconds. It shows a specific coefficients distribution, presenting a great number of low amplitude coefficients. This differs from most antenna's expansions that usually present strong amplitude coefficients on the low n-levels.

3.5.7 Conclusion

In this section, the spin spherical harmonics transforms of specific radiation patterns have been performed. Firstly, the analytical field of an elementary dipole has been derived in terms of spin spherical harmonics, and a simulation has illustrated the results of the transform. Additionally, a combination of dipoles that yield a pure right hand circularly polarised field has been conducted to highlight the relationship between the sign of the spin parameter and the far-field polarisation of the antenna.

Next, the radiation of a linearly polarised horn has been expanded using spin spherical harmonics and then converted into the Hansen harmonics. This computation has shown the advantage, in term of computation time, of SSHT over the Feko spherical transform algorithm. For example SSHT takes 7.2s to compute the spherical transform up to N=256 when Altair Feko takes 38 min.

Then, the spin transform of the radiation pattern of D2R2 has been done, exposing the perturbations in the measurement environment.

Additionally, to illustrate the performance of spin spherical harmonics in terms of band-limitation, the radiation of a GPS antenna mounted on an aircraft has been simulated, and

This document may not be reproduced, modified, adapted, published, translated in any way, in whole or in part, nor disclosed to a third party without the prior written consent of ENAC. © 2023, ENAC

the spin spherical harmonic coefficients have been computed, until $N = 1116$. This has illustrated the capability of SSHT to compute coefficients at very high levels, as 4,990,752 coefficients have been computed in 2 min 8s. This transform has demonstrated the ability of the spherical harmonic transform to localise coefficients coming from perturbation, as they occupy higher n-ranks than the coefficients of the antenna alone. However this representation has limitations, when power is divided on a lot of coefficients, their contribution to the spectrum becomes negligible, while the sum of those weak amplitudes coefficients does possess power.

Finally, the bistatic RCS of an aircraft has been simulated and expanded in terms of spin spherical harmonics. The transform has been computed for $N = 2048$. In 9 min 24 s, 8,386,560 coefficients have been computed.

3.6 Conclusion

In this chapter, the concept of spin spherical harmonics has been introduced and adapted for antenna radiation analysis. Indeed, these expansions exhibit appealing properties in terms of representing tangent vectors on the sphere, and fast algorithms are available.

Firstly, the theoretical foundation of spin spherical harmonics has been presented, encompassing the definition of spin functions, spin spherical harmonics, and the expansion of spin functions using these harmonics. Additionally, the spin expression for tangent vectors over the sphere has been derived, along with the introduction of rotational properties associated with the spin.

Secondly, the sampling theorems and associated fast algorithms have been reviewed to efficiently compute exact spherical harmonic transforms. The McEwen & Wiaux approach, in particular, is compatible with the spin representation and exhibits high performance in terms of complexity and computation time.

Next, the relation between Hansen and spin spherical harmonics have been derived.

Finally, spin spherical harmonics transforms have been performed on various radiation patterns, from canonical cases with very few coefficients ($N = 1$) to the RCS of an aircraft ($N = 2048$). These transforms have been performed in very short computation time, the longest computation being 9 min 24 s.

However the study of DUT radiating high orders spherical harmonics has shown a limitation of this transform. A significant amount of power can be spread over a lot of weak coefficients, making this power bearly visible in the spherical harmonic representation. Consequently, the next chapter focuses on spin spherical wavelets that present interesting localisation properties.

Chapter 4

Spin spherical wavelets

4.1 Introduction

Wavelets are a wide-spread powerful concept that has found applications in a wide range of fields, such as signal processing, data compression and image analysis. Their main advantage is their ability to represent and analyse data in different scales, from the broad information to small localized features [23,104,105,106,107]. This ensures good localisation properties that regular signal analysis tools, like Fourier, lacks.

The objective of this chapter is to introduce spin spherical wavelets in the continuity of the spin spherical harmonics and how they complete these in terms of electromagnetic radiation analysis.

For the sake of clarity, multiresolution wavelets are firstly presented for a 1D signal in Section 4.2. Then, spherical wavelets are derived in Section 4.3. Finally, examples of wavelet expansions of simulated and antenna radiation patterns are given in Section 4.4.

4.2 Multiresolution wavelets for 1D signals

4.2.1 Introduction

Multiresolution wavelets lead to the representation of a signal as a linear combination of elementary, localised, functions as they form an orthonormal basis. They are obtained by means of translations and dilations of two functions: the scaling function and the mother wavelet. Any signal can be decomposed over this basis; this is known as the wavelet transform. A wavelet is localised both in space and frequency. This property allows wavelets to take into account both the local and global properties of the signal. They offer a versatile framework for analysing and manipulating data.

This section draws a review of the multiresolution wavelet analysis for 1D signals. This constitutes a pedagogical approach to the spin spherical wavelets, that are adapted to the post-processing of antenna radiation. This type of expansion will also be used in Chapter 6.

In Section 4.2.2, the construction of a wavelet family and a wavelet basis is explained. Then the Fast Wavelet Transform algorithm for 1D signals is described in Section 4.2.3. Finally, an example of the wavelet expansion of a 1D signal is shown in Section 4.2.4.

This document may not be reproduced, modified, adapted, published, translated in any way, in whole or in part, nor disclosed to a third party without the prior written consent of ENAC. © 2023, ENAC

4.2.2 Multiresolution wavelet analysis of a continuous signal

As illustrated in Figure 4.1, a multiresolution wavelet basis is constructed from two primary functions: the scaling function φ of zero mean, and the mother wavelet ψ of non-zero mean.

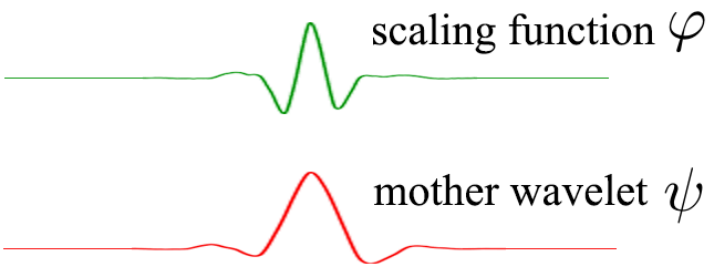

Figure 4.1: Example of a scaling function and a mother wavelet

Dilations and translations of these functions are denoted

$$\psi_p^{(j)} = 2^{-j/2}\psi(2^{-j}x - p), \qquad \varphi_p^{(j)} = 2^{-j/2}\varphi(2^{-j}x - p), \tag{4.1}$$

where $j \in \mathbb{Z}$ corresponds to dilations, and $p \in \mathbb{Z}$ corresponds to translations. Note also that $2^{j/2}$ is a normalisation factor that is introduced to keep $\|\psi_p^{(j)}\|_2 = 1$ and $\|\varphi_p^{(j)}\|_2 = 1$. As shown in Figure 4.2, in order to form the multiresolution basis that is used in the wavelet transform, we keep:

- one level of dilation J for the scaling functions, $\varphi_p^{(J)}$,
- J levels of dilations for the wavelet functions, $\psi_p^{(j)}$, with $j \in [1, J]$.

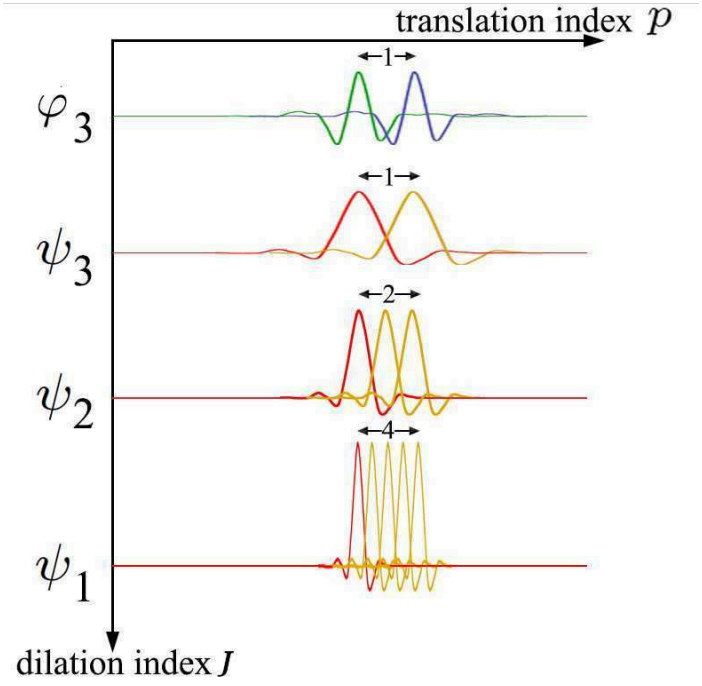

Figure 4.2: Example of a scaling function and a mother wavelet

These functions constitute an orthogonal basis of $L^2(\mathbb{R})$, which means that any signal can be written as

$$u(x) = \sum_p A_p \varphi_p^{(J)}(x) + \sum_{j=1}^{J} \sum_{p \in \mathbb{Z}} D_p^{(j)} \psi_p^{(j)}(x), \tag{4.2}$$

where

- A_p are called the approximation coefficients,
- $D_p^{(j)}$ are called the detail coefficients.

A particularity of wavelets is their localisation in both the spatial and spectral domains. Indeed, when j increases of one unit, wavelets are dilated by a factor 2. This allows slower variations of the signal to be captured. This means that the scaling function and each wavelet level j addresses different part of the spectral domain. As shown in Figure 4.3, the scaling function is associated with the smallest frequencies, while wavelet functions are associated with domains of larger and larger frequencies when j decreases. This is due to the fact that a dilation of a signal by a factor 2 becomes a contraction by a factor 2 in the Fourier domain.

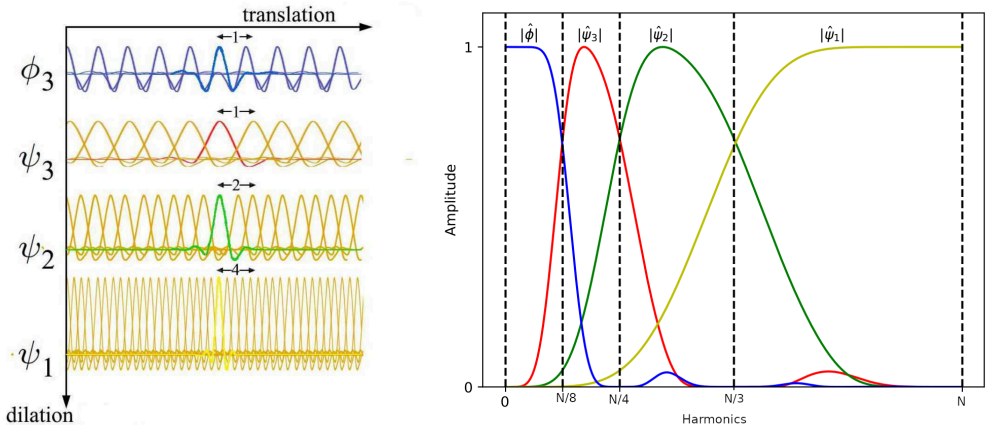

(a) Wavelet basis (b) Spectral coverage

Figure 4.3: A wavelet basis and its spectral coverage

This means that the approximation coefficients describe the signal with a lower resolution and take into account the slowest variations, while the detail coefficients give the faster variations of the signal, for each scale j. Consequently, a multi-resolution decomposition of the signal is obtained.

4.2.3 Discrete signals and the fast wavelet transform

In practice, most of the time, the multiresolution wavelet transform is applied on a discrete, i.e. sampled, signal. In such a case, the continuous variable x is replaced by an index p_x. In this case, a fast algorithm, the fast wavelet transform, exists to compute in an efficient way the approximation and detail coefficients from the discrete values of the signal $u[p_x]$.

From the Fourier domain interpretation of the wavelets, the discrete wavelet transform can be carried out by using successive high-pass (h) and low-pass filters (ℓ) and downsampling as illustrated in Figure 4.4. The first step of this process is as follows:

This document may not be reproduced, modified, adapted, published, translated in any way, in whole or in part, nor disclosed to a third party without the prior written consent of ENAC. © 2023, ENAC

- a high-pass filter is used to extract the fastest variations of the signal, that correspond to the detail coefficients $D_p^{(1)}$;
- a low-pass filter is used to extract the remaining components of the signal;
- a downsampling of factor 2 is performed without loosing information due to the spectral occupation of both signals.

This process is then repeated J times to obtain all the detail coefficients $D_p^{(j)}$. The output of the last low-pass filter can be viewed as a low resolution approximation of u and corresponds to the approximation coefficients A_p. The high-pass / low-pass filters are said to be mirror conjugate. They typically have a small size impulse response. This small size and the successive downsampling render this algorithm very efficient. For a signal of size P, the complexity is of order $O(P)$, which is even better than the Fast Fourier Transform that is of complexity of order $O(P \log P)$.

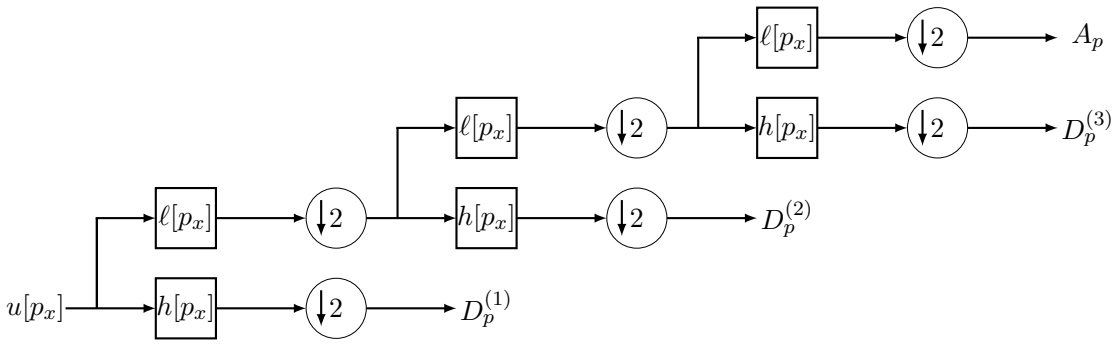

Figure 4.4: Fast Wavelet Transform (FWT) using mirror filters.

Note that the inverse transform, that goes from the detail and approximation coefficients to the original signal, works in a similar way by replacing downsampling by upsampling as shown in Figure 4.5.

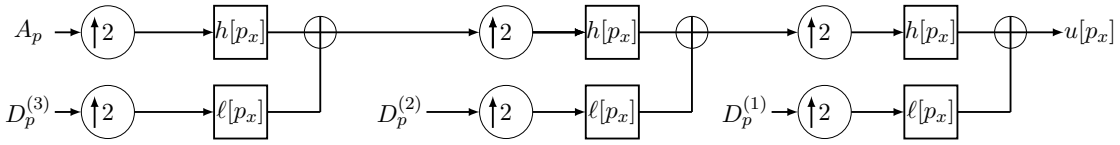

Figure 4.5: Inverse FWT using mirror filters.

4.2.4 Example of the wavelet transform of a signal

This subsection illustrates the wavelet transform of a signal consistent with the radiation of an antenna. The signal corresponds to the radiation pattern of a square aperture antenna of width 4λ, on a circle situated in the far-field zone in the plane $\theta = 90°$, at a frequency $f = 10$ GHz. The radiation of this antenna corresponds to a sinc function, with the main lobe centered in $\phi = 0°$. A white Gaussian noise of power -40 dB with regard to the main lobe is added.

The wavelet transform is done on symlets, until level 4, and represented in Figure 4.6.

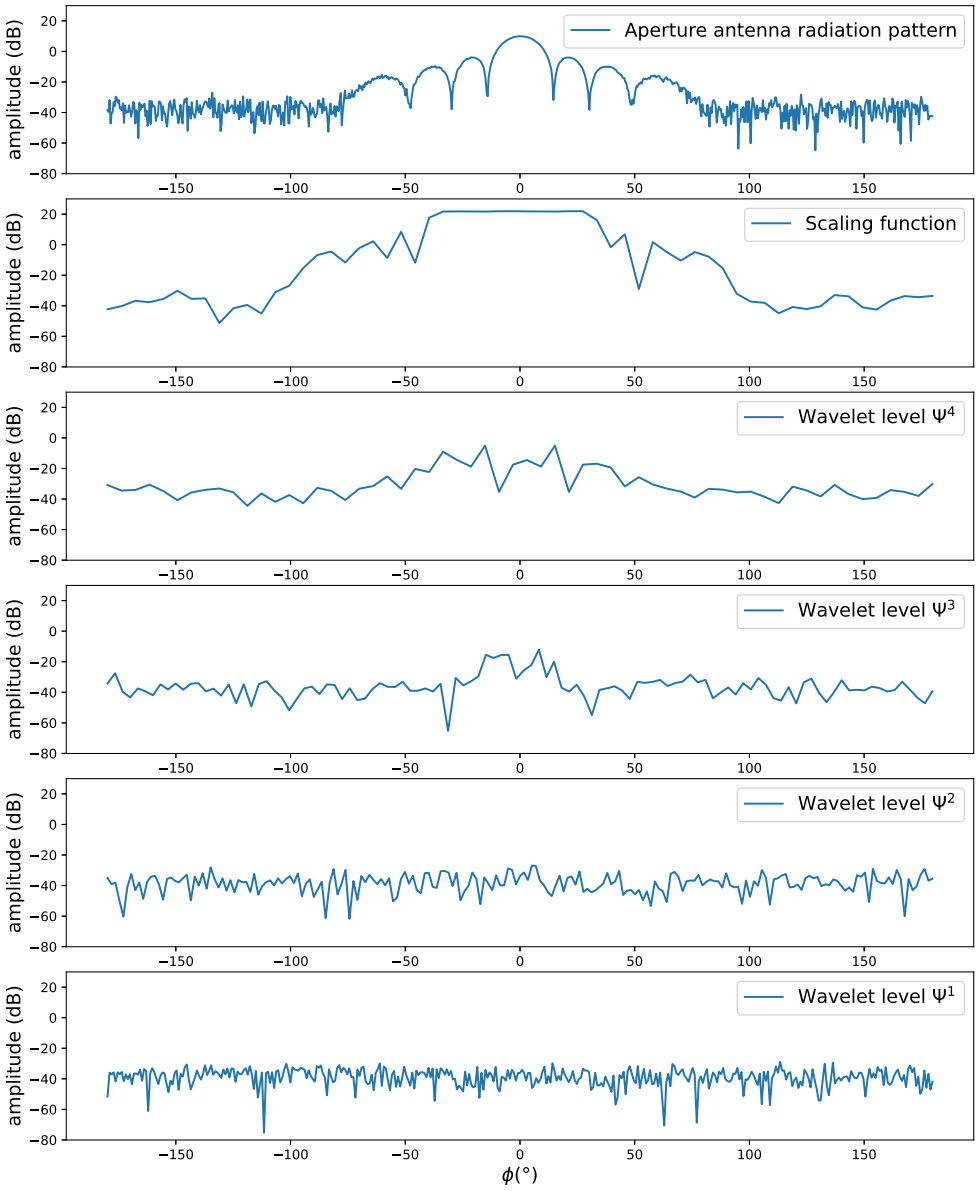

Figure 4.6: Wavelet expansion of the noisy radiation pattern of an aperture antenna.

The first plot corresponds to the studied signal, which is sampled respecting to the Shannon criteria (at least 2 sampling points per wave-length). Consequently, the number of approximation coefficients on the circle is chosen such as

$$N \geq \frac{4\pi r}{\lambda}. \tag{4.3}$$

In the simulation the parameters are chosen such that $N = 804$, for $\lambda = 3$ cm and

This document may not be reproduced, modified, adapted, published, translated in any way, in whole or in part, nor disclosed to a third party without the prior written consent of ENAC. © 2023, ENAC

$r = 1.92$ m. The second plot is the scaling function, a low resolution approximation of the signal, correponding to the approximation coefficients A_p. Then, detail coefficients $D_p^{(j)}$ are splitted on each wavelet levels, from 1 to 4. Each of them presents faster variations of the signal than the level before. On levels 1 and 2, the signal amplitude is around -40 dB, consequently, they probably contain the coefficients related to the noise. This means wavelets can be valuable tools for denoising, which is notably used in Chapter 6.

4.2.5 Conclusion

This section has constituted a review of the multiresolution wavelet analysis of 1D signals. Firstly, the presentation of 1D wavelets has been done, along with the derivation of the formulation of a signal on 1D wavelet levels. Secondly, the Discrete Fast Wavelet Transform has been presented. Finally a wavelet expansion of a noisy radiation pattern has been performed as an illustration.

4.3 Spherical wavelets

4.3.1 Introduction

Antenna measurements are usually performed in spherical geometry, consequently, post-processing with wavelets implies to adapt them to the sphere. During a project performed at ENAC and founded by CNES in 2018 [108], mapping methods have been considered. Indeed, spherical data can be mapped into two-dimensional signals, either using the θ, ϕ parameterisation or using Lambert projections for examples. However, all projections of a sphere on a 2D map necessarily distort the signal in some way and to some extent [109]. For this reason, wavelet transform suitable for spherical data have been developed, for example in planetary science [88], geophysics [110] and cosmology, in particular for the analysis of the cosmic microwave background (CMB) [26]. Thus a few wavelet framework on the sphere lead to exact transform in discrete and continuous settings.

Data acquired on a sphere can come in diverse forms, scalar, vector or tensor signals defined on the sphere. Consequently, the spin parameter as presented in Chapter 3 is particularly suitable and spin wavelet transforms on the sphere have been developed recently [95].

This section focuses on the concept of spin scale-discretised spherical wavelets, built on the tiling of the harmonics line to yield an exact wavelet transform in both the continuous and discrete settings [111, 112, 113]. These properties can be an asset for the study of antenna radiation pattern and measurement correction.

Firstly, the mother wavelet and scaling functions are introduced in Section 4.3.2, then the tiling of the harmonic line is illustrated in Section 4.3.3, explaining the derivation of the scaling function and wavelet levels. Then, wavelets are rotated in order to cover the entire sphere, in Section 4.3.4. Finally the axisymmetric scale discretised spin spherical wavelet representation of a signal is derived in Section 4.3.5.

4.3.2 Mother wavelet and scaling function

As for 1D wavelets, the multiresolution wavelet analysis for spin signals on a sphere is constructed from two types of functions: the wavelet Ψ of zero mean, and the scaling

function Φ of non-zero mean. These functions are originally centered at the $+z$ axis. They are of spin s. These functions are shown in Figure 4.7. In the framework of this PhD thesis, we only consider spin $s = \pm 1$ axisymmetric spherical wavelets. This means that these functions only depends on θ.

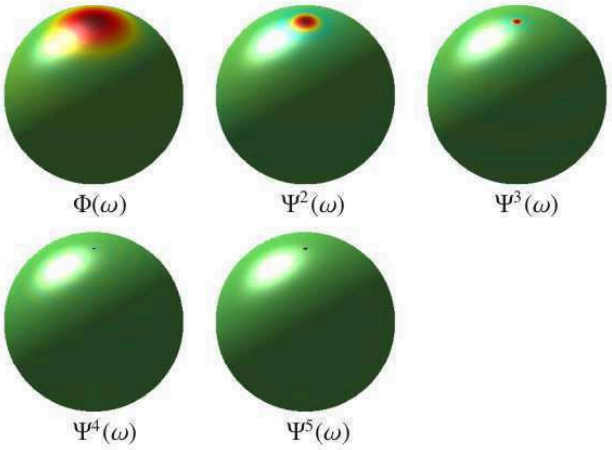

Figure 4.7: Axysimmetric wavelet functions [111]

As for 1D wavelets, we need to enlarge or to narrow the wavelet function in order to capture the various scales of variations of the signal. However, this can not be done with a simple dilation. Similarly, we need to move the wavelet and the scaling functions so as to describe the complete sphere. However, on the sphere, this can not be done by means of simple translations in θ and ϕ.

These two points are discussed in the next subsections.

4.3.3 Scaling function: tiling the harmonic space

With 1D wavelets, various scales are introduced by dilating the mother wavelet by powers of 2. In the Fourier domain, this allows to capture the different levels of variations of the signal. The underlying reason for that is that a dilation of 2 of a signal, becomes a dilation of 1/2 in the Fourier domain.

For spin signals over a sphere, the Fourier transform must be replaced by the spin spherical harmonics transform presented in the previous chapter. There are no simple rules associated with dilations for this transform. Therefore, another solution has to be proposed to obtain wavelets at various scales. In this PhD thesis, we use scale-discretised wavelets, a solution proposed by McEwen and Wiaux, that relies on a tiling of the harmonic space.

The wavelet and scaling functions are assumed to be axisymmetric, i.e. they do not depend on ϕ, their angular profile are represented in Figure 4.8b. This means that the spin spherical harmonic coefficients of these functions are zero for $m \neq 0$. Determining the wavelet at various scales denoted $\Psi^{s,(j)}$ with j the scale level, amounts to find the values of the spin spherical harmonic coefficients

$$C_{0,n}^{s,\Psi^{s,(j)}}. \tag{4.4}$$

This document may not be reproduced, modified, adapted, published, translated in any way, in whole or in part, nor disclosed to a third party without the prior written consent of ENAC. © 2023, ENAC

Similarly, determining the scaling function amounts to find the values of the spin spherical harmonic coefficients

$$C_{0,n}^{s,\Phi^s}. \tag{4.5}$$

The construction of these function are detailed in Annex **??**. Several criteria must be fulfilled to find these values:

- the transform must allow to recover completely and uniquely the signal.
- the scaling function must capture the slowest variations of the signal.
- each wavelet scale covers a different part of the spectrum in n. When j increases, faster variations are captured. This convention is the usual one for spherical wavelet, even if it is the opposite as the one used for 1D wavelet.
- smooth functions should be preferred

In this PhD thesis, the spectrum domains covered by each wavelet scale are separated by power of 2.

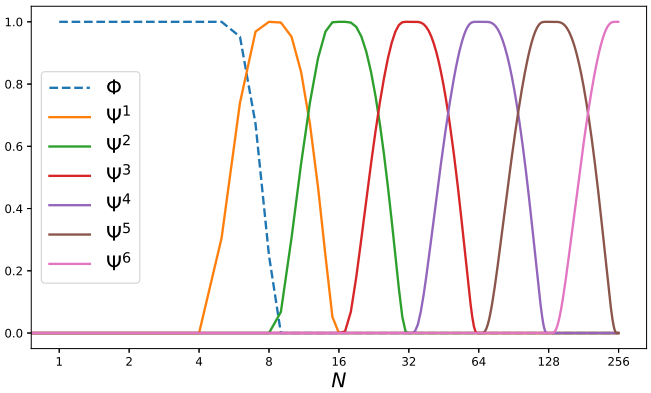

(a) Tiling of the harmonics line for scale discretised wavelets

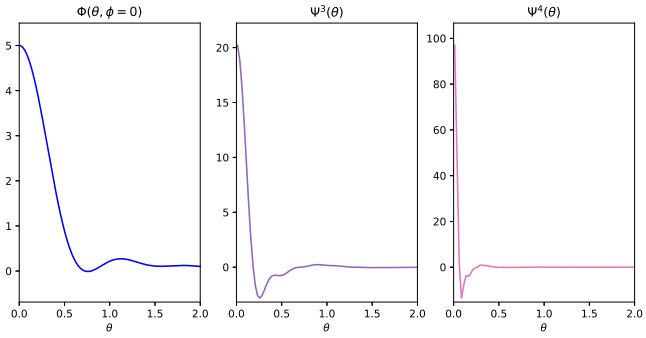

(b) Angular profiles of the scaling function and first levels of wavelets

Figure 4.8: Construction of wavelet functions, for axisymmetric wavelets, with parameters $J_{\min} = 3$ and $N = 256$.

The scaling levels are so that $j \in [J_{\min}, J_{\max}]$. The value of $J_{\max}$ must be chosen so as to reach the band limit of the signal $J_{\max} = \log_2(N-1)$. The value of $J_{\min}$ is a parameter that must be chosen so that $1 \leq J_{\min} \leq J_{\max}$. The scaling function captures the signal variations up to a band limit of $2^{J_{\min}}$. Note that the wavelet functions overlap as shown in 4.8a thus a wavelet of scale j is associated with a bandwidth from 2^{j-1} to 2^{j+1}.

4.3.4 Rotations

In order to cover the complete sphere, the scaling and wavelet functions should be moved from their original center (along $+z$) to other angular positions. With 1D wavelet, this is done using translations. On the sphere, this corresponds to global rotations as defined in Section 2.2.4. These rotations can be parameterised by means of Euler angles. Since the wavelet and scaling functions are assumed to be axisymmetric, the third Euler angle does not play any role and can be set to zero. The density of the grid on which the scaling and wavelet functions should be rotated depends on the band-limit of $\Psi^{s,(j)}$ and Φ^s. Greater band limits imply denser grids so as to grasp faster variations. McEwen and Wiaux have shown that their grid can be used on that purpose [95]. Finally, rotated wavelets are given by

$$\Psi^{(j),s}_{p_\theta,p_\phi}(\theta,\phi) = \mathcal{R}^s_{\epsilon^{(j)}_{p_\theta,p_\phi}} \Psi^{(j),s}(\theta,\phi), \tag{4.6}$$

with p_θ, p_ϕ previously defined in (3.18), parameterising the Euler angles

$$\epsilon^{(j)}_{p_\theta,p_\phi} = (\phi^{(2^{j+1})}_{p_\phi}, \theta^{(2^{j+1})}_{p_\theta}, 0). \tag{4.7}$$

For the scaling function, we have

$$\Phi^s_{p_\theta,p_\phi}(\theta,\phi) = \mathcal{R}^s_{\epsilon^{(j)}_{p_\theta,p_\phi}} \Phi^s(\theta,\phi). \tag{4.8}$$

4.3.5 Transform

The axisymmetric scale-discretised spin spherical wavelet representation of a signal u_s of spin s is finally given by

$$u_s(\theta,\phi) = \sum_j \sum_{p_\theta,p_\phi} D^{(j),s}_{p_\theta,p_\phi} \Psi^{(j),s}_{p_\theta,p_\phi}(\theta,\phi) + \sum_{p_\theta,p_\phi} A^s_{p_\theta,p_\phi} \Phi^s_{p_\theta,p_\phi}(\theta,\phi), \tag{4.9}$$

where the approximation coefficients $A^s_{p_\theta,p_\phi}$ provides a low resolution approximation of the signal, and the details coefficients $D^{(j),s}_{p_\theta,p_\phi}$ add the variations at the different scales.

For a discrete, i.e. sampled, and band-limited signal, the computation of the transform can be performed as follows [95]:

- spin spherical harmonic transform of the signal,
- filtering to obtain the spin spherical harmonic coefficients associated with the scaling function, and the various wavelet scales,
- inverse spherical harmonic transform, on downsampled grids.

The McEwen and Wiaux sampling theorem ensures that the downsamplings are done without losing information.

A representation of the tiling of a spin spherical harmonic expansion in wavelet levels is shown in Figure 4.9.

This document may not be reproduced, modified, adapted, published, translated in any way, in whole or in part, nor disclosed to a third party without the prior written consent of ENAC. © 2023, ENAC

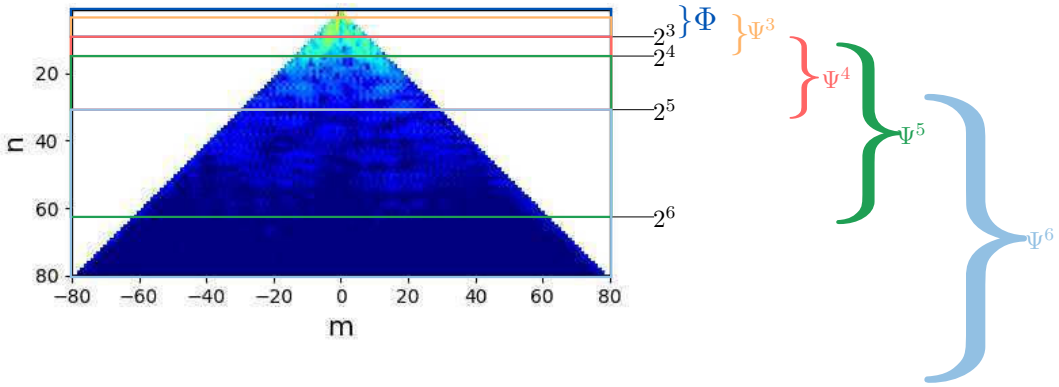

Figure 4.9: Tiling of the spin spherical harmonic expansion

This is noticeable that the higher the wavelet level is, the more spin spherical harmonics coefficients it contains. This is due to the dilation of the wavelet functions and to the relations between the indexes n and m of the spherical harmonic transform.

4.3.6 Conclusion

This section has defined a wavelet family allowing an exact wavelet representation of data on the sphere. Firstly, axisymmetric spin scale discretised scaling function and mother wavelet have been introduced. Then the construction of this basis has been detailed: first, a tiling of the spin spherical harmonic line is done, allowing to split the data on level of variation, then rotations of these functions allow to cover the entire sphere. Finally, the complete wavelet transform of a signal has been derived.

4.4 Spin spherical wavelets transforms of radiation pattern

4.4.1 Introduction

This section illustrates the use of spin spherical wavelets with various types of radiations. The radiations under study are some of the ones already presented in Section 3.5. Firstly, the wavelet expansion of the horn antenna is performed in Section 4.4.2, followed by the GPS antenna installed on an aircraft in Section 4.4.3 and finally the RCS of the aircraft in Section 4.4.4.

4.4.2 Horn antenna

This section presents the spin spherical wavelet transform of the horn antenna radiation presented in section 3.5.3. The radiation pattern of the horn antenna and the expansion in wavelet coefficients on the sphere are plotted in Figures 4.10, 4.11, 4.12 and 4.13, for spin +1 and -1, respectively. The indexes j and np, situated above the plots, indicate the wavelet level and the number of points on the plot, respectively. The reason for the white

disk in the $+z$ direction in the plot is the absence of a grid point at $\theta = 0°$ in the McEwen & Wiaux grid.

The plots correspond to the approximation and wavelet coefficients at all scales. The first wavelet level starts at $J_{\min} = 3$ and the highest wavelet level is 8, as the spherical wave expansion goes up to $2^8 = 256$.

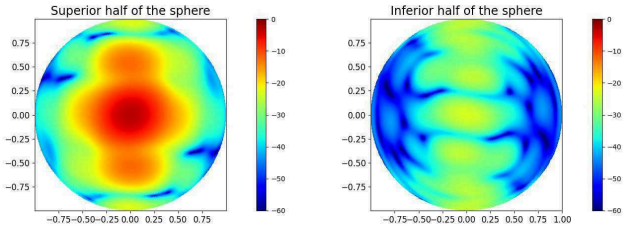

Figure 4.10: Normalised spin +1 components of the radiation pattern of the horn antenna (dB)

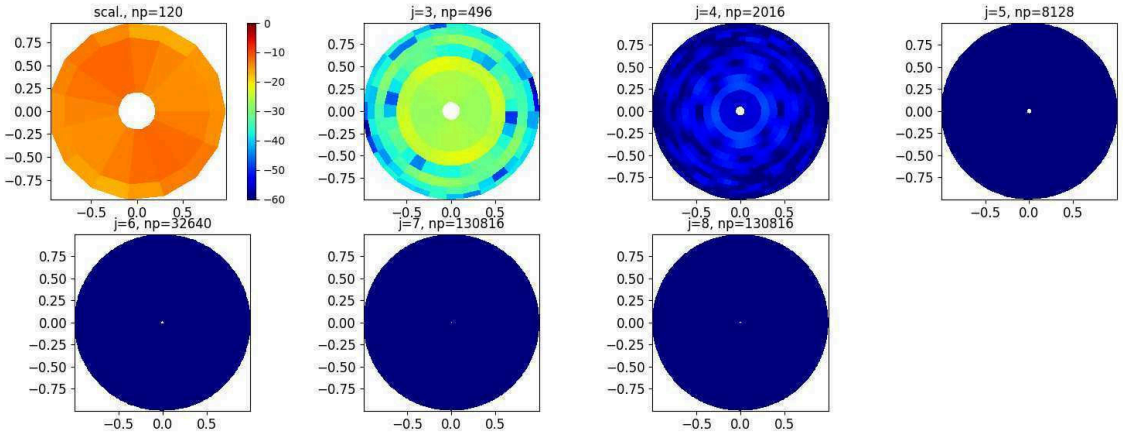

(a) Wavelet expansion of the upper half of the sphere

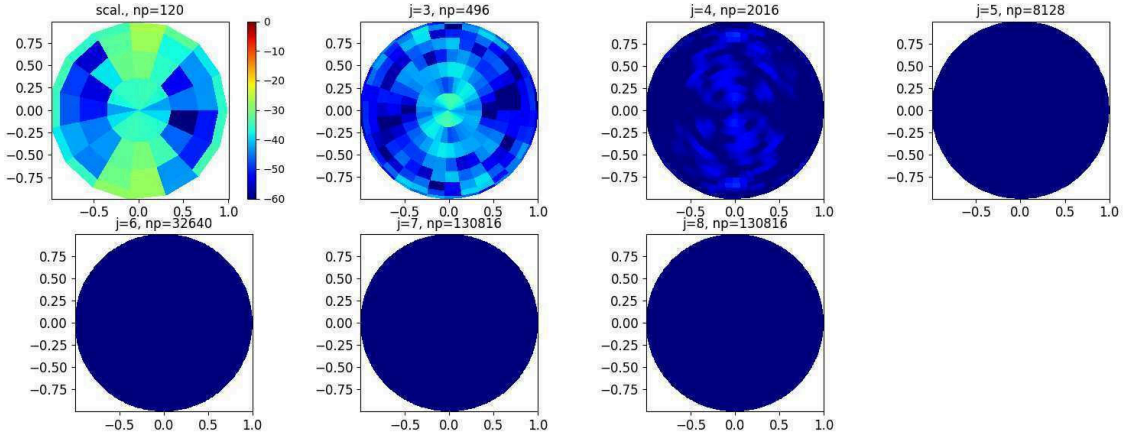

(b) Wavelet expansion of the lower half of the sphere

Figure 4.11: Normalised wavelet expansion of spin +1 component of the radiation pattern of the horn antenna (dB)

This document may not be reproduced, modified, adapted, published, translated in any way, in whole or in part, nor disclosed to a third party without the prior written consent of ENAC. © 2023, ENAC

The scaling function covers the $2^3 = 8$ first n-rows of the spin spherical harmonics expansions of Figure 3.8, they are the rows with the strongest coefficients. The first wavelet corresponds to the wavelet function that covers the coefficients from $n = 4$ to $n = 16$, which have weaker amplitudes. For greater values of n, Figure 3.8 shows that coefficients are mostly negligible.

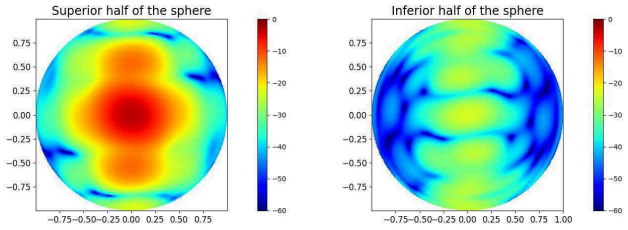

Figure 4.12: Normalised radiation pattern of the spin -1 of the horn antenna (dB)

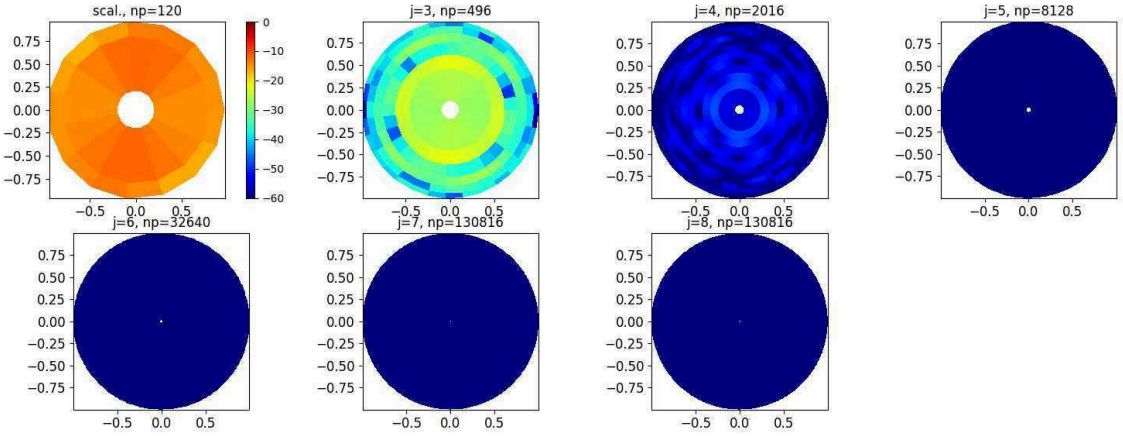

(a) Wavelet expansion of the upper half of the sphere

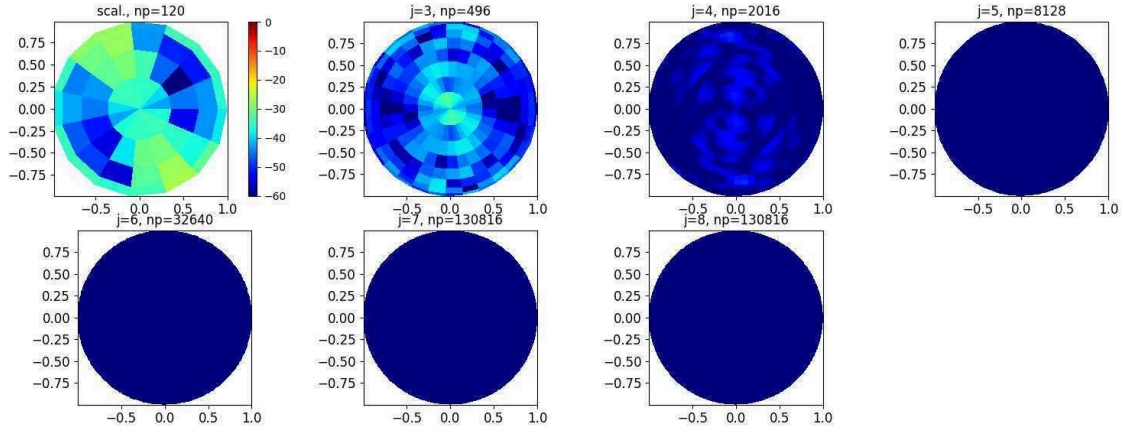

(b) Wavelet expansion of the lower half of the sphere

Figure 4.13: Normalised wavelet expansion of spin -1 component of the radiation pattern of the horn antenna (dB)

As the expansion is performed in multiresolution, the number of point for each plot in-

creases with the wavelet scale. For the first levels, the information is contained on a small number of coefficients, demonstrating the compression potential of the wavelets.

4.4.3 GPS antenna on an aircraft

In this section, the wavelet transform of a GPS antenna fixed on an aircraft is performed. This corresponds to the antenna described in Section 3.5.5. Firstly the spin wavelet expansion of the antenna alone is computed. Then the same wavelet expansion is performed with the antenna on the aircraft.

The wavelet expansion of the antenna alone is performed in order to compare it to the one of the antenna on the aircraft. The spin +1 component (or right hand polarisation) of the antenna radiation has been shown in Figure 3.12. Its wavelet expansion is shown in Figure 4.14.

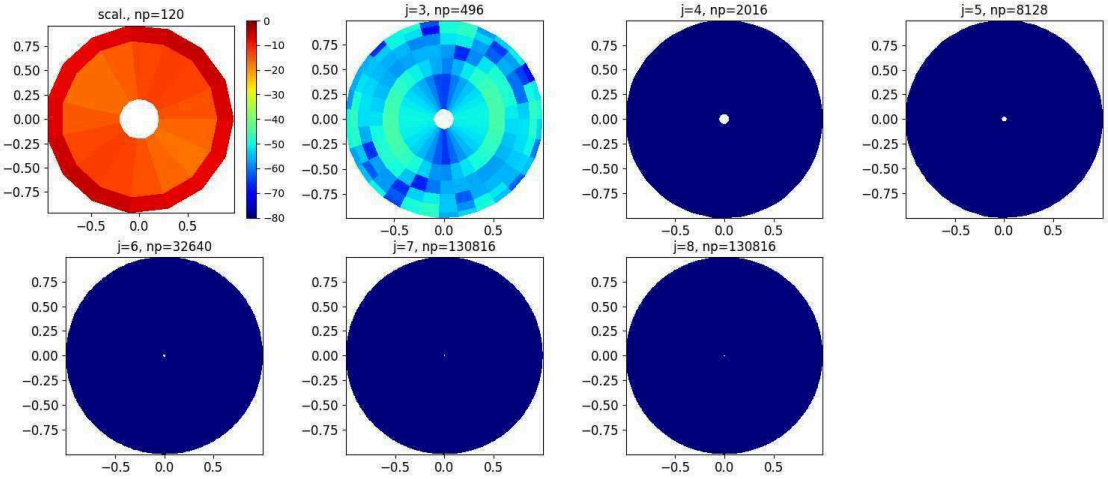

(a) Wavelet expansion of the upper half of the sphere

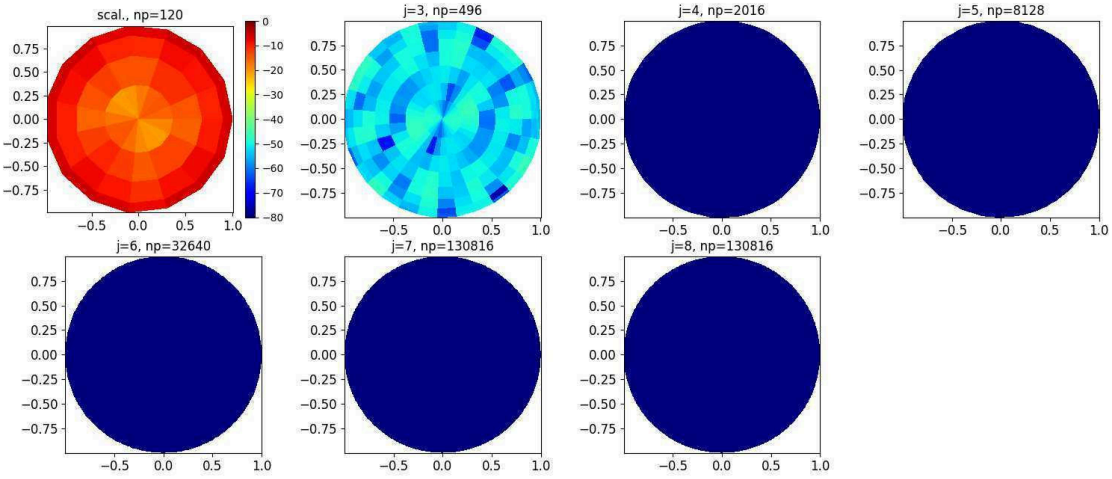

(b) Wavelet expansion of the lower half of the sphere

Figure 4.14: Normalised wavelet expansion of spin +1 component of the radiation pattern of the GPS antenna (dB)

This document may not be reproduced, modified, adapted, published, translated in any way, in whole or in part, nor disclosed to a third party without the prior written consent of ENAC. © 2023, ENAC

Secondly, wavelet expansion of the spin -1 component of the antenna radiation, that has been shown in Figure 3.12, is performed and displayed in Figure 4.15.

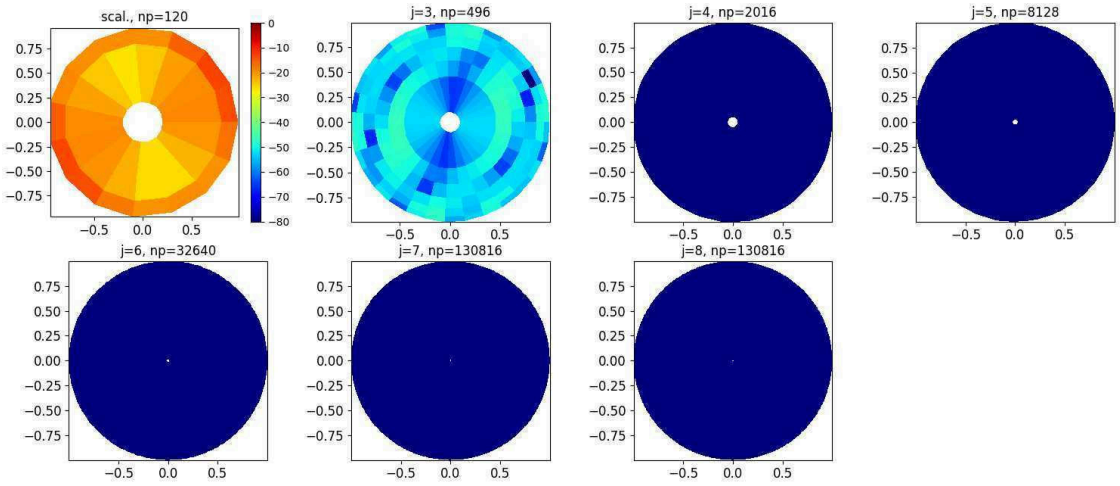

(a) Wavelet expansion of the upper half of the sphere

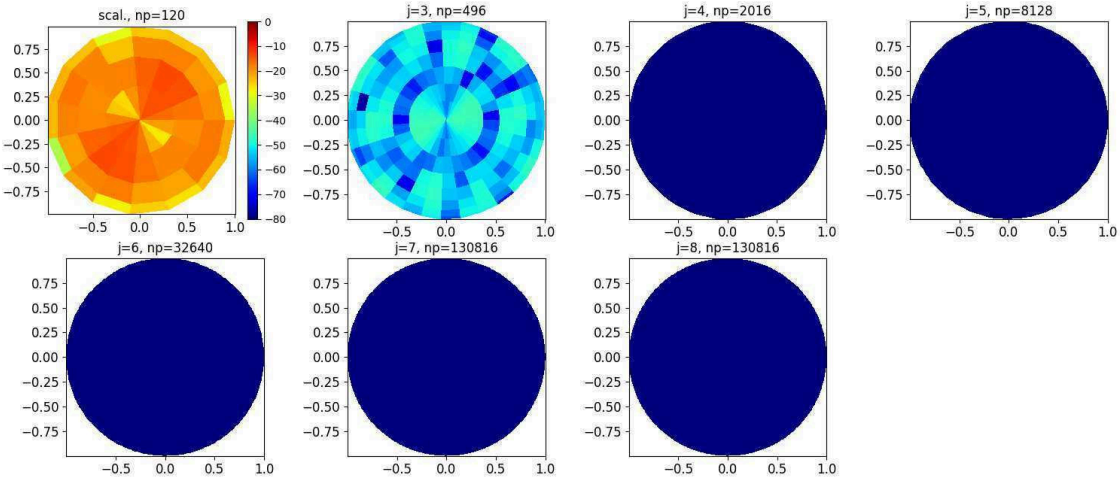

(b) Wavelet expansion of the lower half of the sphere

Figure 4.15: Normalised wavelet expansion of spin -1 component of the radiation pattern of the GPS antenna (dB)

As expected, the antenna being small and having a bandlimit $N_{\mathrm{AUT}} = 7$, only the scaling function ($n = 0$ to $n = 8$) and the first wavelet levels ($n = 4$ to $n = 16$) contain non negligible coefficients. Since the antenna is in RHCP, the +1 spin component is stronger than the -1 spin component.

Then wavelet expansion is performed on the radiation of the GPS antenna on top of the aircraft. From Section 3.5.5, expectations are that this radiation must be expanded on more wavelet scales than the one of the antenna alone. The expansion in spherical harmonic is performed until $N = 1116$, which means 11 wavelet levels are computed.

The wavelet expansion of the spin +1 and -1 components is performed and shown in Figure 4.16 and in Figure 4.17, respectively.

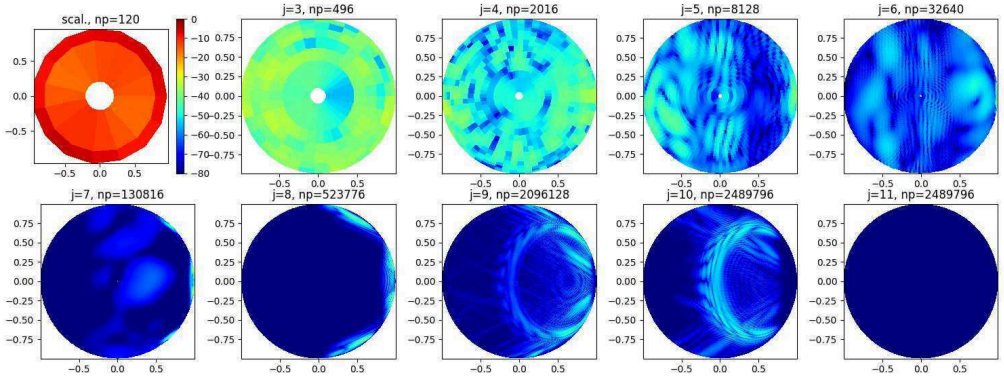

(a) Wavelet expansion of the upper half of the sphere

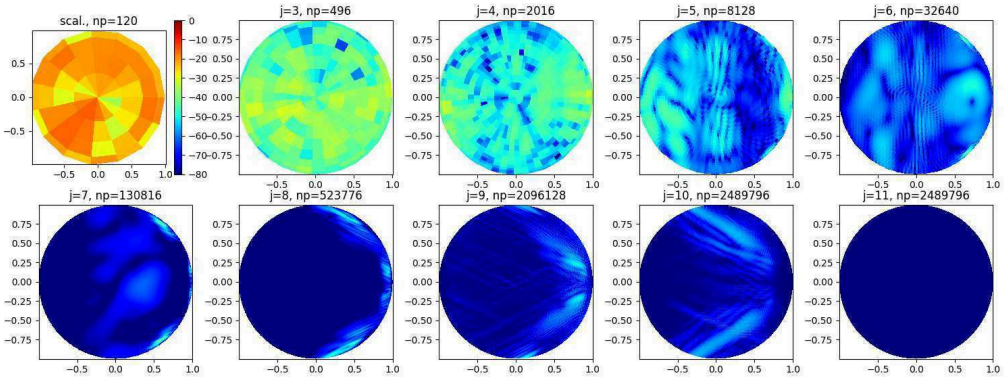

(b) Wavelet expansion of the lower half of the sphere

Figure 4.16: Normalised wavelet expansion of spin +1 component of the radiation pattern of the GPS antenna on the aircraft (dB)

This document may not be reproduced, modified, adapted, published, translated in any way, in whole or in part, nor disclosed to a third party without the prior written consent of ENAC. © 2023, ENAC

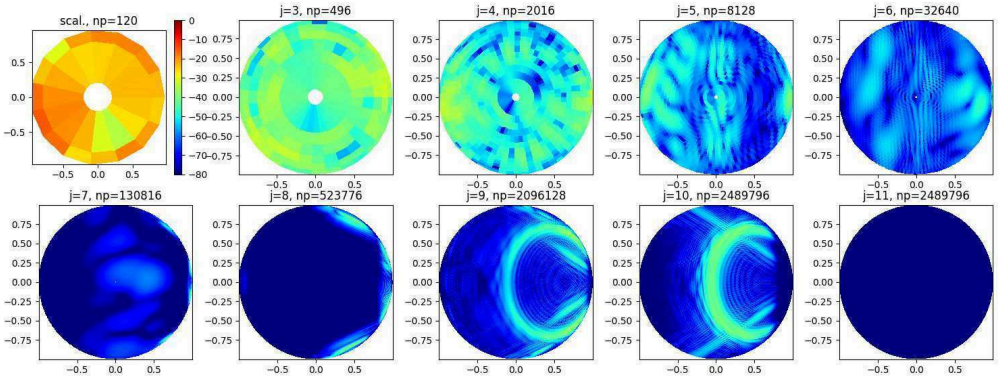

(a) Wavelet expansion of the upper half of the sphere

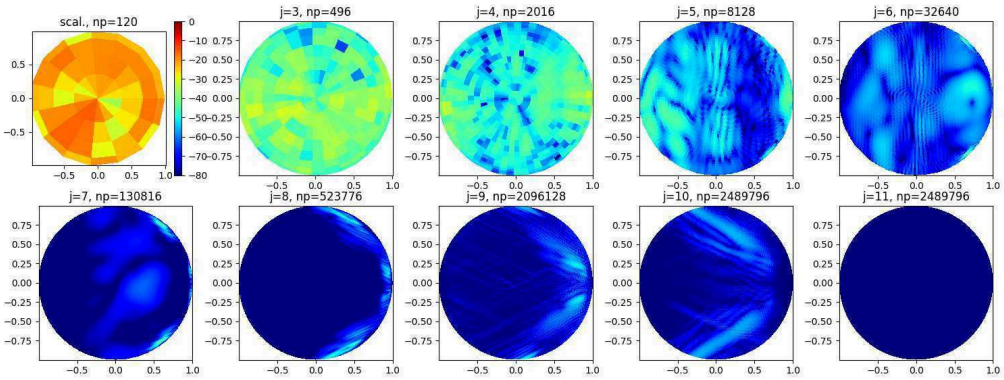

(b) Wavelet expansion of the lower half of the sphere

Figure 4.17: Normalised wavelet expansion of spin -1 component of the radiation pattern of the GPS antenna on the aircraft (dB)

Firstly, what catches the eye immediately, compared to Figures 4.14 and 4.15 is the presence of coefficients on wavelet levels $j > 3$. Their amplitude are weak but very characteristic of the signature of the presence of the aircraft, which front is oriented to the right. We can notice that this expansion is much more visual than the spherical harmonic one. Indeed the coefficients corresponding to the signatures on level 8, 9 and 10 are invisible to the naked eye on a spherical harmonic diagram because the values are too weak, and spread over a great number of coefficients. For example, the wavelet function n°8 covers the harmonic line from 2^7 to 2^9 which makes 295680 spin spherical harmonic coefficients, for the wavelet function n°9 2360832 coefficients and n°10 9440256 coefficients. Consequently amplitude of the coefficients is more diffuse.

The presence of non-zero coefficients on those levels also coincides with the results in Figure 3.17.

4.4.4 RCS of an aircraft

This section presents the wavelet expansion of the RCS of the aircraft presented in Section 3.5.6. The number of points on the grid is given by the parameter N=2048, meaning that $J_{\max}$ is 11, ($2^{11} = 2048$).

The spin +1 component of the field and its wavelet transform are shown in Figure 4.18 and 4.19, respectively. Figures 4.20 and 4.21 are associated with the spin -1 component. On these expansions, the aircraft points downwards.

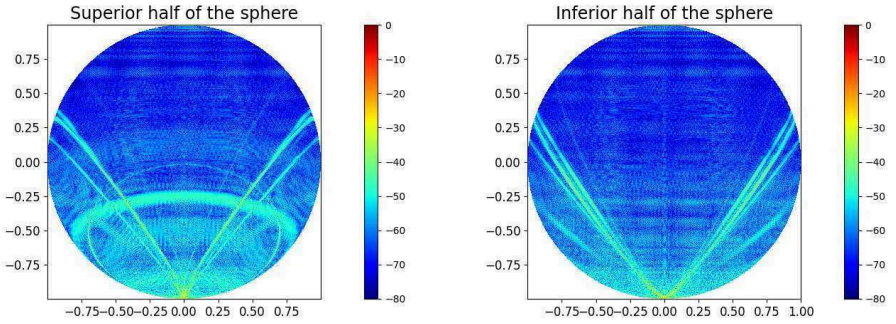

Figure 4.18: Radiation pattern of the spin +1 component (right polarisation) of the RCS (dB)

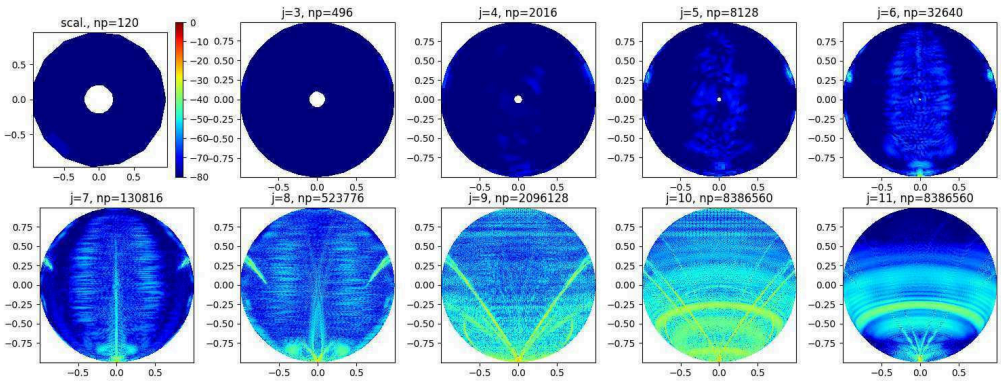

(a) Wavelet expansion of the upper half of the sphere

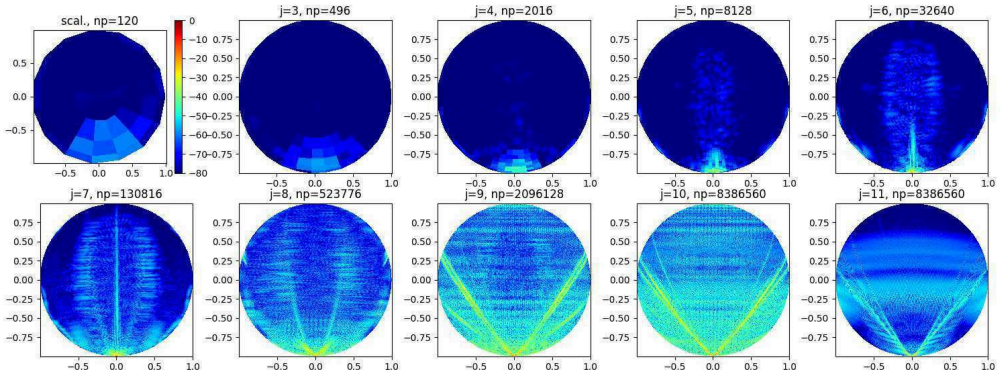

(b) Wavelet expansion of the lower half of the sphere

Figure 4.19: Wavelet expansion of the spin+1 component of the RCS (dB)

This document may not be reproduced, modified, adapted, published, translated in any way, in whole or in part, nor disclosed to a third party without the prior written consent of ENAC. © 2023, ENAC

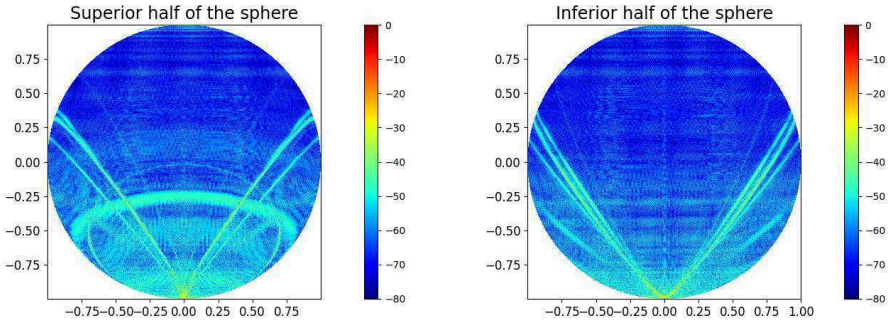

Figure 4.20: Radiation pattern of the spin -1 component (left polarisation) of the RCS (dB)

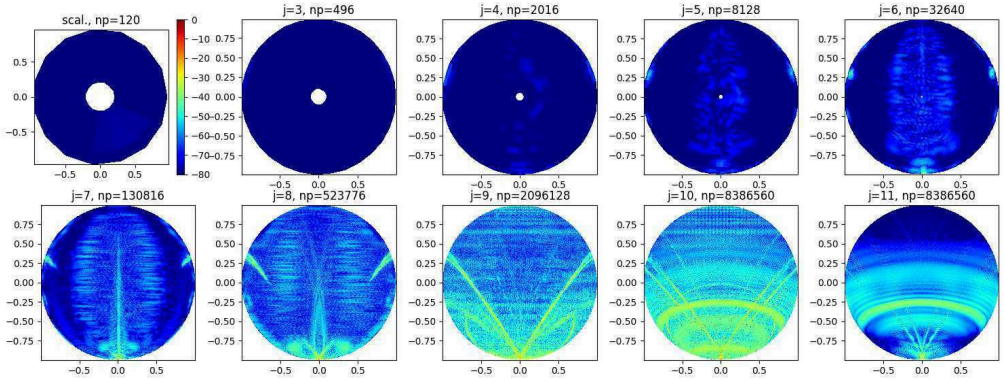

(a) Wavelet expansion of the upper half of the sphere

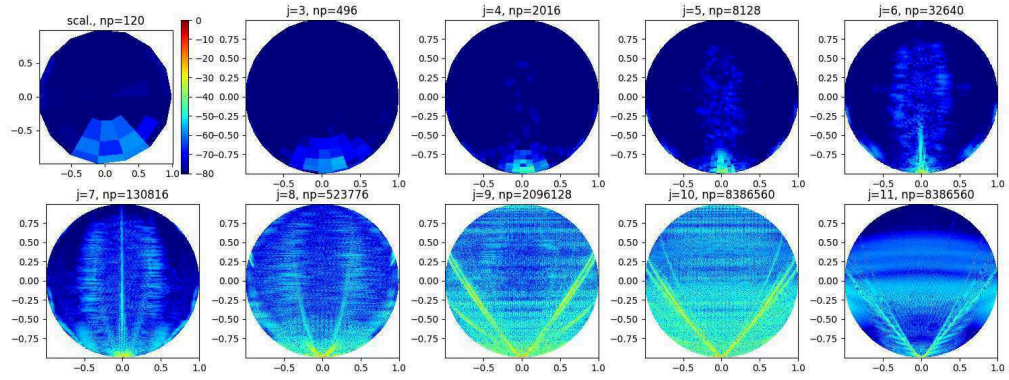

(b) Wavelet expansion of the lower half of the sphere

Figure 4.21: Wavelet expansion of the spin-1 component of the RCS (dB)

The high wavelet levels are the one with the most coefficients, this corresponds to the fast variations of the radiation pattern. The low levels are almost empty, which differ from the previous plots. However, this was expectable as Figure 3.23 shows that the power is not concentrated on the first coefficients. The computation time to compute the wavelet expansion is of 162 seconds for each spin, so about 5 minutes 24 seconds for the whole computation. However this representation is much more visual for large spherical harmonic diagram and allows to focus on coefficients that would be invisible otherwise, as they are very weak and widely spread in the spherical harmonic diagram.

4.4.5 Conclusion

This section has constituted an illustration of the application of spin spherical wavelet to electromagnetic radiations. These are based on the tiling of spin spherical harmonic expansions. Firstly, the spin wavelet expansion of the radiation pattern of a horn antenna has been performed. This expansion has not lead to interesting conclusion, as the antenna does not radiate high level coefficients. Secondly, the same expansion has been performed in the case of a GPS antenna on top of an aircraft. This has shown that the scattering of the radiation of the antenna on the aircraft has a signature on high wavelet levels which is invisible on the spherical harmonic expansion. Thus, this confirm the utility of using wavelets to study signals with harmonics of high order. Finally the wavelet expansion of an RCS has been performed. Here again, this expansion contains harmonic coefficients of high order. Also this section has shown the performance of the algorithm, as the wavelet expansion of the RCS took only 5 minutes, 24 seconds. This corresponds to the computation of nearly 40 millions (39134480) coefficients. To conclude, spin spherical wavelet expansion shows good potential as a tool to analyse and eventually correct antenna radiation patterns and RCS measurements.

4.5 Conclusion

This chapter has introduced spin spherical wavelets, a promising tool for antenna radiation pattern analysis. Wavelets are widely used in signal processing and compression problems but are less commonly used for spherical geometries.

Firstly, the construction of a wavelet basis in 1D geometry has been presented. Then the construction of spin spherical wavelets from spin spherical harmonic has been derived. Next, the algorithm exploited to perform the spin spherical wavelet expansion has been presented. Finally, spin spherical wavelet expansions of simulated radiations have been presented. This type of expansion can be very interesting for the analysis of very directive antennas, with fast variations on their diagrams, or for radar cross section processing.

This document may not be reproduced, modified, adapted, published, translated in any way, in whole or in part, nor disclosed to a third party without the prior written consent of ENAC. © 2023, ENAC

Chapter 5

Formulation of the measurement problem

5.1 Introduction

The antenna measurement problem can be described by many formulations. In [6], Hansen presents the scattering matrix as a tool to describe the interaction between the antenna and the probe, leading to the transmission formula. This formula is also adopted by Yaghjian in [114] and [14] and Gemmer and Herberling in [115]. However, this is remarkable that few articles or books derive the measurement problem as a convolution, whereas many present deconvolution methods to obtain the radiation pattern of the AUT from the measured signal [17, 116, 117].

The objective of this chapter is to rigorously formulate the measurement problem as a convolution, in spherical geometry, from basic electromagnetic theorems.

The problem statement is presented in Section 5.2. Section 5.3 shows how the equivalence principle can simplify the formulation of the measurement problem. Then in Section 5.4 the reciprocity theorem is used to relate the signal corresponding to the AUT radiation and the signal corresponding to the fields radiated by the probe in the environment near the antenna. Next, in Section 5.5, the rotation of the antenna introduced by the measurement process is accounted so as to formulate the measurement as a convolution which can be formulated in terms of spin components. Finally, Section 5.6 constitutes a validation by means of simulations of the hypothesis that the AUT can be replaced by its free-space equivalent currents.

5.2 Problem statement

The objective of the chapter is to define and prove the existence of a type of convolution between a quantity related to the fields radiated by the AUT, p, and a quantity related to the fields radiated by the probe in the environment nearby the antenna h, in absence of the antenna. It is not accurate to talk about radiation pattern here because the far-field hypothesis is not employed. These signals are represented in Figure 5.1. The aim is to write the measured signal b as

$$b(\epsilon) = h(\epsilon) \circledast p(\epsilon) + n_0(\epsilon), \tag{5.1}$$

This document may not be reproduced, modified, adapted, published, translated in any way, in whole or in part, nor disclosed to a third party without the prior written consent of ENAC. © 2023, ENAC

with $\circledast$ the convolution operator, n_0 the spatial noise, and ϵ the Euler angles corresponding to the AUT orientation.

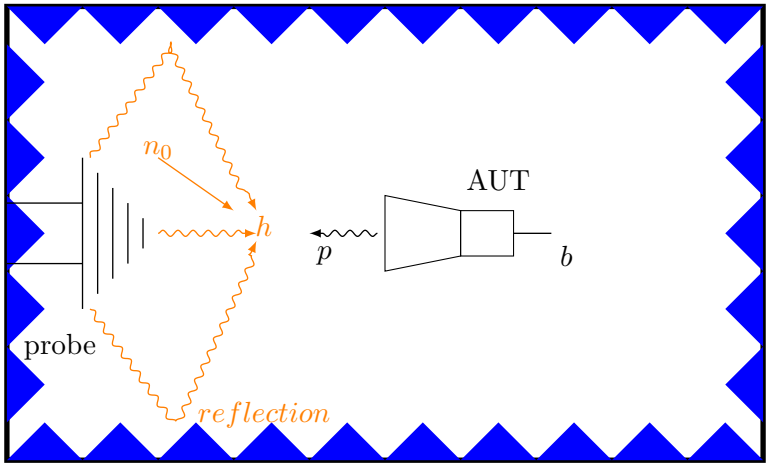

Figure 5.1: AUT and probe in an anechoic chamber, when the antenna is receiving

5.3 Equivalence principle

5.3.1 Introduction

In this section, the equivalence principle is used to formulate the relation between h and p. The rotation is not considered yet as the system is considered to be fixed in this section. The objective of this section is to show how the use of equivalent currents in free space and in the measurement environment, under certain assumptions, can simplify the formulation of the measurement problem. Firstly, the equivalence principle is reminded in Section 5.3.2, then the formulation of the feeding of the antenna is detailed in Section 5.3.3. In Section 5.3.4 the equivalence principle in free space is presented, followed by the equivalence principle in the measurement environment in Section 5.3.5. Then in Section 5.3.6, a discussion is done on the impact of the measurement environment on the equivalent currents.

5.3.2 The equivalence principle

The equivalence principle states that a domain Ω, containing sources, characterized by currents distributions $(\boldsymbol{J}_\mathrm{e}, \boldsymbol{J}_\mathrm{m})$ radiating electromagnetic fields $(\boldsymbol{E},\boldsymbol{H})$, as shown in Figure 5.2a, is always splitable in two subdomains Ω_1 and Ω_2, as shown in Figure 5.2b [118, 119].

This yields two subproblems:

- In the subproblem 1, Ω_1 remains unchanged and Ω_2 is replaced by a source-free region. This is made possible by the introduction of equivalent currents $(\boldsymbol{J}^\mathrm{eq}_\mathrm{es1},\boldsymbol{J}^\mathrm{eq}_\mathrm{ms1})$ on the surface separating both domains. They are given by

$$\boldsymbol{J}^\mathrm{eq}_\mathrm{es1} = \hat{\boldsymbol{n}}_{2\to1} \times \boldsymbol{H}, \tag{5.2}$$

and

$$\boldsymbol{J}^\mathrm{eq}_\mathrm{ms1} = -\hat{\boldsymbol{n}}_{2\to1} \times \boldsymbol{E}, \tag{5.3}$$

with $\hat{\boldsymbol{n}}_{2\to1}$ the normal coming out of Ω_1, as shown in Figure 5.2c. The characteristics of the domain Ω_2 can be freely modified.

- In the subproblem 2, Ω_2 remains unchanged and Ω_1 can be freely modified. For example is can be replaced by a source-free region, field-free region (Love formalism [119]), as shown in Figure 5.2d. This time, the equivalent currents introduced are given by

$$\boldsymbol{J}^{\text{eq}}_{\text{es2}} = \hat{\boldsymbol{n}}_{1\to2} \times \boldsymbol{H} = -\boldsymbol{J}^{\text{eq}}_{\text{es1}}, \tag{5.4}$$

and

$$\boldsymbol{J}^{\text{eq}}_{\text{ms2}} = -\hat{\boldsymbol{n}}_{1\to2} \times \boldsymbol{E} = -\boldsymbol{J}^{\text{eq}}_{\text{ms1}}. \tag{5.5}$$

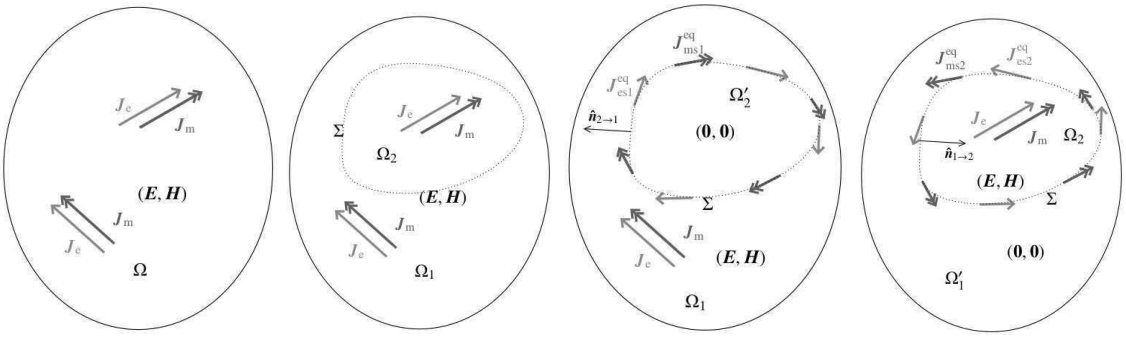

(a) Initial situation (b) Cutting of Ω (c) Subproblem 1 (d) Subproblem 2

Figure 5.2: Equivalence principle-Equivalent currents [118]

5.3.3 Feeding the antenna or the probe: wave generator

By definition, an antenna is a transition from a wave propagating in a waveguide to a radiation in free space [5]. This subsection aims to define the way the antenna or the probe are fed for the case studied in the chapter.

The antenna is fed from a port, which, in this PhD, is considered to be a waveguide. Sources are noted $\boldsymbol{j}^+_{\text{e}}$, $\boldsymbol{j}^+_{\text{m}}$. These currents are normalised in order to induce a wave amplitude of 1 $W^{\frac{1}{2}}$ They radiate a single mode of this waveguide, through the surface of the port S, as shown in Figure 5.3, which is very common in the domain of antennas. This mode is propagating toward the antenna ($+z$) and is described by its transverse fields $\boldsymbol{h}^+_{\text{t}}$, $\boldsymbol{e}^+_{\text{t}}$.

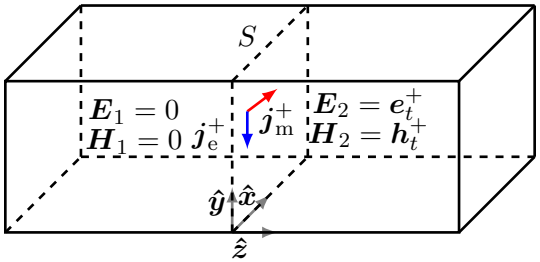

Figure 5.3: Ideal and unitary plus wave generator

To do so, the sources are defined by

$$\boldsymbol{j}^+_{\text{e}} = \hat{\boldsymbol{n}}_{1\to2} \times (\boldsymbol{H}_1 - \boldsymbol{H}_2) = \hat{\boldsymbol{z}} \times (\boldsymbol{h}^+_{\text{t}} - 0) = \hat{\boldsymbol{z}} \times \boldsymbol{h}^+_{\text{t}}, \tag{5.6}$$

This document may not be reproduced, modified, adapted, published, translated in any way, in whole or in part, nor disclosed to a third party without the prior written consent of ENAC. © 2023, ENAC

$$\boldsymbol{j}_{\mathrm{m}}^{+} = -\hat{\boldsymbol{n}}_{1\to 2} \times (\boldsymbol{E}_1 - \boldsymbol{E}_2) = -\hat{\boldsymbol{z}} \times (\boldsymbol{e}_{\mathrm{t}}^{+} - 0) = -\hat{\boldsymbol{z}} \times \boldsymbol{e}_{\mathrm{t}}^{+}, \tag{5.7}$$

with $\hat{\boldsymbol{n}}_{1\to 2}$ the vector normal to the surface S on which the sources are applied, $\boldsymbol{H}_1$, $\boldsymbol{H}_2$, $\boldsymbol{E}_1$, $\boldsymbol{E}_2$, are the magnetic and electric fields created by the sources, from either side of S, as shown in Figure 5.3, respectively.

5.3.4 Equivalence principle in free space

The equivalence principle is now applied to an antenna surrounded by free space. The antenna is fed with surface sources $\boldsymbol{j}_{\mathrm{e}}^{+}$, $\boldsymbol{j}_{\mathrm{m}}^{+}$ and is radiating a field ($\boldsymbol{E}$,$\boldsymbol{H}$). In this situation, we have $\Omega = \mathbb{R}^3$.

According to the equivalence principle, Ω can be splitted in two subdomains: Ω_1^{free} is delimited by a sphere $\mathcal{S}_r^2$ of radius r that contains the AUT and the sources, Ω_2^{free} is the free space surrounding Ω_1^{free}. An equivalent situation exists, where Ω_1^{free} is free space, the sources and the fields inside are zero, with equivalent currents, $\boldsymbol{J}_{\mathrm{es}}^{\mathrm{eq,\ free}}$, $\boldsymbol{J}_{\mathrm{ms}}^{\mathrm{eq,\ free}}$ on $\mathcal{S}_r^2$. The domain Ω_2^{free} remains unchanged, as shown in Figure 5.4.

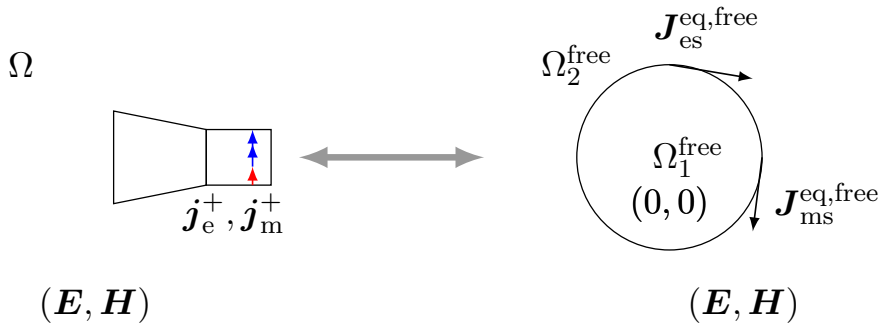

Figure 5.4: Equivalence principle applied on an antenna radiating in free space

5.3.5 Equivalence principle in the measurement environment

This principle is applied in the measurement environment. In this situation $\Omega = \mathbb{R}^3$ with the measurement room and the antenna and the probe inside. Let's suppose that the room is isolated enough to consider that this is surrounded by free space. The difference with the free space case of Section 5.3.4 is that the environment is composed of the probe and of the elements of the room. Thus the definition of $\Omega_1^{\mathrm{meas}} = \Omega_1^{\mathrm{free}}$ but Ω_2^{meas} becomes the entire room with the probe and the free space around. The equivalence principle is applied, yielding $\boldsymbol{J}_{\mathrm{es}}^{\mathrm{eq,meas}}$, $\boldsymbol{J}_{\mathrm{ms}}^{\mathrm{eq,meas}}$, equivalent currents on the surface of Ω_1^{meas}, as shown in Figure 5.5. The field $(\boldsymbol{E}, \boldsymbol{H})$ is unchanged in Ω_2^{meas}.

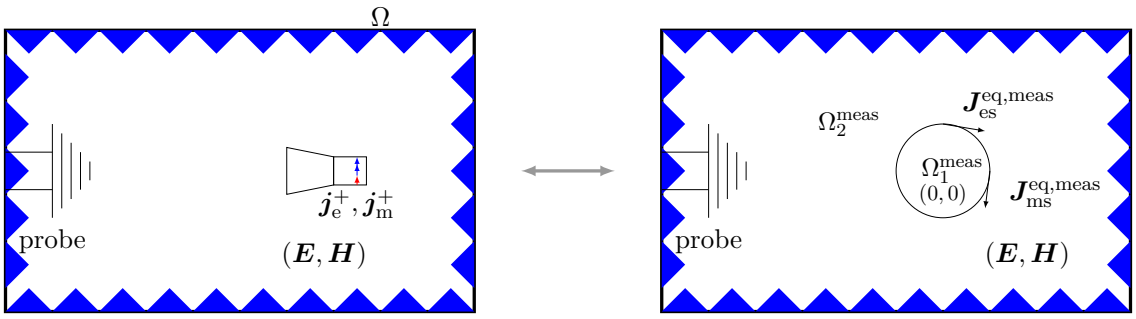

Figure 5.5: Equivalence principle applied on an antenna radiating in a measurement environment

5.3.6 Comparison of both cases

This section is a discussion on the impact of the environment and the probe on the equivalent currents $\boldsymbol{J}_{\mathrm{es}}^{\mathrm{eq,meas}}, \boldsymbol{J}_{\mathrm{ms}}^{\mathrm{eq,meas}}$ of Section 5.3.5, compared to the equivalent currents of the free space case, $\boldsymbol{J}_{\mathrm{es}}^{\mathrm{eq,free}}, \boldsymbol{J}_{\mathrm{ms}}^{\mathrm{eq,free}}$ of Section 5.3.4. Indeed, in addition to the direct path between the antenna and the probe, the environment will induce multipath and coupling.

In the case where the antenna is radiating and the probe receiving, different paths must be considered:

- from the AUT to the probe,
- from the AUT, to an element of the environment, to the probe,
- from the AUT, to the probe, to an element of the environment, to the probe,
- from the AUT, to an element of the environment, to the AUT, to the probe,
- from the AUT to the probe, to the AUT, to the probe.

Higher-orders paths could be considered too. For the first three cases, the probe and the environment will not play a role in the value of $\boldsymbol{J}_{\mathrm{es}}^{\mathrm{eq,meas}}, \boldsymbol{J}_{\mathrm{ms}}^{\mathrm{eq,meas}}$. If only these interactions exist, this means that $\boldsymbol{J}_{\mathrm{es}}^{\mathrm{eq,meas}} = \boldsymbol{J}_{\mathrm{es}}^{\mathrm{eq,free}}$ and $\boldsymbol{J}_{\mathrm{ms}}^{\mathrm{eq,meas}} = \boldsymbol{J}_{\mathrm{ms}}^{\mathrm{eq,free}}$. In contrast, for the 2 last ones, the probe and the environment may modify $\boldsymbol{J}_{\mathrm{es}}^{\mathrm{eq,meas}}, \boldsymbol{J}_{\mathrm{ms}}^{\mathrm{eq,meas}}$, which implies that $\boldsymbol{J}_{\mathrm{es}}^{\mathrm{eq,meas}}, \boldsymbol{J}_{\mathrm{ms}}^{\mathrm{eq,meas}}$ may not be the same as in free space.

In this chapter, we decide to make the hypothesis that the environment has a neglectable effect on the AUT equivalent currents. This will be validated by means of simulations in Section 5.6. From now on, the difference between the equivalent currents $\boldsymbol{J}_{\mathrm{es}}^{\mathrm{eq,meas}}, \boldsymbol{J}_{\mathrm{ms}}^{\mathrm{eq,meas}}$ and $\boldsymbol{J}_{\mathrm{es}}^{\mathrm{eq,free}}, \boldsymbol{J}_{\mathrm{ms}}^{\mathrm{eq,free}}$ is neglected and they are noted $(\boldsymbol{J}_{\mathrm{es}}^{\mathrm{eq}}, \boldsymbol{J}_{\mathrm{ms}}^{\mathrm{eq}})$ on $\mathcal{S}_r^2$.

5.3.7 Conclusion

This section has shown how the antenna can be substituted by equivalent currents on a surface surrounding the antenna, under some assumptions that have been detailed. The measurement is supposed to provide the signal radiated by the antenna on the sphere, by means of methods using the equivalent currents. This is a first step to simplify the problem and the calculations. The next section explains how this can be combined with the reciprocity theorem to formulate the antenna measurement problem.

This document may not be reproduced, modified, adapted, published, translated in any way, in whole or in part, nor disclosed to a third party without the prior written consent of ENAC. © 2023, ENAC

5.4 Reciprocity and antenna measurements

5.4.1 Introduction

Let us consider a measurement situation, the AUT and the probe are in an anechoic room, they both can radiate or receive signals. The objective of this section is to define the measured signal b in a fixed configuration. Section 5.4.2 is a reminder of the Lorentz reciprocity theorem, then two cases will be considered in Sections 5.4.3 and 5.4.4 : when the antenna is a source and when it is substituted by its equivalent currents. Finally, the formulation of the measured signal is given in Section 5.4.5, by combining both cases.

5.4.2 Lorentz reciprocity theorem

There are several forms of reciprocity theorems for electromagnetic field problems. The Lorentz reciprocity theorem will be used here with its corollary: the Rumsay theorem.

Let us consider a domain Ω composed of linear and isotropic medium, subject to two distinct and independent excitation states [3]:

- State (A) is corresponding to the sources $\boldsymbol{J}_{\mathrm{e}}^{(A)}$, $\boldsymbol{J}_{\mathrm{m}}^{(A)}$, yielding the fields $\boldsymbol{E}^{(A)}$, $\boldsymbol{H}^{(A)}$
- State (B) is corresponding to the sources $\boldsymbol{J}_{\mathrm{e}}^{(B)}$, $\boldsymbol{J}_{\mathrm{m}}^{(B)}$, yielding the fields $\boldsymbol{E}^{(B)}$, $\boldsymbol{H}^{(B)}$

The Lorentz reciprocity theorem states that the reaction of the fields A on the sources B and the reaction of the fields B on the sources A are related by

$$R_{B,A} - R_{A,B} = \oiint_{\partial\Omega} (\boldsymbol{E}^{(A)} \times \boldsymbol{H}^{(B)} - \boldsymbol{E}^{(B)} \times \boldsymbol{H}^{(A)}) \cdot d\Omega, \tag{5.8}$$

with the reaction of the fields A on the sources B defined by

$$R_{A,B} = \iiint_{\Omega} (\boldsymbol{E}^{(A)} \cdot \boldsymbol{J}_{\mathrm{e}}^{(B)} - \boldsymbol{H}^{(A)} \cdot \boldsymbol{J}_{\mathrm{m}}^{(B)}) d\Omega, \tag{5.9}$$

and the reaction of the fields B on the sources A by

$$R_{B,A} = \iiint_{\Omega} (\boldsymbol{E}^{(B)} \cdot \boldsymbol{J}_{\mathrm{e}}^{(A)} - \boldsymbol{H}^{(B)} \cdot \boldsymbol{J}_{\mathrm{m}}^{(\mathrm{A})}) d\Omega. \tag{5.10}$$

Moreover, a corollary of the reciprocity theorem, the Rumsey reaction theorem [3] states that

$$R_{A,B} = R_{B,A}, \tag{5.11}$$

when the contour integral is zero. This is the case for antenna measurement, if we consider that $\Omega = \mathbb{R}^3$. This can be demonstrated using the far-field conditions and considering that $\partial\Omega$ is a sphere of infinite radius [119]. This theorem will be applied to two cases in the following sections.

5.4.3 Reciprocity theorem applied to the antenna ports

The reciprocity theorem is now applied to the case of the antenna measurement in the measurement domain $\Omega = \mathbb{R}^3$, composed of linear and isotropic medium. Two excitation states are defined and illustrated in Figure 5.6:

- State (A): the AUT is excited by the sources $\boldsymbol{j}_{\mathrm{e}}^{+}$, $\boldsymbol{j}_{\mathrm{m}}^{+}$ that propagates from the port in a waveguide, yielding the fields $\boldsymbol{E}$, $\boldsymbol{H}$. These fields yield b at the output of the probe.
- State (B): the probe is fed through its port by the sources $\boldsymbol{j}_{\mathrm{e}}^{(\mathrm{pb})+}$, $\boldsymbol{j}_{\mathrm{m}}^{(\mathrm{pb})+}$, yielding the fields $\boldsymbol{E}^{(\mathrm{pb})}$, $\boldsymbol{H}^{(\mathrm{pb})}$.

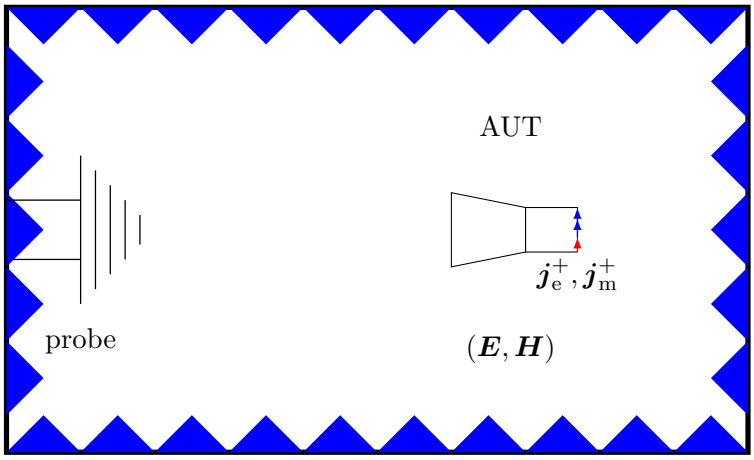

(a) State A, the antenna is radiating

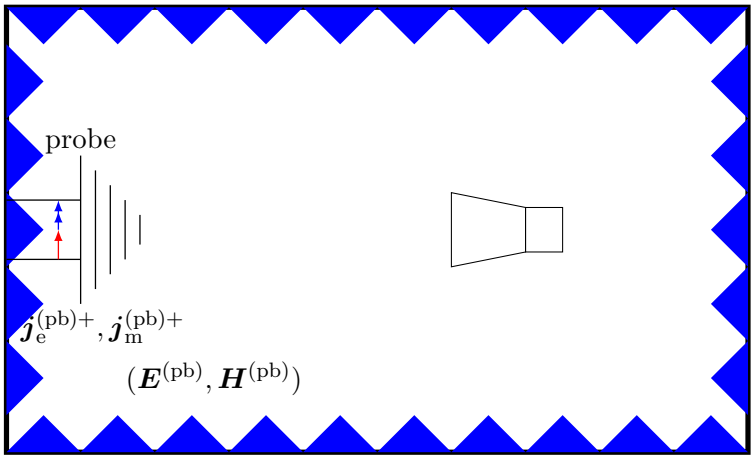

(b) State B, the probe is radiating

Figure 5.6: Configurations for the two considered states, with the AUT

According to the reciprocity theorem, the reaction of state (A) on state (B) is given by

$$R_{A,B} = \iiint_{\Omega} (\boldsymbol{E} \cdot \boldsymbol{j}_{\mathrm{e}}^{(\mathrm{pb})+} - \boldsymbol{H} \cdot \boldsymbol{j}_{\mathrm{m}}^{(\mathrm{pb})+}) d\Omega. \tag{5.12}$$

For the reaction of state (B) on state (A), $R_{B,A}$ is given by

$$R_{B,A} = \iint_{S} (\boldsymbol{E}^{(\mathrm{pb})} \cdot \boldsymbol{j}_{\mathrm{e}}^{+} - \boldsymbol{H}^{(\mathrm{pb})} \cdot \boldsymbol{j}_{\mathrm{m}}^{+}) dS = \iint_{S} (\boldsymbol{E}^{(\mathrm{pb})} \cdot (\hat{\boldsymbol{z}} \times \boldsymbol{h}_{\mathrm{t}}^{+}) - \boldsymbol{H}^{(\mathrm{pb})} \cdot (\hat{\boldsymbol{z}} \times \boldsymbol{e}_{\mathrm{t}}^{+})) dS, \tag{5.13}$$

with the integration directly done on S, the surface of the port of the antenna, since $\boldsymbol{j}_{\mathrm{e}}^{+}$, $\boldsymbol{j}_{\mathrm{m}}^{+}$ are zero everywhere else. This is possible to demonstrate that in this case $R_{B,A}$ corresponds to a received wave amplitude [118], i.e. the measured signal b, on the antenna port. Consequently, this gives

$$R_{B,A} = -2b, \tag{5.14}$$

This document may not be reproduced, modified, adapted, published, translated in any way, in whole or in part, nor disclosed to a third party without the prior written consent of ENAC. © 2023, ENAC

when the probe is transmitting. Finally, since our entire domain is reciprocal, we have

$$R_{B,A} = R_{A,B} = -2b. \tag{5.15}$$

To conclude, b can be defined both by the measured signal by the probe when the AUT is transmitting, and as the measured signal by the AUT when the probe is transmitting.

5.4.4 Reciprocity theorem applied to the equivalent currents of the antenna

The reciprocity theorem is now applied to the case where the equivalent currents replace the AUT, as defined in section 5.5. The measurement domain (composed of linear and isotropic medium), is subject to two distinct and independent excitation states [3] and illustrated in Figure 5.7:

- State (A): the equivalent currents of the AUT $\boldsymbol{J}_{\text{es}}^{\text{eq}}$, $\boldsymbol{J}_{\text{ms}}^{\text{eq}}$ are yielding the fields $\boldsymbol{E}$, $\boldsymbol{H}$.
- State (B): the probe is fed by a mode on its port and is radiating the sources $\boldsymbol{j}_{\text{e}}^{(\text{pb})+}$, $\boldsymbol{j}_{\text{m}}^{(\text{pb})+}$, yielding the fields $\boldsymbol{E}^{\text{inc}}$, $\boldsymbol{H}^{\text{inc}}$. This corresponds to the field radiated by the probe in the environment, nearby the AUT, in absence of the AUT.

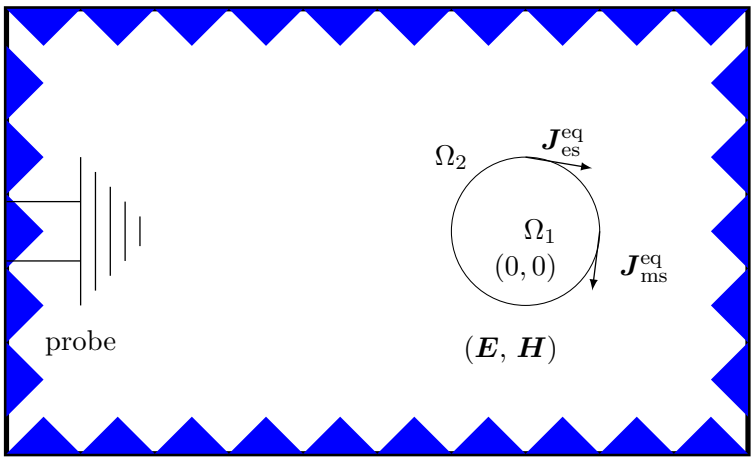

(a) State A, the antenna is radiating

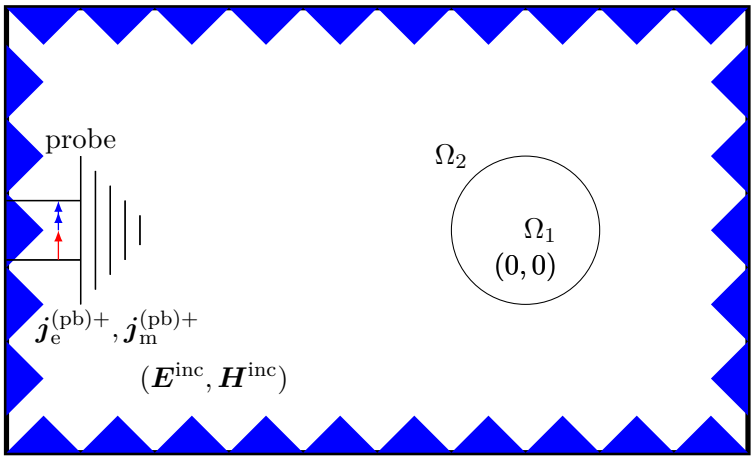

(b) State B, the probe is radiating

Figure 5.7: Configurations for the two considered states, with the AUT equivalent currents.

Then the reciprocity theorem states that

$$R^{\text{eq}}_{A,B} = \iiint_{\Omega} (\boldsymbol{E} \cdot \boldsymbol{j}^{(\text{pb})+}_{\text{e}} - \boldsymbol{H} \cdot \boldsymbol{j}^{(\text{pb})+}_{\text{m}}) d\Omega, \tag{5.16}$$

and

$$R^{\text{eq}}_{B,A} = \iiint_{\Omega} (\boldsymbol{E}^{\text{inc}} \cdot \boldsymbol{J}^{\text{eq}}_{\text{es}} - \boldsymbol{H}^{\text{inc}} \cdot \boldsymbol{J}^{\text{eq}}_{\text{ms}}) d\Omega. \tag{5.17}$$

We can also remark that our entire domain is reciprocal so $R^{\text{eq}}_{B,A} = R^{\text{eq}}_{A,B}$.

5.4.5 Link between both applications of the reciprocity theorem

We notice that (5.16) is identical to (5.12), which leads to

$$R^{\text{eq}}_{B,A} = R^{\text{eq}}_{A,B} = R_{A,B} = R_{B,A} = -2b, \tag{5.18}$$

according to (5.15). Here, the probe is transmitting and the AUT is receiving. This yields the conclusion that the measured signal b can be computed from the equivalent currents of the antenna and the incident field on the sphere surrounding the antenna, giving

$$b = -\frac{1}{2} \iint_{\mathcal{S}^2_r} (\boldsymbol{E}^{\text{inc}} \cdot \boldsymbol{J}^{\text{eq}}_{\text{es}} - \boldsymbol{H}^{\text{inc}} \cdot \boldsymbol{J}^{\text{eq}}_{\text{ms}}) dS_r, \tag{5.19}$$

with $\boldsymbol{E}^{\text{inc}}, \boldsymbol{H}^{\text{inc}}$ the radiations of the probe in absence of the AUT.

5.4.6 Conclusion

The formulation of the measurement has finally been obtained under the form of a reaction on the sphere. This reaction is composed of the component of the incident field and of the equivalent currents of the AUT on the sphere surrounding the antenna.
The next step is to demonstrate that the measurement is a convolution between the incident field coming from the probe and the equivalent currents of the AUT by introducing the rotation performed during the measurement.

5.5 Convolution and spin formulation

5.5.1 Introduction

We consider the case of a measurement configuration where the antenna can execute any rotation. The objective of section 5.5.2 is to show that b, the measured signal on the port of the antenna is a convolution on the sphere $\mathcal{S}^2_r$ between $\boldsymbol{E}^{\text{inc}}, \boldsymbol{H}^{\text{inc}}$ and $\boldsymbol{J}^{\text{eq}}_{\text{es}}, \boldsymbol{J}^{\text{eq}}_{\text{ms}}$. Then, section 5.5.3 presents the derivation of the measurement formulation in terms of spin.

5.5.2 Application of the rotation to the electric fields

$\boldsymbol{E}^{\text{inc}}, \boldsymbol{H}^{\text{inc}}, \boldsymbol{J}^{\text{eq}}_{\text{es}}, \boldsymbol{J}^{\text{eq}}_{\text{ms}}$ are functions of $\theta \in [0, \pi]$ and $\phi \in [0, 2\pi]$, the spherical coordinates.

This document may not be reproduced, modified, adapted, published, translated in any way, in whole or in part, nor disclosed to a third party without the prior written consent of ENAC. © 2023, ENAC

A convolution on a spherical geometry is defined as the integral of the product of the two functions after one is reversed and rotated. Consequently, one signal has to be reversed so the function $\boldsymbol{J}_{\text{es}}^{\text{eq}\prime}(-\theta,-\phi) = \boldsymbol{J}_{\text{es}}^{\text{eq}}(\theta,\phi)$ are defined in order to give, from (5.19),

$$b = -\frac{1}{2}\iint_{\mathcal{S}_r^2}(\boldsymbol{E}^{\text{inc}}(\theta,\phi)\cdot\boldsymbol{J}_{\text{es}}^{\text{eq}\prime}(-\theta,-\phi) - \boldsymbol{H}^{\text{inc}}(\theta,\phi)\cdot\boldsymbol{J}_{\text{ms}}^{\text{eq}\,\prime}(-\theta,-\phi))dS_r. \tag{5.20}$$

Then the rotation of the AUT is accomplished with the rotation operator $\mathcal{R}_\epsilon$, as defined in Chapter 1, on the equivalent currents. The measurement becomes

$$b(\epsilon) = -\frac{1}{2}\iint_{\mathcal{S}_r^2}(\boldsymbol{E}^{\text{inc}}(\theta,\phi)\cdot(\mathcal{R}_\epsilon\boldsymbol{J}_{\text{es}}^{\text{eq}\prime})(-\theta,-\phi) - \boldsymbol{H}^{\text{inc}}(\theta,\phi)\cdot(\mathcal{R}_\epsilon\boldsymbol{J}_{\text{ms}}^{\text{eq}\,\prime})(-\theta,-\phi))dS_r, \tag{5.21}$$

with ϵ the Euler angles. For obvious physical reasons, the total power obtained by summing the power for all possible AUT orientations ϵ must remain finite. Thus, b is a scalar signal of finite power, containing the measured signal, depending on the orientation of the antenna. Consequently, $b \in L^2(\text{SO}(3))$ the space of square integrable functions on the rotation group.

From (5.21), it is clear that the measurement b has been characterized by a convolution, which corresponds to

$$b = (\boldsymbol{E}^{\text{inc}}, \boldsymbol{H}^{\text{inc}}) \circledast (\boldsymbol{J}_{\text{es}}^{\text{eq}\prime}, \boldsymbol{J}_{\text{ms}}^{\text{eq}\,\prime}), \tag{5.22}$$

with $\circledast$ the operator of the convolution on the sphere.

5.5.3 Spin expression of the measured signal

In Chapter 3, tangent vectors have been expressed on the sphere in terms of components of spin ± 1. The objective of this section is to introduce the spin parameter in the measurement formulation, in particular because the spin facilitates the expression of the rotation operator.

Firstly, from (5.2) and (5.3), the equivalent currents are related to the fields radiated by the AUT by

$$\boldsymbol{J}_{\text{es}}^{\text{eq}}(\theta,\phi) = \hat{\boldsymbol{r}}\times\boldsymbol{H}(\theta,\phi), \qquad \boldsymbol{J}_{\text{ms}}^{\text{eq}}(\theta,\phi) = -\hat{\boldsymbol{r}}\times\boldsymbol{E}(\theta,\phi), \tag{5.23}$$

which means that (5.21) becomes

$$b(\epsilon) = -\frac{1}{2}\iint_{\mathcal{S}_r^2}\boldsymbol{E}^{\text{inc}}(\theta,\phi)\cdot(\hat{\boldsymbol{r}}\times\mathcal{R}_\epsilon(\boldsymbol{H}(\theta,\phi))) - \boldsymbol{H}^{\text{inc}}(\theta,\phi)\cdot(-\hat{\boldsymbol{r}}\times\mathcal{R}_\epsilon(\boldsymbol{E}(\theta,\phi)))dS_r. \tag{5.24}$$

With the properties of the mixed product, (5.24) becomes

$$b(\epsilon) = -\frac{1}{2}\iint_{\mathcal{S}_r^2}\hat{\boldsymbol{r}}\cdot(\mathcal{R}_\epsilon(\boldsymbol{H}(\theta,\phi))\times\boldsymbol{E}^{\text{inc}}(\theta,\phi)) + \hat{\boldsymbol{r}}\cdot(\mathcal{R}_\epsilon(\boldsymbol{E}(\theta,\phi))\times\boldsymbol{H}^{\text{inc}}(\theta,\phi))dS_r. \tag{5.25}$$

For the sake of clarity, we only develop the left term of the integral. The calculations are similar for the right term.

Firstly, from (3.9) and (3.17) the vectors are expanded in terms of spin which gives

$$\begin{aligned}
&\mathcal{R}_\epsilon(\boldsymbol{H}(\theta,\phi)) \times \boldsymbol{E}^{\text{inc}}(\theta,\phi) \\
&= \mathcal{R}_\epsilon(\boldsymbol{H}_{+1}(\theta,\phi)\hat{\boldsymbol{u}}_{+1} + \boldsymbol{H}_{-1}(\theta,\phi)\hat{\boldsymbol{u}}_{-1}) \times (\boldsymbol{E}^{\text{inc}}_{+1}(\theta,\phi)\hat{\boldsymbol{u}}_{+1} + \boldsymbol{E}^{\text{inc}}_{-1}(\theta,\phi)\hat{\boldsymbol{u}}_{-1}) \\
&= (e^{-i\chi_g} H_{+1}(\theta',\phi')\hat{\boldsymbol{u}}_{+1} + e^{i\chi_g} H_{-1}(\theta',\phi')\hat{\boldsymbol{u}}_{-1}) \times (\boldsymbol{E}^{\text{inc}}_{+1}(\theta,\phi)\hat{\boldsymbol{u}}_{+1} + \boldsymbol{E}^{\text{inc}}_{-1}(\theta,\phi)\hat{\boldsymbol{u}}_{-1}),
\end{aligned} \tag{5.26}$$

with (θ',ϕ') the position of the AUT's field on the sphere after the rotation.

Then from (3.10), we notice that

$$\begin{aligned}
\hat{\boldsymbol{u}}_{+1} \times \hat{\boldsymbol{u}}_{+1} &= 0, \\
\hat{\boldsymbol{u}}_{-1} \times \hat{\boldsymbol{u}}_{-1} &= 0, \\
\hat{\boldsymbol{u}}_{+1} \times \hat{\boldsymbol{u}}_{-1} &= i\hat{\boldsymbol{r}}, \\
\hat{\boldsymbol{u}}_{-1} \times \hat{\boldsymbol{u}}_{+1} &= -i\hat{\boldsymbol{r}}.
\end{aligned} \tag{5.27}$$

Consequently, once the vector products are simplified, (5.26) becomes

$$\mathcal{R}_\epsilon(\boldsymbol{H}(\theta,\phi)) \times \boldsymbol{E}^{\text{inc}}(\theta,\phi) = (e^{-i\chi_g} H_{+1}(\theta',\phi')E^{\text{inc}}_{-1} - e^{i\chi_g} H_{-1}(\theta',\phi')E^{\text{inc}}_{1})i\hat{\boldsymbol{r}}. \tag{5.28}$$

Finally, the measured signal can be expressed as

$$\begin{aligned}
b(\epsilon) = -\frac{i}{2} \iint_{\mathcal{S}^2_r} & e^{-i\chi_g} H_{+1}(\theta',\phi')E^{\text{inc}}_{-1}(\theta,\phi) - e^{i\chi_g} H_{-1}(\theta',\phi')E^{\text{inc}}_{+1}(\theta,\phi) \\
& + e^{-i\chi_g} E_{+1}(\theta',\phi')H^{\text{inc}}_{-1}(\theta,\phi) - e^{i\chi_g} E_{-1}(\theta',\phi')H^{\text{inc}}_{+1}(\theta,\phi))dS_r.
\end{aligned} \tag{5.29}$$

Thus, the spin convention provides a ready-to-use formulation of the rotation of the AUT during the measurement.

5.5.4 Conclusion

This section has demonstrated that the rotations performed during a measurement can lead to the modeling of the measurement as a convolution of the fields and the equivalent currents on the sphere. Finally, the measurement formulation has also been written in terms of the $\pm$ 1 spin components of the fields.

5.6 Validation

5.6.1 Introduction

This section constitutes the validation of the hypothesis we have made in Section 5.3.6: the environment has a neglectable effect on the AUT equivalent currents. The objective is to show that the antenna can be replaced by its free space equivalent currents, i.e. that its physical presence does not impact the measurement. This will validate the measurement formulation derived in this chapter. Firstly in Section 5.6.2 the principle of the validation is presented, then in Section 5.6.3 the parameters chosen for the simulations are detailled and finally in Section 5.6.4, the results of the simulations are displayed.

This document may not be reproduced, modified, adapted, published, translated in any way, in whole or in part, nor disclosed to a third party without the prior written consent of ENAC. © 2023, ENAC

5.6.2 Principle of the validation

The considered situation is as follows:

- The AUT is transmitting, can rotate and is centered at the origin of the reference frame O.
- The probe is an ideal electric probe which output is one component of the electric field situated at a distance d along the z axis.

In order to test our hypothesis, the output of the probe is simulated for the three following situations:

- The complete AUT alone.
- The complete AUT in presence of a perturbation.
- The free space equivalent current in presence of a perturbation.

The objective is to prove that the complete AUT and the free space equivalent currents produce the same output on the probe even when the perturbation has a significant effet.

5.6.3 Configuration

The simulations are run with Altair Feko, for a frequency $f = 1.575$ GHz. The antenna chosen for this validation is a patch antenna of dimension 5.98 cm $\times$ 8.85 cm, with a substrate of dimension 15.95 cm $\times$ 10.76 cm $\times$ 0.56 cm and of relative permittivity of 2.15. Its equivalent currents are computed on a sphere $\mathcal{S}_r^2$ of radius $r = 12$ cm.
The perturbation is a plate of size 1 m $\times$ 1 m of thickness 3 cm that is either metallic or dielectric of relative permittivity 3. At normal incidence, the dielectric plate has a reflexion coefficient of order -10 dB. Its position obviously has an effect on the intensity of the perturbation, this is why we chose run the simulations for two positions of the plate.

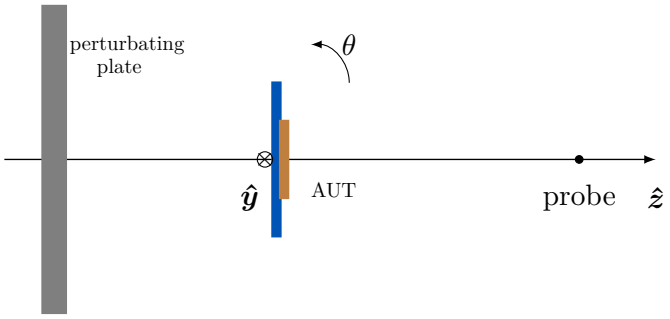

(a) Configuration with the antenna

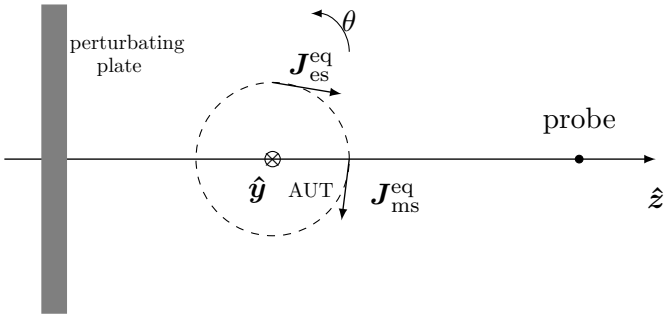

(b) Configuration with the antenna replaced by its equivalent currents

Figure 5.8: Sketch of the first configuration

In terms of positioning of the elements, the dimensions of the ENAC measurement range are used:

- In the first configuration, the probe is situated at 1.6 m from the antenna and the plate is 1 m behind the antenna. These configurations are represented in Figure 5.8, where the plate is represented as a grey box. This is the worst case for what we want to demonstrate because the AUT is on the path between the probe and the plate.
- In the second configuration, the plate is on the side, parallel to the $\hat{\boldsymbol{z}}$ axis. It is situated at an equivalent distance of the probe and the AUT, as represented in Figure 5.9.

This document may not be reproduced, modified, adapted, published, translated in any way, in whole or in part, nor disclosed to a third party without the prior written consent of ENAC. © 2023, ENAC

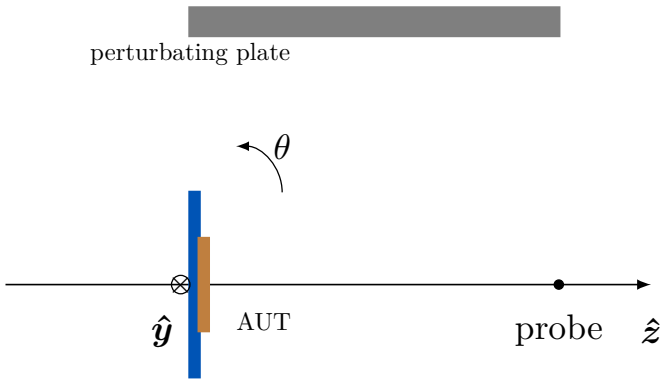

(a) Configuration with the antenna

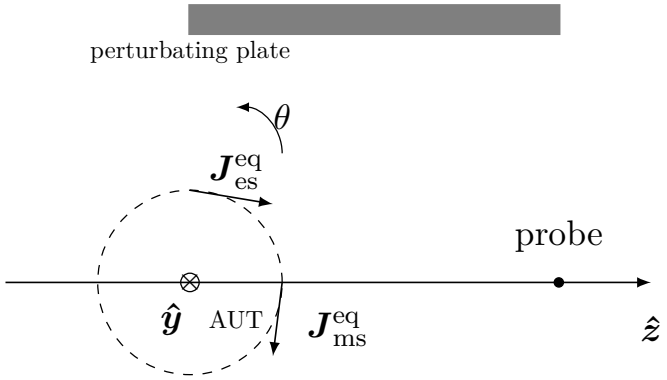

(b) Configuration with the antenna replaced by its equivalent currents

Figure 5.9: Sketch of the second configuration

5.6.4 Simulations and results

The objective of this section is to visualise the impact of the antenna physical presence in the measurement environment can be negligible. The measured signal, are displayed for the three situations mentioned in Section 5.6.2: the results of the configuration with the plate behind is shown in Figure 5.10 and the one with the plate on the side in Figure 5.11.

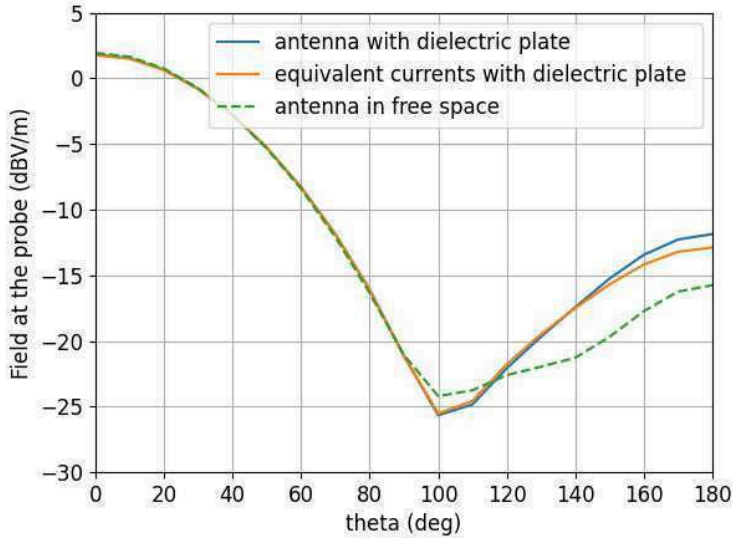

(a) Plate of dielectric

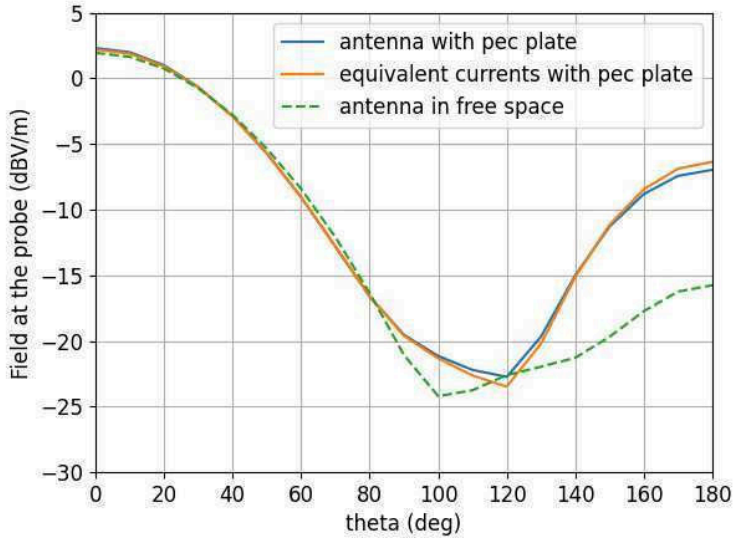

(b) Plate of metal

Figure 5.10: Field measured by the probe with a disturbing element behind the antenna

Firstly, in Figure 5.10, we can observe the effect of the plate, compared to the measured signals of the antenna in free space in green dotted points. Until $\theta = 90°$, the three curves are identical. Above 90°, this is visible that the probe measures also the reflection on the plate, as the measurements drifts from the measured signal of the antenna in free space. As expected, when we compare the orange and blue curves from Figures 5.10a and 5.11b, the metallic plate is more disturbing than the dielectric.

The objective being to show that we can replace the antenna by its equivalent currents, the orange and blue lines are compared. The two curves are very close, which confirms our hypothesis, except between 160° and 180°, where the antenna is facing the plate. This is consistent because the physical antenna is in the path of the reflection so this probably

This document may not be reproduced, modified, adapted, published, translated in any way, in whole or in part, nor disclosed to a third party without the prior written consent of ENAC. © 2023, ENAC

obstruates the reflection, whereas the equivalent currents do not. Additionaly, in the case of the metal plate, between 110° and 130°, the measurements differ slightly. However, this difference is of maximum 1 dB, widely under the impact of the plate. Moreover, such a large metallic plate that close to the AUT as being part of the environnement is not realistic. Yet differences in the radiation pattern are negligible for the most part or very small.

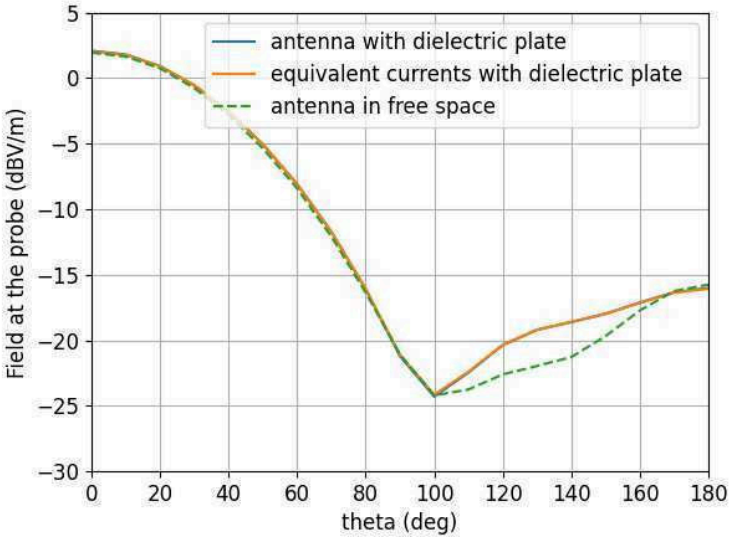

(a) Plate of dielectric

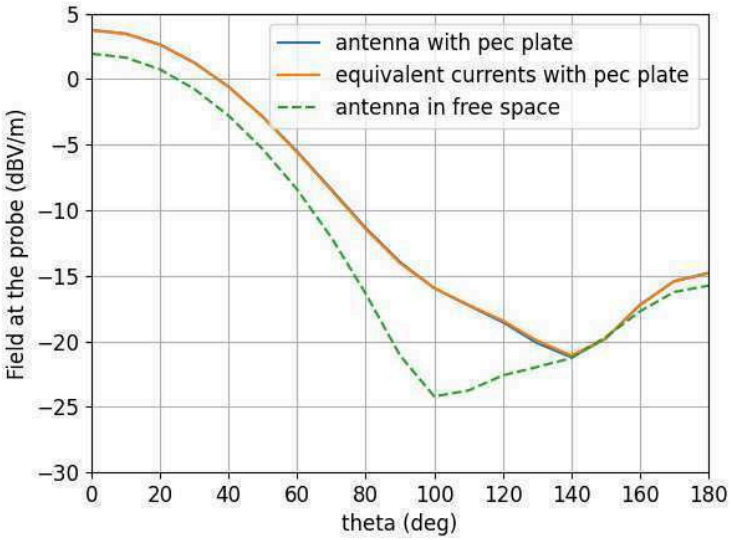

(b) Plate of metal

Figure 5.11: Field measured by the probe with a disturbing element on the side of the antenna

Finally, the results displayed in Figure 5.11 show that the field measured by the probe is identical whether the AUT is physically present or replaced by its free space equivalent

currents when the plate is on the side. Thus, we consider our hypothesis valid, the antenna radiation can be formulated with its free space equivalent currents.

5.6.5 Conclusion

This validation has shown that the effect of the physical presence of the AUT is negligible from the probe point of view. Consequently, the hypothesis made in Section 5.3.6 is valid and the AUT can be replaced by its equivalent currents.

5.7 Conclusion

This chapter has derived a formulation of the measurement problem as a convolution. Firstly the equivalence principle has led to a simplification of the problem, with the expression of the antenna radiation by its equivalent currents.

Secondly, the reciprocity theorem has allowed a formulation to relate the measured signal, the probe signal in the measurement environment and the radiation pattern of the antenna.

Then, we have demonstrated that the rotation of the antenna in the measurement environment can be formulated as a convolution between the radiation of the probe in the measurement environment and the AUT radiation pattern. This formulation has been developed explicitly in terms of spin afterwards.

Finally, the hypothesis according to which the AUT can be replaced by its free space equivalent currents has been tested by showing the little impact of multiple order reflections in a highly pessimistic and unrealistic measurement scenario in an anechoic chamber. This confirms the obtained measurement formulation.

From this formalism, deconvolution methods can be used to extract the actual antenna pattern from measurements.

This document may not be reproduced, modified, adapted, published, translated in any way, in whole or in part, nor disclosed to a third party without the prior written consent of ENAC. © 2023, ENAC

Chapter 6

Correction of Measurements in 2D

6.1 Introduction

Deconvolution methods exist in many domains of signal and image processing, for image deblurring, or correction of degradations in atmospheric observation [120], [121]. These methods mostly rely on the transform of the signals to the harmonic domain. The spectrum is then processed to extract the signal of interest, the radiation pattern of the antenna in this thesis. The main advantage of this method relies on the properties of the convolution that becomes a product in the spectral domain. Consequently many problems can be solved by a division [116]. However, specific methods are used since the deconvolution of a measured signal often yields an ill-conditioned problem [122]. Indeed the noise can be increased by this deconvolution, degrading the correction.

The objectives of this chapter are firstly to show that the measurement formula derived in Chapter 4 reduces to a classic deconvolution problem between 2π-periodic signals in 2D, and secondly to apply it to simulations of 2D measurements. The content of this chapter is not directly applicable to real measurements but is a first step towards a general 3D method.

Firstly, in Section 6.2, the convolution is developed for a 2D configuration. Then in Section 6.3 the deconvolution method chosen for antenna measurement correction, is presented. Finally, this method is put into practice in Section 6.4, on a simulation of measurement correction.

6.2 2D measurement formulation

6.2.1 Introduction

This section constitutes the formulation of the measurement problem in a 2D geometry, assuming an invariance along one axis. The aim is to simplify the problem. Indeed, the measurement signal on the sphere is in $L^2(\mathrm{SO}(3))$ as explained in Section 5.5.2, a brute force deconvolution would imply to make measurements with rotations along 3 axes which is time consuming. Alternatively, in 2D, the sphere becomes a circle and the signals are 1D and 2π-periodic.

This document may not be reproduced, modified, adapted, published, translated in any way, in whole or in part, nor disclosed to a third party without the prior written consent of ENAC. © 2023, ENAC

Firstly, the 2D configuration is described in Section 6.2.2. Next, the expression of the measurement signal is given in Section 6.2.3.

6.2.2 2D configuration

In order to simplify the problem, the measurement is formulated in a 2D configuration. We assume that there is an invariance along the $\hat{\boldsymbol{z}}$ axis. This implies that the problem can be splitted in two cases, considering either a transverse electric (TE) or transverse magnetic (TM) polarisation with respect to z.

From now on, we consider the TMz case as shown in Figure 6.1. Similar results could be obtained in the TEz case. In this case, $\boldsymbol{E}^{\text{inc}} = E^{\text{inc}}\hat{\boldsymbol{z}}$, $\boldsymbol{J}^{\text{eq}}_{\text{es}} = J^{\text{eq}}_{\text{es}}\hat{\boldsymbol{z}}$. Then $\boldsymbol{H}^{\text{inc}}$, $\boldsymbol{J}^{\text{eq}}_{\text{ms}}$ are in the xOy plane. The unit vector $\hat{\boldsymbol{r}}$ and the incident magnetic field $\boldsymbol{H}^{\text{inc}}$ are coplanar and orthogonal to $\boldsymbol{E}^{\text{inc}}$. In 2D, $\mathcal{S}^2_r$, as defined in Section 5.3.4, corresponds to the circle $\mathcal{C}$ of radius r surrounding the antenna and described by the angle $\phi \in [0, 2\pi]$. Besides, in this chapter $\mathcal{C}$ is assumed considered to be far enough from the AUT to be in its far field.

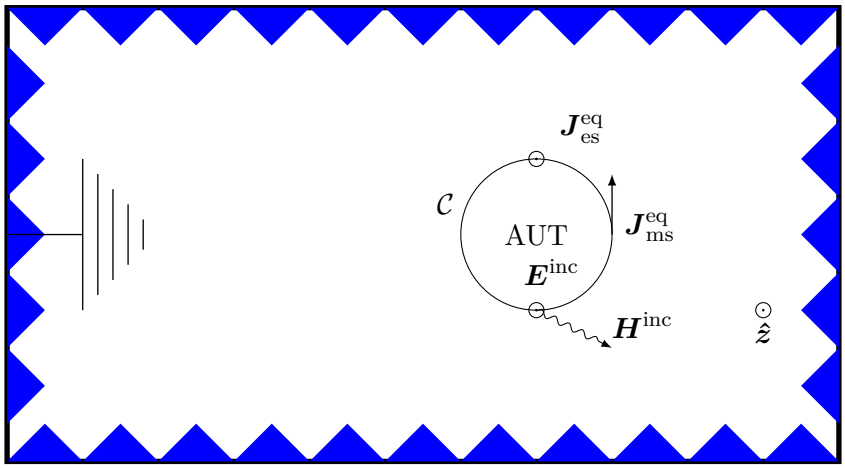

Figure 6.1: 2D configuration for transverse magnetic polarisation

In this configuration, electric and magnetic fields are linked by

$$\boldsymbol{E} = \zeta_0 \boldsymbol{H} \times \hat{\boldsymbol{r}} \tag{6.1}$$

and currents by

$$\boldsymbol{J}^{\text{eq}}_{\text{ms}} = \zeta_0 \hat{\boldsymbol{r}} \times \boldsymbol{J}^{\text{eq}}_{\text{es}}. \tag{6.2}$$

6.2.3 Derivation of the formulation

If the antenna rotates of an angle $\phi \in [0, 2\pi]$, according to (5.19), (5.20) and (5.21), the expression of the measurement becomes

$$b(\phi) = \int_0^{2\pi} (\boldsymbol{E}^{\text{inc}}(\phi') \cdot \boldsymbol{J}^{\text{eq}}_{\text{es}}(\phi' - \phi) - \boldsymbol{H}^{\text{inc}}(\phi') \cdot \boldsymbol{J}^{\text{eq}}_{\text{ms}}(\phi' - \phi)) r d\phi'. \tag{6.3}$$

Consequently, from (6.2) we end up with

$$\begin{aligned} b(\phi) &= \int_0^{2\pi} (\boldsymbol{E}^{\text{inc}}(\phi') \cdot \boldsymbol{J}_{\text{es}}^{\text{eq}}(\phi - \phi') - \boldsymbol{H}^{\text{inc}}(\phi') \cdot (\zeta_0 \boldsymbol{r} \times \boldsymbol{J}_{\text{es}}^{\text{eq}}(\phi - \phi')) r d\phi', \\ &= \int_0^{2\pi} (\boldsymbol{E}^{\text{inc}}(\phi) \cdot \boldsymbol{J}_{\text{es}}^{\text{eq}}(\phi - \phi') - \zeta_0 \boldsymbol{J}_{\text{es}}^{\text{eq}}(\phi - \phi') \cdot (\hat{\mathbf{r}} \times \boldsymbol{H}^{\text{inc}}(\phi')) r d\phi', \\ &= \int_0^{2\pi} (\boldsymbol{E}^{\text{inc}}(\phi') - \zeta_0 \boldsymbol{r} \times \boldsymbol{H}^{\text{inc}}(\phi')) \cdot \boldsymbol{J}_{\text{es}}^{\text{eq}}(\phi - \phi')) r d\phi'. \end{aligned} \tag{6.4}$$

For the sake of clarity, for the TMz configuration, we can denote

$$h(\phi) = (\boldsymbol{E}^{\text{inc}}(\phi) - \zeta_0 \boldsymbol{r} \times \boldsymbol{H}^{\text{inc}}(\phi)) \cdot \hat{\boldsymbol{z}}, \tag{6.5}$$

which corresponds to the formulation of the radiation of the probe in the environment nearby the antenna. This gives

$$b(\phi) = \int_0^{2\pi} h(\phi') J_{\text{es}}^{\text{eq}}(\phi - \phi') r d\phi'. \tag{6.6}$$

Finally, in TMz, the problem reduces to a convolution between two 2π-periodic signals. In the previous chapter, the measurement is formulated in (5.1) as $b(\epsilon) = h(\epsilon) \circledast p(\epsilon)$. Consequently, we are able to identify p as

$$p(\phi) = r J_{\text{es}}^{\text{eq}}(\phi). \tag{6.7}$$

6.2.4 Conclusion

This section has presented the derivation of the measurement formula in 2D, for the TMz case. This formulation is a convolution between 2-π periodic signals.

6.3 Deconvolution for antenna measurement correction

6.3.1 Introduction

The previous chapter section has demonstrated that the measurement problem can be formulated as some type of convolution between the AUT pattern and the probe radiation. In order to process the measurement data, analysis tools are required. The most common method is to use the spectral domain, through Fourier series for a 2D configuration or spherical harmonics for 3D configuration. Then deconvolution can be performed in order to obtain the radiation pattern of the AUT. However, deconvolution methods are generally ill-conditioned, meaning that this operation introduces error, by amplifying noise. The deconvolved signal needs to be regularised in order to diminish the effect of the noise. The Fourier-Based Regularized Deconvolution (FoRD) and Fourier-Wavelet Regularized Deconvolution (ForWaRD) method are regularisation methods based on the use of two types of transforms, the harmonic or Fourier transforms and the wavelet expansion [122].

This section details the process developed in this PhD thesis, to extract the radiation pattern of the AUT from the measurement signal. Firstly, in Section 6.3.2, the problem is

This document may not be reproduced, modified, adapted, published, translated in any way, in whole or in part, nor disclosed to a third party without the prior written consent of ENAC. © 2023, ENAC

formulated in terms of Fourier series. Then in Section 6.3.3, the convolution is presented as an ill-conditioned problem that needs regularisation, next the FoRward method is detailed in Section 6.3.4 and finally the complete correction process is described in Section 6.3.5.

6.3.2 Fourier series

The advantage of formulating the antenna measurements as a convolution is that this is equivalent in the Fourier domain to a multiplication. This section derives the Fourier expansion of each term of the measurement formula.

Firstly, the measurement signal $b(\phi)$ can be expressed by the Fourier series given by

$$b(\phi) = \sum_{n=-\infty}^{+\infty} \hat{b}_n e^{in\phi} \tag{6.8}$$

with $\hat{b}_n$ the Fourier coefficients defined by

$$\hat{b}_n = \frac{1}{2\pi} \int_0^{2\pi} b(\phi') e^{-in\phi'} d\phi'. \tag{6.9}$$

Similar expressions exist for h and p, with $\hat{h}_n$ and $\hat{p}_n$ their respective Fourier series coefficients. Their convolution is given by

$$h \circledast p = \int_0^{2\pi} p(\phi') h(\phi - \phi') d\phi'. \tag{6.10}$$

The Fourier transform of this convolution is given by

$$\begin{aligned}
\widehat{(h \circledast p)}_n &= \frac{1}{2\pi} \int_0^{2\pi} \left(\int_0^{2\pi} p(\phi') \cdot h(\phi - \phi') d\phi' \right) e^{-in\phi} d\phi \\
&= 2\pi \int_0^{2\pi} \frac{1}{2\pi} p(\phi') \left(\frac{1}{2\pi} \int_0^{2\pi} h(\phi - \phi') e^{-in\phi} d\phi \right) d\phi' \\
&= 2\pi \int_0^{2\pi} \frac{1}{2\pi} p(\phi') e^{-in\phi'} \left(\frac{1}{2\pi} \int_0^{2\pi} h(\phi - \phi') e^{-in(\phi - \phi')} d\phi \right) d\phi' \\
&= 2\pi \int_0^{2\pi} \frac{1}{2\pi} p(\phi') e^{-in\phi'} \hat{h}_n d\phi' \\
&= 2\pi \hat{p}_n \hat{h}_n.
\end{aligned} \tag{6.11}$$

From (5.1), we deduce that

$$\hat{b}_n = 2\pi \hat{h}_n \hat{p}_n. \tag{6.12}$$

Then b can be formulated by

$$b(\phi) = \sum_{n \text{ in } \mathbb{Z}} 2\pi \hat{h}_n \hat{p}_n e^{jn\phi}. \tag{6.13}$$

In the spectral domain, the formulation of the problem becomes a multiplication that depends on the radiation of the probe in the environment nearby the antenna and on the antenna pattern.

6.3.3 The convolution as an ill-conditioned problem

In the following, the harmonic domain is the Fourier series domain. In an ideal case, the measured signal b can be post-processed by a single division if the spectrum of h is known. Then the antenna signal can be computed by a single inversion and an inverse Fourier Series Transform, noted FS^{-1}, which is given by

$$p(\phi) = \frac{1}{2\pi} FS^{-1}\left(\frac{\hat{b}_n}{\hat{h}_n}\right). \tag{6.14}$$

However, this case is unrealistic, in every signal processing case a noise is present in the signal. At least numerical noise is present, thus taking into account the noise gives

$$\hat{b}_n = 2\pi \hat{p}_n \cdot \hat{h}_n + \hat{n}_{on}. \tag{6.15}$$

Thus the Fourier inversion becomes

$$\hat{p}_n = \begin{cases} \frac{1}{2\pi}\left(\frac{\hat{b}_n}{\hat{h}_n} - \frac{\hat{n}_{on}}{\hat{h}_n}\right) & \text{si } |h_n| > 0 \\ 0 & \text{otherwise.} \end{cases} \tag{6.16}$$

This yields an amplification of the noise Fourier coefficients when $\hat{h} \approx 0$. This effect is always present because the Fourier series coefficients of a signal tend to zero when n tends to $+\infty$. Thus, this amplification of the noise needs to be mitigated, by means of regularisation or thresholding methods.

6.3.4 Fourier-Wavelet Regularized Deconvolution method

6.3.4.1 Fourier shrinkage

To regularize the deconvolution, the estimate of the radiation pattern is defined as

$$\tilde{p}_f = \sum_{n=0}^{N-1} \hat{p}_n \xi_n^f e^{in\phi}, \tag{6.17}$$

with $\xi_n^f \in [0, 1]$ a regularisation term. Its value can be defined for each Fourier coefficients. If $\xi_n^f = 1$, the corresponding component of the spectrum is not attenuated and if $\xi_n^f = 0$, this component is shrinked. Consequently, this parameter has to be chosen wisely, in order to keep the relevant part of the signal while attenuating the noise amplification.

In [122] the value of ξ_n^f is defined by

$$\xi_n^f = \frac{|\hat{h}_n|^2}{|\hat{h}_n|^2 + \tau}, \text{with } \tau > 0. \tag{6.18}$$

We notice that $\xi_n^f \approx 1$ when $\hat{h}_n$ is large and $\lim_{\hat{h}_n \to 0} \xi_n^f = 0$. Consequently, the amplification of the noise is stopped when $\hat{h}_n$ tends to zero. Then, the estimate of $\hat{p}_n$, noted $\tilde{\hat{p}}_{nf}$, is

This document may not be reproduced, modified, adapted, published, translated in any way, in whole or in part, nor disclosed to a third party without the prior written consent of ENAC. © 2023, ENAC

given by

$$\tilde{\hat{p}}_{nf} = \hat{p}_n \xi_n^f = \left(\frac{\hat{b}_n - \hat{n}_{on}}{2\pi \hat{h}_n}\right)\left(\frac{|\hat{h}_n|^2}{|\hat{h}_n|^2 + \tau}\right) = \frac{1}{2\pi}\left(\hat{b}_n - \hat{n}_{on}\right)\left(\frac{\hat{h}_n^*}{|\hat{h}_n|^2 + \tau}\right), \tag{6.19}$$

with τ a parameter that should be chosen in order to minimise the RMSE. This parameter depends on caracteristics of the signal and the noise.

The limitations of this method is that the Fourier coefficients corresponding to the fast variations of the signal can not be distinguished from the coefficients corresponding to the noise. So a compromise has to be done, either the noise is not amplified but the fast variations are filtered out, either it is well estimated but noisy. Consequently a way to improve the correction is to choose the signal well estimated, but noisy and to add another kind of shrinkage.

6.3.4.2 Wavelet shrinkage

The wavelet shrinkage comes in addition of the Fourier shrinkage, as a tool for denoising. Firstly a "loose" Fourier regularisation is performed, that does not erase all the noise, secondly a wavelet shrinkage is performed that selectively atenuates the noise, without deleting the fast variations of the signal. Indeed the wavelet shrinkage allows the signal to keep fast variations while denoising, while Fourier would attenuate these fast variations. This section explains how this shrinkage is performed.

The Discrete Wavelet Transform (DWT) of the Fourier estimation of p, $p_{\xi f}$ is subjected to a threshold ξ^w, which gives

$$DWT(\tilde{p}_w) = DWT(\tilde{p}_f)\xi^w, \tag{6.20}$$

with ξ^w the regularisation coefficient. This can be defined by

$$\xi_j^w = \frac{|D^j|^2}{|D^j|^2 + \tilde{\sigma}^2}, \tag{6.21}$$

with D^j the wavelet coefficients of h and $\tilde{\sigma}$ an estimation of the level of noise [122].

6.3.5 Complete method

This section focuses on the initial problem, that is to say to estimate p from b as defined in (5.1). This implies to know the spectrum of h. In the case described in Section 6.2, the signal h corresponds to the radiation of the probe in the measurement environment, in absence of the antenna. However, in most antenna measurement situations this signal is unknown. This explains why a preliminary measurement is performed with a reference antenna, in order to estimate the signal of the environment.

The antenna measurement method developed in this thesis thus includes two steps:

- First step: the estimation of $\tilde{h}$ from the deconvolution of the measurement $b_1 = h \circledast p_{ref} + n$, with p_{ref} the radiation of the reference antenna.
- Second step: the estimation of $\tilde{p}_{aut}$ from the deconvolution of the measurement $b_2 = h \circledast p_{aut} + n$, using $\tilde{h}$ as h.

This method is summarised in Figure 6.2

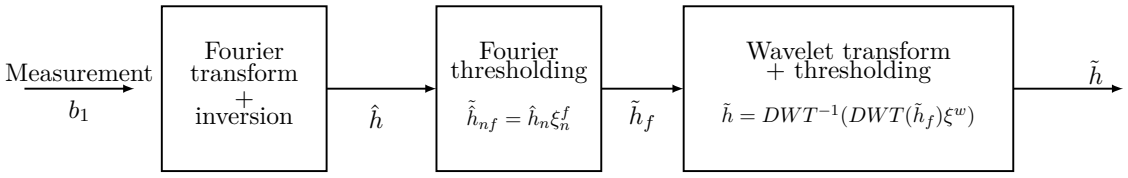

(a) First step

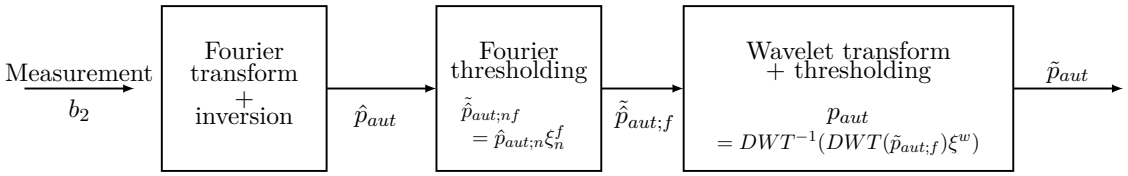

(b) Second step

Figure 6.2: Steps of the correction method

Finally, a compromise must be found between both regularisations. The first shrinkage must be loose to let the entire signal of interest and the wavelet regularisation should get rid of the noise. Thus, the parameters (τ,σ) have to be chosen consistently in both steps to obtain the best RMSE.

6.3.6 Conclusion

This section has presented a regularised deconvolution method in 2D configuration. Firstly the Fourier series has been presented as a tool to analyse a 2D measurement situation. Then, the convolution has been presented as an ill-conditioned problem, this means that the deconvolution method amplifies the noise. Consequently, the ForWaRD method, a regularisation method combining regularisation in the harmonic and in the wavelet domains, has been presented. Finally, the complete antenna measurement correction method has been detailled as an application of the ForWaRD regularisation twice, firstly to estimate the environment signature and then to obtain the antenna pattern.

6.4 Illustration of the deconvolution method on a simulation

6.4.1 Introduction

This section constitutes an illustration of the ForWaRD method used in the case of an antenna measurement post-processing. Here, we focus on the simple particular case in which the incident field is a sum of plane waves. Firstly, the formulation of the incident field is detailed in subsection 6.4.2, then the configuration and parameters of the simulations are presented in subsection 6.4.3. Next the first step of the correction method is performed in subsection 6.4.4, leading to the estimation of h with the ForWaRD method. Finally, in subsection 6.4.5 the estimation of p is performed.

This document may not be reproduced, modified, adapted, published, translated in any way, in whole or in part, nor disclosed to a third party without the prior written consent of ENAC. © 2023, ENAC

6.4.2 Formulation of the incident field

This section focuses on the formulation of h the radiation of the probe in the environment nearby the antenna, which expression has been expressed in (6.4). This is defined on the circle $\mathcal{C}$ of radius r surrounding the antenna, where its equivalent currents are defined. We are going to develop each term of (6.4), $\boldsymbol{E}^{\text{inc}}$ and $\boldsymbol{H}^{\text{inc}}$

The incident field on $\mathcal{C}$ is considered to be a sum of plane waves, which gives

$$\boldsymbol{E}^{\text{inc}} = \sum_{p=0}^{n-1} \boldsymbol{E}_p e^{-j\hat{\mathbf{k}}_p \hat{\mathbf{r}}}, \tag{6.22}$$

with $p = 0$ corresponding to the direct path and $p = \{1, .., n-1\}$ the multipath, which have an attenuated amplitude.

The multipath can come from all around $\mathcal{C}$ with an angle of arrival ϕ_p^{oa}, as represented in Figure 6.3. On the circle $\mathcal{C}$ of radius r, the term of the exponential becomes

$$\begin{aligned} \boldsymbol{k}_p \cdot \boldsymbol{r} &= (k\cos\phi_p^{oa}\hat{\boldsymbol{x}} + k\sin\phi_p^{oa}\hat{\boldsymbol{y}}) \cdot (x\hat{\boldsymbol{x}} + y\hat{\boldsymbol{y}}) \\ &= (k\cos\phi_p^{oa}\hat{\boldsymbol{x}} + k\sin\phi_p^{oa}\hat{\boldsymbol{y}}) \cdot (r\cos\phi\hat{\boldsymbol{x}} + r\sin\phi\hat{\boldsymbol{y}}) \\ &= kr\cos\Big(\phi_p^{oa} - \phi\Big). \end{aligned} \tag{6.23}$$

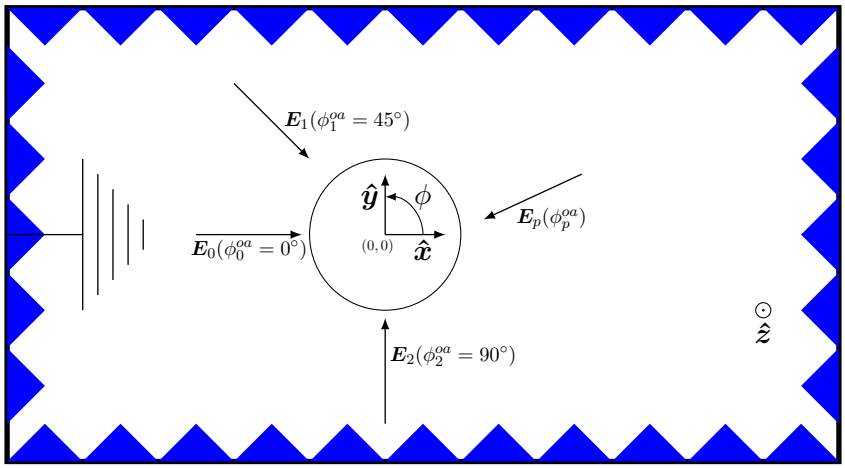

Figure 6.3: Representation of the incident field

Then the incident magnetic field can be computed from (6.22). In the TMz configuration, this becomes

$$\begin{aligned} \boldsymbol{H}^{\text{inc}}(\phi) &= \frac{\boldsymbol{k} \times \boldsymbol{E}^{\text{inc}}}{\zeta_0} \\ &= \sum_{p=0}^{p-1} E_p \frac{\boldsymbol{k}_p \times \hat{\boldsymbol{z}}}{\zeta_0} \mathrm{e}^{-ikr\cos\left(\phi_p^{oa} - \phi\right)} \\ &= \sum_{p=0}^{p-1} kE_p \frac{\sin\left(\phi_p^{oa}\right)\hat{\boldsymbol{x}} - \cos\left(\phi_p^{oa}\right)\hat{\boldsymbol{y}}}{\zeta_0} e^{-ikr\cos\left(\phi_p^{oa} - \phi\right)}. \end{aligned} \tag{6.24}$$

Finally, the radiation of the probe in the environment nearby the antenna can be expressed by a function $h(\phi)$ given by

$$h(\phi) = (\boldsymbol{E}^{\text{inc}}(\phi) - \zeta_0 \boldsymbol{r} \times \boldsymbol{H}^{\text{inc}}(\phi)) \cdot \hat{\boldsymbol{z}}. \tag{6.25}$$

From (6.4), (6.22) and (6.24), the incident field is given by

$$\begin{aligned} h(\phi) &= \sum_{p=0}^{p-1} E_p(\hat{\boldsymbol{z}} - k\hat{\boldsymbol{r}} \times (\sin\left(\phi_p^{oa}\right)\hat{\boldsymbol{x}} - \cos\left(\phi_p^{oa}\right)\hat{\boldsymbol{y}}))e^{-ikr\cos\left(\phi_p^{oa}-\phi\right)} \cdot \hat{\boldsymbol{z}} \\ &= \sum_{p=0}^{p-1} E_p(\hat{\boldsymbol{z}} + k\cos\left(\phi_p^{oa} - \phi\right)\hat{\boldsymbol{z}})e^{-ikr\cos\left(\phi_p^{oa}-\phi\right)} \cdot \hat{\boldsymbol{z}} \\ &= \sum_{p=0}^{p-1} (k\cos\left(\phi_p^{oa} - \phi\right) + 1)E_p e^{-ikr\cos\left(\phi_p^{oa}-\phi\right)}. \end{aligned} \tag{6.26}$$

6.4.3 Configuration of the simulations

This section presents the parameters of the simulations, which are run for a frequency of $f = 10$ GHz. This incident field consists in two plane waves: the direct path, with $\phi_0^{oa} = 0°$ has an amplitude of 1 V/m. The multipath has an angle of arrival $\phi_1^{oa} = 40.8°$ and an amplitude attenuated of 20 dB compared to the amplitude of the direct field.

The fields in presence and in absence of the multipath are represented in Figure 6.4.

This document may not be reproduced, modified, adapted, published, translated in any way, in whole or in part, nor disclosed to a third party without the prior written consent of ENAC. © 2023, ENAC

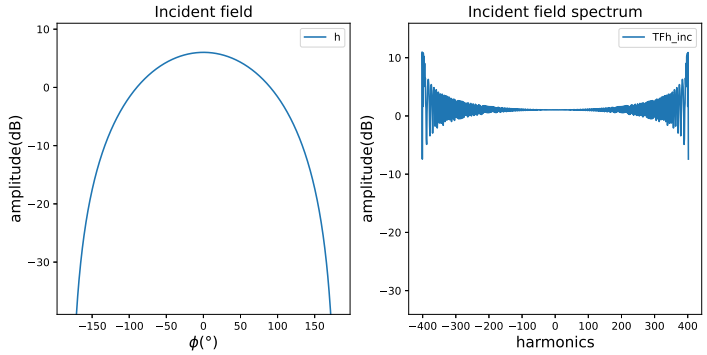

(a) Direct path of the incident field

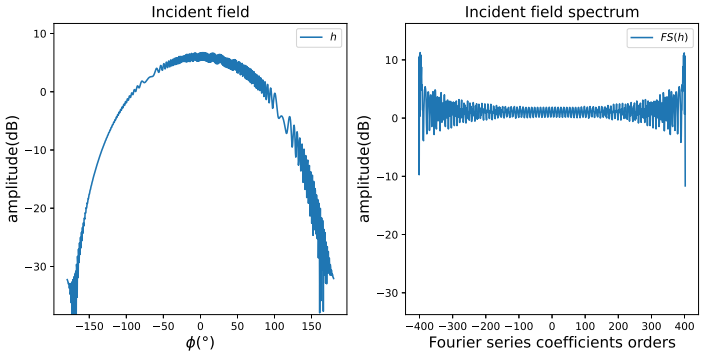

(b) Incident field, i.e. a plane wave with a multipath

Figure 6.4: h and its spectrum (dB), on $\mathcal{C}$

The direct path yields a field that is maximal for $\phi = 0°$, which corresponds to its direction of arrival. The field decreases smoothly for other angles. There is a large number of strong Fourier series coefficients. In presence of the multipath, more oscillations are visible, both in the angular and Fourier domains.

6.4.4 First measurement: estimation of the incident field

The first step of the method is to estimate h, with the ForWaRD method.

6.4.4.1 Configuration

The chosen reference antenna is radiating a Gaussian beam. Its field on $\mathcal{C}$ and its spectrum are shown in Figure 6.5.

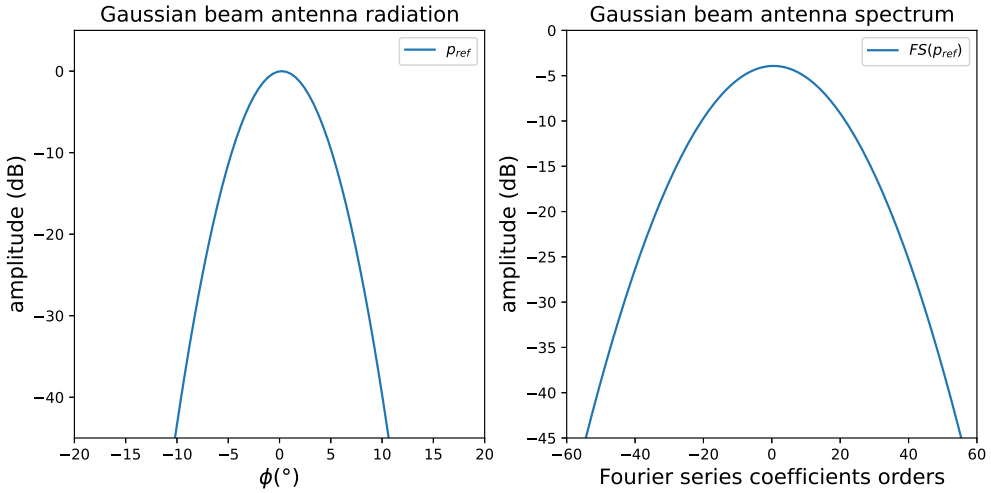

Figure 6.5: Amplitude of the field of the reference antenna and its spectrum (dB)

The measured signal is obtained by the convolution between h and p_{ref}, additioned with white Gaussian noise, with an amplitude 20dB below the amplitude of the convolution signal. Its field and spectrum are shown in Figure 6.6.

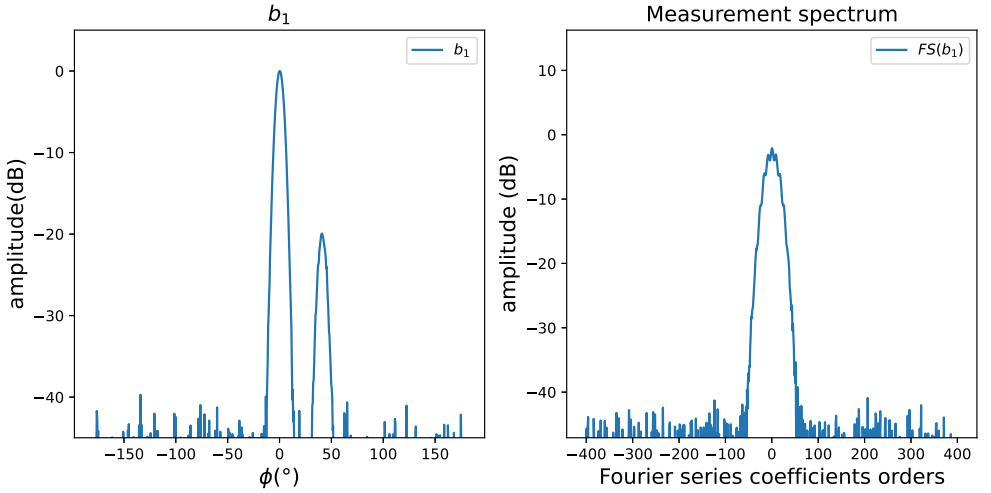

Figure 6.6: Amplitude of the field of the measurement and its spectrum (dB)

To estimate h, the ForWaRD method is used. The wavelet regularisation is performed on 4 wavelet levels. The type of wavelet chosen are the 'symlet6' from the Python package pywt. The regularisation parameters are taken such that $\tau_h = 0.0003$ and $\sigma_h = 0.01$.

6.4.4.2 Estimation of h

The estimation of the h field and spectrum are plotted in Figures 6.7 and 6.8 along with the field reference value of h, the measured signal, and the ref antenna radiation.

This document may not be reproduced, modified, adapted, published, translated in any way, in whole or in part, nor disclosed to a third party without the prior written consent of ENAC. © 2023, ENAC

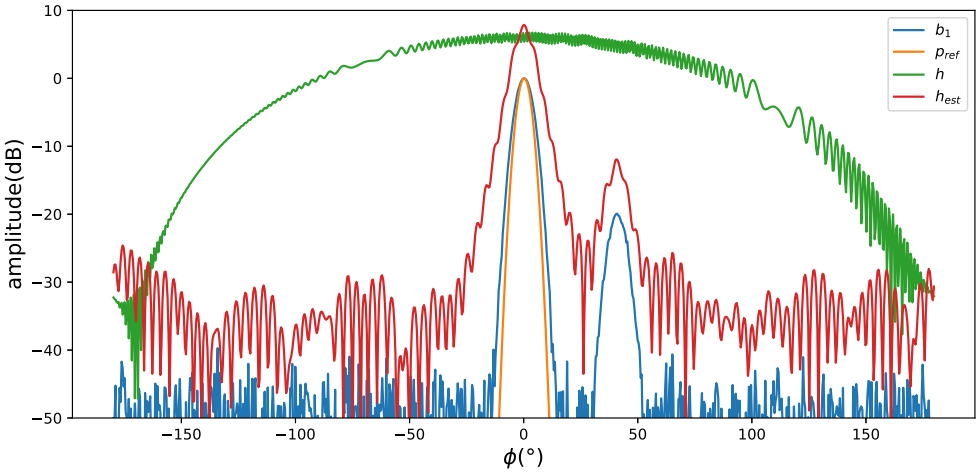

Figure 6.7: Simulated fields of h, b_1, p_{ref} and h_{est} (dB)

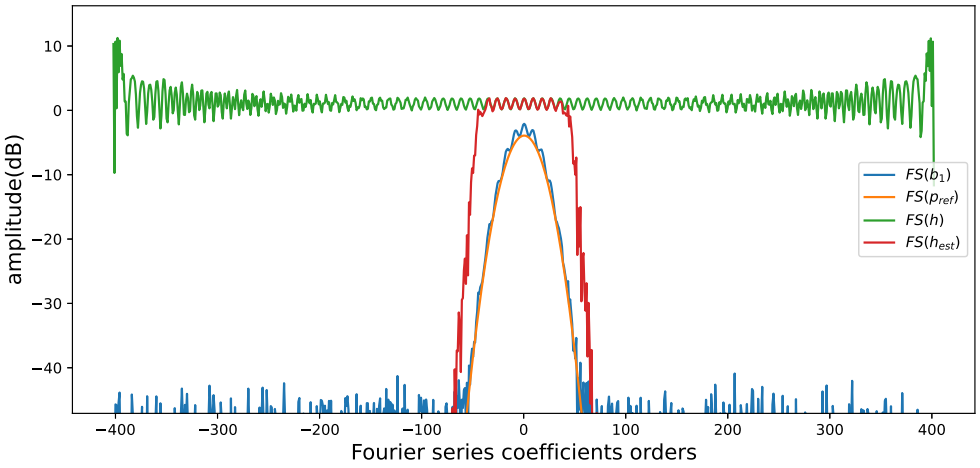

Figure 6.8: Spectrum of h, b_1, p_{ref} and h_{est} (dB)

The estimation of h looks really poor but its spectrum shows that in the bandwidth of the reference antenna, its spectrum is well estimated. This was expectable as the reference antenna spectrum has a much smaller bandlimit than the incident field. Consequently, the measurement acts as a filter on h, eliminating harmonics situated out of the reference antenna band-limit.

However, the estimation of h does not have to be perfect, as long as the estimation of its spectrum is correct until the bandlimit of the AUT. Consequently, the bandlimit of the Gaussian beam antenna being $N_{\text{AUT}} = 55$, the correction method can only work with antenna with a lower bandlimit.

6.4.5 Second measurement: estimation of the AUT radiation pattern

This section is the second step of the antenna measurement correction.

6.4.5.1 Configuration

The antenna under test is an aperture with a width of the opening of 4λ, radiating a sinc function. The radiation pattern on $\mathcal{C}$ and its spectrum are presented in Figure 6.9.

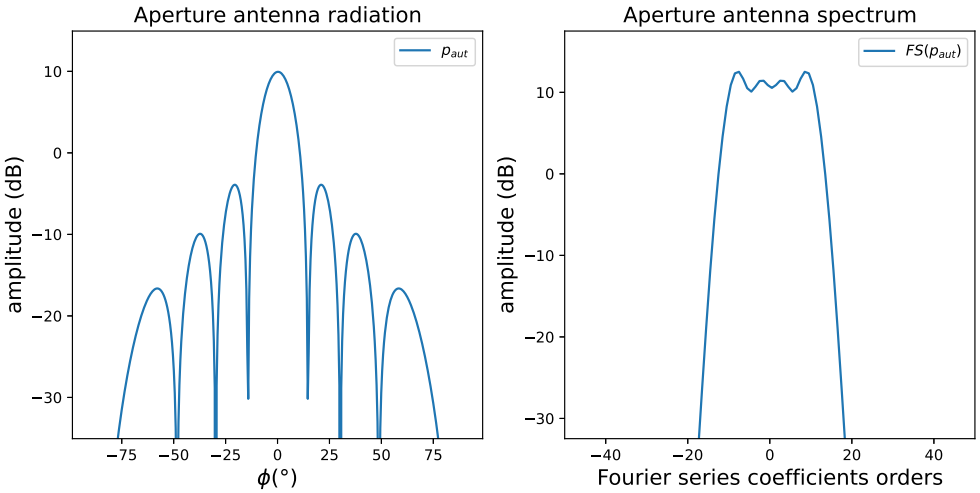

Figure 6.9: Amplitude of the field and of its spectrum (dB)

The bandwidth of the AUT is smaller than the one of the reference gaussian beam antenna used to estimate h, thus we can expect the deconvolution to work.

Here, the measured signal b is the convolution between this field and h, additioned with white Gaussian noise, with an amplitude 20dB under the amplitude of the convolution. It is shown in Figure 6.10.

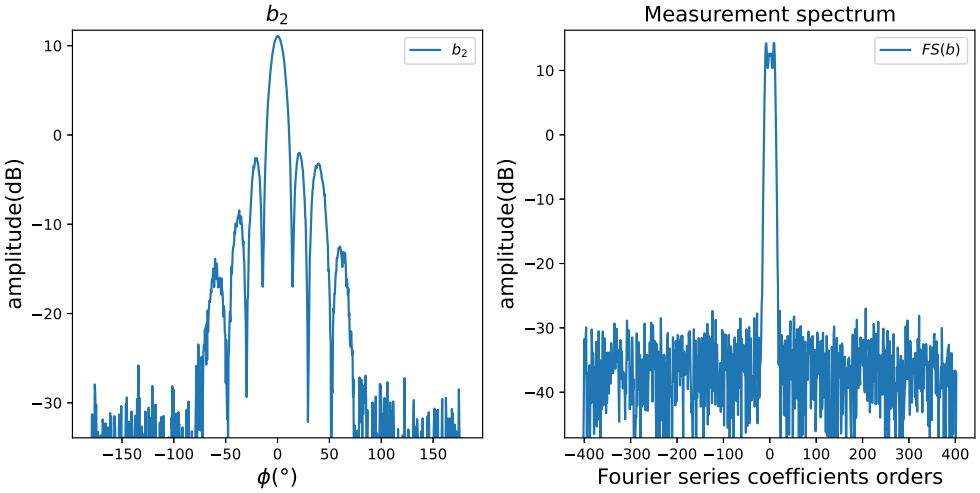

Figure 6.10: Amplitude of the field of the measurement and its spectrum (dB)

Then, we estimate the field of the antenna from the estimation of h. This time, the Fourier and wavelet regularisation parameters are chosen as $(\tau_p, \sigma_p) = (0.02, 0.7)$.

This document may not be reproduced, modified, adapted, published, translated in any way, in whole or in part, nor disclosed to a third party without the prior written consent of ENAC. © 2023, ENAC

6.4.5.2 Results

The results of the regularisation correction method are shown in Figure 6.11.

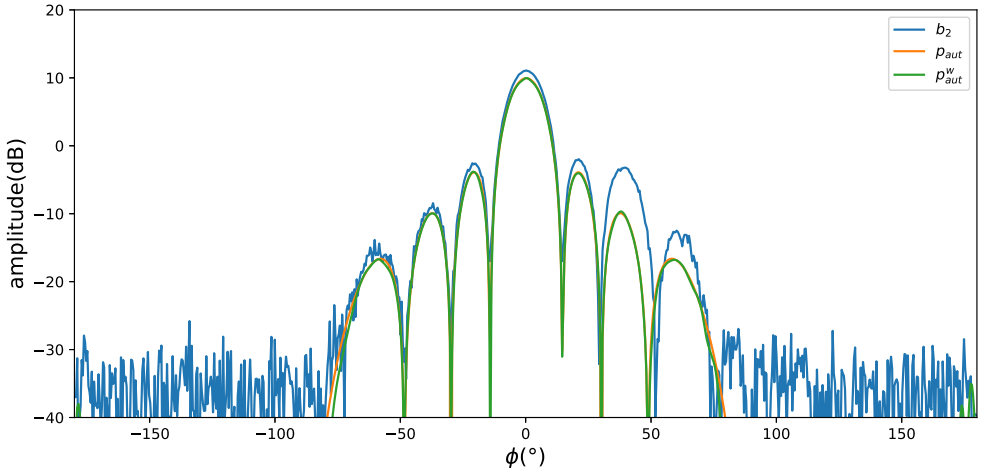

(a) Amplitude of the fields

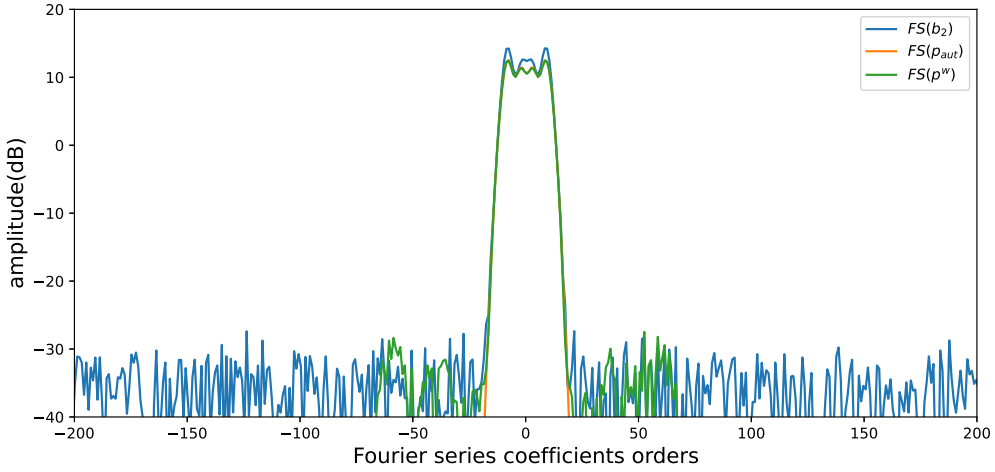

(b) Spectrum

Figure 6.11: Amplitude of the field and spectrum of b_2, p_{aut} and its estimation p^w_{aut} (dB)

In Figure 6.11, a notable reduction of the perturbations is obvious. The central and secondary lobes are corrected and close to the antenna radiation pattern. The RMSE between the theorical radiation pattern and the estimated one is of -36.6 dB, considereing that the simulated measured signal is disturbed by a multipath 20 dB under the amplitude of the incident field and a noise level of -20dB. This is interesting to observe that h do not need to be fully estimated to notice a distinct improvement in the processed measurement signal. The estimation of the harmonics in the bandwidth of the AUT is sufficient. This method could be improved by choosing better values for $(\tau_h, \sigma_h, \tau_p, \sigma_p)$.

6.4.6 Conclusion

This section has derived the 2D formulation of the measurement and introduced a deconvolution method combining Fourier and wavelets regularisation.

Firstly, the formulation of the incident field has been explicited assuming a simple case for which it is a sum of plane waves. Then, the first measurement of the deconvolution method has been simulated by computing the convolution of h with a reference antenna and by adding noise. Next, the ForWaRD method has been performed to estimate h. Finally, the estimation of the AUT signal is computed, from the estimation of h. This method yields an estimation of the antenna radiation pattern from a disturbed and noisy measurement. With a multipath 20 dB under the amplitude of the incident field and a noise level of -20dB, the amplitude of the antenna is estimated with an RMSE of -36.6 dB. However, the ForWaRD method has not been fully optimised, better results are probably reachable by a study of the regularisation parameters.

6.5 Conclusion

This chapter has constituted an application case of antenna measurement correction, in a 2D configuration.

Firstly the formulation of the measurement on the circle has been derived in the TMz case, yielding a convolution between two 2π-periodic signals on the sphere.

Then, the deconvolution of this function has been detailed and it has been shown that the deconvolution is an ill-conditioned problem. Thus, a regularisation method has been used to obtain an estimation of the signal of interest. This method has been adapted to a measurement correction case, in two steps. The first step constitutes an estimation of the signal corresponding to the effect of the environment on the radiation of the probe. Then, this estimation is used to deconvolve the measurement signal and obtain the radiation pattern of the antenna.

Finally, this method has been applied to a simulation. From a measurement disturbed by noise and multipath, an estimation of the antenna signal has been obtained with a RMSE of -36.6 dB. This method has not been pushed to its limits and might give better results.

To conclude, this chapter has presented an antenna measurement correction using deconvolution with wavelet regularisation, on a simplified 2D case.

This document may not be reproduced, modified, adapted, published, translated in any way, in whole or in part, nor disclosed to a third party without the prior written consent of ENAC. © 2023, ENAC

Conclusion

Summary

This PhD thesis aimed at developing analysis and correction tools for antenna measurements based on spin spherical harmonics and wavelets.

In the **first chapter**, the background of the thesis and the experimental aspect of antenna measurements have been outlined. Firstly, an examination of antenna measurement environments has been undertaken, encompassing various configurations and environments. Then, typical antenna measurement equipments have been presented, along with their function within the RF measurement chain. The discussion extends to absorbing materials and their properties, diverse types of probes, and mechanical systems responsible for motion within the measurement range. Finally, the antenna range employed for the antenna measurements in this thesis has been introduced. Its characteristics have been detailed, along with an illustrative measurement example.

In the **second chapter**, the tools and techniques for post-processing antenna measurements in spherical geometries have been introduced. To begin with, the establishment of the coordinate system and operators has been addressed, as they play a crucial role in describing motions within the measurement range. A recapitulation of spherical coordinates has been provided, followed by a presentation of the mathematical tools and operators formulating rotations over the sphere. The subsequent sections has introduced the derivation of standard vector spherical harmonics for antennas. This process comprises two stages: first, the scalar spherical harmonics, followed by the vector spherical harmonics. The transform of electromagnetic fields has then been discussed, in particular the truncation of this expansion due to the properties of spherical harmonics. To illustrate, examples of spherical harmonic transforms have been displayed. These illustrations involve various radiation patterns. Concluding the chapter, brief insights into antenna measurement post-processing methods have been presented. The covered topics include the concept of near-field to far-field transformation, techniques for speeding up antenna measurements, and the correction of the probe and perturbations originating from the environment.

In the **third chapter**, the concept of spin spherical harmonics for the analysis of antenna radiation has been introduced. These expansions possess attractive features for representing tangent vectors on the sphere, and efficient algorithms are available. To begin with, the theoretical foundation of spin spherical harmonics, covering the definition of spin functions, spin spherical harmonics, and the expansion of spin functions using these harmonics have been presented. Additionally, the spin expression for tangent vectors over the sphere has been derived, introducing rotational properties associated with the spin parameterisation. Then, sampling theorems and associated fast algorithms to efficiently compute exact spherical harmonic transforms have been reviewed. Notably, the McEwen & Wiaux

This document may not be reproduced, modified, adapted, published, translated in any way, in whole or in part, nor disclosed to a third party without the prior written consent of ENAC. © 2023, ENAC

approach, compatible with the spin representation, has demonstrated high performance in terms of complexity and computation time. Furthermore, the relation and compatibility between the spin spherical harmonics and the Hansen spherical harmonics have been derived. Finally, spin spherical harmonics transforms have been applied to various radiation patterns, ranging from canonical cases with very few coefficients (N = 1) to the RCS of an aircraft (N = 2048). These transforms have been executed in remarkably short computation times, with the longest computation taking 9 minutes and 24 seconds. The versatility and efficiency of spin spherical harmonics in these diverse contexts have underscored their potential as a valuable tool in antenna radiation analysis. However, the examination of DUT radiating high-order spherical harmonics has shown a limitation of this transform. A significant amount of power can be distributed across numerous weak coefficients, rendering this power barely visible in the spherical harmonic representation. Consequently, the next chapter has focused on spin spherical wavelets, which exhibit interesting localisation properties.

In the **fourth chapter**, spin spherical wavelets have been introduced as a promising tool for the analysis of antenna radiation patterns. While wavelets are commonly employed in signal processing and compression problems, their application in spherical geometry is less frequent. To begin with, the construction of wavelet bases in 1D geometry has been presented. Then, the derivation of spin spherical wavelets from spin spherical harmonics has been explained, followed by the presentation of the algorithm performing the spin spherical wavelet transform. Finally, the chapter has provided several examples of wavelet transforms of simulated radiation patterns. In particular, the wavelet transform of the Radar Cross Section (RCS) of an aircraft has emphasized the ability of wavelets to highlight fast variations, in contrast to spherical harmonics. Furthermore, these examples have shown the algorithm's efficiency, as the computation of 39,134,480 wavelet coefficients has taken only 5 minutes and 24 seconds. As a result, the spin spherical wavelet transform has exhibited significant potential as a tool for analysing and potentially correcting fast variating fields.

In the **fifth chapter**, a formulation of the measurement problem has been established. The measurement signal on the port of an Antenna Under Test (AUT) has been expressed as the convolution between the radiation pattern of the antenna and the radiation of the probe in the measurement environment. The demonstration has started with the application of the equivalence principle. This has simplified the problem by expressing the antenna radiation through its equivalent currents. Secondly, the reciprocity theorem has facilitated the connection between the signal received on the antenna port (i.e., the measurement signal) and the signal corresponding to the probe's radiation in the measurement environment, along with the radiation of the antenna. Then, the rotation of the antenna in the measurement environment results in a convolution with the radiation of the probe in that environment. This formulation has been decomposed on spin components, yielding a simplified formulation of the measurement. Finally, the validity of the hypothesis according to which the antenna can be replaced by its equivalent currents has been verified. With this formulation, deconvolution methods can be employed to extract the actual antenna pattern from the measurements.

In the **sixth chapter**, an application case of an antenna measurement correction has been performed, in a 2D configuration. Firstly, the formulation of measurement on the circle has been derived in a Transverse Magnetic (TMz) configuration, resulting in a convolution between two 2π-periodic signals on the sphere. Then, the deconvolution process for this function has been presented, showing that deconvolution is a challenging problem due to

its ill-conditioned nature. Consequently, a regularisation method has been presented to obtain an estimation of the signal of interest. This method has then been adapted for a measurement correction scenario in two steps. The first step involves estimating the signal corresponding to the environmental impact on the probe's radiation. In a second step, this estimation is used to deconvolve the measurement signal, ultimately yielding the radiation pattern of the antenna. This method implies to use 1D expansion bases such as the classic Fourrier series. Moreover, as in the Fourier-Wavelet Regularisation (ForWard) [122], the 1D wavelet expansions have been introduced, in order to refine the regularisation on Fourier series. Then, this method has been applied to an antenna measurement simulation, including perturbations under the form of 20 dB attenuated multipath and a -20dB level of noise. This has resulted in an estimation of the antenna signal with a Root Mean Square Error (RMSE) of -36.6 dB. This is worth noting that this method has not been pushed to its limits and may yield better results under more optimised conditions. Besides, the extension to actual 3D spherical measurements has been left to furture works. To sum up, this chapter represents an initial attempt at correcting antenna measurements using deconvolution with wavelet regularisation.

Perspectives

This PhD thesis is the first thesis dealing with antenna measurements in the ENAC lab, marking a beginning in various projects, under various forms. For example, the two first chapters will be used for pedagogical or bibliographical purposes as they introduce many aspects of antenna measurements. Secondly, spin spherical harmonics and the conversion into Hansen spherical harmonic may be used in other projects, due to the fast computation time they provide. As an example, a PhD student at ENAC is already using the spin harmonics to develop stochastic models of the radiation of antennas when installed on aircraft.

Additionally, many aspects of this thesis can to be further explored. The order of the paragraphs is an intent to prioritise further works, from short term to long term.

In terms of spin spherical harmonics, a study of very directive antennas could be added to the studies already performed in this thesis. Moreover a simplication of the Hansen-spin spherical harmonics relations in the far-field zone, would be of interest notably in terms of computation times. This would consist in only considering outgoing waves and in replacing the Hankel functions by their far-field asymptotic equivalents.

Then, in terms of spin spherical wavelets, a further study would be needed to better understand how they can help analyzing the radiation of large systems (RCS, antennas installed on a platform, ...). The aim would be to find a method to determine the exact origins of the coefficients on high wavelet levels, and correct them.

In further works, the deconvolution should be formulated in spherical geometry. Spherical measurements being defined on $L^2(\mathrm{SO}(3))$, this means that a convenient spin parameterised basis will be needed, as Wigner functions according to [65]. Then, the correction using the ForWard method could be adapted to spherical configurations and optimised. Firstly, a method combining the spin spherical harmonics and the spin spherical wavelets has to be developed.

Then the criteria the reference antenna has to fullfill to estimate in the best way the incident field on the AUT have to been clearly characterised. Finally, the choice of the

This document may not be reproduced, modified, adapted, published, translated in any way, in whole or in part, nor disclosed to a third party without the prior written consent of ENAC. © 2023, ENAC

regularisation parameters has to be the subject of a study, either theoretical or numerical studies. In particular, the wavelet regularisation could be applied in function of the wavelet level, as the highest levels probably contain noise only, thus could be regulated more harshly.

Besides, this is important to remember that every antenna measurement facilities do not permit full measurement on $L^2(\mathrm{SO}(3))$, i.e. for each Euler angle combination possible, and the time cost of such measurement. Thus correction methods will have to be optimised by taking into account such limitations. The objective could be to minimise the number of measurement points.

Finally, a perspective for antenna measurement correction is to combine frequency and angular correction with wavelets. Post-processing methods should be able to correct measurement on the sphere in the measurement environment, using all the information contained in a given frequency band. This is expected to improve the measurement accuracy, but post-processing might be challenging due to the huge amount of data involved.

A PhD student at ENAC is already working in the continuity of my work, in order to develop efficient analysis and postprocessing methods for spherical electromagnetic measurements.

Appendix A

Demonstration of the rotation properties of a vector spin signal

A.1 Rotation of spin

The goal of this appendix is to demonstrate the phase shift that appears in the expression of the global rotation of a spin function (3.17). Only the cases $s = \pm 1$ will be considered. The principle of the calculation relies on applying a global rotation to a field of vectors tangent to the sphere, and to look at the effect of the rotation on its spin components.

To do so, we consider a field $\boldsymbol{V}_\mathrm{t}$ of vectors tangent to the unit sphere $\mathcal{S}^2$. This field can be expanded in terms of ± 1 spin components. At any position $\hat{\boldsymbol{r}}_0$, this can be written as

$$\boldsymbol{V}_\mathrm{t}(\hat{\boldsymbol{r}}_0) = V_{+1}(\hat{\boldsymbol{r}}_0)\hat{\boldsymbol{u}}_{+1}(\hat{\boldsymbol{r}}_0) + V_{-1}(\hat{\boldsymbol{r}}_0)\hat{\boldsymbol{u}}_{-1}(\hat{\boldsymbol{r}}_0). \tag{A.1}$$

A global rotation of Euler angles ϵ of this field can be defined as

$$\boldsymbol{V}'_\mathrm{t}(\hat{\boldsymbol{r}}_1) = \left(\mathcal{R}_\epsilon \boldsymbol{V}_\mathrm{t}\right)(\hat{\boldsymbol{r}}_1) \equiv \boldsymbol{R}_\epsilon \boldsymbol{V}_\mathrm{t}(\hat{\boldsymbol{r}}_0), \tag{A.2}$$

with

$$\hat{\boldsymbol{r}}_0 = \boldsymbol{R}_\epsilon^{-1}\hat{\boldsymbol{r}}_1. \tag{A.3}$$

We remind that $\hat{\boldsymbol{r}}_0$ and $\hat{\boldsymbol{r}}_1$ are the positions before and after the rotation, respectively. The component of spin $+1$ in (A.2) is given by

$$\begin{aligned} V'_{+1}(\hat{\boldsymbol{r}}_1) &= \boldsymbol{V}'_\mathrm{t}(\hat{\boldsymbol{r}}_1) \cdot \hat{\boldsymbol{u}}^*_{+1}(\hat{\boldsymbol{r}}_1) \\ &= \left[\boldsymbol{R}_\epsilon \left(V_{+1}(\hat{\boldsymbol{r}}_0)\hat{\boldsymbol{u}}_{+1}(\hat{\boldsymbol{r}}_0) + V_{-1}(\hat{\boldsymbol{r}}_0)\hat{\boldsymbol{u}}_{-1}(\hat{\boldsymbol{r}}_0)\right)\right] \cdot \hat{\boldsymbol{u}}^*_{+1}(\hat{\boldsymbol{r}}_1) \\ &= V_{+1}(\hat{\boldsymbol{r}}_0)\ \left[\boldsymbol{R}_\epsilon \hat{\boldsymbol{u}}_{+1}(\hat{\boldsymbol{r}}_0) \cdot \hat{\boldsymbol{u}}^*_{+1}(\hat{\boldsymbol{r}}_1)\right] + V_{-1}(\hat{\boldsymbol{r}}_0)\ \left[\boldsymbol{R}_\epsilon \hat{\boldsymbol{u}}_{-1}(\hat{\boldsymbol{r}}_0) \cdot \hat{\boldsymbol{u}}^*_{+1}(\hat{\boldsymbol{r}}_1)\right]. \end{aligned} \tag{A.4}$$

To continue the calculation, we need to calculate

$$B_s = \boldsymbol{R}_\epsilon \hat{\boldsymbol{u}}_s(\hat{\boldsymbol{r}}_0) \cdot \hat{\boldsymbol{u}}^*_{+1}(\hat{\boldsymbol{r}}_1), \qquad \text{for } s = \pm 1. \tag{A.5}$$

To do so, we notice that the spherical-coordinates unit-vectors at $\hat{\boldsymbol{r}}_0$ can be obtained from a rotation of Euler angles $(\phi_0, \theta_0, 0)$ of $\hat{\boldsymbol{x}}$, $\hat{\boldsymbol{y}}$ and $\hat{\boldsymbol{z}}$. This can be written as

$$\hat{\boldsymbol{\theta}}_0 = \mathbf{R}_{(\phi_0,\theta_0,0)}\hat{\boldsymbol{x}}, \qquad \hat{\boldsymbol{\phi}}_0 = \mathbf{R}_{(\phi_0,\theta_0,0)}\hat{\boldsymbol{y}}, \qquad \hat{\boldsymbol{r}}_0 = \mathbf{R}_{(\phi_0,\theta_0,0)}\hat{\boldsymbol{z}}. \tag{A.6}$$

This document may not be reproduced, modified, adapted, published, translated in any way, in whole or in part, nor disclosed to a third party without the prior written consent of ENAC. © 2023, ENAC

Similarly, we have

$$\hat{\boldsymbol{\theta}}_1 = \mathbf{R}_{(\phi_1,\theta_1,0)}\hat{\boldsymbol{x}}, \qquad \hat{\boldsymbol{\phi}}_1 = \mathbf{R}_{(\phi_1,\theta_1,0)}\hat{\boldsymbol{y}}, \qquad \hat{\boldsymbol{r}}_1 = \mathbf{R}_{(\phi_1,\theta_1,0)}\hat{\boldsymbol{z}}. \tag{A.7}$$

Therefore, the unit vectors associated with ± 1 spins can ve expressed as

$$\hat{\boldsymbol{u}}_s(\hat{\boldsymbol{r}}_0) = \mathbf{R}_{(\phi_0,\theta_0,0)}\left(\frac{\hat{\boldsymbol{x}} - is\hat{\boldsymbol{y}}}{\sqrt{2}}\right), \qquad \hat{\boldsymbol{u}}_s(\hat{\boldsymbol{r}}_1) = \mathbf{R}_{(\phi_1,\theta_1,0)}\left(\frac{\hat{\boldsymbol{x}} - is\hat{\boldsymbol{y}}}{\sqrt{2}}\right). \tag{A.8}$$

Consequently, we have

$$B_s = \left[\boldsymbol{R}_\epsilon \mathbf{R}_{(\phi_0,\theta_0,0)}\left(\frac{\hat{\boldsymbol{x}} - is\hat{\boldsymbol{y}}}{\sqrt{2}}\right)\right] \cdot \left[\mathbf{R}_{(\phi_1,\theta_1,0)}\left(\frac{\hat{\boldsymbol{x}} - i\hat{\boldsymbol{y}}}{\sqrt{2}}\right)^*\right]. \tag{A.9}$$

From (A.3) and the last equation in (A.7), we also have

$$\hat{\boldsymbol{r}}_0 = \boldsymbol{R}_\epsilon^{-1}\boldsymbol{R}_{(\phi_1,\theta_1,0)}\hat{\boldsymbol{z}}. \tag{A.10}$$

Comparing this result with the last equation in (A.6), we obtain

$$\mathbf{R}_{(\phi_0,\theta_0,0)} = \left[\boldsymbol{R}_\epsilon^{-1}\boldsymbol{R}_{(\phi_1,\theta_1,0)}\right]^{(3)}, \tag{A.11}$$

where the upperscrit (3) means that the third Euler angle of the rotation is set to zero. Therefore, (A.9) becomes

$$B_s = \left[\boldsymbol{R}_\epsilon \left[\boldsymbol{R}_\epsilon^{-1}\boldsymbol{R}_{(\phi_1,\theta_1,0)}\right]^{(3)}\left(\frac{\hat{\boldsymbol{x}} - is\hat{\boldsymbol{y}}}{\sqrt{2}}\right)\right] \cdot \left[\boldsymbol{R}_{(\phi_1,\theta_1,0)}\left(\frac{\hat{\boldsymbol{x}} - i\hat{\boldsymbol{y}}}{\sqrt{2}}\right)^*\right]. \tag{A.12}$$

Applying the rotation $\boldsymbol{R}_\epsilon^{-1}$ on both terms of the dot product, we end up with

$$B_s = \left[\left[\boldsymbol{R}_\epsilon^{-1}\boldsymbol{R}_{(\phi_1,\theta_1,0)}\right]^{(3)}\left(\frac{\hat{\boldsymbol{x}} - is\hat{\boldsymbol{y}}}{\sqrt{2}}\right)\right] \cdot \left[\left[\boldsymbol{R}_\epsilon^{-1}\boldsymbol{R}_{(\phi_1,\theta_1,0)}\right]\left(\frac{\hat{\boldsymbol{x}} - i\hat{\boldsymbol{y}}}{\sqrt{2}}\right)^*\right], \tag{A.13}$$

or equivalently

$$B_s = \left[\left[\boldsymbol{R}_\epsilon^{-1}\boldsymbol{R}_{(\phi_1,\theta_1,0)}\right]^{-1}\left[\boldsymbol{R}_\epsilon^{-1}\boldsymbol{R}_{(\phi_1,\theta_1,0)}\right]^{(3)}\left(\frac{\hat{\boldsymbol{x}} - is\hat{\boldsymbol{y}}}{\sqrt{2}}\right)\right] \cdot \left(\frac{\hat{\boldsymbol{x}} - i\hat{\boldsymbol{y}}}{\sqrt{2}}\right)^*. \tag{A.14}$$

In the xy complex plane, a rotation amouts to a phase shift. This yields

$$B_s = e^{-i\chi_g}\left(\frac{\hat{\boldsymbol{x}} - is\hat{\boldsymbol{y}}}{\sqrt{2}}\right) \cdot \left(\frac{\hat{\boldsymbol{x}} - i\hat{\boldsymbol{y}}}{\sqrt{2}}\right)^* = \begin{cases} e^{-\chi_g} & \text{for } s = 1 \\ 0 & \text{for } s = -1 \end{cases} \tag{A.15}$$

where the angle χ_g is the third Euler angle of the rotation $\boldsymbol{R}_\epsilon^{-1}\boldsymbol{R}_{(\phi_1,\theta_1,0)}$. Inserting this result in (A.4), we obtain

$$V'_{+1}(\hat{\boldsymbol{r}}_1) = e^{-i\chi_g}V_{+1}(\hat{\boldsymbol{r}}_0). \tag{A.16}$$

The demonstration is similar for the component of spin -1.

Appendix B

Calculations of the relations between Hansen and Spin Spherical Harmonics

B.1 Calculations of spin coefficients from Hansen coefficients

We are going to develop here each term of the sum (3.31), for $p = \{\text{TE}, \text{TM}\}$ and $c = \pm$. For $p = \text{TM}$ and $s = +1$, operations similar to the ones developed in Section 3.4.3 give

$$\left\langle \boldsymbol{e}_{\text{t}\,m,n}^{\text{TM},(c)}, Y_{1,m',n'}\ \hat{\boldsymbol{u}}_1 \right\rangle = \iint_{\mathcal{S}^2} k\sqrt{\zeta} A_{mn} \mathrm{d}z_n^{(c)}(kr) e^{im\phi} \cdot \left[\frac{\mathrm{d}\bar{P}_n^{|m|}(\cos\theta)}{\mathrm{d}\theta} \hat{\boldsymbol{\theta}} + \frac{im\bar{P}_n^{|m|}(\cos\theta)}{\sin\theta} \hat{\boldsymbol{\phi}} \right] Y_{1,m',n'}^*\ \hat{\boldsymbol{u}}_1^* dS. \tag{B.1}$$

This time, the dot product gives

$$\begin{aligned} \left[\frac{\mathrm{d}\bar{P}_n^{|m|}(\cos\theta)}{\mathrm{d}\theta} \hat{\boldsymbol{\theta}} + \frac{im\bar{P}_n^{|m|}(\cos\theta)}{\sin\theta} \hat{\boldsymbol{\phi}} \right] \cdot \hat{\boldsymbol{u}}_1^* &= \left[\frac{\mathrm{d}\bar{P}_n^{|m|}(\cos\theta)}{\mathrm{d}\theta} \hat{\boldsymbol{\theta}} + \frac{im\bar{P}_n^{|m|}(\cos\theta)}{\sin\theta} \hat{\boldsymbol{\phi}} \right] \left(\frac{\hat{\boldsymbol{\theta}} + i\hat{\boldsymbol{\phi}}}{\sqrt{2}} \right) \\ &= \frac{1}{\sqrt{2}} \left(\frac{\mathrm{d}\bar{P}_n^{|m|}(\cos\theta)}{\mathrm{d}\theta} - \frac{m\bar{P}_n^{|m|}(\cos\theta)}{\sin\theta} \right) \\ &= \frac{-1}{s_m \sqrt{2} A_{mn} e^{im\phi}} Y_{1,m,n}. \end{aligned} \tag{B.2}$$

Thus the dot product becomes

$$\left\langle \boldsymbol{e}_{\text{t}\,m,n}^{\text{TM},(c)}, Y_{1,m',n'}\ \hat{\boldsymbol{u}}_1 \right\rangle = \frac{-s_m}{\sqrt{2}} k\sqrt{\zeta} \mathrm{d}z_n^{(c)}(kr) \delta_{m,m'} \delta_{n,n'}. \tag{B.3}$$

This comes from of the orthogonality relation given by

$$\iint_{\mathcal{S}^2} Y_{smn} \cdot Y_{s'm'n'}^* \sin\theta d\theta d\phi = \delta_{s,s'} \delta_{m,m'} \delta_{n,n'}. \tag{B.4}$$

This document may not be reproduced, modified, adapted, published, translated in any way, in whole or in part, nor disclosed to a third party without the prior written consent of ENAC. © 2023, ENAC

By inserting (3.36) and (3.37) in (3.31), the spin+1 coefficients finally are

$$\begin{aligned} C^{(\mathrm{E}),+1}_{m',n'}(r) &= \frac{s_m}{\sqrt{2}} kr \sum_{p,c,m,n} Q^{p,(c)}_{m,n} \left\langle \boldsymbol{e}^{\,p,(c)}_{\mathrm{t}\,m,n}, Y_{+1,m',n'}\, \hat{\boldsymbol{u}}_{+1} \right\rangle \\ &= \frac{s_m}{\sqrt{2}} kr \sum_{c,m,n} \left[iQ^{\mathrm{TE},(c)}_{m,n} z^{(c)}_n(kr)\delta_{m,m'}\delta_{n,n'} - Q^{\mathrm{TM},(c)}_{m,n} \mathrm{d}z^{(c)}_n(kr)\delta_{m,m'}\delta_{n,n'} \right] \\ &= \frac{s_m}{\sqrt{2}} kr \sum_{c} \left[iQ^{\mathrm{TE},(c)}_{m',n'} z^{(c)}_n(kr) - Q^{\mathrm{TM},(c)}_{m',n'} \mathrm{d}z^{(c)}_n(kr) \right]. \end{aligned} \tag{B.5}$$

The term of (3.31) corresponding to $p = \mathrm{TE}$ and $s = -1$, becomes

$$\begin{aligned} \left\langle \boldsymbol{e}^{\,\mathrm{TE},(c)}_{\mathrm{t}\,m,n}, Y_{-1,m',n'}\, \hat{\boldsymbol{u}}_{-1} \right\rangle = \iint_{\mathcal{S}^2} k\sqrt{\zeta} A_{mn} z^{(c)}_n(kr) e^{im\phi} \cdot \\ \left[\frac{im\bar{P}^{|m|}_n(\cos\theta)}{\sin\theta} \hat{\boldsymbol{\theta}} - \frac{\mathrm{d}\bar{P}^{|m|}_n(\cos\theta)}{\mathrm{d}\theta} \hat{\boldsymbol{\phi}} \right] Y^*_{-1,m',n'}\, \hat{\boldsymbol{u}}^*_{-1} dS, \end{aligned} \tag{B.6}$$

with the dot product that yield the spin−1 spherical harmonic

$$\begin{aligned} \left[\frac{im\bar{P}^{|m|}_n(\cos\theta)}{\sin\theta} \hat{\boldsymbol{\theta}} - \frac{\mathrm{d}\bar{P}^{|m|}_n(\cos\theta)}{\mathrm{d}\theta} \hat{\boldsymbol{\phi}} \right] \hat{\boldsymbol{u}}^*_{-1} &= \left[\frac{im\bar{P}^{|m|}_n(\cos\theta)}{\sin\theta} \hat{\boldsymbol{\theta}} - \frac{\mathrm{d}\bar{P}^{|m|}_n(\cos\theta)}{\mathrm{d}\theta} \hat{\boldsymbol{\phi}} \right] \left(\frac{\hat{\boldsymbol{\theta}} - i\hat{\boldsymbol{\phi}}}{\sqrt{2}} \right) \\ &= \frac{i}{\sqrt{2}} \left(\frac{m\bar{P}^{|m|}_n(\cos\theta)}{\sin\theta} + \frac{\mathrm{d}\bar{P}^{|m|}_n(\cos\theta)}{\mathrm{d}\theta} \right) \\ &= \frac{i}{s_m A_{mn} e^{im\phi}} Y_{-1,m,n}. \end{aligned} \tag{B.7}$$

And finally, we have

$$\begin{aligned} \left\langle \boldsymbol{e}^{\,\mathrm{TE},(c)}_{\mathrm{t}\,m,n}, Y_{-1,m',n'}\, \hat{\boldsymbol{u}}_{-1} \right\rangle &= \frac{is_m}{\sqrt{2}} k\sqrt{\zeta} z^{(c)}_n(kr) \sqrt{2\pi} \iint_{\mathcal{S}^2} Y^*_{-1,m',n'} Y_{-1,m,n} dS \\ &= \frac{is_m}{\sqrt{2}} k\sqrt{\zeta} z^{(c)}_n(kr) \delta_{m,m'}\delta_{n,n'}. \end{aligned} \tag{B.8}$$

Then, the term of (3.31) corresponding to $p = \mathrm{TM}$ and $s = -1$ is given by

$$\begin{aligned} \left\langle \boldsymbol{e}^{\,\mathrm{TM},(c)}_{\mathrm{t}\,m,n}, Y_{-1,m',n'}\, \hat{\boldsymbol{u}}_{-1} \right\rangle = \iint_{\mathcal{S}^2} k\sqrt{\zeta} A_{mn} \frac{1}{kr} \frac{\mathrm{d}}{\mathrm{d}kr} \left(kr z^{(c)}_n(kr) \right) e^{im\phi} \cdot \\ \left[\frac{\mathrm{d}\bar{P}^{|m|}_n(\cos\theta)}{\mathrm{d}\theta} \hat{\boldsymbol{\theta}} + \frac{im\bar{P}^{|m|}_n(\cos\theta)}{\sin\theta} \hat{\boldsymbol{\phi}} \right] Y^*_{-1,m',n'}\, \hat{\boldsymbol{u}}^*_{-1} dS, \end{aligned} \tag{B.9}$$

with the dot product that gives

$$\begin{aligned}\left[\frac{\mathrm{d}\bar{P}_n^{|m|}(\cos\theta)}{\mathrm{d}\theta}\hat{\boldsymbol{\theta}}+\frac{im\bar{P}_n^{|m|}(\cos\theta)}{\sin\theta}\hat{\boldsymbol{\phi}}\right]\hat{\boldsymbol{u}}_{-1}^{*}&=\left[\frac{\mathrm{d}\bar{P}_n^{|m|}(\cos\theta)}{\mathrm{d}\theta}\hat{\boldsymbol{\theta}}+\frac{im\bar{P}_n^{|m|}(\cos\theta)}{\sin\theta}\hat{\boldsymbol{\phi}}\right]\left(\frac{\hat{\boldsymbol{\theta}}-i\hat{\boldsymbol{\phi}}}{\sqrt{2}}\right)\\&=\frac{1}{\sqrt{2}}\left(\frac{\mathrm{d}\bar{P}_n^{|m|}(\cos\theta)}{\mathrm{d}\theta}+\frac{m\bar{P}_n^{|m|}(\cos\theta)}{\sin\theta}\right)\\&=\frac{1}{\sqrt{2}s_m A_{mn}e^{im\phi}}Y_{-1,m,n},\end{aligned}\tag{B.10}$$

and

$$\left\langle \boldsymbol{e}_{\mathrm{t}\,m,n}^{\mathrm{TM},(c)},Y_{-1,m',n'}\,\hat{\boldsymbol{u}}_{-1}\right\rangle=\frac{s_m}{\sqrt{2}}k\sqrt{\zeta}\mathrm{d}z_n^{(c)}(kr)\delta_{m,m'}\delta_{n,n'}.\tag{B.11}$$

Finally the spin -1 coefficients are given by

$$C_{m',n'}^{(\mathrm{E}),-1}(r)=\frac{s_m}{\sqrt{2}}kr\sum_c\left[iQ_{m',n'}^{\mathrm{TE},(c)}z_{n'}^{(c)}(kr)+Q_{m',n'}^{\mathrm{TM},(c)}\mathrm{d}z_{n'}^{(c)}(kr)\right].\tag{B.12}$$

B.2 Calculations of Hansen coefficients from spin coefficients

This calculation can be done by inverting the matrix 3.41.

To do so a Gauss pivot is done, first the matrix is developed as follows

$$\begin{aligned}C_{m,n}^{(\mathrm{E}),+1}(r)=kr\frac{s_m}{\sqrt{2}}(&iz_n^{(+)}(kr)Q_{m,n}^{\mathrm{TE},(+)}+iz_n^{(-)}(kr)Q_{m,n}^{\mathrm{TE},(-)}\\&-dz_n^{(+)}(kr)Q_{m,n}^{\mathrm{TM},(+)}-dz_n^{(-)}(kr)Q_{m,n}^{\mathrm{TM},(-)}),\end{aligned}\tag{B.13}$$

$$\begin{aligned}C_{m,n}^{(\mathrm{E}),-1}(r)=kr\frac{s_m}{\sqrt{2}}(&iz_n^{(+)}(kr)Q_{m,n}^{\mathrm{TE},(+)}+iz_n^{(-)}(kr)Q_{m,n}^{\mathrm{TE},(-)}\\&+dz_n^{(+)}(kr)Q_{m,n}^{\mathrm{TM},(+)}+dz_n^{(-)}(kr)Q_{m,n}^{\mathrm{TM},(-)}),\end{aligned}\tag{B.14}$$

$$\begin{aligned}C_{m,n}^{(\mathrm{H}),+1}(r)=kr\frac{s_m}{\sqrt{2}}(&-dz_n^{(+)}(kr)Q_{m,n}^{\mathrm{TE},(+)}-dz_n^{(-)}(kr)Q_{m,n}^{\mathrm{TE},(-)}\\&+iz_n^{(+)}(kr)Q_{m,n}^{\mathrm{TM},(+)}+iz_n^{(-)}(kr)Q_{m,n}^{\mathrm{TM},(-)}),\end{aligned}\tag{B.15}$$

$$\begin{aligned}C_{m,n}^{(\mathrm{H}),-1}(r)=kr\frac{s_m}{\sqrt{2}}(&dz_n^{(+)}(kr)Q_{m,n}^{\mathrm{TE},(+)}+dz_n^{(-)}(kr)Q_{m,n}^{\mathrm{TE},(-)}\\&+iz_n^{(+)}(kr)Q_{m,n}^{\mathrm{TM},(+)}+iz_n^{(-)}(kr)Q_{m,n}^{\mathrm{TM},(-)}).\end{aligned}\tag{B.16}$$

The following operations are performed on these equations

- (B.13) and (B.14) are added, which gives

$$C_{m,n}^{(\mathrm{E}),+1}(r)+C_{m,n}^{(\mathrm{E}),-1}(r)=\sqrt{2}ikrs_m(z_n^{(+)}(kr)Q_{m,n}^{\mathrm{TE},(+)}+z_n^{(-)}(kr)Q_{m,n}^{\mathrm{TE},(-)}).\tag{B.17}$$

This document may not be reproduced, modified, adapted, published, translated in any way, in whole or in part, nor disclosed to a third party without the prior written consent of ENAC. © 2023, ENAC

- (B.13) and (B.14) are substracted, yielding

$$C_{m,n}^{(\mathrm{E}),+1}(r) - C_{m,n}^{(\mathrm{E}),-1}(r) = -\sqrt{2}krs_m(dz_n^{(+)}(kr)Q_{m,n}^{\mathrm{TM},(+)} + dz_n^{(-)}(kr)Q_{m,n}^{\mathrm{TM},(-)}). \quad \text{(B.18)}$$

- (B.15) and (B.16) are added, which gives

$$C_{m,n}^{(\mathrm{H}),+1}(r) + C_{m,n}^{(\mathrm{H}),-1}(r) = \sqrt{2}ikrs_m(z_n^{(+)}(kr)Q_{m,n}^{\mathrm{TM},(+)} + z_n^{(-)}(kr)Q_{m,n}^{\mathrm{TM},(-)}). \quad \text{(B.19)}$$

- (B.15) and (B.16) are substracted, which yields

$$C_{m,n}^{(\mathrm{H}),+1}(r) - C_{m,n}^{(\mathrm{H}),-1}(r) = -\sqrt{2}krs_m(dz_n^{(+)}(kr)Q_{m,n}^{\mathrm{TE},(+)} + dz_n^{(-)}(kr)Q_{m,n}^{\mathrm{TE},(-)}). \quad \text{(B.20)}$$

Combining (B.17) and (B.20), we end up with

$$\begin{aligned} &Q_{m,n}^{\mathrm{TE},(+)}(z_n^{(+)}(kr)dz_n^{(-)}(kr) - z_n^{(-)}(kr)dz_n^{(+)}(kr)) \\ &\qquad = \frac{dz_n^{(-)}(kr)C_{m,n}^{(\mathrm{E}),+1}(r) + dz_n^{(-)}(kr)C_{m,n}^{(\mathrm{E}),-1}(r) + iz_n^{(-)}(kr)C_{m,n}^{(\mathrm{H}),+1}(r) - iz_n^{(-)}(kr)C_{m,n}^{(\mathrm{H}),-1}(r)}{\sqrt{2}ikrs_m}. \end{aligned} \quad \text{(B.21)}$$

On the left-hand side, we can identify the wronksian as defined in (3.42), which gives

$$\begin{aligned} Q_{m,n}^{\mathrm{TE},(+)} = \frac{-s_m kr}{2\sqrt{2}}&(dz_n^{(-)}(kr)C_{m,n}^{(\mathrm{E}),+1}(r) + dz_n^{(-)}(kr)C_{m,n}^{(\mathrm{E}),-1}(r) \\ &+ iz_n^{(-)}(kr)C_{m,n}^{(\mathrm{H}),+1}(r) - iz_n^{(-)}(kr)C_{m,n}^{(\mathrm{H}),-1}(r)). \end{aligned} \quad \text{(B.22)}$$

Similarly, $Q_{m,n}^{\mathrm{TE},(-)}$, $Q_{m,n}^{\mathrm{TM},(+)}$ and $Q_{m,n}^{\mathrm{TE},(-)}$ become

$$\begin{aligned} Q_{m,n}^{\mathrm{TE},(-)} = \frac{s_m kr}{2\sqrt{2}}&(dz_n^{(+)}(kr)C_{m,n}^{(\mathrm{E}),+1}(r) + dz_n^{(+)}(kr)C_{m,n}^{(\mathrm{E}),-1}(r) \\ &+ iz_n^{(+)}(kr)C_{m,n}^{(\mathrm{H}),+1}(r) - iz_n^{(+)}(kr)C_{m,n}^{(\mathrm{H}),-1}(r)), \end{aligned} \quad \text{(B.23)}$$

$$\begin{aligned} Q_{m,n}^{\mathrm{TM},(+)} = \frac{s_m kr}{2\sqrt{2}}&(-iz_n^{(-)}(kr)C_{m,n}^{(\mathrm{E}),+1}(r) + iz_n^{(-)}(kr)C_{m,n}^{(\mathrm{E}),-1}(r) \\ &- dz_n^{(-)}(kr)C_{m,n}^{(\mathrm{H}),+1}(r) - dz_n^{(-)}(kr)C_{m,n}^{(\mathrm{H}),-1}(r)), \end{aligned} \quad \text{(B.24)}$$

and

$$\begin{aligned} Q_{m,n}^{\mathrm{TM},(-)} = \frac{s_m kr}{2\sqrt{2}}&(iz_n^{(+)}(kr)C_{m,n}^{(\mathrm{E}),+1}(r) - iz_n^{(+)}(kr)C_{m,n}^{(\mathrm{E}),-1}(r) \\ &+ dz_n^{(+)}(kr)C_{m,n}^{(\mathrm{H}),+1}(r) + dz_n^{(+)}(kr)C_{m,n}^{(\mathrm{H}),-1}(r)). \end{aligned} \quad \text{(B.25)}$$

The inverse matrix of (3.43) is deduced from (B.22), (B.23), (B.24) and (B.25).

Appendix C

Construction of axysimmetric spin scale-discretised wavelets

This appendix presents one way to obtain the wavelet and scaling functions of the spin spherical wavelet transform presented in Chapter 4. The equations presented here come from [111]. This has been demonstrated in [123], that a spin function may be reconstructed exactly from its wavelet and scaling coefficients. This is possible if the spherical harmonic coefficients of the scaling and wavelet functions respect an admissibiliy condition given by

$$\frac{4\pi}{2n+1}\left(|C_{0,n}^{s,\Phi^s}|^2+\sum_j|C_{0,n}^{s,\Psi^{s,(j)}}|^2\right)=1,\quad\forall n. \tag{C.1}$$

As demonstrated in [123], a solution to build the scaling and wavelet functions is then to start with the infinitely differentiable Schwartz function given by

$$s(t)\equiv\begin{cases}\mathrm{e}^{\frac{-1}{1-t^2}}, & t\in[-1,1]\\ 0, & t\notin[-1,1]\end{cases}, \tag{C.2}$$

for $t\in\mathbb{R}$. Then the positive real parameter $\lambda\in\mathbb{R}_*^+$ to map $s(t)$ is introduced by

$$s_\lambda(t)\equiv s\left(\frac{2\lambda}{\lambda-1}(t-\frac{1}{\lambda})-1\right), \tag{C.3}$$

which has compact support in $[1/\lambda,\,1]$. Then, the smoothly decreasing function k_λ is defined as

$$k_\lambda(t)\equiv\frac{\int_t^1\frac{\mathrm{d}t'}{t'}s_\lambda^2(t')}{\int_{1/\lambda}^1\frac{\mathrm{d}t'}{t'}s_\lambda^2(t')}, \tag{C.4}$$

which is unity for $t\leq\frac{1}{\lambda}$, zero for $t>1$, and is smoothly decreasing from unity to zero for $t\in[\frac{1}{\lambda},1]$. Finally, the wavelet generating function is defined by

$$\kappa_\lambda(t)\equiv\sqrt{k_\lambda(t/\lambda)-k_\lambda(t)}, \tag{C.5}$$

and the scaling function generating function by

$$\eta_\lambda(t)\equiv\sqrt{k_\lambda(t)}. \tag{C.6}$$

This document may not be reproduced, modified, adapted, published, translated in any way, in whole or in part, nor disclosed to a third party without the prior written consent of ENAC. © 2023, ENAC

From these generating functions, spherical harmonic coefficients of the scaling and wavelet functions can be defined so that they respect the admissibility conditions. They are given by

$$C_{m,n}^{s,\Psi^{s,(j)}} \equiv \sqrt{\frac{2n+1}{4\pi}} \kappa_\lambda \left(\frac{n}{\lambda^j} \right) \delta_{m0}, \tag{C.7}$$

and

$$C_{m,n}^{s,\Phi^s} \equiv \sqrt{\frac{2n+1}{4\pi}} \eta_\lambda \left(\frac{n}{\lambda^{J_0}} \right) \delta_{m0}, \tag{C.8}$$

with δ the Kronecker symbole.

Appendix D

Summary in French (Résumé en français)

D.1 Introduction

La conception d'une nouvelle antenne commence généralement par plusieurs étapes de simulation [1]. Néanmoins, cela ne suffit pas à vérifier les performances de l'Antenne Sous Test (AST), par conséquent une maquette est construite et est testée à travers plusieurs étapes de mesure. Elles permettent de vérifier le bon fonctionnement de l'AST selon différents critères et applications comme les communications sans fils, les systèmes radar et les communications par satellite (satcom) [2, 3].
Le processus de mesure a pour but d'évaluer le diagramme de rayonnement en polarisations principale et croisée, dans toutes les directions, que l'antenne soit seule ou installée sur sa plateforme d'utilisation, le tout formant un Dispositif Sous Test (DST). Idéalement, le signal de mesure est recueilli par une sonde, en général une autre antenne placée suffisement loin de l'AST pour respecter les conditions de champ lointain [4, 5]. Cette condition est remplie quand la distance d entre l'antenne et la sonde correspond à la condition

$$d > \frac{2D^2}{\lambda}, \tag{D.1}$$

avec D la taille de l'AST et λ la longueur d'onde.
Néanmoins, cette condition peut mener à des distances irréalistes entre la sonde et l'antenne. Par conséquent, les mesures sont généralement faites dans des installations spécifiques, adaptées à l'émulation de conditions de champ lointain, comme les bases compactes de mesure d'antennes. Un post-traitement du signal est aussi possible, comme ce qui est fait dans les bases de mesure champ proche [2].
Ces installations de mesures sont conçues de manière à éviter les perturbations, ce qui permet de considérer que l'AST ou le DST sont en espace libre. En général ces installations sont des chambres anéchoïques, dont les murs sont couverts de matériaux absorbants.
Néanmoins, des réflexions parasites, du bruit et des multi-trajets sont toujours résiduellement présents dans ces chambres, même les plus précises. Ces perturbations peuvent venir de nombreuses sources comme des reflexions sur des appareils de mesure métalliques, du couplage, du bruit électronique ou thermique, ou le rayonnement cosmique. Par ailleurs, la donnée de mesure brute doit être traitée pour extraire l'information utile. Par conséquent, dans la littérature, on retrouve le développement de méthodes de cor-

This document may not be reproduced, modified, adapted, published, translated in any way, in whole or in part, nor disclosed to a third party without the prior written consent of ENAC. © 2023, ENAC

rection en post-traitement, en plus de la recherche sur l'amélioration du matériel de mesure. Les objectifs sont d'améliorer la précision et d'accélérer les temps de mesure. En premier, on retrouve les méthodes de transformation champ-proche champ-lointain qui permettent de déterminer le diagramme champ lointain de l'antenne à partir de mesures effectuées en champ proche [6, 7, 8]. Des méthodes sont aussi développées pour raccourcir les temps de mesure, par exemple en diminuant et en simplifiant les points de mesure [9, 10]. Finalement, beaucoup de méthodes ont pour but de diminuer l'effet de l'environnement comme les méthodes de fenêtrage temporel qui isolent le signal d'intérêt des multi-trajets grâce au retard existant entre eux [11]. Les méthodes actuelles de reconstruction et de filtrage spatial reposent sur la représentation en courants équivalents de l'AST [12, 13]. Dans de nombreuses méthodes, la correction repose sur la décomposition du champ en harmoniques comme dans la correction de sonde [6, 14], le filtrage spectral [15] ou la méthode de compensation de champ de zone de test [16, 17, 18]. Ces méthodes profitent des différentes propriétés du spectre et ont pour but d'isoler le plus précisément possible le diagramme de rayonnement de l'antenne de l'environnement électromagnétique.
Dans le cas de la mesure d'antennes, les données sont principalement de géométrie sphérique, comme les diagrammes de rayonnements champ lointain sont définis sur la sphère. Ainsi de nombreuses installations de mesure d'antennes sont conçues pour la mesure sphérique. C'est pourquoi des outils d'analyse sphériques ont été développés. En particulier, les harmoniques sphériques sont les bases de décomposition les plus connues pour l'analyse de mesure d'antennes [6]. Par ailleurs, le rayonnement d'une antenne est un champ de vecteurs, d'où l'intérêt pour le concept de spin. Ce concept a été développé et appliqué aux harmoniques sphériques par Penrose [19, 20]. Il permet d'exprimer des champs de vecteurs tangents à une sphère en terme de composantes de spin qui ont d'intéressantes propriétés de rotations. De plus, McEwen & Wiaux ont développé des algorithmes de transformation en harmoniques sphériques de spin rapides et stables, en parallèle de théorèmes d'échantillonnage sur la sphère [21].
Ces chercheurs ont aussi mené récemment des travaux sur les décompositions en ondelettes sur la sphère. Les ondelettes sont généralement utilisées pour compresser des données comme des images (JPEG), pour effectuer de la déconvolution et du débruitage dans de nombreux domaines de la physique et de l'ingénieurie [22, 23]. Des fonctions d'ondelettes spécifiques ont récemment été développées pour analyser des données sur la sphère [24] et l'analyse multirésolution en ondelettes a été utilisée pour décrire le fond diffus cosmologique [25]. McEwen & Wiaux ont aussi développé des algorithmes rapides de transformées en ondelettes sphériques dans [26]. Par conséquent, ce type de décomposition pourrait apporter une autre dimension à l'analyse de mesures d'antennes sur la sphère et au développement de nouvelles méthodes de correction. En particulier, la transformée en ondelettes permet de localiser des composantes dans les domaines spatial et spectral ce qui permettrait de reconnaître les effets de perturbations indésirées dans la mesure. C'est une manière d'améliorer la correction basée sur les décompositions en harmoniques sphériques.
Les objectifs principaux de cette thèse sont de développer des méthodes d'analyse et de correction pour la mesure d'antennes sphérique, basées sur les harmoniques et les ondelettes sphériques de spin. Ces méthodes doivent remplir des objectifs de performance en terme de précision et de temps de mesure. Les objectifs détaillés de la thèse sont:

- l'analyse des avantages des harmoniques sphériques de spin, dans le domaine des

antennes et la formulation de leur relation avec les harmoniques sphériques définies par Hansen [6],

- l'utilisation des ondelettes sphériques de spin en temps qu'outils d'analyse de diagrammes de rayonnement,
- la formulation rigoureuse du problème de la mesure d'antenne, à partir de théorèmes basiques d'électromagnétisme,
- le test de méthodes de correction basées sur la déconvolution et le débruitage, à partir de transformées de Fourier et en ondelettes. Ces tests ont été réalisés sur un cas simple simulé.

D.2 Mesure d'antennes

D.2.1 Introduction

Les performances d'une AST sont caractérisées par ses paramètres en champ lointain, tels que son diagramme de rayonnement, son gain, sa directivité et sa polarisation [5]. Elles sont généralement évaluées à travers la mesure d'une transmission, dans des espaces spécifiques à l'aide d'une instrumentation particulière. L'objet de ce chapitre a été de dresser un état de l'art de la mesure d'antennes. Dans une première partie, les différents environnements et configurations de mesure sont présentés, puis les équipements requis. Finalement, la chambre de mesure de l'ENAC est présentée.

D.2.2 Bases de mesure d'antennes

Le choix du banc d'essai pour une antenne dépend du type d'antenne, de la gamme de fréquences et des exigences spécifiques de mesure. Le banc d'essai et les instruments forment l'environnement physique de la mesure. Quant à l'environnement électromagnétique, il est défini comme tous les rayonnements présents dans le volume de mesure qui ne font pas partie du diagramme de rayonnement de l'antenne. Ces deux environnements ont une influence considérable sur la précision de la mesure. Les environnements de mesure les plus communs sont présentés dans cette section, ainsi que les différentes configurations de mesure permettant d'obtenir le diagramme champ lointain de l'AST.

D.2.2.1 Environnements de mesure

Il existe de nombreux environnements de mesure, qui présentent chacun des intérêts et des inconvénients:

- Les **mesures en espace libre** ne présentent aucun équipement permettant d'isoler l'AST des perturbations extérieurs, venant des télécommunications mobiles ou des radars par exemple. Elles peuvent être effectuées en laboratoire ou à l'extérieur. Elles présentent l'avantage de pouvoir effectuer des mesures lorsque les conditions de champ lointain nécessitent que l'AST soit très loin de la sonde. Néanmoins, elles sont généralement peu précises.
- Les **chambres faradisées** arrêtent ou atténuent les rayonnements électromagnétiques venant de l'extérieur.

This document may not be reproduced, modified, adapted, published, translated in any way, in whole or in part, nor disclosed to a third party without the prior written consent of ENAC. © 2023, ENAC

- Une **chambre de réverbération** est une chambre faradisée dans laquelle un champ électromagnétique aléatoire est crée [29, 30, 31]. Le diagramme de rayonnement de l'AST en émission dans une telle chambre se distingue en ce qu'il est déterministe et peut ainsi être mesuré.

- Les **chambres anéchoïques** sont des chambres faradisées dont les murs sont recouverts de matériaux anéchoïques qui atténuent les réflexions. Ce sont les chambres de mesure les plus communes car elles constituent des environnements contrôlés. Elles sont néanmoins très coûteuses, notamment pour les plus grandes qui ne sont parfois que partiellement recouvertes de matériaux anéchoïques. La chambre anéchoïque du CNES est montrée sur la Figure D.1a et la chambre semi-anéchoïque de la Direction Générale de l'Armement (Solange) sur la Figure D.1b

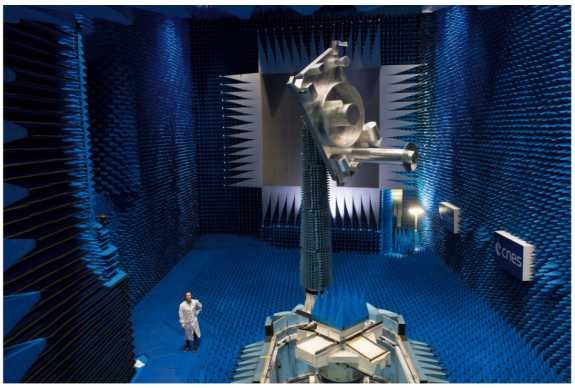

(a) Base compacte du CNES [33]

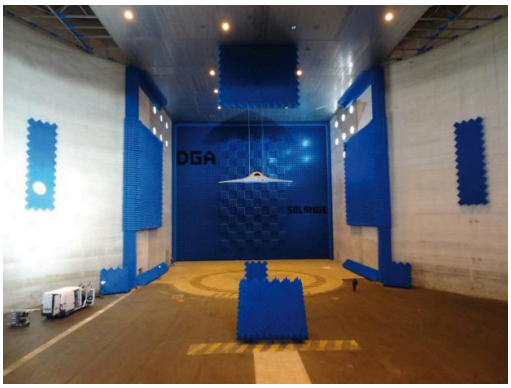

(b) Chambre semi-anéchoïque Solange, Bruz, DGA-MI [34]

Figure D.1: Chambres de mesure anéchoïques

D.2.2.2 Les configurations de mesure

Afin d'obtenir le diagramme champ lointain d'un antenne, sa mesure peut être effectuée de différentes manières :

- La **mesure champ lointain** permet d'obtenir directement le diagramme de rayonnement de l'antenne [2, 5]. La sonde est fixe et mesure le signal émis par l'antenne fixée sur un positionneur qui lui permet de parcourir toute la sphère. Ainsi on obtient le rayonnement de l'antenne en champ lointain, dans toute les directions. Néanmoins, ce type de mesure nécessite que l'antenne et la sonde soient suffisamment loin l'une de l'autre, selon l'équation (D.1), ce qui peut mener à des tailles de chambre de mesure irréalistes. Par exemple, la condition de champ lointain d'une antenne émettant à 30 GHz montée sur un satellite large est de 80 m.

- Dans une **base compacte de mesure d'antennes (BCMA)**, les conditions de champ lointain sont émulées en éclairant l'AST par une onde plane, à l'aide d'un réflecteur. La chambre de mesure du CNES est une BCMA, comme on peut le voir sur la Figure D.1a.

- Les **mesures champ proche** permettent de s'affranchir des conditions de champ lointain en passant par un post-traitement du signal mesuré, la transformation champ proche-champ lointain. Ainsi les chambres de mesure champ proche sont

souvent de plus petite dimension et moins coûteuses, comme la chambre Starlab de MVG, sur la Figure D.2.

Figure D.2: Base champ proche Starlab [42]

D.2.3 Les équipements d'une salle de mesure

Une salle de mesure présente des équipements spécifiques, dont le choix est crucial pour atteindre les précisions de mesure attendu. Un schéma d'une configuration générale de mesure d'antenne est présenté sur la Figure D.3. La rotation de l'antenne est permise par un positionneur contrôlé par logiciel. L'analyseur de réseaux vectoriel (VNA) alimente la sonde et collecte le signal mesuré. La sonde peut être à double polarisation ou montée sur un positionneur pour mesurer les deux polarisations de l'antenne. Enfin des calibrations et post-traitements peuvent être effectuées, avec du matériel de calibration et des logiciels spécifiques.

This document may not be reproduced, modified, adapted, published, translated in any way, in whole or in part, nor disclosed to a third party without the prior written consent of ENAC. © 2023, ENAC

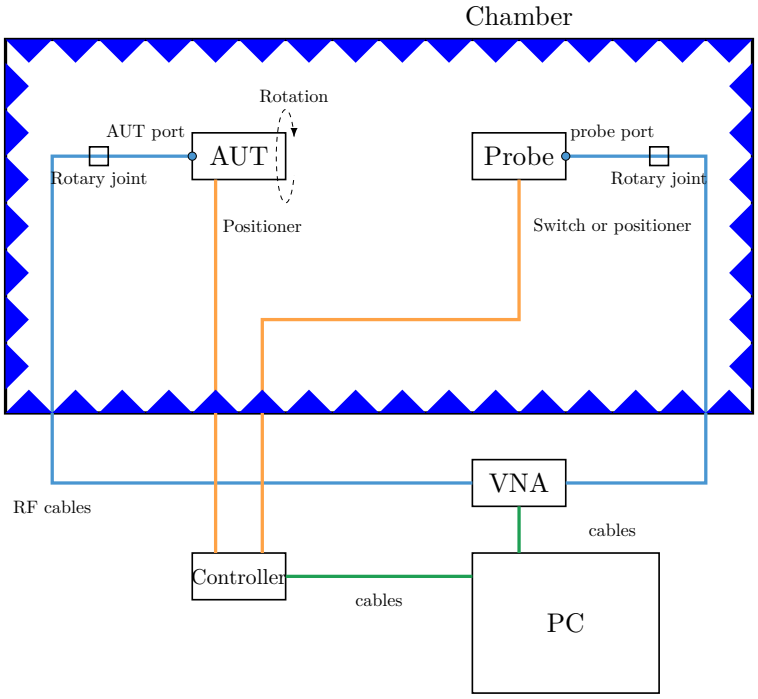

Figure D.3: Base de mesure RF

D.2.4 Base de mesure de l'ENAC

La base de mesure de l'ENAC a constitué un atout pour les recherches effectuées durant cette thèse. C'est une base qui est utilisée pour la recherche et l'enseignement. On peut en voir une photo sur la Figure D.4.

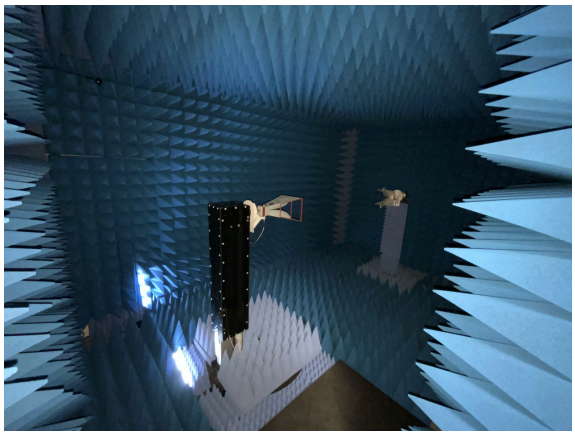

Figure D.4: Base de mesure de l'ENAC

D.2.5 Conclusion

Ce chapitre a permis d'établir le contexte de la thèse, en introduisant les différents environments et configurations de mesures.

D.3 Outils théoriques pour la mesure sphérique d'antenne

D.3.1 Introduction

Dans le chapitre précédent, il est expliqué que la mesure est souvent soumise à des post-traitements et des analyses. Ce chapitre a pour but d'introduire les outils classiques d'analyses de diagrammes d'antennes. Dans un premier temps, les systèmes de coordonnées et opérateurs de la mesure sphérique sont introduits, suivis par les harmoniques sphériques qui sont des bases de décomposition. Finalement, les méthodes de post-traitement habituellement appliquées aux diagrammes d'antennes sont présentées.

D.3.2 Systèmes de coordonnées et opérateurs

La mesure consiste en la détermination du niveau de signal émis par l'antenne, en fonction d'une position ou d'une direction dans l'espace. Celles-ci doivent donc être paramétrées sur la sphère à travers plusieurs outils :

- les **coordonnées sphériques** qui permettent de positionner la donnée de mesure sur la sphère,
- les **angles d'Euler**, pour paramétrer les rotations effectuées par l'antenne,
- **l'opérateur de rotation**, pour paramétrer les données après la rotation.

D.3.3 Harmoniques sphériques standards

Les harmoniques sphériques sont des outils d'analyse classiques dans le domaine des mesures d'antennes. Ce sont des solutions particulières des équations de Maxwell, formant une base orthonormale sur la sphère. Elles permettent l'analyse de champs électromagnétiques sur la sphère, comme décrit dans les livres de Stratton [27], Felsen and Marcuvitz [66], et Van Bladel [67]. Cette section présente les harmoniques sphériques standards, comme définies par Hansen [6].
Une fonction transverse d'harmonique sphérique vectorielle peut s'écrire

$$\boldsymbol{e}_{\mathrm{t}\,m,n}^{\,p,(c)}(r,\theta,\phi) \text{ ou } \boldsymbol{h}_{\mathrm{t}\,m,n}^{\,p,(c)}(r,\theta,\phi) \tag{D.2}$$

selon qu'elle serve à décomposer un champ électrique ou magnétique. Ces fonctions dépendent de la nature TE ou TM du champ, des fonctions de Hankel, et des fonctions de Legendre, paramétrées respectivement par les indices $p = \{TE, TM\}$, $c = \pm$, et les indices m, n.
Ainsi, dans une région sans source, les composantes transverses $\boldsymbol{E}_{\mathrm{t}}$ et $\boldsymbol{H}_{\mathrm{t}}$ du champ électromagnétique peuvent s'écrire

$$\begin{aligned}
\boldsymbol{E}_{\mathrm{t}} &= \sum_{p=\mathrm{TE,TM}} \sum_{c=\pm} \sum_{n=1}^{\infty} \sum_{m=-n}^{n} Q_{m,n}^{p,(c)} \boldsymbol{e}_{\mathrm{t}\,m,n}^{\,p,(c)}(r,\theta,\phi), \\
\boldsymbol{H}_{\mathrm{t}} &= \sum_{p=\mathrm{TE,TM}} \sum_{c=\pm} \sum_{n=1}^{\infty} \sum_{m=-n}^{n} Q_{m,n}^{p,(c)} \boldsymbol{h}_{\mathrm{t}\,m,n}^{\,p,(c)}(r,\theta,\phi),
\end{aligned} \tag{D.3}$$

avec $Q_{m,n}^{p,(c)}$ les coefficients d'harmoniques sphériques, avec $p = \mathrm{TE}$ or $p = \mathrm{TM}$, calculés à partir de la relation orthogonalité [6].
La Figure D.1 présentent une illustration des premières fonctions d'harmoniques. Les premières harmoniques, avec $n = 1$ présentent des variations lentes, alors que les niveaux supérieurs présentent des variations plus rapides.

This document may not be reproduced, modified, adapted, published, translated in any way, in whole or in part, nor disclosed to a third party without the prior written consent of ENAC. © 2023, ENAC

n/|m|	0	1	2	3
1	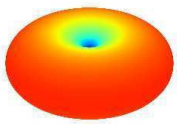	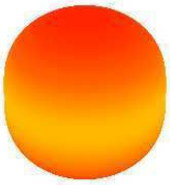		
2	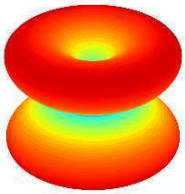	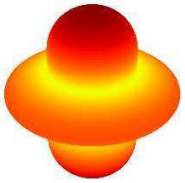	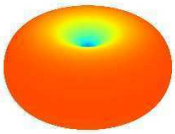	
3	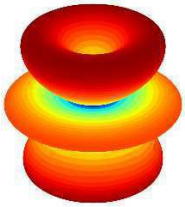	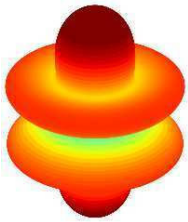	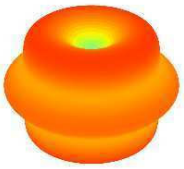	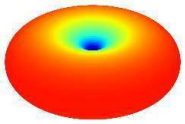

Table D.1: Amplitude du champ des harmoniques sphériques pour $n \in [1, 3]$ et $m \in [-3, 3]$

Physiquement, il existe une limite N_{AUT} au nombre d'harmoniques qu'une antenne peut rayonner. Celle-ci dépend de la taille de l'antenne et de la fréquence, et est donnée par

$$N_{\mathrm{AUT}} = [kr_0] + n_1, \tag{D.4}$$

avec r_0 le rayon de la plus petite sphère entourant l'antenne et n_1 dépend du niveau de précision attendu.

D.3.4 Exemples d'analyse en harmoniques sphériques

Cette section a pour but d'illustrer l'utilisation des harmoniques sphériques pour l'analyse de diagrammes de rayonnement d'antennes. Le cas présenté ici est celui du rayonnement d'une antenne cornet simulée avec Altair Feko à 5 GHz. Son diagramme de rayonnement et sa décomposition en harmoniques sphériques sont présentés sur les Figures D.5 et D.6.

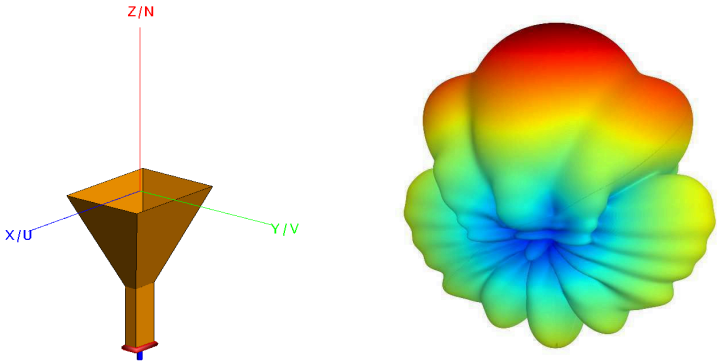

(a) Antenne cornet

(b) Champ E rayonné par le cornet (dB)

Figure D.5: Caractéristiques de l'antenne cornet

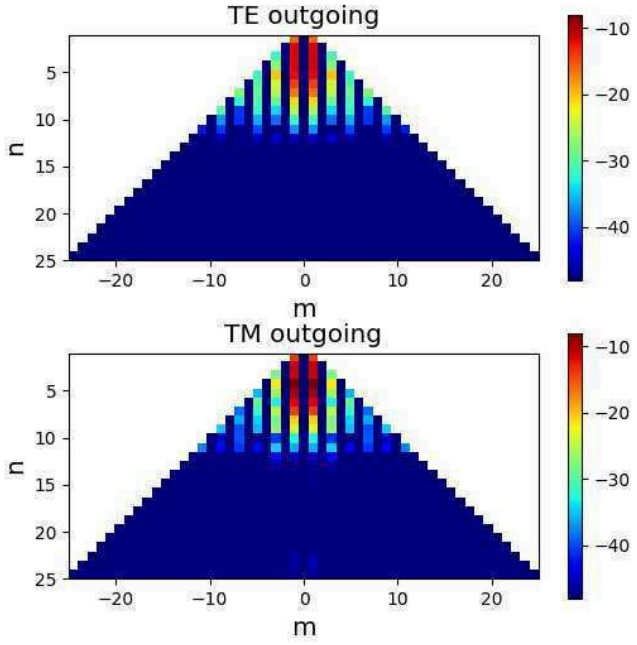

Figure D.6: Coefficients normalisés d'harmoniques sphériques TE et TM de l'antenne cornet (dB)

D.3.5 Post-traitement pour la mesure d'antennes

Cette section présente les principaux post-traitements appliqués au signal de mesure. Certains ont pour but d'émuler les conditions de champ lointain comme l'algorithme de transformation champ proche-champ lointain [6, 7, 8], d'autres de compenser les perturbations introduites par l'environnement de mesure. On peut par exemple citer la correction de sonde [6, 14], le fenêtrage temporel [11], le filtrage spatial et la reconstruction de courants [12, 13], le filtrage spectral et la compensation de zone de

This document may not be reproduced, modified, adapted, published, translated in any way, in whole or in part, nor disclosed to a third party without the prior written consent of ENAC. © 2023, ENAC

test [15,16,17,18]. Enfin certaines visent à accélérer les temps de calcul, en minimisant le nombre de points de mesure nécessaires sur la sphère, à partir de connaissances à priori sur l'AST [9,10].

D.3.6 Conclusion

Ce chapitre a permis de présenter les outils classiques d'analyse et de corrections de mesure de diagramme de rayonnement d'antennes.

D.4 Harmoniques sphériques de spin

D.4.1 Introduction

Les harmoniques sphériques de spin sont une alternative aux harmoniques sphériques classiques. Le paramètre spin a été introduit par Penrose dans [19], il permet de décomposer un vecteur sur la sphère et présente des propriétés de rotation avantageuses. Cette section présente la théorie des harmoniques sphériques de spin et l'algorithme rapide qui permet de calculer rapidement la transformée en spin. Le lien avec les harmoniques classiques de Hansen est calculé et des exemples de ce type de décomposition sont présentés.

D.4.2 Théorie des harmoniques sphériques de spin

D.4.2.1 Fonction de spin

Les fonctions de spin sont des fonctions de carré intégrable sur la sphère, notées $u_s \in L^2(\mathcal{S}^2)$, paramétrées par le spin $s \in \mathbb{Z}$. Une fonction de spin est définie par son comportement lors d'une rotation locale, notée $'$, de $\chi_l \in [0, 2\pi[$. Celle-ci introduit un déphasage χ_l donné par

$$u'_s(\theta,\phi) = \mathrm{e}^{-is\chi_l} u_s(\theta,\phi). \tag{D.5}$$

D.4.2.2 Harmoniques sphériques de spin

Les harmoniques sphériques de spin sont proches des harmoniques sphériques de Hansen. Elles sont notées $Y_{smn} \in L^2(\mathcal{S}^2)$ avec $s \in \mathbb{Z}$, $n \geq |s|$, et $|m| \leq n$. Elles forment une base orthogonale de $L^2(\mathcal{S}^2)$.

D.4.2.3 Expression d'un vecteur tangent sur la sphère en harmoniques sphériques

Considérons la composante tangentielle $\boldsymbol{V}_\mathrm{t}$ d'un champ $\boldsymbol{V}$. Ce vecteur peut être exprimé comme

$$\boldsymbol{V_t}(\theta,\phi) = \sum_{n=0}^{\infty} \sum_{m=-n}^{n} V_{+1,m,n} Y_{1,m,n} \hat{\boldsymbol{u}}_{+1} + V_{-1,m,n} Y_{-1,m,n} \hat{\boldsymbol{u}}_{-1}. \tag{D.6}$$

en terme d'harmoniques sphériques de spin.

D.4.2.4 Propriété de rotation globale d'une fonction de spin sur la sphère

La rotation globale $\mathcal{R}_{s\epsilon}$ d'une fonction de spin $u_s \in L^2(\mathcal{S}^2)$ sur la sphère est donnée par

$$(\mathcal{R}_{s\epsilon} u_s)(\hat{\boldsymbol{r}}_1) = e^{-is\chi_g} u_s(\mathbf{R}_\epsilon^{-1}\hat{\boldsymbol{r}}_0), \tag{D.7}$$

avec $\mathbf{R}_\epsilon$ la matrice de rotation 3D. $\chi_g \in [0, 2\pi]$ est défini comme le troisième angle d'Euler de la rotation $\mathbf{R}_{\epsilon'} = \mathbf{R}_\epsilon^{-1}\mathbf{R}_{(\theta,\phi,0)}$ i.e. $\epsilon' = (.,.,\chi_g)$. Ainsi, on constate qu'un simple déphasage apparaît lors de la rotation.

D.4.3 Transformée en harmoniques sphériques de spin : échantillonnage et algorithme rapide

La transformée en harmoniques sphériques de spin repose sur un théorème d'échantillonnage et un algorithme, développés par McEwen & Wiaux qui permettent des calculs rapides, comparé à d'autres algorithmes classiques.
Les points de la grille d'échantillonnage sont donnés par

$$\begin{aligned} \theta_{p_\theta}^{N_{\mathrm{AUT}}} &= \frac{\pi(2p_\theta + 1)}{2N_{\mathrm{AUT}} - 1}, && \text{for } p_\theta \in \{0, 1, ..., N_{\mathrm{AUT}} - 1\}, \\ \phi_{p_\phi}^{N_{\mathrm{AUT}}} &= \frac{2\pi p_\phi}{2N_{\mathrm{AUT}} - 1}, && \text{for } p_\phi \in \{0, 1, ..., 2N_{\mathrm{AUT}} - 2\}, \end{aligned} \tag{D.8}$$

avec N_{AUT} le dernier niveau d'harmonique, *i.e.*. Ainsi la grille est définie à partir de la taille de l'antenne, dont dépend N_{AUT}. Néanmoins, il peut être intéressant, notamment dans le contexte de la correction de mesure d'antenne de calculer les harmoniques de niveau supérieurs, jusqu'à un niveau qu'on notera N. En effet, les perturbations introduites par l'environnement sont souvent rapides et excitent des harmoniques qui ne peuvent pas faire partie du spectre de l'antenne, ce qui les rend détectables.
L'algorithme de calcul de la transformée en harmoniques sphériques de spin repose sur l'utilisation des fonctions de Wigner et de transformées de Fourier rapides, effectuées sur une extension périodique de la sphère, le tore. Sa complexité est en $O(N^3)$ et sa précision est la précision-machine. Cet algorithme se distingue aussi par sa stabilité.

D.4.4 Relation entre les harmoniques de spin et les harmoniques de Hansen

Cette thèse relie deux formulations d'harmoniques sphériques, chacune présentant des avantages et des inconvénients. L'approche Hansen est communément utilisée dans le traitement d'antenne et prend en compte les effets de la propagation. La formulation en spin permet de représenter simplement la donnée sous plusieurs formes, sur la sphère, de calculer des rotations locales et globales simplement et de considérer de hauts ordres d'harmoniques sphériques. Par ailleurs elles ont été développées en parallèle d'algorithmes rapides et stables. Par conséquent, il est avantageux de formuler le lien entre ces type harmoniques.
Ainsi, les coefficients d'harmoniques sphériques de spin $(C_{m,n}^{(\mathrm{E}),s}(r), C_{m,n}^{(\mathrm{H}),s}(r))$ et les coefficients d'harmoniques sphériques de Hansen $Q_{m,n}^{p,(c)}$ sont liés par

This document may not be reproduced, modified, adapted, published, translated in any way, in whole or in part, nor disclosed to a third party without the prior written consent of ENAC. © 2023, ENAC

$$\begin{bmatrix} C_{m,n}^{(\mathrm{E}),+1}(r) \\ C_{m,n}^{(\mathrm{E}),-1}(r) \\ C_{m,n}^{(\mathrm{H}),+1}(r) \\ C_{m,n}^{(\mathrm{H}),-1}(r) \end{bmatrix} = kr\frac{s_m}{\sqrt{2}} \begin{bmatrix} iz_n^{(+)}(kr) & iz_n^{(-)}(kr) & -dz_n^{(+)}(kr) & -dz_n^{(-)}(kr) \\ iz_n^{(+)}(kr) & iz_n^{(-)}(kr) & dz_n^{(+)}(kr) & dz_n^{(-)}(kr) \\ -dz_n^{(+)}(kr) & -dz_n^{(-)}(kr) & iz_n^{(+)}(kr) & iz_n^{(-)}(kr) \\ dz_n^{(+)}(kr) & dz_n^{(-)}(kr) & iz_n^{(+)}(kr) & iz_n^{(-)}(kr) \end{bmatrix} \begin{bmatrix} Q_{m,n}^{\mathrm{TE},(+)} \\ Q_{m,n}^{\mathrm{TE},(-)} \\ Q_{m,n}^{\mathrm{TM},(+)} \\ Q_{m,n}^{\mathrm{TM},(-)} \end{bmatrix}. \tag{D.9}$$

Cette matrice est inversible, ce qui permet d'utiliser un type d'harmonique ou l'autre en fonction du contexte.

D.4.5 Analyses de diagrammes d'antennes au moyen d'harmoniques sphériques de spin

Dans la thèse, la décomposition en harmoniques sphériques de spin a été effectuée sur plusieurs simulations et une mesure d'antenne. Ces décompositions ont notamment permis de montrer leur capacité à visualiser la polarisation d'une antenne. En effet les coefficients de spin +1 correspondent aux coefficients de la composante de polarisation droite du rayonnement, tandis que les coefficients de spin -1 correspondent à la polarisation gauche. Dans ce résumé, seuls deux exemples sont présentés.
Le cornet présenté dans la section D.3.4 a été décomposé en harmoniques sphériques de spin, comme montré sur la Figure D.7. Ce cornet est en polarisation linéaire, ce qui peut être décomposé en une polarisation droite et une polarisation gauche, correspondant aux coefficients de spin +1 et -1 respectivement.

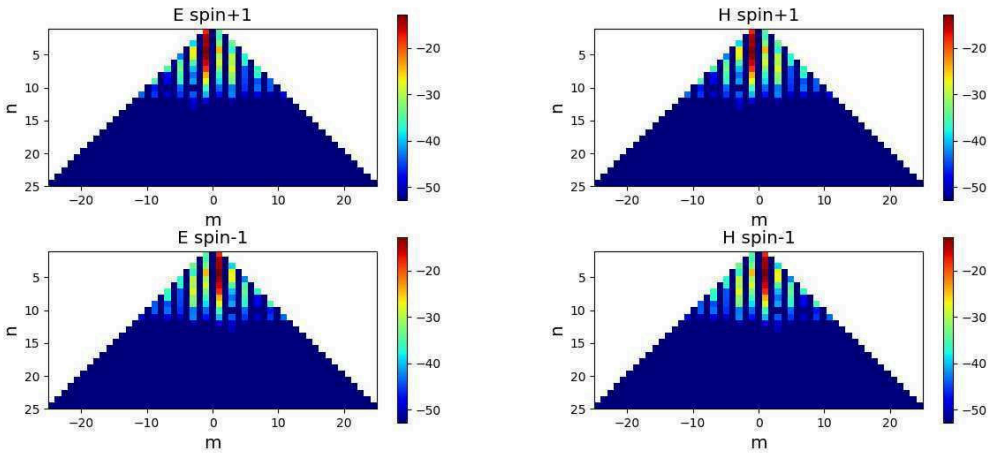

Figure D.7: Décomposition en harmoniques sphériques de +1 and -1 du diagramme de rayonnement d'un cornet en polarisation linéaire (dB)

La conversion de ces coefficients en coefficients de Hansen a également été effectuée, grâce à (D.9).
Afin de tester les performances de l'algorithme rapide de calcul d'harmoniques sphériques de spin, la décomposition a été effectuée sur une simulation de Surface Equivalente Radar (SER) d'un avion, la simulation est illustrée sur la Figure D.8. Une onde plane rayonne en direction de l'avion et sa réflexion est simulée. Ce cas est intéressant car les différentes réflexions et diffractions sur les éléments de l'avion introduisent des variations très rapides et variées, qu'il est difficile de simuler avec une antenne seule.

Ainsi, la décomposition en harmoniques sphériques de spin de cette SER a été calculée jusqu'au niveau $N = 2048$, comme on peut le voir sur la Figure D.9.

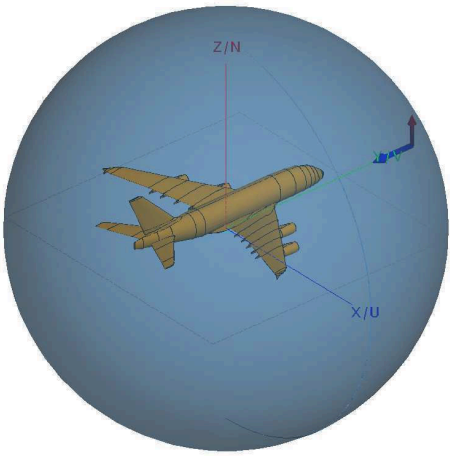

Figure D.8: Simulation de la SER de l'avion

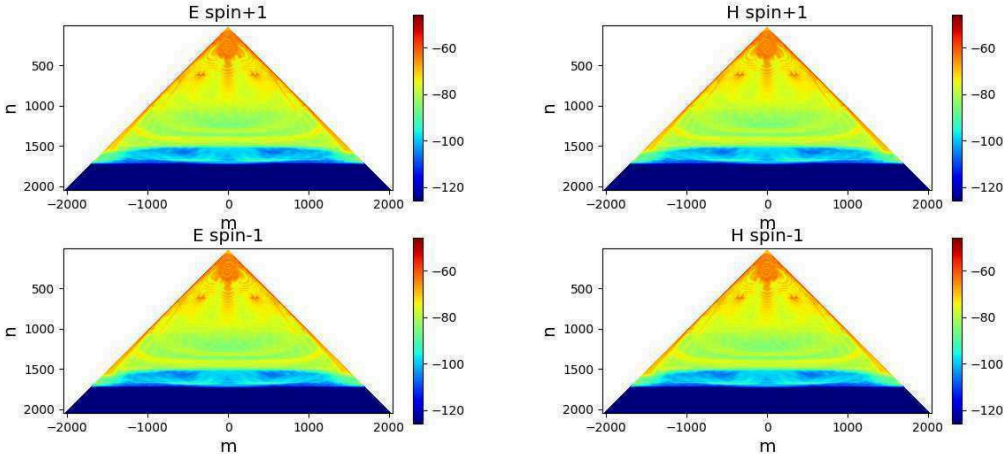

Figure D.9: Décomposition en harmoniques sphériques jusqu'au niveau $N = 2048$

Au total, 16,793,600 coefficients ont été calculés en 4 minutes ce qui démontre les performances remarquables de l'algorithme développé par McEwen & Wiaux. La conversion en coefficients de Hansen prend 5 min 24 s.

D.4.6 Conclusion

Ce chapitre a présenté la théorie des harmoniques sphériques de spin et les algorithmes de calculs associés. Une formulation permettant de les calculer à partir des harmoniques sphériques de Hansen et vice-versa a été fournie. Des transformées en harmoniques sphériques de spin ont été calculées, vérifiant les performances remarquables des algorithmes de calcul. Néanmoins, dans le cadre de son utilisation pour la détection de perturbations lors de mesure d'antennes, la décomposition en harmoniques sphériques

This document may not be reproduced, modified, adapted, published, translated in any way, in whole or in part, nor disclosed to a third party without the prior written consent of ENAC. © 2023, ENAC

ne fournit pas de visualisation claire. Les coefficients parasites sont peu visibles sur les diagrammes. Ainsi l'étude des ondelettes sphériques de spin vise à obtenir une meilleure visualisation.

D.5 Ondelettes sphériques de spin

D.5.1 Introduction

Les ondelettes constituent un concept largement répandu, ayant trouvé des applications dans divers domaines tels que le traitement de signal, la compression de données et l'analyse d'images. Leur principal avantage réside dans leur capacité à représenter et analyser les données à différentes échelles, couvrant des informations générales jusqu'aux caractéristiques localisées de petite taille [23, 104, 105, 106, 107]. Cette caractéristique assure de bonnes propriétés de localisation spatiales et spectrales, qui manquent aux outils d'analyse classiques comme Fourier.

D.5.2 Ondelettes multi-résolution pour les signaux 1D

Une base d'ondelette est définie par une fonction d'échelle et des fonctions d'ondelettes. Elle permet de décomposer un signal en niveau de variations. Une illustration d'une telle décomposition est proposée sur la Figure D.10. Le signal correspondant au rayonnement champ lointain bruité d'une ouverture rayonnante carrée d'une largeur 4λ est décomposé en 4 niveaux d'ondelettes.

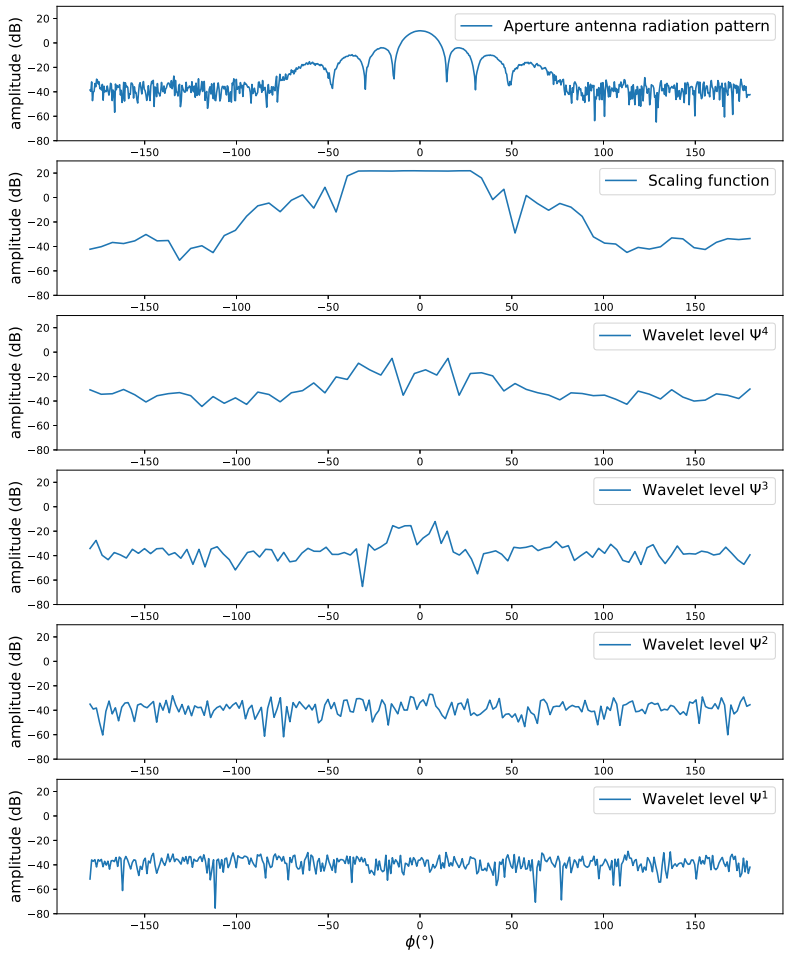

Figure D.10: Décomposition en ondelette du signal bruité d'une ouverture rayonnante

On peut observer la fonction d'échelle et les niveaux d'ondelettes. Les niveaux d'ondelettes élevés contiennent probablement l'information correspondant au bruit introduit dans le signal. En effet les fonctions d'ondelettes sont de bons outils de débruitage.

D.5.3 Ondelettes sphériques

Les ondelettes sphériques sont définies sur la sphère, elles sont formées à partir des harmoniques sphériques de spin [111]. On peut en voir une illustration sur la Figure D.11.

This document may not be reproduced, modified, adapted, published, translated in any way, in whole or in part, nor disclosed to a third party without the prior written consent of ENAC. © 2023, ENAC

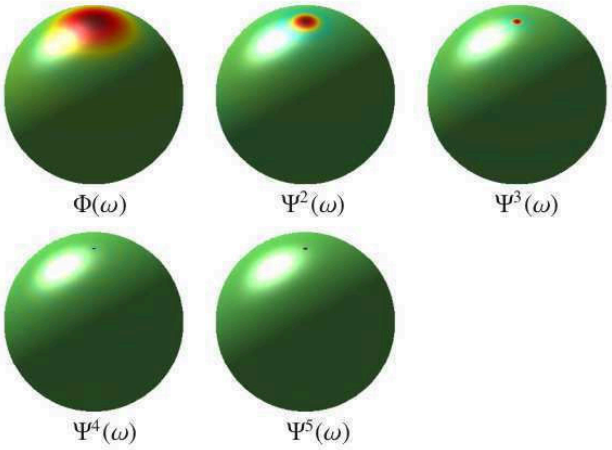

Figure D.11: Fonctions d'ondelettes axisymétriques [111]

Pour couvrir toute la sphère et former une base de $L^2(\mathcal{S}^2)$, ces fonctions sont soumises à des rotations.
Pour réaliser une décomposition en ondelettes sphériques, le signal sur la sphère est d'abord décomposé en harmoniques sphériques de spin. Les coefficients sont ensuite regroupés dans des niveaux d'ondelettes distincts, grâce à des filtres, ainsi qu'illustré sur la Figure D.12.

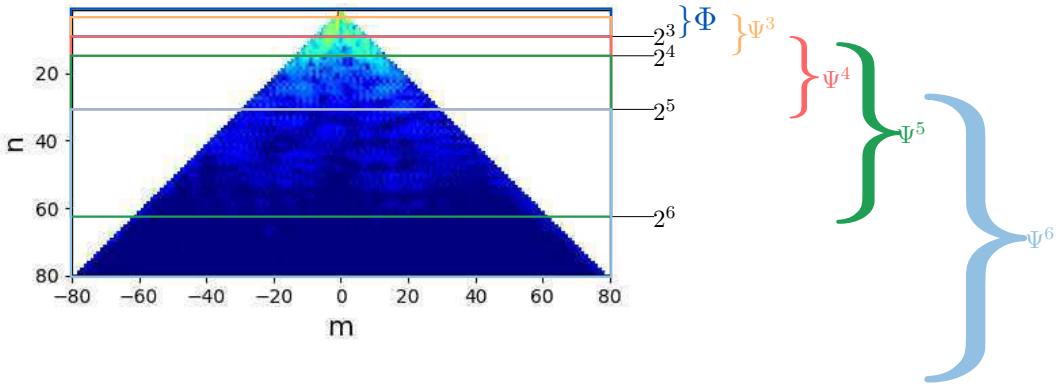

Figure D.12: Découpage de la décomposition en harmoniques sphériques de spin, pour la construction des niveaux d'ondelettes

Une transformée en harmoniques inverse est appliquée à chaque groupe de coefficients ce qui donne les différents niveaux d'ondelettes sur la sphère.

D.5.4 Analyses de diagrammes d'antennes au moyen d'ondelettes sphériques de spin

Dans cette thèse, plusieurs rayonnements de diagrammes d'antennes simulés ont été décomposés en ondelettes sphériques de spin. Dans ce résumé, il n'est montré que la

décomposition en niveaux d'ondelettes de la SER de l'avion présentée dans la Section D.4.5.
On peut voir la composante de spin +1 de ce diagramme de rayonnement sur la Figure D.13. La Figures D.14 montre la décomposition en ondelettes de cette composante du champ.

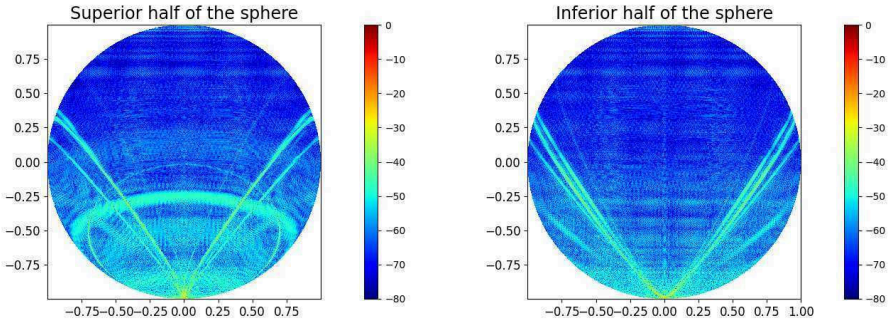

Figure D.13: Diagramme de rayonnement de la composante de spin +1 de la SER (polarisation droite) (dB)

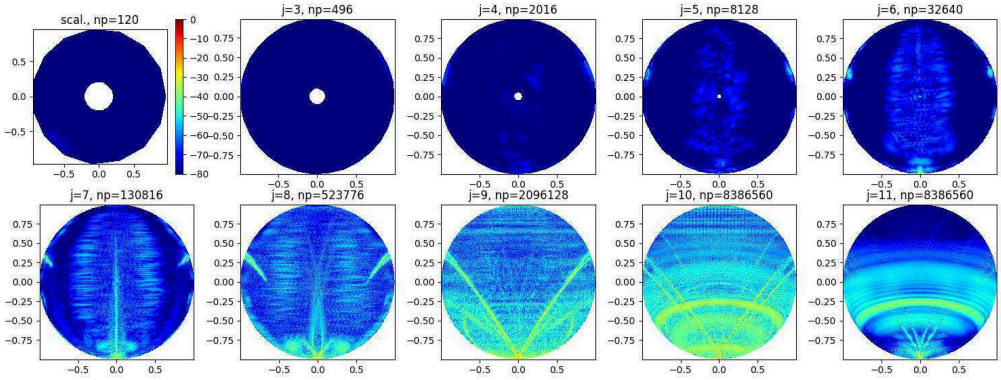

(a) Décomposition en ondelettes de la partie supérieure de la sphère

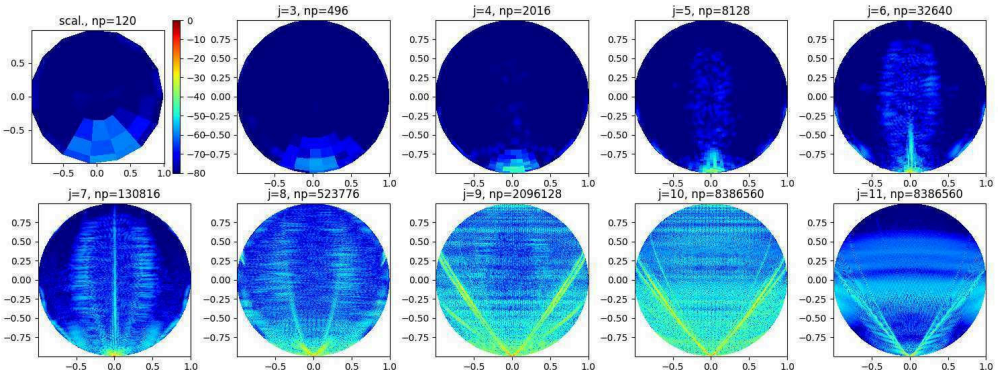

(b) Décomposition en ondelettes de la partie inférieure de la sphère

Figure D.14: Décomposition en ondelettes de la composante de spin +1 de la SER (dB)

Il est remarquable que les niveaux d'ondelettes élevés présentent des formes particulières correspondant probablement aux divers éléments réflecteurs de l'avion, comme

This document may not be reproduced, modified, adapted, published, translated in any way, in whole or in part, nor disclosed to a third party without the prior written consent of ENAC. © 2023, ENAC

l'empennage et les ailes. Ainsi, la décomposition en ondelettes permet la visualisation des variations rapides du champ, qui seraient invisibles sur une représentation en coefficients d'harmoniques sphériques.

D.5.5 Conclusion

Ce chapitre a permis de présenter les principales caractéristiques des ondelettes et plus particulièrement des ondelettes sphériques de spin. Cette transformée a permis de visualiser sur des simulations des éléments du diagramme de rayonnement qui ne sont pas discernables sur un diagramme de coefficients d'harmoniques sphériques classiques.

D.6 Formulation de la mesure d'antenne

D.6.1 Introduction

Il existe dans la littérature plusieurs manières de formuler la mesure d'antenne [6, 14, 114, 115]. Néanmoins, peu la formulent comme une convolution, alors que de nombreuses méthodes sont développées pour corriger la mesure par déconvolution [17, 116, 117]. L'objectif de ce chapitre est donc de formuler rigoureusement le problème de la mesure comme une convolution, en géométrie sphérique, à partir de théorèmes électromagnétiques classiques.

D.6.2 Énonce du problème

L'objective est de montrer que la mesure peut s'exprimer comme une convolution entre une quantité correspondant au champ rayonné par l'AST, p, et une quantité correspondant au champ rayonné par la sonde, dans l'environnement de mesure h, en absence de l'antenne. Ces signaux sont représentés sur la Figure D.15. L'objectif est d'écrire le signal de mesure b comme

$$b(\epsilon) = h(\epsilon) \circledast p(\epsilon) + n_0(\epsilon), \tag{D.10}$$

avec $\circledast$ l'opérateur de convolution, n_0 le bruit spatial, et ϵ les angles d'Euler correspondant à l'orientation de l'AST.

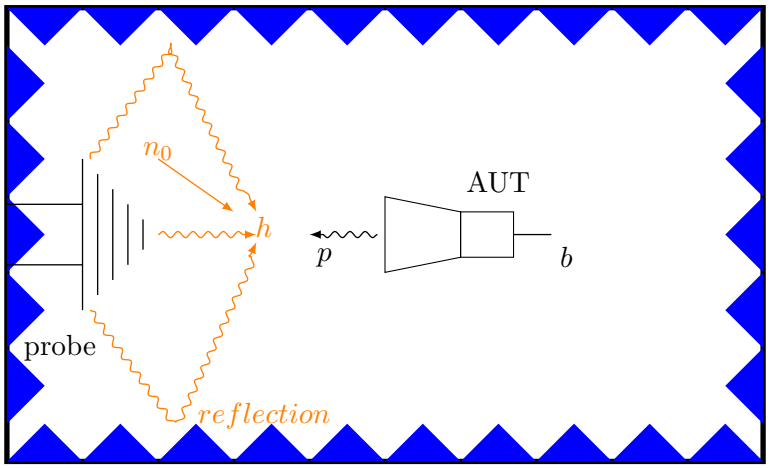

Figure D.15: L'AST (en réception) et la sonde dans une chambre anéchoïque

D.6.3 Principe d'équivalence

Le principe d'équivalence [118,119] permet d'établir que le rayonnement de l'AST dans l'environnement de mesure peut être remplacé par ses courants équivalents $(\boldsymbol{J}_{\text{es}}^{\text{eq}}, \boldsymbol{J}_{\text{ms}}^{\text{eq}})$ sur $\mathcal{S}_r^2$. $\mathcal{S}_r^2$ est la sphère de rayon r entourant l'AST. Cette équivalence est représentée sur la Figure D.16.

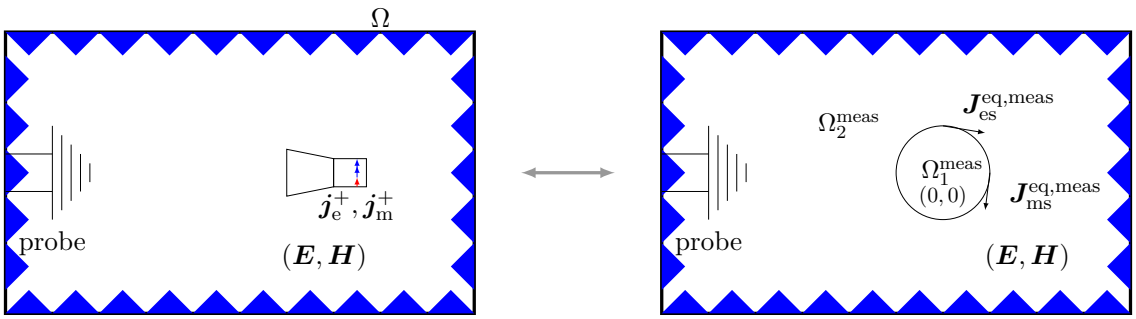

Figure D.16: Principe d'équivalence appliqué à une antenne rayonnant dans un environnement de mesure

Néanmoins, cet énoncé n'est pas immédiatement correct, en effet on peut supposer que l'antenne dans l'environnement de mesure perturbe son propre rayonnement, du point de vue de la sonde. Ces perturbations ne sont pas prise en compte par la représentation de l'AST par ses courant équivalents. Par conséquent, il a été nécessaire de valider ce résultat par des simulations, qui ont montré que la perturbation introduite par l'antenne elle-même était négligeable.

D.6.4 Réciprocité et mesure d'antennes

Le théorème de réciprocité mène à une formulation liant le champ de la sonde dans l'environnement aux courants équivalents de l'AST sur la sphère $\mathcal{S}_r^2$. Cette relation est

$$b = -\frac{1}{2} \iint_{\mathcal{S}_r^2} (\boldsymbol{E}^{\text{inc}} \cdot \boldsymbol{J}_{\text{es}}^{\text{eq}} - \boldsymbol{H}^{\text{inc}} \cdot \boldsymbol{J}_{\text{ms}}^{\text{eq}}) dS_r, \tag{D.11}$$

avec $\boldsymbol{E}^{\text{inc}}, \boldsymbol{H}^{\text{inc}}$ le champ de la sonde en absence de l'AST.

D.6.5 Convolution et formulation en spin

Lors de la mesure, on applique une rotation $\mathcal{R}_\epsilon$ à l'AST, la mesure devient

$$b(\epsilon) = -\frac{1}{2} \iint_{\mathcal{S}_r^2} (\boldsymbol{E}^{\text{inc}}(\theta,\phi) \cdot (\mathcal{R}_\epsilon \boldsymbol{J}_{\text{es}}^{\text{eq}\prime})(-\theta,-\phi) - \boldsymbol{H}^{\text{inc}}(\theta,\phi) \cdot (\mathcal{R}_\epsilon \boldsymbol{J}_{\text{ms}}^{\text{eq}\,\prime})(-\theta,-\phi)) dS_r, \tag{D.12}$$

avec ϵ les angles d'Euler. Ceci correspond à la formulation d'une convolution sur la sphère. Ainsi, on peut écrire

$$b = (\boldsymbol{E}^{\text{inc}}, \boldsymbol{H}^{\text{inc}}) \circledast (\boldsymbol{J}_{\text{es}}^{\text{eq}\prime}, \boldsymbol{J}_{\text{ms}}^{\text{eq}\,\prime}), \tag{D.13}$$

avec $\circledast$ l'opérateur de convolution sur la sphère.
Enfin, cette formulation a été développée en terme de spin, ce qui donne

This document may not be reproduced, modified, adapted, published, translated in any way, in whole or in part, nor disclosed to a third party without the prior written consent of ENAC. © 2023, ENAC

$$b(\epsilon) = -\frac{i}{2}\iint_{\mathcal{S}_r^2} e^{-i\chi_g} H_{+1}(\theta',\phi') E_{-1}^{\text{inc}}(\theta,\phi) - e^{i\chi_g} H_{-1}(\theta',\phi') E_{+1}^{\text{inc}}(\theta,\phi) \\ + e^{-i\chi_g} E_{+1}(\theta',\phi') H_{-1}^{\text{inc}}(\theta,\phi) - e^{i\chi_g} E_{-1}(\theta',\phi') H_{+1}^{\text{inc}}(\theta,\phi)) dS_r. \tag{D.14}$$

Cette formulation confirme l'avantage de l'utilisation du spin, il permet de simplifier les opérateurs de rotation et d'obtenir une formulation aboutie.

D.6.6 Conclusion

Ce chapitre a permis de formuler de manière rigoureuse le problème de la mesure, révélant la convolution résultante de l'impact de l'environnement sur le rayonnement de la sonde et de l'AST. Une formulation en spin a également permis de simplifier la formulation.

D.7 Correction de mesure en 2D

D.7.1 Introduction

Des méthodes de déconvolution existent dans de nombreux domaines du traitement de signal et de l'image, par exemple pour l'observation atmosphérique [120, 121]. Ce chapitre introduit une méthode de correction par déconvolution intégrant les ondelettes. Cette méthode est appliquée en 2D sur une simulation de mesure.

D.7.2 Formulation de la mesure en 2D

Dans ce chapitre, on considère la configuration de la Figure D.17, en configuration Transverse Magnétique 'TMz'.

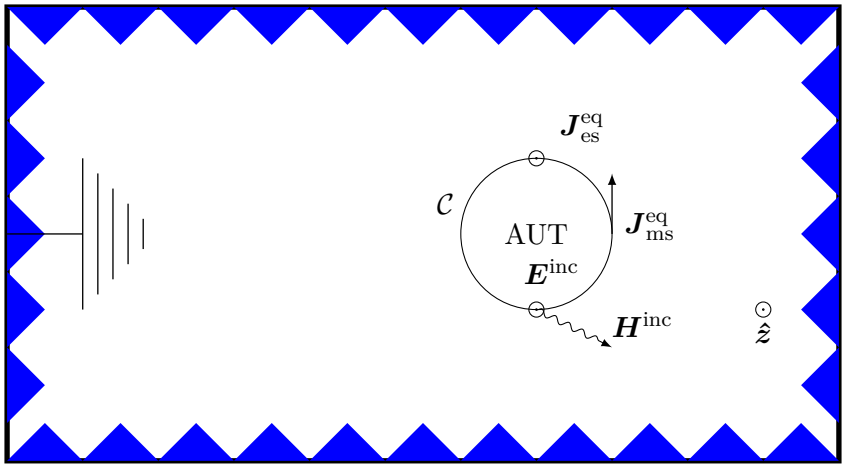

Figure D.17: Configuration 2D pour la polarisation transverse magnétique

Dans ce cas, la formulation de la mesure sur le cercle devient une convolution entre deux signaux 2π-périodiques

$$b(\phi) = \int_0^{2\pi} h(\phi') J_{\text{es}}^{\text{eq}}(\phi - \phi') r d\phi'. \tag{D.15}$$

D.7.3 Déconvolution pour la correction de mesure d'antennes

Les méthodes de déconvolution pour la correction de mesure en 2D reposent généralement sur les séries de Fourier. En passant dans le domaine spectral, une convolution devient une multiplication, ce qui simplifie les calculs. Le désavantage de la déconvolution est qu'elle entraîne une amplification du bruit, de par sa nature mal conditionnée. Par conséquent des méthodes de régularisation ont été développées. La méthode ForWaRD choisie dans cette thèse ajoute à la régularisation en Fourier une régularisation en ondelettes [122]. Ainsi la méthode de correction de mesure d'antennes se fait en deux mesures, comme schématisé sur la Figure D.18. La première mesure permet d'estimer le rayonnement de la sonde dans l'environnement, grâce à une antenne de référence. La seconde mesure consiste à utiliser cette estimation pour déconvoluer le signal de mesure, aboutissant finalement au rayonnement de l'antenne.

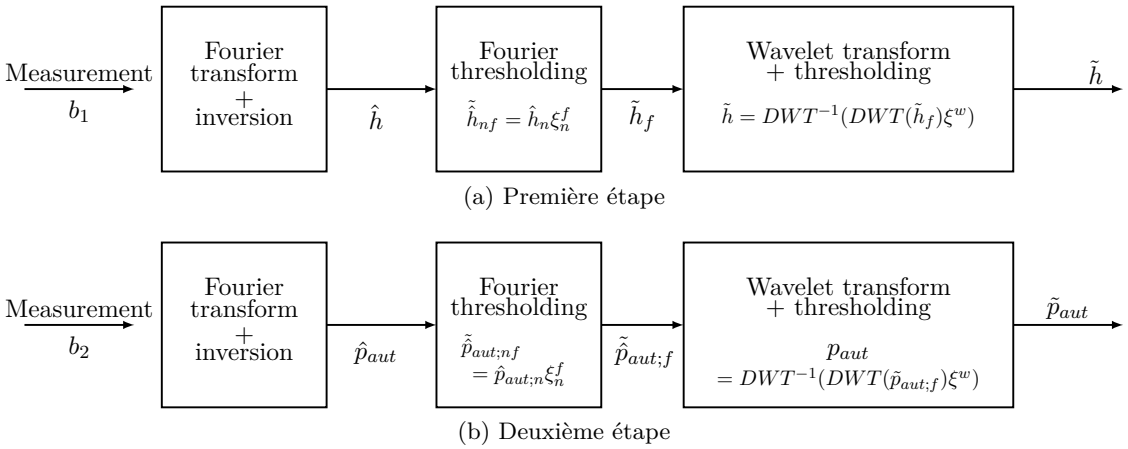

(a) Première étape

(b) Deuxième étape

Figure D.18: Étapes de la méthode de correction

D.7.4 Illustration de la méthode de déconvolution dans une simulation

Cette méthode a été simulée, comme on peut le voir sur la Figure D.19. Le signal de mesure b est perturbé par l'ajout d'un multi-trajet atténué de 20 dB et d'un niveau de bruit de -20 dB. p_{aut} correspond au diagramme théorique de l'antenne et p_{aut}^w à son diagramme après la correction.

This document may not be reproduced, modified, adapted, published, translated in any way, in whole or in part, nor disclosed to a third party without the prior written consent of ENAC. © 2023, ENAC

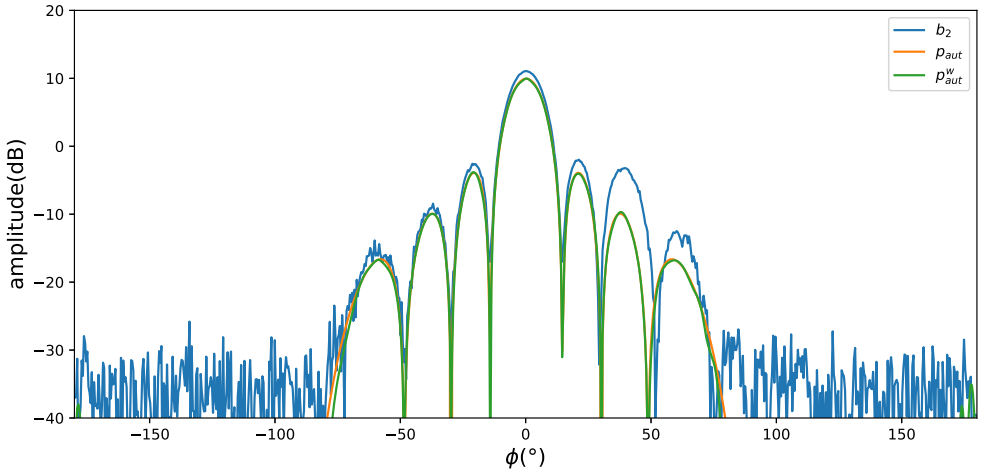

(a) Amplitude du champ

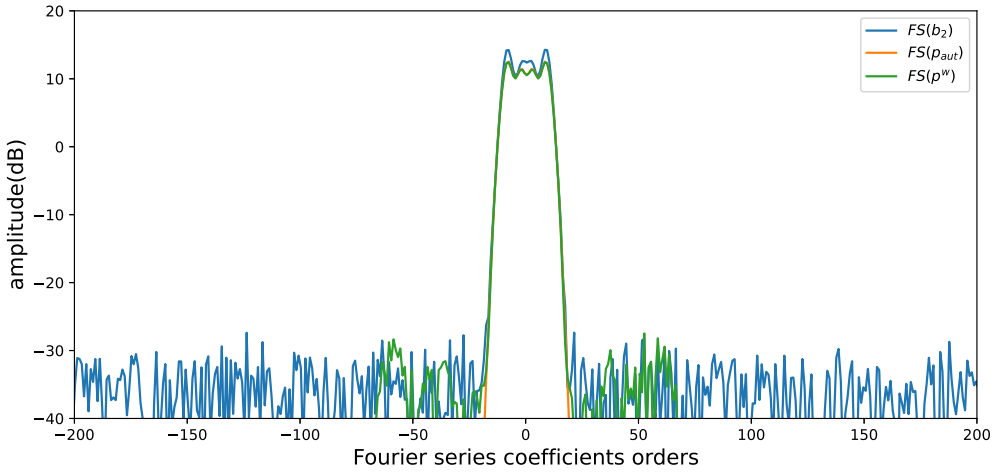

(b) Spectre du chambre

Figure D.19: Amplitudes et spectres des champs b_2, p_{aut} et de son estimation p^w_{aut} (dB)

On peut observer une forte ressemblance entre le diagramme théorique et le diagramme corrigé de l'antenne. L'Erreur Quadratique Moyenne (EQM) est de -36,6 dB.

D.7.5 Conclusion

Ce chapitre a constitué un cas d'application d'une correction d'une mesure d'antenne simulée, dans une configuration 2D. Il a permis de montrer qu'ajouter une régularisation en ondelettes au processus de déconvolution est avantageux. Néanmoins il est important de noter que ce processus peut être amélioré par une étude plus approfondie de certains paramètres de régularisation.

D.8 Conclusion

D.8.1 Résumé

Cette thèse avait pour but de développer les outils d'analyse et de correction pour la mesure d'antenne, basées sur les harmoniques et les ondelettes sphériques.
Dans le **premier chapitre**, le contexte de la thèse et les aspects expérimentaux de la mesure d'antenne ont été présentés. Premièrement, les différents environnements et configurations de mesure d'antenne ont été décrits. Ensuite, une présentation des équipements classiques de mesure d'antenne et leur rôle dans la chaîne RF de mesure a été faite. Finalement, le banc de mesure de l'ENAC, utilisé pour les mesures d'antenne effectuées durant cette thèse a été présenté.
Dans le **deuxième chapitre**, les outils et techniques de post-traitement de mesure d'antenne en géométrie sphérique ont été introduits. Le chapitre commence par un résumé des coordonnées sphériques, des outils mathématiques et des opérateurs nécessaires pour modéliser les rotations sur la sphère. Nous avons ensuite abordé la création des harmoniques sphériques vectorielles standards, un élément clé dans le domaine des antennes. Pour illustrer ce concepts, un exemple de transformations par harmoniques sphériques a été présentés. Le chapitre se clôt par un aperçu concis des méthodes de post-traitement utilisées dans les mesures d'antennes.
Dans le **troisième chapitre**, le concept des harmoniques sphériques de spin pour l'analyse du rayonnement d'antennes a été introduit. Ces décompositions offrent des caractéristiques avantageuses pour représenter des vecteurs tangents sur la sphère, et des algorithmes efficaces sont disponibles. Pour commencer, les fondations théoriques des harmoniques sphériques de spin ont été présentées, abordant la définition des fonctions de spin, des harmoniques sphériques de spin, et la décomposition de ces fonctions en harmoniques de spin. Par ailleurs, la formulation en spin des vecteurs tangents sur la sphère a été introduite, ainsi que ses propriétés rotationnelles. Ensuite, les théorèmes d'échantillonnage et les algorithmes rapides associés pour calculer efficacement les transformations exactes en harmoniques sphériques de spin ont été étudiés. Notamment, l'approche de McEwen Wiaux, compatible avec la représentation en spin, a démontré de hautes performances en termes de complexité et de temps de calcul. En outre, la relation et la compatibilité entre les harmoniques sphériques de spin et les harmoniques sphériques de Hansen ont été établies. Finalement, divers modèles de rayonnement ont été décomposés en harmoniques de spin. Ces transformations ont été exécutées en des temps de calcul remarquablement courts, la plus longue prenant 9 minutes et 24 secondes (N = 2048). La polyvalence et l'efficacité des harmoniques sphériques de spin dans ces contextes variés ont souligné leur potentiel en tant qu'outil pour l'analyse de rayonnements d'antennes. Cependant, l'examen d'un DUT rayonnant des harmoniques sphériques d'ordre élevé a révélé une limitation de cette transformation. Une quantité significative de puissance peut être répartie sur de nombreux coefficients faibles, rendant cette puissance à peine visible dans la représentation par harmoniques sphériques. Par conséquent, le chapitre suivant s'est concentré sur les ondelettes sphériques de spin, qui présentent des propriétés de localisation intéressantes.
Dans le **quatrième chapitre**, les ondelettes sphériques de spin ont été présentées comme un outil prometteur pour l'analyse des modèles de rayonnement d'antennes. Alors que les ondelettes sont couramment utilisées pour le traitement du signal et la compression de données, leur application en géométrie sphérique est moins fréquente. Le chapitre a débuté par la présentation des ondelettes en géométrie 1D. Ensuite, sont successivement présentés la formulation des ondelettes sphériques de spin à partir des

This document may not be reproduced, modified, adapted, published, translated in any way, in whole or in part, nor disclosed to a third party without the prior written consent of ENAC. © 2023, ENAC

harmoniques sphériques de spin et l'algorithme effectuant la transformation par ondelettes sphériques de spin. Le chapitre s'est conclut en fournissant un exemple de transformation par ondelettes de modèle de rayonnement simulé. La transformation par ondelettes de la SER d'un avion a mis en lumière la capacité des ondelettes à souligner les variations rapides, contrairement aux harmoniques sphériques. De plus, ces exemples ont démontré l'efficacité de l'algorithme : le calcul de 39 134 480 coefficients d'ondelettes n'a pris que 5 minutes et 24 secondes. Ainsi, la transformation par ondelettes sphériques de spin s'est révélée être un outil significatif pour l'analyse et potentiellement la correction de champs à variations rapides.

Dans le **cinquième chapitre**, une formulation du problème de la mesure a été établie. Le signal mesuré sur le port d'une AST a été exprimé comme la convolution entre le modèle de rayonnement de l'antenne et le rayonnement de la sonde dans l'environnement de mesure. La démonstration a commencé par l'application du principe d'équivalence, simplifiant le problème en exprimant le rayonnement de l'antenne à travers ses courants équivalents. Ensuite, le théorème de réciprocité a facilité la mise en relation du signal reçu sur le port de l'antenne (c'est-à-dire, le signal de mesure) avec le signal correspondant au rayonnement de la sonde dans l'environnement de mesure, ainsi qu'avec le rayonnement de l'antenne. La rotation de l'antenne dans l'environnement de mesure entraîne alors une convolution avec le rayonnement de la sonde dans cet environnement. Cette formulation a été décomposée en composantes de spin, aboutissant à une formulation simplifiée de la mesure. Enfin, la validité de l'hypothèse selon laquelle l'antenne peut être remplacée par ses courants équivalents a été vérifiée. Grâce à cette formulation, des méthodes de déconvolution peuvent être employées pour extraire le véritable modèle de rayonnement de l'antenne à partir des mesures.

Dans le **sixième chapitre**, un cas d'application de la correction de mesure d'antenne a été réalisé, pour une configuration 2D. Tout d'abord, la formulation de la mesure sur le cercle a été dérivée dans une configuration Magnétique Transverse (TMz), résultant en une convolution entre deux signaux 2π-périodiques sur la sphère. Ensuite, le processus de déconvolution pour cette fonction a été présenté, montrant que la déconvolution est un problème délicat en raison de sa nature mal conditionnée. Par conséquent, une méthode de régularisation a été présentée pour obtenir une estimation du signal d'intérêt. Cette méthode a ensuite été adaptée à un scénario de correction de mesure en deux étapes. La première étape consiste à estimer le signal correspondant à l'impact environnemental sur le rayonnement de la sonde. Dans une seconde étape, cette estimation est utilisée pour déconvoluer le signal de mesure, aboutissant finalement au modèle de rayonnement de l'antenne. Cette méthode implique l'utilisation de bases d'expansion 1D telles que les séries classiques de Fourier. De plus, comme dans la Régularisation Fourier-Ondelette (ForWard) [122], les expansions en ondelettes 1D ont été introduites pour affiner la régularisation sur les séries de Fourier. Cette méthode a ensuite été appliquée à une simulation de mesure d'antenne, incluant des perturbations sous la forme d'un multi-trajet atténué de 20 dB et un niveau de bruit de -20dB. Cela a abouti à une estimation du signal de l'antenne avec une Erreur Quadratique Moyenne (EQM) de -36,6 dB. Il est important de noter que cette méthode n'a pas été poussée à ses limites et pourrait donner de meilleurs résultats dans des conditions plus optimisées. Par ailleurs, l'extension à de véritables mesures sphériques 3D a été laissée à des travaux futurs. En résumé, ce chapitre représente une première tentative de correction des mesures d'antennes en utilisant la déconvolution avec régularisation par ondelettes.

D.8.2 Perspectives

Cette thèse de doctorat est la première à traiter des mesures d'antennes au laboratoire ENAC, marquant le début de divers projets sous différentes formes. Par exemple, les deux premiers chapitres seront utilisés à des fins pédagogiques ou bibliographiques, car ils introduisent de nombreux aspects des mesures d'antennes. Ensuite, les harmoniques sphériques de spin et leur conversion en harmoniques sphériques de Hansen pourraient être utilisées dans d'autres projets, grâce au temps de calcul rapide qu'elles offrent. À titre d'exemple, un doctorant de l'ENAC utilise déjà les harmoniques de spin pour développer des modèles stochastiques du rayonnement des antennes lorsqu'elles sont installées sur des avions.
De plus, de nombreux aspects de cette thèse peuvent être explorés plus avant. L'ordre des paragraphes vise à prioriser les travaux futurs, du court au long terme.
En termes d'harmoniques sphériques de spin, une étude sur des antennes très directives pourrait être ajoutée aux études déjà réalisées dans cette thèse. De plus, une simplification des relations entre les harmoniques sphériques de Hansen et de spin dans la zone de champ lointain serait intéressante, notamment en termes de temps de calcul. Cela consisterait à ne considérer que les ondes sortantes et à remplacer les fonctions de Hankel par leurs équivalents asymptotiques en champ lointain.
Puis, en ce qui concerne les ondelettes sphériques de spin, une étude plus approfondie serait nécessaire pour mieux comprendre comment elles peuvent aider à analyser le rayonnement de grands systèmes (section radar transversale, antennes installées sur une plateforme, ...). L'objectif serait de trouver une méthode pour déterminer précisément l'origine des coefficients aux niveaux élevés des ondelettes et les corriger.
Dans les travaux futurs, la déconvolution devrait être formulée en géométrie sphérique. Les mesures sphériques étant définies sur $L^2(\mathrm{SO}(3))$, cela signifie qu'une base paramétrée par le spin sera nécessaire, comme les fonctions de Wigner selon [65]. Ensuite, la correction utilisant la méthode ForWard pourrait être adaptée aux configurations sphériques et optimisée. Premièrement, une méthode combinant les harmoniques sphériques de spin et les ondelettes sphériques de spin doit être développée.
Ensuite, les critères que l'antenne de référence doit remplir pour estimer de la meilleure façon le champ incident sur l'ACT doivent être clairement caractérisés. Enfin, le choix des paramètres de régularisation doit faire l'objet d'une étude, soit théorique, soit numérique. En particulier, la régularisation par ondelettes pourrait être appliquée en fonction du niveau de l'ondelette, car les niveaux les plus élevés ne contiennent probablement que du bruit et pourraient donc être régulés plus sévèrement.
Par ailleurs, il est important de se rappeler que toutes les installations de mesure d'antennes ne permettent pas une mesure complète sur $L^2(\mathrm{SO}(3))$, c'est-à-dire pour chaque combinaison possible d'angles d'Euler, et le coût temporel d'une telle mesure. Ainsi, les méthodes de correction devront être optimisées en tenant compte de telles limitations. L'objectif pourrait être de minimiser le nombre de points de mesure.
Enfin, une perspective pour la correction des mesures d'antennes est de combiner la correction fréquentielle et angulaire avec des ondelettes. Les méthodes de post-traitement devraient être capables de corriger les mesures sur la sphère dans l'environnement de mesure, en utilisant toutes les informations contenues dans une bande de fréquences donnée. Cela devrait améliorer la précision des mesures, mais le post-traitement pourrait être difficile en raison de la quantité énorme de données impliquées.
Une doctorante de l'ENAC travaille déjà dans la continuité de ma thèse, à développer des méthodes efficaces d'analyse et de post-traitement pour les mesures électromagnétiques sphériques.

This document may not be reproduced, modified, adapted, published, translated in any way, in whole or in part, nor disclosed to a third party without the prior written consent of ENAC. © 2023, ENAC

Acronyms

AUT Antenna Under Test
DUT Device Under Test
VNA Vector Network Analyzer
TE Transverse Electric
TM Transverse Magnetic
CATR Compact Antenna Test Range
UAVs Unmanned Aerial Vehicles
NFFT Near-field to Far-Field Transformation
TZF Test Zone Field
CNES Centre National d'Etudes Spatiales
SOLT Short Open Load Through
DGA Direction Générale de l'Armement
RCS Radar Cross Section
FFT Fast Fourier Transform
IFFT Inverse Fast Fourier Transform
FWT Fast Wavelet Transform
PANTERE Processing of ANtenna TEsts REsults
EMC Electromagnetic Compatibility
FoRD Fourier-Based Regularized Deconvolution
ForWaRD Fourier-Wavelet Regularized Deconvolution
GPS Global Positioning System
RMSE Root Mean Square Error
DWT Discrete Wavelet Transform

This document may not be reproduced, modified, adapted, published, translated in any way, in whole or in part, nor disclosed to a third party without the prior written consent of ENAC. © 2023, ENAC

Glossary

Symbols

$D^n_{m,m'}$ Wigner functions.

J_0 Index of the lowest wavelet scale.

$J_{\mathbf{max}}$ Index of the highest wavelet scale.

$L^2(\mathcal{S}^2)$ square integrable functions on the sphere.

$L^2(\mathbf{SO(3)})$ the group of finite power square integrable functions over the rotation group.

L Number of sampling point on a grid.

N Truncation order to define the sampling grid.

$N_{\mathbf{AUT}}$ Bandlimit of the signal, or max(n).

S Surface of the port of the antenna.

$W^{\Psi^j_s}$ j^{th} spin wavelet scale.

$Y_{s,m,n}$ Spin spherical harmonic.

Ω_1 subdomain 1.

Ω_2 subdomain 2.

Ω domain.

Φ_s scaling function for spin wavelet expansion.

Ψ^j_s spin wavelet function of the j^{th} scale.

$\mathbf{d}z^{(c)}_{n'}(kr)$ simplified notation for $\frac{1}{kr}\frac{\mathrm{d}}{\mathrm{d}kr}\left(krz^{(c)}_{n'}(kr)\right)$.

$\mathbf{d}z^{(c)}_{n}(kr)$ simplified notation for $\frac{1}{kr}\frac{\mathrm{d}}{\mathrm{d}kr}\left(krz^{(c)}_{n}(kr)\right)$.

ϕ^{oa} angles of arrival of multipath on the sphere or the circle surrounding the AUT.

χ_g Phase shift appearing under a global rotation.

χ_l Phase shift appearing under a local rotation.

ϵ corresponds to the orientation of the AUT. Euler angles $\epsilon = (\phi_e, \theta_e, \chi_e) \in \mathrm{SO}(3)$.

$\hat{b}$ In the case of an analysis of the measurement harmonics, $\hat{b}$ correspond to the coefficients of the harmonic spectrum.

$\hat{n}_o$ Fourier transform of the spatial noise.

$\mathbf{R}_\epsilon$ Matrice de rotation.

$\mathcal{R}_{s\epsilon}$ Opérateur de rotation de spin.

$\mathcal{R}$ Rotational operator.

$\mathcal{S}^2$ Unit sphere.

ψ 1D wavelet function.

$\boldsymbol{E}_{\mathbf{probe}}$ Field radiated by the probe, considered to be the main component of the incident field on the sphere/circle surrounding the AUT..

$\boldsymbol{E}$ Electric Field.

$\boldsymbol{H}$ Magnetic Field.

$\boldsymbol{J}_{\mathbf{es}}^{\mathbf{eq,free}}$ Electric surface current in a free space situation.

$\boldsymbol{J}_{\mathbf{ms}}^{\mathbf{eq,free}}$ Magnetic surface current in a free space situation.

$\boldsymbol{J}_{\mathbf{ms}}^{\mathbf{eq,meas}}$ Magnetic surface current in a measurement situation.

$\boldsymbol{J}_{\mathbf{es1}}^{\mathbf{eq}}$ Equivalent electric current for the subproblem 1.

$\boldsymbol{J}_{\mathbf{es2}}^{\mathbf{eq}}$ Equivalent electric current for the subproblem 2.

$\boldsymbol{J}_{\mathbf{ms1}}^{\mathbf{eq}}$ Equivalent magnetic current for the subproblem 1.

$\boldsymbol{J}_{\mathbf{ms2}}^{\mathbf{eq}}$ Equivalent magnetic current for the subproblem 2.

$\boldsymbol{J}_{\mathbf{es}}^{\mathbf{eq,meas}}$ Electric surface current in a measurement situation.

$\boldsymbol{J}_{\mathbf{e}}$ Electric current.

$\boldsymbol{J}_{\mathbf{m}}$ Magnetic current.

φ 1D scaling function.

ζ specific wave impedance.

b The measurement signal will be noted b, it's a wave amplitude arriving on the port of the receiving device, it can be the AUT or the probe depending on which configuration is considered..

h A field corresponding to the radiation of the probe in the environment nearby the antenna, in absence of the antenna.

n_0 spatial noise.

p antenna pattern.

R

r Radius of the sphere/circle surrounding the AUT..

Bibliography

[1] J. S. Hollis, T. Lyon, and L. Clayton, *Microwave antenna measurements*. Scientific-Atlanta, 1985.

[2] "IEEE recommended practice for antenna measurements," *IEEE Std 149-2021 (Revision of IEEE Std 149-1977)*, pp. 1–207, 2022.

[3] W. L. Stutzman and G. A. Thiele, *Antenna theory and design*. John Wiley & Sons, 2012.

[4] "IEEE recommended practice for near-field antenna measurements," *IEEE Std 1720-2012*, pp. 1–102, 2012.

[5] C. A. Balanis, *Antenna theory: analysis and design*. John wiley & sons, 2015.

[6] J. E. Hansen, *Spherical near-field antenna measurements*. Iet, 1988, vol. 26.

[7] F. R. Varela, B. G. Iragüen, and M. S. Castañer, "Probe-corrected near-field to far-field transformation using multiple spherical wave expansions," *2019 13th European Conference on Antennas and Propagation (EuCAP)*, pp. 1–5, 2019.

[8] F. Rodríguez Varela, B. Galocha Iragüen, and M. Sierra-Castañer, "Near-field to far-field transformation on arbitrary surfaces via multi-level spherical wave expansion," *IEEE Transactions on Antennas and Propagation*, vol. 68, no. 1, pp. 500–508, 2020.

[9] D. Löschenbrand and C. Mecklenbrauker, "Fast antenna characterization via a sparse spherical multipole expansion," in *2016 4th International Workshop on Compressed Sensing Theory and its Applications to Radar, Sonar and Remote Sensing (CoSeRa)*. IEEE, 2016, pp. 212–216.

[10] R. Cornelius, D. Heberling, N. Koep, A. Behboodi, and R. Mathar, "Compressed sensing applied to spherical near-field to far-field transformation," in *2016 10th European Conference on Antennas and Propagation (EuCAP)*. IEEE, 2016, pp. 1–4.

[11] Y.-T. Hsiao, Y.-Y. Lin, Y.-C. Lu, and H.-T. Chou, "Applications of time-gating method to improve the measurement accuracy of antenna radiation inside an anechoic chamber," in *Antennas and Propagation Society International Symposium*, 2003.

[12] MVG, "Insight," https://www.mvg-world.com/fr/produits/mesure-dantenne/software/insight.

[13] L. J. Foged, L. Scialacqua, F. Saccardi, F. Mioc, D. Tallini, E. Leroux, U. Becker, J. L. Araque Quijano, and G. Vecchi, "Bringing numerical simulation and antenna measurements together," in *The 8th European Conference on Antennas and Propagation (EuCAP 2014)*, 2014, pp. 3421–3425.

[14] A. Yaghjian, "An overview of near-field antenna measurements," *IEEE Transactions on antennas and propagation*, vol. 34, no. 1, pp. 30–45, 1986.

[15] Z. Tian and S. F. Gregson, "Examination of spherical antenna far-field scattering suppression through electromagnetic simulation," in *Antennas and Propagation Conference 2019 (APC-2019)*, 2019, pp. 1–5.

[16] D. A. Leatherwood and E. B. Joy, "Plane wave, pattern subtraction, range compensation," *IEEE Transactions on Antennas and Propagation*, vol. 49, no. 12, pp. 1843–1851, 2001.

[17] D. N. Black and E. Joy, "Test zone field compensation," *IEEE Transactions on Antennas and Propagation*, vol. 43, no. 4, pp. 362–368, 1995.

[18] J. T. Toivanen, T. A. Laitinen, and P. Vainikainen, "Modified test zone field compensation for small-antenna measurements," *IEEE transactions on Antennas and Propagation*, vol. 58, no. 1, pp. 3471–3479, 2010.

[19] E. Newman and R. Penrose, "An approach to gravitational radiation by a method of spin coefficients," *Journal of Mathematical Physics*, vol. 3, no. 3, pp. 566–578, 1962.

[20] E. T. Newman and R. Penrose, "Note on the Bondi-Metzner-Sachs Group," *Journal of Mathematical Physics*, vol. 7, no. 5, pp. 863–870, 05 2005. [Online]. Available: https://doi.org/10.1063/1.1931221

[21] J. D. McEwen and Y. Wiaux, "A novel sampling theorem on the sphere," *IEEE Transactions on Signal Processing*, vol. 59, no. 12, pp. 5876–5887, 2011.

[22] I. Daubechies, *Ten lectures on wavelets*. SIAM, 1992.

[23] S. Mallat, *A wavelet tour of signal processing*. Elsevier, 1999.

[24] J.-L. Starck, Y. Moudden, P. Abrial, and M. Nguyen, "Wavelets, ridgelets and curvelets on the sphere," *Astronomy & Astrophysics*, vol. 446, no. 3, pp. 1191–1204, 2006.

[25] D. Marinucci, D. Pietrobon, A. Balbi, P. Baldi, P. Cabella, G. Kerkyacharian, P. Natoli, D. Picard, and N. Vittorio, "Spherical needlets for cosmic microwave background data analysis," *Monthly Notices of the Royal Astronomical Society*, vol. 383, no. 2, pp. 539–545, 2008.

[26] J. D. McEwen, M. Büttner, B. Leistedt, H. V. Peiris, P. Vandergheynst, and Y. Wiaux, "On spin scale-discretised wavelets on the sphere for the analysis of cmb polarisation," *Proceedings of the International Astronomical Union*, vol. 10, no. S306, p. 64–67, 2014.

[27] J. A. Stratton, *Electromagnetic theory*. John Wiley & Sons, 2007, vol. 33.

[28] V. Platzgummer, V. Raida, G. Krainz, P. Svoboda, M. Lerch, and M. Rupp, "UAV-based coverage measurement method for 5g," in *2019 IEEE 90th Vehicular Technology Conference (VTC2019-Fall)*, 2019, pp. 1–6.

[29] C. L. Holloway, H. A. Shah, R. J. Pirkl, W. F. Young, D. A. Hill, and J. Ladbury, "Reverberation chamber techniques for determining the radiation and total efficiency of antennas," *IEEE transactions on antennas and propagation*, vol. 60, no. 4, pp. 1758–1770, 2012.

[30] J. Knapp and T. F. Eibert, "Accurate determination of radiation patterns from near-field measurements in highly reflective environments," *12th European Conference on Antennas and Propagation (EuCAP 2018)*, pp. 1–3, 2018.

[31] Q. Xu, Y. Huang, L. Xing, C. Song, Z. Tian, S. S. Alja'afreh, and M. Stanley, "3-d antenna radiation pattern reconstruction in a reverberation chamber using spherical wave decomposition," *IEEE Transactions on Antennas and Propagation*, vol. 65, no. 4, pp. 1728–1739, 2016.

[32] J. Rosengren *et al.*, "Measurements of terminal antennas performance in multimode reverberation chambers," in *Antenn 00, Lund, Sweden, Sep. 12-14, 2000*, 2000.

[33] CNES, "CNES website consulted the 04.14.2020," https://cnes.fr/fr/web/CNES-fr/3349-le-cnes-en-bref.php.

[34] DGA, "Solange, la base de mesure de la Direction Générale de l'armement." https://www.espace-sciences.org/sciences-ouest/312/dossier/il-combat-en-toute-discretion.

[35] W. Burnside, M. Gilreath, B. Kent, and G. Clerici, "Curved edge modification of compact range reflector," *IEEE transactions on Antennas and Propagation*, vol. 35, no. 2, pp. 176–182, 1987.

[36] T.-H. Lee and W. D. Burnside, "Compact range reflector edge treatment impact on antenna and scattering measurements," *IEEE Transactions on Antennas and Propagation*, vol. 45, no. 1, pp. 57–65, 1997.

[37] Astrolabe, "ESA website, consulted the 07.05.2023," https://www.esa.int/ESA_Multimedia/Images/2019/04/EDRS-C_in_Airbus_s_Compact_Antenna_Test_Range_facility.

[38] F. Scattone, D. Sekuljica, A. Giacomini, F. Saccardi, A. Scannavini, L. J. Foged, E. Kaverine, N. Gross, and P. O. Iversen, "Comparative testing of devices in a spherical near field system and plane wave generator," in *2019 Antenna Measurement Techniques Association Symposium (AMTA)*, 2019, pp. 1–3.

[39] O. Breinbjerg, "Spherical near-field antenna measurements—the most accurate antenna measurement technique," in *2016 IEEE International Symposium on Antennas and Propagation (APSURSI)*. IEEE, 2016, pp. 1019–1020.

[40] S. Gregson, J. McCormick, and C. Parini, *Principles of planar near-field antenna measurements*. IET, 2007, vol. 53.

This document may not be reproduced, modified, adapted, published, translated in any way, in whole or in part, nor disclosed to a third party without the prior written consent of ENAC. © 2023, ENAC

[41] MVG, "Dual Polarized Probes 800 MHz - 40000 MHz on the MVG website," https://www.mvg-world.com/fr/produits/antennes/measurement-probes-and-feeds/dual-polarized-probes.

[42] ——, "Stalab 650MHz-18GHz, on MVG website, consulted the 05.31.2023," https://www.mvg-world.com/fr/produits/mesure-dantenne/multi-probe-systems/starlab.

[43] C. L. Holloway, R. R. Delyser, R. F. German, P. McKenna, and M. Kanda, "Comparison of electromagnetic absorber used in anechoic and semi-anechoic chambers for emissions and immunity testing of digital devices," *IEEE Transactions on Electromagnetic Compatibility*, vol. 39, no. 1, pp. 33–47, 1997.

[44] B. Chung and H. Chuah, "Modeling of rf absorber for application in the design of anechoic chamber," *Progress In Electromagnetics Research*, vol. 43, pp. 273–285, 2003.

[45] C. Méjean, L. Pometcu, R. Benzerga, A. Sharaiha, C. Le Paven-Thivet, M. Badard, and P. Pouliguen, "Electromagnetic absorber composite made of carbon fibers loaded epoxy foam for anechoic chamber application," *Materials Science and Engineering: B*, vol. 220, pp. 59–65, 2017.

[46] H. Severin, "Non-reflecting absorbers for microwave radiation," *IRE Transactions on Antennas and Propagation*, vol. 4, no. 3, pp. 385–392, 1956.

[47] H. shielding systems BV, "Holland shielding systems BV, absorbers constructors," https://hollandshielding.com/?_gl=1*1obmg0h*_up*MQ..&gclid=Cj0KCQjwk96lBhDHARIsAEKO4xaaOFL_5JJV1lY9mV0_A72EjqpsoohCs55_AmrL7iZalR2j3XOBchgaApNEEALw_wcB.

[48] Siepel, "Dual Polarized Probes 800 MHz - 40000 MHz," https://www.siepel.com/.

[49] T. Hansen and A. D. Yaghjian, *Plane-wave theory of time-domain fields: near-field scanning applications*. IEEE Press, 1999.

[50] RFspin, "Probe antenna RF SPIN DRH18EX," https://www.rfspin.com/product/drh18-ex/.

[51] NSI, "Dual Polarized Probes data sheet," https://www.nsi-mi.com/images/PDF_Datasheets/NSI-MI-ANT-DPP-Dual-Polarized-Probes-datasheet-v1.9.pdf.

[52] T. Laitinen *et al.*, "Advanced spherical antenna measurements," *Helsinki University of Technology Radio Laboratory publications. Report S, 273*, 2005.

[53] K. A. Yinusa and T. F. Eibert, "A multi-probe antenna measurement technique with echo suppression capability," *IEEE transactions on Antennas and Propagation*, vol. 61, no. 10, pp. 5008–5016, 2013.

[54] J. A. Graham and P. O. Iversen, "Rapid spherical near-field antenna test system for vehicle mounted antennas," in *Antenna Measurement Techniques Association, 26th Annual Meeting and Symposium (AMTA'04), Stone Mountain, GA, USA*, 2004.

[55] L. Duchesne, P. Garreau, N. Robic, A. Gandois, P. O. Iversen, and G. Barone, "Compact multi-probe antenna test station for rapid testing of antennas and wireless terminals," *IET*, 2004.

[56] Kapteo, "KAPTEO website consulted the 06.08.2023," https://www.kapteos.com/products-services.

[57] A. Geise, O. Neitz, J. Migl, H.-J. Steiner, T. Fritzel, C. Hunscher, and T. F. Eibert, "A crane-based portable antenna measurement system—system description and validation," *IEEE Transactions on Antennas and Propagation*, vol. 67, no. 5, pp. 3346–3357, 2019.

[58] Anyfields, "Anyfields website, consulted the 06.02.2023," https://anyfields.eu/.

[59] P. Levesque, L. Leylekian, and D. Balageas, "Vectorial characterisation of electromagnetic fields by infrared thermography," *Office national d'etudes et de recherches aerospatiales ONERA-PUBLICATIONS-TP*, no. 189, 2000.

[60] D. Novotny, J. Gordon, J. Coder, M. Francis, and J. Guerrieri, "Performance evaluation of a robotically controlled millimeter-wave near-field pattern range at the nist," in *2013 7th European Conference on Antennas and Propagation (EuCAP)*, 2013, pp. 4086–4089.

[61] C. systems, "CT systems website consulted the 06.04.2023," https://www.ctsystemes.com/.

[62] RFSPINDRH10, "Probe antenna RF SPIN DRH10E," https://www.rfspin.com/product/drh10/.

[63] A. C. Newell and G. Hindman, "Scattering reduction in spherical near-field measurements," in *2008 IEEE Antennas and Propagation Society International Symposium*. IEEE, 2008, pp. 1–4.

[64] F. D'Agostino, F. Ferrara, C. Gennarelli, R. Guerriero, and M. Migliozzi, "Reconstruction of the far field radiated by an offset mounted volumetric aut from non-redundant spherical spiral near-field measurements," *IET Microwaves, Antennas Propagation*, vol. 14, no. 14, pp. 1711–1718, 2020.

[65] J. D. McEwen, M. Büttner, B. Leistedt, H. V. Peiris, and Y. Wiaux, "A novel sampling theorem on the rotation group," *IEEE Signal Processing Letters*, vol. 22, no. 12, pp. 2425–2429, 2015.

[66] L. B. Felsen and N. Marcuvitz, *Radiation and scattering of waves*. John Wiley & Sons, 1994, vol. 31.

[67] J. G. Van Bladel, *Electromagnetic fields*. John Wiley & Sons, 2007, vol. 19.

[68] R. F. Harrington, *Time-harmonic electromagnetic fields*. McGraw-Hill College, 1961.

[69] C. Morlaas, B. Souny, and A. Chabory, "Helical-ring antenna for hemispherical radiation in circular polarization," *IEEE Transactions on Antennas and Propagation*, vol. 63, no. 11, pp. 4693–4701, 2015.

This document may not be reproduced, modified, adapted, published, translated in any way, in whole or in part, nor disclosed to a third party without the prior written consent of ENAC. © 2023, ENAC

[70] J. Marti-Canales, "Time domain antenna measurements in compact ranges and small anechoic chambers," Ph.D. dissertation, Ph.D. thesis, European Space Agency, 2000.

[71] A. Chen, A. Chabory, A.-C. Escher, and C. Macabiau, "Development of a GPS deterministic multipath simulator for an efficient computation of the positioning errors," in *Proceedings of the 22nd International Technical Meeting of the Satellite Division of The Institute of Navigation (ION GNSS 2009)*, 2009, pp. 2378–2390.

[72] J. Kornprobst, J. Knapp, R. A. M. Mauermayer, O. Neitz, A. Paulus, and T. F. Eibert, "Accuracy and conditioning of surface-source based near-field to far-field transformations," *IEEE Transactions on Antennas and Propagation*, vol. 69, no. 8, pp. 4894–4908, 2021.

[73] J. L. Araque Quijano, L. Scialacqua, J. Zackrisson, L. J. Foged, M. Sabbadini, and G. Vecchi, "Suppression of undesired radiated fields based on equivalent currents reconstruction from measured data," *IEEE Antennas and Wireless Propagation Letters*, vol. 10, pp. 314–317, 2011.

[74] T. F. Eibert and C. H. Schmidt, "Multilevel fast multipole accelerated inverse equivalent current method employing rao–wilton–glisson discretization of electric and magnetic surface currents," *IEEE Transactions on Antennas and Propagation*, vol. 57, no. 4, pp. 1178–1185, 2009.

[75] F. Jensen and A. Frandsen, "On the number of modes in spherical wave expansions," *Proc. 26th AMTA*, vol. 2, no. 1, pp. 489–494, 2004.

[76] M. Elad, *Sparse and redundant representations: from theory to applications in signal and image processing*. Springer, 2010, vol. 2, no. 1.

[77] C. Culotta-López, D. Heberling, A. Bangun, A. Behboodi, and R. Mathar, "A compressed sampling for spherical near-field measurements," in *2018 AMTA Proceedings*. IEEE, 2018, pp. 1–6.

[78] D. L. Donoho and J. Tanner, "Precise undersampling theorems," *Proceedings of the IEEE*, vol. 98, no. 6, pp. 913–924, 2010.

[79] B. Hofmann, O. Neitz, and T. F. Eibert, "On the minimum number of samples for sparse recovery in spherical antenna near-field measurements," *IEEE Transactions on Antennas and Propagation*, vol. 67, no. 12, pp. 7597–7610, 2019.

[80] N. Mézières, B. Fuchs, L. Le Coq, J.-M. Lerat, R. Contreres, and G. Le Fur, "On the application of sparse spherical harmonic expansion for fast antenna far-field measurements," *IEEE Antennas and Wireless Propagation Letters*, vol. 19, no. 5, pp. 746–750, 2020.

[81] N. Mézières, M. Mattes, and B. Fuchs, "Antenna characterization from a small number of far-field measurements via reduced-order models," *IEEE Transactions on Antennas and Propagation*, vol. 70, no. 4, pp. 2422–2430, 2022.

[82] R. Ramamoorthi and P. Hanrahan, "A signal-processing framework for reflection," *ACM Transactions on Graphics (TOG)*, vol. 23, no. 4, pp. 1004–1042, 2004.

[83] C. H. Choi, J. Ivanic, M. S. Gordon, and K. Ruedenberg, "Rapid and stable determination of rotation matrices between spherical harmonics by direct recursion," *The Journal of Chemical Physics*, vol. 111, no. 19, pp. 8825–8831, 1999.

[84] D. W. Ritchie and G. J. Kemp, "Fast computation, rotation, and comparison of low resolution spherical harmonic molecular surfaces," *Journal of Computational Chemistry*, vol. 20, no. 4, pp. 383–395, 1999.

[85] F. J. Simons, F. Dahlen, and M. A. Wieczorek, "Spatiospectral concentration on a sphere," *SIAM review*, vol. 48, no. 3, pp. 504–536, 2006.

[86] S. Swenson and J. Wahr, "Methods for inferring regional surface-mass anomalies from gravity recovery and climate experiment (grace) measurements of time-variable gravity," *Journal of Geophysical Research: Solid Earth*, vol. 107, no. B9, pp. ETG–3, 2002.

[87] K. Whaler, "Downward continuation of magsat lithospheric anomalies to the earth's surface," *Geophysical Journal International*, vol. 116, no. 2, pp. 267–278, 1994.

[88] P. Audet, "Directional wavelet analysis on the sphere: Application to gravity and topography of the terrestrial planets," *Journal of Geophysical Research: Planets*, vol. 116, no. E1, 2011.

[89] D. Turcotte, R. Willemann, W. Haxby, and J. Norberry, "Role of membrane stresses in the support of planetary topography," *Journal of Geophysical Research: Solid Earth*, vol. 86, no. B5, pp. 3951–3959, 1981.

[90] M. Wieczorek, "Gravity and topology of terrestrial planets," *submitted to Treatise on Geophysics*, 2006.

[91] M. A. Wieczorek and R. J. Phillips, "Potential anomalies on a sphere: Applications to the thickness of the lunar crust," *Journal of Geophysical Research: Planets*, vol. 103, no. E1, pp. 1715–1724, 1998.

[92] C. Bennett *et al.*, "4-year cobe dmr cosmic microwave background observations: maps and basic results, 1996," *Astrophys. J*, vol. 464, p. L1.

[93] N. Jarosik, C. Bennett, J. Dunkley, B. Gold, M. Greason, M. Halpern, R. Hill, G. Hinshaw, A. Kogut, E. Komatsu *et al.*, "Seven-year wilkinson microwave anisotropy probe (wmap*) observations: sky maps, systematic errors, and basic results," *The Astrophysical Journal Supplement Series*, vol. 192, no. 2, p. 14, 2011.

[94] E. T. Newman and R. Penrose, "Note on the bondi-metzner-sachs group," *Journal of Mathematical Physics*, vol. 7, no. 5, pp. 863–870, 1966.

[95] J. D. McEwen, B. Leistedt, M. Büttner, H. V. Peiris, and Y. Wiaux, "Directional spin wavelets on the sphere," *arXiv preprint arXiv:1509.06749*, 2015.

[96] E. A. Matute, "On the vector solutions of Maxwell equations with the spin-weighted spherical harmonics," *arXiv preprint physics/0604096*, 2006.

[97] C. E. Shannon, "Communication in the presence of noise," *Proceedings of the IRE*, vol. 37, no. 1, pp. 10–21, 1949.

This document may not be reproduced, modified, adapted, published, translated in any way, in whole or in part, nor disclosed to a third party without the prior written consent of ENAC. © 2023, ENAC

[98] J. R. Driscoll and D. M. Healy, "Computing fourier transforms and convolutions on the 2-sphere," *Advances in applied mathematics*, vol. 15, no. 2, pp. 202–250, 1994.

[99] J. D. McEwen, "Fast, exact (but unstable) spin spherical harmonic transforms," *arXiv preprint arXiv:0807.4494*, 2008.

[100] D. A. Varshalovich, A. N. Moskalev, and V. K. Khersonskii, *Quantum theory of angular momentum*. World Scientific, 1988.

[101] T. Risbo, "Fourier transform summation of legendre series and d-functions," *Journal of Geodesy*, vol. 70, pp. 383–396, 1996.

[102] J. D. McEwen, Y. Wiaux, and M. Büttner, "ssht website consulted the 08.31.2023," https://github.com/astro-informatics/ssht.

[103] C. Amielh, "GNSS multipath model for aircraft surface navigation," 2021.

[104] A. Grossmann and J. Morlet, "Decomposition of hardy functions into square integrable wavelets of constant shape," *SIAM journal on Mathematical Analysis*, vol. 15, no. 4, pp. 723–736, 1984.

[105] Y. Meyer, "Ondelettes et opérateurs," *I: Ondelettes*, 1990.

[106] I. Daubechies, "Orthonormal bases of compactly supported wavelets," *Communications on Pure and Applied Mathematics*, vol. 41, no. 7, pp. 909–996, 1988.

[107] S. G. Mallat, "A theory for multiresolution signal decomposition: the wavelet representation," *IEEE transactions on Pattern Analysis and Machine Intelligence*, vol. 11, no. 7, pp. 674–693, 1989.

[108] A. Chabory, "Analyse de mesures de rayonnement d'antennes par ondelettes," in *Etude Métier CNES*, 2018.

[109] L. M. Bugayevskiy and J. Snyder, *Map projections: A reference manual*. CRC Press, 1995.

[110] F. J. Simons, I. Loris, G. Nolet, I. C. Daubechies, S. Voronin, J. Judd, P. A. Vetter, J. Charléty, and C. Vonesch, "Solving or resolving global tomographic models with spherical wavelets, and the scale and sparsity of seismic heterogeneity," *Geophysical Journal International*, vol. 187, no. 2, pp. 969–988, 2011.

[111] B. Leistedt, J. D. McEwen, P. Vandergheynst, and Y. Wiaux, "S2let: A code to perform fast wavelet analysis on the sphere," *Astronomy & Astrophysics*, vol. 558, p. A128, 2013.

[112] F. J. Narcowich, P. Petrushev, and J. D. Ward, "Localized tight frames on spheres," *SIAM Journal on Mathematical Analysis*, vol. 38, no. 2, pp. 574–594, 2006.

[113] B. T. T. Yeo, W. Ou, and P. Golland, "On the construction of invertible filter banks on the 2-sphere," *IEEE Transactions on Image Processing*, vol. 17, no. 3, pp. 283–300, 2008.

[114] A. D. Yaghjian, *Near-field antenna measurements on a cylindrical surface: A source scattering-matrix formulation*. Department of Commerce, National Bureau of Standards, 1977, vol. 696.

[115] T. M. Gemmer and D. Heberling, "Accurate and efficient computation of antenna measurements via spherical wave expansion," *IEEE Transactions on Antennas and Propagation*, vol. 68, no. 12, pp. 8266–8269, 2020.

[116] H. Cui, R. Caldeirinha, and J. Richter, "A deconvolution method to remove distortion caused by antenna radiation pattern from measurement," in *2010 International Workshop on Antenna Technology (iWAT)*. IEEE, 2010, pp. 1–4, pas lu.

[117] J. Bennet and A. Griziotis, "Removal of environmental effects from antenna radiation patterns by deconvolution processing," in *Proceedings of the IEE Conference*, 1983, pp. 224–228.

[118] A. Chabory and R. Douvenot, *Électromagnétisme pour les télécommunications*. Éditions Cépaduès, 2014.

[119] E. J. Rothwell and M. J. Cloud, *Electromagnetics*. CRC press, 2018.

[120] J.-L. Starck, E. Pantin, and F. Murtagh, "Deconvolution in astronomy: A review," *Publications of the Astronomical Society of the Pacific*, vol. 114, no. 800, p. 1051, 2002.

[121] R. H. Herrera, R. Orozco, and M. Rodriguez, "Wavelet-based deconvolution of ultrasonic signals in nondestructive evaluation," *Journal of Zhejiang University-SCIENCE A*, vol. 7, no. 10, pp. 1748–1756, 2006.

[122] R. Neelamani, H. Choi, and R. Baraniuk, "Forward: Fourier-wavelet regularized deconvolution for ill-conditioned systems," *IEEE Transactions on signal processing*, vol. 52, no. 2, pp. 418–433, 2004.

[123] Y. Wiaux, J. McEwen, P. Vandergheynst, and O. Blanc, "Exact reconstruction with directional wavelets on the sphere," *Monthly Notices of the Royal Astronomical Society*, vol. 388, no. 2, pp. 770–788, 2008.

This document may not be reproduced, modified, adapted, published, translated in any way, in whole or in part, nor disclosed to a third party without the prior written consent of ENAC. © 2023, ENAC

Publication list

Conference Papers

1. A. Quennelle, A. Chabory, P. Pouliguen, R. Contreres G. Le Fur. Analysis of Antenna Radiation Patterns by Means of Spherical Wavelets. *EuCAP* 2022.

2. A. Quennelle, A. Chabory, P. Pouliguen, R. Contreres G. Le Fur. Analyse de diagrammes de rayonnements d'antennes au moyen d'ondelettes sphériques. *JNM* 2022.

3. A. Quennelle, A. Chabory, P. Pouliguen, R. Contreres G. Le Fur. Formulation of the measurement problem and application to antenna measurement correction. *ICEAA* 2023.

This document may not be reproduced, modified, adapted, published, translated in any way, in whole or in part, nor disclosed to a third party without the prior written consent of ENAC. © 2023, ENAC

RÉPUBLIQUE FRANÇAISE
Liberté
Égalité
Fraternité

Université de Toulouse

Titre : Méthode de correction a-posteriori de mesures d'antennes par ondelettes

Mots clés : Antenne, Mesures, Ondelettes

Résumé : En antennes, les phases de conception et de prototypage sont suivies par une phase de mesures qui doit permettre d'évaluer avec fiabilité les performances atteintes par rapport aux spécifications attendues. Ces mesures sont effectuées sur des bancs de mesure ou des salles de mesure adaptées. La précision de la mesure est limitée par des perturbations d'origines diverses. En effet, des réflexions parasites proviennent des parois, des supports et des équipements présents dans la chambre. Une autre source de perturbations provient de la précision du positionnement et de l'orientation des différents éléments. Afin d'améliorer la précision de la mesure, une approche consiste à utiliser des algorithmes de correction en post-traitement. Quant aux ondelettes, ce sont des fonctions utilisées de manière générale pour la compression de données car elles permettent de séparer l'information en niveaux de détails (pour une image par exemple) ou en niveaux de variations (lentes à rapides) pour un signal. La thèse a donc pour objectif de développer des méthodes de corrections de mesures d'antennes basées sur une représentation des ondes en décomposition en ondelettes sphériques.
Un état de l'art est effectué sur les différentes méthodes de mesure d'antennes et bases de mesure existantes, sur les outils d'analyse de diagramme telles que les harmoniques sphériques, les plus communes en antennes étant celles définies par Hansen. Enfin une étude de différentes méthode de corrections a été établie.
Dans cette thèse, un nouveau type d'harmoniques sphériques est utilisé : les harmoniques sphériques de spin sont des outils d'analyse de données en géométrie sphérique développés à l'origine pour étudier le fond diffus cosmologique. Le spin est un paramètre qui permet de désigner un type de donnée sur la sphère. Pour les données étudiées dans la thèse, qui sont scalaires ou vectorielles, on ira jusqu'à l'ordre 1. En particulier, en champ lointain, il existe un lien entre la polarisation du champ électromagnétique et le signe du spin. Cet outil d'analyse a été développé en parallèle d'un théorème d'échantillonnage sur la sphère qui permet la reconstruction exacte du champ après décomposition ainsi que la possibilité de monter haut en ordre d'harmoniques. Par ailleurs des algorithmes de résolution permettent une analyse rapide des diagrammes étudiés. Finalement ces harmoniques de spin sont à la base de la construction des ondelettes sphériques de spin.
Les ondelettes sphériques de spin sont des outils d'analyse basées sur la décomposition en harmoniques sphériques de spin. Elles ont de bonnes propriétés de localisation spatiales/spectrales. Elles permettent donc d'extraire des informations localisées sur la sphère comme par exemple un multi-trajet dans le cas de la mesure d'antenne. Durant cette thèse, des analyses en harmoniques et en ondelettes sphériques de spin ont été réalisées, avec des performances très intéressantes.
Dans une seconde partie, une formulation de la mesure a été démontrée grâce au principe d'équivalence, au théorème de réciprocité et aux propriétés de rotations d'un champ sur la sphère. La mesure peut ainsi s'écrire comme une convolution angulaire entre le signal mesuré au niveau du port de l'antenne ou de la sonde et le champ de la sonde dans l'environnement de mesure, sur la sphère entourant l'antenne en champ lointain. Cette formulation permet d'utiliser des méthodes de déconvolution/régularisation pour corriger les mesures. Dans l'idéal la déconvolution dans le domaine spectrale demande de pouvoir effectuer des mesures sur trois axes de rotations. Toutefois, il existe dans la littérature des méthodes prometteuses de correction sans la contrainte du troisième axe de rotation car les mesures sont généralement faites selon deux axes de rotation.
Les résultats de la thèse ont été testés sur des cas canoniques, des simulations et des mesures en chambre anéchoïque.

Title: A-posteriori Correction Methods for Antenna Measurements by Wavelets

Key words: Antenna, Measurements, Wavelets

Abstract: In antennas manufacturing, the design and prototyping phases are followed by a measurement phase, which aims to reliably evaluate the achieved performance compared to the expected specifications. These measurements are conducted using dedicated measurement ranges or chambers. The accuracy of the measurement is limited by various sources of disturbances. Spurious reflections, for instance, arise from the walls, supports, and equipment present in the chamber. Another source of disturbances is the precision of positioning and orientation of the different elements. To enhance measurement accuracy, one approach involves the use of post-processing correction algorithms. As for wavelets, they are functions commonly employed for data compression since they allow separating information into levels of details (e.g., for an image) or levels of variation (from slow to fast) for a signal. Therefore, the objective of the thesis is to develop methods for correcting antenna measurements based on a representation of waves decomposed using spherical wavelets.
A state of the art is conducted on different antenna measurement methods and existing measurement bases, as well as on analysis tools such as spherical harmonics, with the most commonly used ones in antennas being those defined by Hansen. Finally, a study of various correction methods has been established.
In this thesis, a new type of spherical harmonics is utilized: spin spherical harmonics, which are data analysis tools in spherical geometry originally developed to study the cosmic microwave background. The spin parameter designates a type of data on the sphere. For the data studied in the thesis, scalar and vector data, the analysis extends up to order 1. In particular, in the far-field, there is a connection between the polarization of the electromagnetic field and the sign of the spin. This analysis tool was developed parallel to a sampling theorem on the sphere that allows exact reconstruction of the field after decomposition and the ability to reach high orders of harmonics. Furthermore, resolution algorithms enable fast analysis of the studied diagrams. Ultimately, these spin harmonics form the basis for constructing spin spherical wavelets.
Spin spherical wavelets are analysis tools based on the decomposition into spin spherical harmonics. They possess good spatial/spectral localization properties, allowing the extraction of localized information on the sphere, such as multipath reflections in the case of antenna measurements. During this thesis, analyses using spin spherical harmonics and spin spherical wavelets were conducted, yielding highly promising results.
In the second part, a measurement formulation was demonstrated using the principle of equivalence, the reciprocity theorem, and the rotation properties of a field on the sphere. The measurement can thus be expressed as an angular convolution between the signal measured at the antenna or probe port and the field of the probe in the measurement environment, on the sphere surrounding the antenna in the far-field. This formulation enables the utilization of deconvolution/regularization methods to correct the measurements. Ideally, deconvolution in the spectral domain requires the ability to perform measurements along three axes of rotation. However, promising methods for correction without the constraint of the third axis of rotation exist in the literature because measurements are typically made along two axes of rotation.
The results of the thesis were tested on canonical cases, simulations, and measurements in an anechoic chamber.